Theoretical study of light scattering and emission from dense ensembles of resonant dipoles

Nicolaas Jacobus Schilder

NNT : 2016SACLO019

THESE DE DOCTORAT
DE L'UNIVERSITE PARIS-SACLAY

préparée à

L'INSTITUT D'OPTIQUE GRADUATE SCHOOL

ÉCOLE DOCTORALE N°572
Ondes et Matière (EDOM)

Spécialité de doctorat : Physique

par

Nicolaas SCHILDER

Theoretical study of light scattering and emission from dense ensembles of resonant dipoles

Thèse présentée et soutenue à Palaiseau, le 16 décembre 2016 :

Composition du jury :

M. Pierre PILLET	Président du jury	Laboratoire Aimé Cotton
M. Rémi CARMINATI	Rapporteur	Institut Langevin
M. Robin KAISER	Rapporteur	Institut Non Linéaire de Nice
Mme Agnès MAÎTRE	Examinatrice	Institut des NanoSciences de Paris
M. Jean-Jacques GREFFET	Directeur de thèse	Laboratoire Charles Fabry
M. Antoine BROWAEYS	Co-directeur de thèse	Laboratoire Charles Fabry
M. Aloyse DEGIRON	Invité	Institut d'Électronique Fondamentale

Contents

Acknowledgements

It is with pleasure that now I can thank those with whom I had the opportunity to interact with and to interfere with constructively over the last couple of years.

One interaction that was crucial in the professional choices I have made afterwards, was with Omar El Gawhary at Delft University of Technology in the academic year 2010-2011. He organized a journal club on negative refraction. Both the topic and the inner enthousiasm on physics of Omar convinced me to do both my BSc. and MSc. theses in the optics research group in Delft under supervision of Paul Urbach. In Delft I had the opportunity to work with Silvania Pereira and Aurèle Adam as well. I would like to thank all of them for the profound scientific discussions we have had, all of your enthousiasm, passion and the curiosity in my Master thesis work on hyperbolic metamaterials.

My next step was doing a Ph.D. at Institut d'Optique. I am very grateful to both Jean-Jacques Greffet (nanophotonics and electromagnetism research group) and Antoine Browaeys (quantum optics research group) for having agreed on working during three years on an interdisciplinary topic with me that has led to the current manuscript. As from the beginning on, people told me that I was very lucky with both Jean-Jacques and Antoine as being my supervisors, since they are both great scientists and pedagogically strong. After having worked with them, I can approve this. The recurrent afternoon meetings that sometimes continued during the beginning of the evening perfectly illustrate to what extent we were able to learn and discuss together. Another aspect of both Jean-Jacques and Antoine that I would like to highlight is their availability. Their office doors are always open and they are always eager to discuss, even though they both have a lot of commitments. Thanks for this as well!

Apart from that I would like to thank Jean-Jacques for the many opportunities he gave me to present my work outside the institute. Thanks to having attended several conferences and workshops, I could learn what other research is done in other groups in France and elsewhere and I could extend my professional network. I have also had the chance to teach tutorials of courses that were taught by Jean-Jacques. He both trusted me in teaching his tutorials in French and he supported me and the other teaching assistants perfectly. Thank you very much for having been my colleague and supervisor over the last three years! You gave me plenty of useful anecdotes and lessons that I will take with me.

Something particular to Antoine that I appreciated are the pats on the shoulder I could receive in good and less good moments. I believe he has a very unique and social way of leading a team. The care for your students translated in the fact that you, while being a group leader, regularly even climbed two stairs to discuss with me about physics. I also want to thank Antoine very much for having been my colleague and supervisor over the last three years!

My research being theoretical, I obviously had a strong interaction with Jean-Paul Hugonin as well. Thanks to Jean-Paul I could numerically study non-trivial electromagnetic problems in an unprecedented accuracy and speed. His door is also always open and he is always very happy to discuss about a new problem. Although we believe that time progresses with the same pace for all of us, sometimes I had the impression that the time of Jean-Paul goes slower: he realizes powerful codes in such a very short time! His quick response, powerful codes and still very modest personality, make him a legend inside the group. Thank you so much for the last three years Jean-Paul! I will take reticolo with me, wherever I will be.

Christophe Sauvan is my next colleague that I would like to thank a lot. Apart from being a very nice, kind and modest person, he is also very rigorous. Whenever he says something, you can be sure that he has thought about it thoroughly. I appreciated this quality a lot. Other characteristics of Christophe is that he takes care of his colleagues and is able to create harmony. Thank you very much Christophe for having worked together the last three years and showing me a very rigorous and kind way of doing physics.

The interactions with Yvan Sortais were very fruitful as well. Yvan had a strong and positive influence on the papers and presentations. Whenever he analyzes a document or presentation, you can be sure that everything has be taken into considerations. On top of that he has a good sense of humor. Thank you very much Yvan for your input in the project over the last three years.

Next, I would like to thank the jury members for having accepted to read and comment my thesis, especially knowing that the December month is typically filled with many Ph.D. defenses in France! Thank you Pierre Pillet, Rémi Carminati, Robin Kaiser, Agnès Maître and Aloyse Degiron.

During my thesis I have had the opportunity to teach labworks and tutorials. Teaching being one of my passions, I am very grateful to my colleagues with whom I could share this passion. In particular, I want to thank Matthieu Boffety, Jean-Jacques Greffet, Lionel Jacubowiez, François Marquier, Yvan Sortais and Julien Villemejane.

Academic research groups are known for being very dynamical, i.e., the group members change a lot in course of time. I have had the occasion to talk, discuss, laugh and share enthousiasm for physics with many colleagues during my thesis: Philippe Ben-Abdallah, Henri Benisty, Mondher Besbes, Florian Bigourdan, Cédric Blanchard, Marie-Christine Dheur, Ioana Doyen, Benjamin Habert, Stephan Jennewein, Anthony Jouanin, Mathieu Langlais, Ivan Latella, Quentin Lévesque, François Marquier, Anton Ovcharenko, Emilie Sakat, Karthik Sasihithlu, Ilan Shlesinger, Benjamin Vest, Léo Wojszvzyk, Cheng Zhang. I would like to thank each of you very much for either your input in my Ph.D. or (the mathematical or) the very nice time we have had at the institute together. One should not underestimate the importance of having nice people surrounding you at work. You were definitely very nice people and I become quite melancholic when thinking about the many funny moments I have had with you. Two of these moments were definitely in the south of Spain and in Volendam, where I went to with a few of you. At last I would like to thank Ilan Shlesinger and Benjamin Vest who guarantee the continuation of my work and more. Based upon our interactions I am sure that the project is lucky of having both

of you involved, since you form a strong experimental and theoretical team!

Apart from having luck at work with my colleagues, I was also very lucky for getting an appartment at the "Cité internationale universitaire de Paris". Over the last three years I have met an enormous amount of people over there. All of them forming together a very international, social, intelligent and diverse group of friends. I would like to highlight a few friends with whom I was in the residents' committee 2014/2015 of Collège Franco-Britannique: Yosr Bouassida, Elena Carloni, Georges Ibrahim, Inna Ivanova, Elias Makoukji, Eduardo Queiroz Peres, Nataly Samoilenko and Zhiyan Zhao. Ever since our mandate, we stay in touch and we organize activities together. This cannot be considered obvious and it is also therefore that I cherish the moments with you guys. Thank you so much for our friendship and your support during my thesis!

During my thesis I went home every now and then to meet up with family and friends over there. It is during the moments you do not see them a lot that you appreciate them much more than before. Everytime I came back I could expect some phonecalls of friends to meet up. My weekends here were never boring, thanks to them. My family was also always ready to make my weekend perfect and I saw their happiness of having their "lost child" with them. I highly admire my grandparents and parents for the way they dealt with their first child or grandchild having plans to go abroad for a long time. They supported me with everything and they have always trusted in me. I could even count on some visits of them in Paris, thank you so much!

Tot slot zou ik in het bijzonder mijn overgrootvader Piet Hutzezon willen bedanken. Helaas overleed hij enkele weken voor mijn vertrek naar Parijs voor mijn promotieonderzoek, maar hij wist dat en waarom ik naar Parijs zou vertrekken voor drie jaar. Ik voel me zeer bevoorrecht dat ik tot mijn 23'ste heel veel met u heb mogen spreken. Het onvoorwaardelijke vertrouwen dat u in mij had, zal ik nooit meer vergeten!

Chapter 1

Introduction

In this Ph.D. thesis we study theoretically light scattering and emission by dense, disordered, and resonant systems. More specifically, we study (1) light scattering by a dense cloud of cold atoms, and (2) light emission by a dense film of quantum dots that is coupled to a plasmonic metasurface. This Ph.D. project is part of a collaboration between the group of prof. dr. Jean-Jacques Greffet and the group of dr. Antoine Browaeys. Both groups are part of Laboratoire Charles Fabry at Institut d'Optique in Palaiseau (France). The group of Browaeys has conducted experimental research on resonant light scattering from clouds of cold rubidium-87 atoms. This work concerns the same atomic systems, but the study is theoretical.

In this first chapter we introduce the main topics of interest of this Ph.D. thesis.

1.1 Light scattering

Light scattering is the physical phenomenon of the deflection of light due to the encounter of an object. Some examples of everyday situations where light scattering occurs are: light scattering by molecules in the sky, reflection of light by a rough surface, and light scattering by milk. These examples illustrate that the consequences of light scattering are experienced by everyone on a daily basis.

Although light scattering is perceived by everyone and there exists extensive literature of this topic, there is still a lot of research going on in the field of light scattering from random media. When we consider light scattering from disordered media, we realize there are actually many different regimes of light scattering. Each regime is characterized by a set of parameters. Examples of such parameters are: (1) resonant or non-resonant light scattering, (2) the size of the scatterers, (3) the density of scatterers, (4) the size of the ensemble of scatterers, (5) elastic or inelastic scattering, (6) the energy level structure of the scatterers, (7) position correlations of scatterers, (8) the oscillator strength of the electric dipole transition, and (9) the intensity of the incident beam. The large variety of light scattering regimes makes it an interesting topic.

We are mainly interested in the interplay between light scattering and interactions between scatterers. The adjective "dense" in this thesis is related to the strength of these interactions. As will become clear in Chapter 2, a cloud is considered dense for resonant light scattering when the average inter-scatterer distance $\langle r \rangle < \lambda/(2\pi)$, where λ is the resonant wavelength. Under this condition, the interactions between the scatterers are significant compared to the coupling between the scatterers and the vacuum electromagnetic field.

1.2 Interactions lead to collective modes

Since we are interested in the effect of strong interactions between resonant scatterers in a disordered ensemble on light scattering, let us first consider some well-known situations encountered in solid state physics of ordered systems in which interactions have an important influence on the modes of the system.

First, we consider a one dimensional periodic chain of N atoms, each atom being able to move around its equilibrium position. When we assume there is no interaction between the atoms, the atoms can be considered independent. This simple model corresponds to the Einstein model of a solid where all atoms oscillate at the same frequency. Next, we include interactions and we assume the atomic displacement to be small, so that the coupling between adjacent atoms can be modeled by a harmonic spring. The introduction of an interaction leads to normal modes. The mechanical normal modes that exist in a solid state medium are called phonons, which are *collective* lattice vibrations. The N degenerate energy levels become a phonon band structure due to the interaction. The important message here is that a collective response of the system is due to the presence of an interaction between the individual particles. This interaction changes the way the ensemble of particles should be studied: not as an ensemble of independent particles, but as an ensemble of collective modes.

Similarly, the Drude model of electric conductivity treats electrons as independent particles and the electric resistivity originates from collisions of electrons on any object that they encounter during electronic transport. It is under the introduction of electron-electron interactions (Coulomb interaction) that collective mechanical excitations are predicted, called plasmons [1]. Plasmons are normal modes of the system. Close to the plasmon frequency the response of electrons to an external excitations strongly deviates from the Drude model that treats electrons as independent entities. It is again the presence of interactions between individual particles that gives rise to collective modes.

1.3 Resonant light scattering from a dense cloud of cold atoms

Similar to the two examples given in the previous section, there exists an interaction between atoms due to light induced dipoles. This interaction is the resonant dipole-dipole interaction. We can modify the interaction strength between atoms in two ways: either by varying the average inter-atomic distance or by changing the frequency of the incident wave with respect to the resonant frequency of each atom. A disordered cloud of cold atoms is therefore an interesting platform to study the interplay between light scattering and the interaction between the scatterers.

However, creating a strongly interacting cloud of atoms is complicated. In order to have a strongly interacting cloud of atoms, one needs to respect the following two conditions: (1) all atoms need to have a large dipole moment, so they all need to be resonantly excited at the same time. Therefore, they all need to have the same resonance frequency. The presence of the Doppler effect in for example a hot atomic vapor leads to a spread of the resonance frequencies, effectively reducing the resonant dipole-dipole interactions. Hence, we need a cold atomic cloud. (2) The cold atomic cloud needs to be dense, i.e., many atoms need to be present inside a volume of λ^3.

Experimentally, it turns out to be difficult to satisfy both conditions. It is around the time this Ph.D. project started, October 2013, that the group of Browaeys had demonstrated that it is possible to load a wavelength-size dipole trap with a few hundred cold atoms, so that the atomic cloud can be considered dense according to the definition of dense in this work [2–4]. By both varying the number of atoms inside the trap and the laser frequency, we are in the position to study the transition of independent light scattering towards scattering mediated by collective modes.

1.4 Topics of this thesis

In order to have strong interactions between dipoles, we need an atomic system where all dipoles have a large dipole moment. By studying light scattering from dense clouds of cold atoms, we try to satisfy this condition. However, strong interactions are themselves believed to prevent any coherence effects to occur for *subwavelength-size* atomic systems [5, 6]. The prevention of coherence effects can be understood by the fact that very strong resonant dipole-dipole interactions between atoms can change their resonance frequency. As the atoms are randomly placed in a trap, they all experience a different interaction with the other atoms, thereby leading to strong inhomogeneous broadening. On the other hand, we might expect that interactions generate collective modes similar to phonons or plasmons. While these modes, called polaritons, are introduced in ordered systems, we may expect to observe delocalized modes for random systems. Such delocalized modes would produce spatial coherence in a disordered system. Hence, we ask ouselves the question: does *collective* light scattering occur in a *dense and wavelength-size* cloud of cold atoms? This question can be formulated differently: should a dense and cold atomic cloud be modeled as an ensemble of independent scatterers or in terms of collective modes, even though interatomic interactions can be so strong that the resonance frequency of each atom changes?

The above question is related to the question if a dense cloud of cold atoms can optically be described by a refractive index. If such a cloud can be described by a refractive index of refraction, light diffraction, which is intrinsically a coherence effect, can take place for a wavelength-size cloud. The amount of diffracted light depends non-linearly on the index of refraction. Similarly, if the dipole moments of the atoms are aligned and the number of atoms increases, it is expected that the ensemble emits more than an ensemble of independent emitters would do, due to constructive interferences between the emitted electric fields. We will study how the refractive index emerges as the atomic density increases and also how collective eigenmodes of the atomic system emerge (or not). By doing so, we will be able to study the connection between a macroscopic model (refractive index) and a microscopic model (atoms) of the atomic cloud.

When one studies a system for which the density gradually increases, a question that arises is how the system moves from a few atoms present in the cloud that scatter light in all directions, towards a homogeneous particle described by an effective refractive index that diffracts light. Such a problem is called a homogenization problem. A question that will be addressed in this work can be formulated as follows: is it possible to describe the optical response of a dense atomic cloud for resonant light scattering *uniquely* by an effective refractive index? Another question is: is it always possible to reach the homogenization regime by increasing the density? Whereas this seems to be the case when moving from a dilute gas to a liquid phase, we will see that subwavelength volumes of strongly interacting cold atoms cannot be homogenized.

Since we are interested in the effects of strong resonant dipole-dipole interactions on the optical behavior of a dense ensemble of scatterers, we will also study a dense ensemble of quantum dots. Motivated by recent experiments performed in the group of dr. Aloyse Degiron at the Institut d'Électronique Fondamentale, Orsay (France), we will study light emission from a dense ensemble of quantum dots embedded in a system that was studied in that group. In this group, they study experimentally the application of quantum dots in quantum-dot based light-emitting devices. An important question for the modeling of these devices is if these quantum dots could be modeled as individual quantum dots or if they should be modeled as an ensemble for which collective modes can be defined. The answer to this question has a big influence on the way such a quantum-dot based light-emitting device needs to be modeled.

1.5 Content

This thesis is organized as follows: **Chapter 2** describes the theory that is needed to understand light scattering as it is treated in what follows. At the end of the chapter the relaxation of energy in an atomic system is treated quantum mechanically. This treatment will allow to establish a connection between (classical) evanescent waves and (quantum) virtual photons. In **Chapter 3**, we will use the notions as introduced in Chapter 2 to study theoretically the experimental results obtained by the group of Browaeys [4,7] on light scattering from a microscopic cloud of cold rubidium-87 atoms for which strong resonant dipole-dipole interactions are expected. From that chapter it will follow that light scattering from a microscopic cloud containing a few hundred cold atoms occurs partially as if the cloud were a homogeneous medium described by a refractive index. In **Chapter 4** we introduce the concept of polaritonic modes in the microscopic description of an atomic cloud and identify these polaritonic modes with Fabry-Perot-like modes of an effective particle. It follows that light scattering is dominated by only a few modes out of all the collective modes that exist, namely the polaritonic modes. This chapter complements Refs. [8, 9] by studying both the eigenvalues and the eigenvectors at the same time and proving the ideas that were presented in the aforementioned works, but this time also for dense atomic systems. In **Chapter 5** we will treat another aspect of light scattering, namely *fluctuations* in light scattering. We ask ourselves the question if a resonant atomic system can be homogenized, i.e., is it possible to describe the optical response of an atomic cloud uniquely by an effective refractive index? This question is important for the understanding of recent experimental works on resonant light scattering. In the last chapter, **Chapter 6**, we replace the atoms by inhomogeneously broadened colloidal quantum dots. We discuss the optical description of a dense ensemble of quantum dots: can the quantum dots be seen as independent entities or should they be considered as being dependent. The answer to this question is needed to develop a model for the study of electroluminescence from a dense film of colloidal quantum dots placed in near vicinity of plasmonic nanoantennas [10, 11]. We propose a model to describe the coupling between quantum dots and a two-dimensional array of plasmonic nanoantennas. The presence of this plasmonic metasurface leads to a modification of the electroluminescence signal. The proposed model of electroluminescence is an adapted version of the conventional theory of electroluminescence from a light-emitting diode.

Chapter 2

Classical and quantum treatment of light scattering

In this thesis we study light scattering from an ensemble of scatterers, e.g., atoms or quantum dots. In Chapter 1 we noted that there exist many regimes of light scattering. We are interested in light scattering from strongly interacting systems, where the interaction is the resonant dipole-dipole interaction in this work. Strong interactions may occur when scatterers are in the near-field region of each other, i.e., when the inter-particle distance is much smaller than the wavelength of the incident wave. Due to strong resonant dipole-dipole interactions in the atomic systems we study, light typically gets scattered many times before it leaves the atomic cloud. We therefore need to consider light scattering that goes beyond the single scattering regime, which is called multiple scattering regime. In this chapter we introduce the necessary concepts to understand multiple scattering theory. This chapter supports the main results that are presented in this thesis.

In Chapter 6 we will discuss the interaction between light and an ensemble of quantum dots. As opposed to cold atoms that all have the same resonance frequency, quantum dots are inherently inhomogeneously broadened, i.e., each quantum dot has a different resonance frequency, which is due to fabrication. Inhomogeneous broadening leads to weaker resonant dipole-dipole interactions. The discussion about multiple scattering will allow us to define a parameter that can quantitatively distinguish both regimes of strong and weak resonant dipole-dipole interactions, both for atoms and quantum dots.

Light scattering is an example of a topic that is of interest for both the classical and quantum optics communities. In this chapter, we will also discuss light scattering within the quantum optics framework. It is expected that both theories give different results for light scattering, since an electric dipole transition in quantum optics can be saturated, which is not possible for a classical dipole. Although a dipole in quantum optics is therefore fundamentally different than one in classical optics, we will show that there is a regime in which both classical and quantum optics predict the same results for light scattering: the weak-excitation regime. No saturation effects are present in the weak-excitation regime.

In strongly interacting systems, dipoles are within each other's near field. It is known from classical optics that evanescent waves exist in the near-field region of any dipole and that they have a major influence on the classical resonant dipole-dipole interaction when two scatterers are in each other's near field. From a quantum optics point of view, systems that are in each other's vicinity are interacting via both real and virtual photons. In the last section of this chapter, we will discuss how (classical) evanescent waves are related to (quantum) virtual photons.

2.1 Polarizability and electric field of a resonant dipole

In this section we recall the electric field created by an electric dipole and the optical response of a resonant dipole upon illumination. For this, we start with a more general situation which will be useful in Chapter 6 on quantum dots embedded in an inhomogeneous electromagnetic environment. We assume to have a continuous electromagnetic environment described by a relative permittivity or dielectric constant ε_r, and the presence of some electromagnetic sources (electric dipoles, quadrupoles etc.). The sources are represented by the polarization density distribution $\tilde{\mathbf{P}}$, where the tilde indicates that the quantity has been Fourier transformed with respect to the time variable [12]:

$$(\nabla^2\bar{\bar{\mathbb{1}}} - \nabla\nabla)\tilde{\mathbf{E}}(\mathbf{r},\omega) + \frac{\omega^2}{c^2}\varepsilon_r(\mathbf{r},\omega)\tilde{\mathbf{E}}(\mathbf{r},\omega) = -\mu_0\omega^2\tilde{\mathbf{P}}(\mathbf{r},\omega), \tag{2.1}$$

where ω is the angular frequency, $c = 1/\sqrt{\varepsilon_0\mu_0}$ the speed of light in vacuum, ε_0 the permittivity, μ_0 the permeability, and $\tilde{\mathbf{P}}(\mathbf{r},\omega)$ is related to the current density $\mathbf{J}$ by $\tilde{\mathbf{P}}(\mathbf{r},\omega) = (-i\omega)^{-1}\tilde{\mathbf{J}}(\mathbf{r},\omega)$. From now on, we will omit the tilde above the Fourier-transformed quantities and also the frequency variable within brackets; both are implicit in the notation $\mathbf{E}(\mathbf{r})$. We notice that we have an inhomogeneous differential equation, where the polarization density is the source of an electromagnetic field. The particular solution of the differential equation, Eq. 2.1, is

$$\mathbf{E}(\mathbf{r}) = \mu_0\omega^2 \iiint \bar{\bar{G}}(\mathbf{r},\mathbf{r}')\mathbf{P}(\mathbf{r}')d^3\mathbf{r}', \tag{2.2}$$

where $\bar{\bar{G}}(\mathbf{r},\mathbf{r}')$ is the solution of Eq. 2.1 with $-\mu_0\omega^2\mathbf{P}(\mathbf{r})$ being replaced by the Dirac distribution $-\delta(\mathbf{r}-\mathbf{r}')\bar{\bar{\mathbb{1}}}$. The double bar indicates that the quantity is a matrix. $\bar{\bar{G}}(\mathbf{r},\mathbf{r}')$ is called the Green's tensor or dyadic Green's function. The Green's tensor describes the electric field produced by a pointlike source. In this thesis we mainly discuss light scattering by an ensemble of scatterers in a homogeneous medium. For a homogeneous medium with refractive index n, the Green's tensor for $\mathbf{r} \neq \mathbf{r}'$ reads

$$\bar{\bar{G}}(\mathbf{r},\mathbf{r}') = \left(\bar{\bar{\mathbb{1}}} + \frac{1}{k^2}\nabla\nabla\right)G(\mathbf{r},\mathbf{r}'), \tag{2.3}$$

where

$$G(\mathbf{r},\mathbf{r}') = \frac{e^{ik|\mathbf{r}-\mathbf{r}'|}}{4\pi|\mathbf{r}-\mathbf{r}'|} \tag{2.4}$$

is the scalar Green's function, with $k = n\omega/c$. Unless stated differently, the scatterers are placed in vacuum, so $n = 1$.

Throughout this work we consider light scattering by an ensemble of scatterers. We assume the scatterers to be very small compared to the optical wavelength and therefore we use the electric dipole approximation. The polarization density in Eq. 2.1 can then be replaced by the electric dipole moment $\mathbf{p}$, according to $\mathbf{P}(\mathbf{r}) = \sum_i \mathbf{p}_i\delta(\mathbf{r}-\mathbf{r}_i)$, where the subscript i indicates to which particle the dipole moment belongs.

In linear optics, the dipole moment and the electric field are linearly related by the polarizability matrix $\bar{\bar{\alpha}}(\omega)$:

$$\mathbf{p}_i = \varepsilon_0\bar{\bar{\alpha}}(\omega)\mathbf{E}(\mathbf{r}_i), \tag{2.5}$$

where the electric field is the total electric field at the position of the dipole, apart from the self field, i.e., the electric field produced by the dipole itself and evaluated at its own position.

In this work, the scatterers are taken to be classical scatterers and therefore isotropic (in atomic physics a classical resonant scatterer corresponds to a $J = 0 \rightarrow J = 1$ transition, where J is the total angular momentum and is the sum of the spin angular momentum S and the orbital angular momentum L). For isotropic scatterers, the polarizability is a scalar quantity [$\bar{\bar{\alpha}}(\omega) = \alpha(\omega)\bar{\bar{\mathbb{1}}}$]. The classical polarizability is

$$\alpha(\omega) = \frac{6\pi c^3 \Gamma_0}{\omega_0^2(\omega_0^2 - \omega^2 - i\omega\Gamma_0)}, \tag{2.6}$$

where ω_0 is the angular frequency corresponding to the energy difference between two energy levels and Γ_0 is the spontaneous emission rate. Classically, Γ_0 is related to the power emission of an oscillating dipole [12]. When near-resonance light scattering is studied, the approximation $\omega + \omega_0 \approx 2\omega_0$ can be made, which gives a commonly used form of the polarizability

$$\alpha(\omega) = \frac{3\pi c^3 \Gamma_0}{\omega_0^3\left(\omega_0 - \omega - i\frac{\Gamma_0}{2}\right)}. \tag{2.7}$$

The imaginary part of the polarizability is a Lorentzian function; a function which will often return in the next chapters. For completeness, let us note that this polarizability is also valid for a two-level system [13]. However, the optical response of a two-level system depends on the polarization of the electric field. The diagonal elements of the polarizability matrix are therefore not the same.

2.2 Light scattering from an ensemble of scatterers

We have now the tools to classically describe light scattering from an ensemble of electric dipoles.

2.2.1 Light scattering from a single atom

First, let us discuss light scattering from a single atom placed at position $\mathbf{r}_0 = (0, 0, 0)$ in vacuum. A plane wave propagating along the z axis with angular frequency $\omega = ck$ [$\mathbf{E}(\mathbf{r}) = \mathbf{E}_{\text{inc}} \exp(ikz)$] is incident upon that atom. From Eq. 2.5 it is seen that the induced dipole moment is given by $\mathbf{p} = \varepsilon_0 \alpha(\omega)\mathbf{E}_{\text{inc}}$. According to Eq. 2.2, the oscillating dipole creates an electric field

$$\mathbf{E}(\mathbf{r}) = \frac{\omega^2}{c^2}\alpha(\omega)\bar{\bar{G}}(\mathbf{r}, \mathbf{0}; \omega)\mathbf{E}_{\text{inc}}, \tag{2.8}$$

where $\mathbf{r}$ is the observation point. The total scattered power is given by

$$P_{\text{sc}}(\omega) = \frac{\omega^4}{c^4}\frac{|\alpha(\omega)|^2}{6\pi}\frac{\varepsilon_0 c}{2}|\mathbf{E}_{\text{inc}}|^2. \tag{2.9}$$

When $\omega \ll \omega_0$, we obtain the well-known ω^4 dependence of the scattered power for Rayleigh scattering [14, 15]. However, for near-resonance light scattering ($\omega \approx \omega_0$), the presence of a resonance in the polarizability $\alpha(\omega)$ dramatically alters light scattering.

From the total scattered power, we can deduce the effective scattering cross section, which is defined as

$$P_{\text{sc}}(\omega) = \sigma_{\text{sc}}(\omega)|\mathbf{S}|, \tag{2.10}$$

where $\mathbf{S}$ is the Poynting vector of an incident plane wave. For a plane wave $|\mathbf{S}| = \varepsilon_0 c/2 \times |\mathbf{E}_{\text{inc}}|^2$, so that the effective scattering cross section is given by

$$\sigma_{\text{sc}}(\omega) = \frac{\omega^4}{c^4} \frac{|\alpha(\omega)|^2}{6\pi}. \tag{2.11}$$

We note that on resonance $\sigma_{\text{sc}} = 3\lambda_0^2/(2\pi)$, with λ_0 being the resonance wavelength. The effective scattering cross section is at resonance much larger than the geometrical cross section of a single atom.

2.2.2 Light scattering from multiple atoms

The presence of more than one scatterer makes light scattering in general more complicated. This can be seen by replacing

$$\mathbf{P}(\mathbf{r}) = \sum_i^N \mathbf{p}_j \delta(\mathbf{r} - \mathbf{r}_i) = \sum_i^N \varepsilon_0 \alpha(\omega) \mathbf{E}(\mathbf{r}_j) \delta(\mathbf{r} - \mathbf{r}_i) \tag{2.12}$$

in Eq. 2.1:

$$(\nabla^2 \bar{\bar{\mathbb{1}}} - \nabla\nabla)\mathbf{E}(\mathbf{r}) + \frac{\omega^2}{c^2}\mathbf{E}(\mathbf{r}) = -\frac{\omega^2}{c^2}\alpha(\omega) \sum_i^N \mathbf{E}(\mathbf{r})\delta(\mathbf{r} - \mathbf{r}_i). \tag{2.13}$$

The general solution of this differential equation is

$$\mathbf{E}(\mathbf{r}) = \mathbf{E}_{\text{inc}}(\mathbf{r}) + \frac{\omega^2}{c^2}\alpha(\omega) \sum_i^N \bar{\bar{G}}(\mathbf{r}, \mathbf{r}_i)\mathbf{E}(\mathbf{r}_i), \tag{2.14}$$

where the incident field $\mathbf{E}_{\text{inc}}$ is a homogeneous solution of Eq. 2.13. As opposed to the scattered electric field of a single atom (see Eq. 2.8), it is seen that the general solution given by Eq. 2.14 is in implicit form. There are at least three different ways of solving this set of equations. The first one is by solving Eq. 2.14 numerically. This is what will be considered in the current section. Two other ways are based on a series expansion of the electric field. One expansion is called the Born series expansion. With this expansion the electric field is substituted recursively in Eq. 2.14. When the recursion is stopped after applying it once, one has applied what is called the first-order Born approximation. More generally, when the recursion is stopped after n iterations, one has applied the nth-order Born approximation. In many cases, like for light scattering from the sky, the Born series expansion is very convenient. However, when near-resonance light scattering is concerned, the Born series expansion is less useful, since it is a divergent series near resonance [16]. The other series expansion we mention in this thesis is a so-called diagrammatic expansion [17]. The diagrammatic expansion leads to a perturbative solution of the scattered electric field in terms of the number density of scatterers. It is based on decomposing the electric field in an ensemble-averaged electric field and a fluctuating electric field. The diagrammatic expansion allows to calculate the effective dielectric constant of the random medium. It turns out that the diagrammatic expansion and the decomposition of the electric field lead to a more intuitive interpretation of light scattering than both the Born expansion and the exact solution for systems that are in the multiple scattering regime. The advantage of a series expansion as compared to numerically finding the solution is that it helps to create

some physical intuition. Yet, one should be careful to know to what extent the expansion is valid, since otherwise wrong conclusions might be drawn.

We start with looking for the exact solution of Eq. 2.13. Instead of inverting Eq. 2.14 immediately, we will pass by a set of coupled-dipole equations, since they will be useful later in this chapter. The electric field in Eq. 2.5 is given by

$$\mathbf{E}(\mathbf{r}_i) = \sum_{j=1, j\neq i}^{N} \mu_0 \omega^2 \bar{\bar{G}}(\mathbf{r}_i, \mathbf{r}_j)\mathbf{p}_j + \mathbf{E}_{\text{inc}}(\mathbf{r}_i), \tag{2.15}$$

where the dipole moments are the unknowns. Substitution of Eq. 2.15 into Eq. 2.5 gives a set of coupled-dipole equations in the presence of an incident field

$$\mathbf{p}_i = \frac{\omega^2}{c^2} \sum_{j=1, j\neq i}^{N} \left[\alpha(\omega)\bar{\bar{G}}(\mathbf{r}_i, \mathbf{r}_j)\mathbf{p}_j\right] + \varepsilon_0 \alpha(\omega)\mathbf{E}_{\text{inc}}(\mathbf{r}_i). \tag{2.16}$$

For classical dipoles, there are $3N$ unknowns (N dipoles, each one having three dipole moment components) and $3N$ independent equations (each dipole moment component from each dipole has its own equation). This set of equations can be written in matrix form:

$$\bar{\bar{A}}(\omega)\mathbf{P} = \varepsilon_0 \frac{3\pi c^3 \Gamma_0}{\omega_0^3}\mathbf{E}_{\text{inc}}, \tag{2.17}$$

where we have defined

$$\mathbf{P} = \begin{pmatrix} \mathbf{p}_1 \\ \mathbf{p}_2 \\ \vdots \\ \mathbf{p}_N \end{pmatrix},$$

which should not be confused with the polarization density vector,

$$\mathbf{E}_{\text{inc}} = \begin{pmatrix} \mathbf{E}_{\text{inc}}(\mathbf{r}_1) \\ \mathbf{E}_{\text{inc}}(\mathbf{r}_2) \\ \vdots \\ \mathbf{E}_{\text{inc}}(\mathbf{r}_N) \end{pmatrix},$$

and the matrix

$$\bar{\bar{A}}(\omega) = \begin{pmatrix} (\omega_0 - \omega - i\frac{\Gamma_0}{2})\bar{\bar{\mathbb{1}}} & \frac{-3\pi\omega^2 c\Gamma_0}{\omega_0^3}\bar{\bar{G}}(\mathbf{r}_1, \mathbf{r}_2; \omega) & \dots \\ \frac{-3\pi\omega^2 c\Gamma_0}{\omega_0^3}\bar{\bar{G}}(\mathbf{r}_2, \mathbf{r}_1; \omega) & (\omega_0 - \omega - i\frac{\Gamma_0}{2})\bar{\bar{\mathbb{1}}} & \\ \vdots & & \ddots \end{pmatrix},$$

of which all submatrices are of size 3×3. This form of $\bar{\bar{A}}$ assumes the atomic polarizability to be given by Eq. 2.7. From this matrix equation, the vector $\mathbf{P}$, which contains all dipole moments, can be obtained by inverting the matrix $\bar{\bar{A}}$. By solving the set of coupled-dipole equations, we find the dipole moments. Once the dipole moments $\mathbf{p}_i$ are known, the total electric field can be calculated:

$$\mathbf{E}(\mathbf{r}) = \mu_0 \omega^2 \sum_{i=1}^{N} \bar{\bar{G}}(\mathbf{r}, \mathbf{r}_i)\mathbf{p}_i + \mathbf{E}_{\text{inc}}(\mathbf{r}), \text{ for all } \mathbf{r} \text{ different from } \mathbf{r}_i. \tag{2.18}$$

We stress that the hereby obtained electric field is exact and does not introduce new approximations to the once already given in Section 2.1: classical dipole assumption, electric dipole approximation, the dipoles have a single resonance frequency ω_0. This is as opposed to any truncated series expansion. When a series expansion is truncated, not all resonant dipole-dipole interactions are properly taken into account. We will briefly discuss this in Section 2.2.4.

In this section we described an approximate way of calculating the scattered electric field by means of a Born series expansion and an exact way of solving light scattering from an ensemble of N scatterers. In the next section we will introduce the ensemble-averaged and fluctuating electric field that are necessary within the diagrammatic expansion. The introduction of these quantities will be particularly useful in Chapter 3.

2.2.3 Introduction of ensemble-averaged and fluctuating electric fields

Another way of studying light scattering from a random medium follows from realizing that random media can be decomposed in a continuous part and a fluctuating part. This idea has profound consequences on the way we understand light scattering.

Because of the random positions of the atoms in a cloud, there exist density fluctuations inside the gas which give rise to fluctuations of the polarization density vector $\mathbf{P}(\mathbf{r})$. For a single realization of the atomic positions $\mathbf{r}_i$, the polarization density can be decomposed into an ensemble-averaged polarization density $\langle\mathbf{P}(\mathbf{r})\rangle$ and a fluctuating polarization density $\delta\mathbf{P}(\mathbf{r})$: $\mathbf{P}(\mathbf{r}) = \langle\mathbf{P}(\mathbf{r})\rangle + \delta\mathbf{P}(\mathbf{r})$, where $\langle\delta\mathbf{P}(\mathbf{r})\rangle = 0$. The ensemble average $\langle\cdots\rangle$, as used throughout this work, is an averaging of quantities that are calculated for several realizations of the atomic cloud. For each realization, the atomic positions are changed according to a given probability distribution. An example of a probability distribution for each coordinate of the atom is the Gaussian distribution in the case of atoms being trapped in an optical trap. Similar as for the polarization density vector, the electric field can be decomposed into an ensemble-averaged field $\langle\mathbf{E}\rangle$ and a fluctuating field $\delta\mathbf{E}$: $\mathbf{E}(\mathbf{r}) = \langle\mathbf{E}(\mathbf{r})\rangle + \delta\mathbf{E}(\mathbf{r})$. It can be shown that the ensemble-averaged electric field satisfies Helmholtz' equation with an effective dielectric constant [16–20]:

$$\nabla^2\langle\mathbf{E}(\mathbf{r})\rangle + \varepsilon_{\text{eff}}(\mathbf{r})\frac{\omega^2}{c^2}\langle\mathbf{E}(\mathbf{r})\rangle = -\frac{\omega^2}{c^2}[\varepsilon_{\text{eff}}(\mathbf{r}) - 1]\mathbf{E}_{\text{inc}}(\mathbf{r}). \tag{2.19}$$

From this equation it follows that the scattered ensemble-averaged electric field from a finite-size gas of randomly positioned atoms actually gets diffracted from that finite-size gas which is optically described by an effective dielectric constant ε_{eff}. From Eq. 2.19 it is seen that the diffracted field keeps the same polarization as the incident field. This is in contrast to the scattered fluctuating field which can lose its polarization after many scattering events due to the randomly orientated dipole moments. The fluctuating field is said to have forgotten its origin. For completeness, we mention that incoherent light scattering is governed by what is called the radiative transfer equation. The radiative transfer equation is similar to the Boltzmann transport equation and amounts basically on a detailed balance of scattering and absorption in a small differential volume element. Incoherent light scattering occurs in all directions as opposed to coherent light scattering that follows a diffraction pattern.

A quantity that is measured in the lab is the power. The measured power is the time-averaged Poynting vector integrated in the far field over a finite solid angle defined by the optical axis of the detection system and its numerical aperture NA:

$$\begin{aligned} P &= \int_{\mathrm{NA}} \frac{\varepsilon_0 c}{2} |\mathbf{E}(\mathbf{r})|^2 r^2 d\Omega = \frac{\varepsilon_0 c}{2} \int_{\mathrm{NA}} \Big[|\langle \mathbf{E}(\mathbf{r}) \rangle|^2 + \langle |\delta \mathbf{E}(\mathbf{r})|^2 \rangle \Big] r^2 d\Omega \\ &\equiv \int_{\mathrm{NA}} [I_{\mathrm{coh}}(\theta, \varphi) + I_{\mathrm{incoh}}(\theta, \varphi)] r^2 d\Omega. \end{aligned} \tag{2.20}$$

In this equation, we have defined the "coherent intensity" as the energy flow from the ensemble-averaged electric field, and the "incoherent intensity" as the energy flow from the fluctuating field. This separation of intensities is very important throughout this thesis. The coherent intensity corresponds to light that gets diffracted from an effective homogeneous medium, whereas the incoherent intensity comes from light scattering by fluctuations in the sample. We will study both coherent and incoherent light scattering in Chapter 3.

Let us briefly discuss some different terminologies for the electric field, where the antonyms are given at each line:

- average – fluctuating,
- coherent – incoherent,
- collimated – diffuse.

The three words on the left are synonyms, like the three words on the right. The words average and fluctuating can be understood from the mathematical notation: $\langle \mathbf{E} \rangle$ (average) and $\delta \mathbf{E}$ (fluctuating). The terms coherent and incoherent are borrowed from the microwave community, where these terms are often used. The last terms: collimated and diffuse, are known in the field of optics. In optics it is known that the intensity of a collimated beam incident upon a lossless and scattering medium decays exponentially during propagation, according to Beer-Lambert law. The power that is lost from the collimated beam is scattered away and forms diffuse light.

The way we use the words coherent and incoherent might lead to confusion between people from the classical and quantum optics communities. In Chapter 5 of the textbook *Atom-Photon Interactions: Basic Processes and Applications*, coherent and incoherent light scattering are explained from a quantum optics perspective [21]. In that chapter, the scattered coherent power of an atom is proportional to the square of the expectation value of the dipole moment operator, whereas the incoherent power is proportional to the square of the fluctuations of the dipole moment operator. The calculation of the expectation value is done in a quantum mechanical way where the dipole moment operator is traced over all possible states of the dipole. For us, the average is an ensemble average (=estimator of the expectation value) over the scatterer positions and therefore fundamentally different. This is why the terms *coherent* and *incoherent* intensity are not the same in classical and quantum optics. However, we will use the terms coherent and incoherent light scattering often in this thesis and they are related to the classical meaning of it.

At last, let us repeat that coherent and incoherent light scattering happens differently. Coherent light scattering follows a diffraction pattern, whereas incoherent light scattering occurs in all directions. Therefore, both forms of light scattering can be measured separately. There are at least two ways for measuring the coherent and incoherent powers individually. A first way is by means of the position of the detector with respect to the

probe beam, since coherent and incoherent light scattering do not occur in the same directions. A second way of separately measuring both powers is by using a polarizer, since for a strong scattering system, the diffuse field does not have the same polarization as the incident field. It is the first way of separately measuring the coherent and incoherent intensities that will be discussed in the next chapter, since two different experiments have been conducted in the group of Browaeys that are based on this idea. With this, we have illustrated qualitatively the intuitive understanding of light scattering that comes with the decomposition of the electric field.

2.2.4 Beyond the mean-field theory of optics

In the previous section we have introduced a decomposition of the electric field. We have seen that, according to Eq. 2.19, the coherent electric field gets diffracted from a homogeneous medium described by an effective dielectric constant.

In general, the effective dielectric constant of a cloud of resonant dipoles that are described by a polarizability α depends on both α and the atomic density distribution. This dependence can be very complicated, but it turns out that in most cases it is not. The simplest possible relationship is [22]

$$\varepsilon_{\text{eff}}(\omega) = 1 + \rho\alpha(\omega), \tag{2.21}$$

where ρ is the number density of scatterers. From solid state physics it is known that for dense systems one needs to take into account the local-field correction due to the screening of a dipole by the other dipoles surrounding it [22,23]. The relationship $\varepsilon_{\text{eff}}(\omega) = 1+\rho\alpha(\omega)$ then turns into the Lorentz-Lorenz relation

$$\frac{\varepsilon_{\text{LL}}(\omega) - 1}{\varepsilon_{\text{LL}}(\omega) + 2} = \frac{\rho\alpha(\omega)}{3}, \tag{2.22}$$

where we used the subscript LL to indicate that it is the effective dielectric constant as given by the Lorentz-Lorenz relation. We call the situation where an ensemble-averaged electric field gets diffracted by an effective object for which the dielectric constant satisfies the Lorentz-Lorenz formula *mean-field theory*. Beyond mean-field theory is defined as a system for which the dielectric constant does not satisfy Eq. 2.22. The presence of strong resonant dipole-dipole interactions would be a possible reason that light scattering from an atomic system should be described by beyond mean-field theory. Strong resonant dipole-dipole interactions lead to dependent light scattering, which is not included in Eq. 2.22 [24]. Equation 2.22 can be generalized by including light scattering processes that involve dependent light scattering processes like recurrent scattering: multiple scattering events between the same atoms.

More generally, the following relationship holds [17,18,20,25]:

$$\frac{\varepsilon_{\text{eff}}(\omega) - 1}{\varepsilon_{\text{eff}}(\omega) + 2} = \frac{\Sigma(\omega, \mathbf{k})}{3k^2}, \tag{2.23}$$

where Σ is the mass operator and is in general a complicated function. For the studies we present in this thesis, we do not need the full machinery of multiple light scattering. We are interested in an estimate of the importance of recurrent scattering that leads to beyond mean-field theory behavior of the atomic cloud [16,26,27]. An estimate for the importance

of recurrent scattering can be derived from Eq. 4.106 of Ref. [16]. Recurrent scattering becomes important for resonant scattering by a cold cloud of resonant scatterers when

$$\frac{9\pi\rho}{2k^3} > 1. \tag{2.24}$$

Similarly, it can be shown that for systems which present strong *inhomogeneous* broadening ($\Delta\omega \gg \Gamma_0$), the condition for having recurrent scattering becomes

$$\frac{9\pi\rho}{8k^3}\left(\frac{\Gamma_0}{\Delta\omega}\right)^2 > 1. \tag{2.25}$$

In this thesis we study mainly light scattering by a cold atomic cloud which is in the regime where mean-field theory fails, because of the presence of recurrent light scattering.

2.3 Relation between mean free path and system size

So far we have been discussing macroscopic bulk properties of an ensemble of scatterers. Next, we discuss the influence of the size of the system on light scattering. Systems with typical size L can either be in the single or multiple scattering regime. In the former case, the electric field gets on average only scattered once inside the cloud. In the latter case, there are more than one scattering events inside the system. A physical quantity that is needed to distinguish both regimes is the mean free path l_{mfp}, which is the average distance between two successive scattering events. A system is in the single scattering regime when $l_{\mathrm{mfp}} \gtrsim L$ and in the multiple scattering regime when $l_{\mathrm{mfp}} < L$. This mean free path corresponds in an effective medium to the decay length of collimated light, which is defined in the Beer-Lambert law by: $I(z) = I(0)\exp(-z/l_{\mathrm{mfp}})$. The mean free path can be related to the index of refraction by noting that the intensity of a beam propagating in an extended medium with index of refraction n_{eff} decays as: $I(z) = I(0)\exp(-2kn''_{\mathrm{eff}}z)$. By comparing both expressions for the light intensity, we find the relationship

$$l_{\mathrm{mfp}}(\omega) = 1/[2kn''_{\mathrm{eff}}(\omega)]. \tag{2.26}$$

It is only in a system where both $\varepsilon_{\mathrm{eff}} = 1+\rho\alpha$ and $\rho\alpha \ll 1$, that one can find the expression: $l_{\mathrm{mfp}}(\omega) = 1/[\rho\sigma_{\mathrm{sc}}(\omega)]$. This identity is expected not to be valid in the atomic systems that we study. However, the Beer-Lambert law is *always* valid for the collimated beam in an extended medium, so also in the presence of recurrent scattering.

2.4 Energy relaxation in quantum optics

As indicated at the beginning of this chapter, we will now treat light scattering by using quantum optics. Although a classical system corresponds in atomic physics to a transition between a $J = 0$ and $J = 1$ state, there is a big difference between the quantum optical response and the classical response of such a transition under illumination. In quantum optics, such a transition can be saturated, i.e., there are no electrons left in the ground state after the atom has absorbed a photon. This makes the system response nonlinear, since a second photon cannot be absorbed after the first one has been absorbed. This form of nonlinear response does not exist in classical optics. In this section we show that under

certain conditions both classical and quantum optics have the same set of coupled-dipole equations, which form the basis of light scattering as we have seen in Section 2.2.

In the formalism treated in this section, we assume the system to be initially excited; so there is no driving field throughout the derivation. We study how such a system relaxes under emission of a photon. To study the atomic relaxation, one often relies on the Weisskopf-Wigner theory to recover the exponential decay in time of a single atomic excitation [28]. An extension of the theory to a system of N interacting dipoles can be found in the work of Svidzinsky *et al.* [29]. In that work both the dipole moments and the electric field were taken to be scalar quantities. Since for dense atomic ensembles, the near-field interactions are important and need to be included, one needs to take into account the vectorial nature of the electric field. This has been done in Ref. [30]. In this section we will describe this vectorial Weisskopf-Wigner theory, since it shows the connection of a quantum optics and classical optics description of light emission from an ensemble of emitters [29]. It serves therefore as a bridge between classical and quantum optics.

Hamiltonian In order to calculate the time evolution of a given quantum state, the Hamiltonian is needed. The Hamiltonian $\hat{H} = \hat{H}_A + \hat{H}_F + \hat{H}_I$ contains three operators that are related to the atom energy ($\hat{H}_A$), the electromagnetic field energy ($\hat{H}_F$), and the interaction potential ($\hat{H}_I$) between the dipoles and the electric field of the vacuum. Under the electric dipole approximation and in the interaction picture, the total Hamiltonian is given by:

$$\begin{aligned}\hat{H} &= \sum_{j=1}^{N} \hbar\omega_0 \hat{\pi}_j^\dagger \hat{\pi}_j + \sum_{\mathbf{k},\lambda} \hbar\omega_{\mathbf{k}} \hat{a}_{\mathbf{k},\lambda}^\dagger \hat{a}_{\mathbf{k},\lambda} \\ &\quad + \sum_{\mathbf{k},\lambda}\sum_{j=1}^{N} g_{\mathbf{k},\lambda,j}\left[\hat{\pi}_j e^{-i\omega_0 t} + \hat{\pi}_j^\dagger e^{i\omega_0 t}\right] \cdot \left[\hat{a}_{\mathbf{k},\lambda}^\dagger e^{i(\omega_{\mathbf{k}} t - \mathbf{k}\cdot\mathbf{r}_j)} + \hat{a}_{\mathbf{k},\lambda} e^{-i(\omega_{\mathbf{k}} t - \mathbf{k}\cdot\mathbf{r}_j)}\right], \quad (2.27)\end{aligned}$$

where $\hat{\pi}_j = |g_j\rangle\langle e_j|$ ($\hat{\pi}_j^\dagger = |e_j\rangle\langle g_j|$) is the lowering (raising) operator for atom j; $\hat{a}_{\mathbf{k},\lambda}$ ($\hat{a}_{\mathbf{k},\lambda}^\dagger$) is the annihilation (creation) operator for the electric field of a plane wave with wave vector $\mathbf{k}$; λ is the polarization of the plane wave; ω_0 is the atomic frequency; and $\omega_{\mathbf{k}}$ is the photon frequency. The coupling strength of the dipoles to the vacuum field

$$g_{\mathbf{k},\lambda,j} = \omega_0 \frac{\mathbf{e}_{\mathbf{k},\lambda}\cdot\hat{\mathbf{p}}_j p_j}{\hbar}\sqrt{\frac{\hbar}{2\varepsilon_0\omega_{\mathbf{k}}V}} = g_{k,j}\mathbf{e}_{\mathbf{k},\lambda}\cdot\mathbf{p}_j, \quad (2.28)$$

where V is the quantization volume, $\omega_{\mathbf{k}} = ck$, $\mathbf{e}_{\mathbf{k},\lambda}$ the polarization of the electric field and $\hat{\mathbf{p}}$ the unit dipole moment vector, i.e., the polarization direction of the dipole. Very often, the terms containing the operators $\hat{\pi}\hat{a}$ and $\hat{\pi}^\dagger\hat{a}^\dagger$ are neglected in quantum optics. The common justification for this approximation is that these terms lead to integrals similar to $\int_0^t \exp[\pm i(\omega_0+\omega_{\mathbf{k}})t']dt'$. The integrand of this integral oscillates rapidly under integration and therefore gives zero. This is in contrast with the integrands of the form $\exp[\pm i(\omega_0 - \omega_{\mathbf{k}})t']$, when $\omega_{\mathbf{k}} \approx \omega_0$, which originate from the terms $\hat{\pi}^\dagger\hat{a}$ and $\hat{\pi}\hat{a}^\dagger$. This approximation where $\omega_{\mathbf{k}} \approx \omega_0$ and therefore the terms $\hat{\pi}\hat{a}$ and $\hat{\pi}^\dagger\hat{a}^\dagger$ are neglected in the Hamiltonian, is called the rotating wave approximation (RWA). In this section we will see that the RWA cannot be applied for systems where dipoles are in each other's near-field region. Since we are precisely interested in this kind of systems, we do not apply the RWA in this thesis and therefore keep the terms $\hat{\pi}\hat{a}$ and $\hat{\pi}^\dagger\hat{a}^\dagger$ in the Hamiltonian.

Wave function and its time evolution - Beyond the rotating wave approximation
The next step in calculating the time evolution of N atoms that initially share a single atomic excitation, is defining the wave function. By means of Weisskopf-Wigner theory, we will be able to derive the time evolution of the system and show under which conditions classical and quantum optics lead to the same set of coupled-dipole equations.

In their original work, Weisskopf and Wigner studied the relaxation of a single atom in vacuum [28]. The wave function for a single atom was chosen, within the Schrödinger picture, to be: $|\Psi(t)\rangle = \beta(t)\exp(-i\omega_0 t)|e\rangle|0\rangle + \sum_{\mathbf{k},\lambda}\gamma_{\mathbf{k},\lambda}(t)\exp(-i\omega_{\mathbf{k}}t)|g\rangle|1_{\mathbf{k},\lambda}\rangle$, where λ indicates the polarization of the plane wave with wave vector $\mathbf{k}$. When the RWA is applied, the *number of excitations* inside the system cannot vary in time. This wave function spans therefore the entire vector space of functions containing a single excitation initially. In the case of N atoms and by applying the RWA, we could similarly write the wave function as

$$\begin{aligned}|\Psi(t)\rangle &= \sum_{j=1}^{N}\beta_j(t)|g_1,\cdots,e_j,\cdots g_N\rangle|0\rangle \\ &\quad + \sum_{\mathbf{k},\lambda}\gamma_{\mathbf{k},\lambda}(t)|g_1,\cdots,g_N\rangle|1_{\mathbf{k},\lambda}\rangle,\end{aligned} \tag{2.29}$$

where we assumed that the system has been excited initially by a single excitation. However, we will not apply the RWA. We assume the wave function to be of the following form:

$$\begin{aligned}|\Psi(t)\rangle &= \sum_{j=1}^{N}\beta_j(t)e^{-i\omega_0 t}|g_1,\cdots,e_j,\cdots g_N\rangle|0\rangle \\ &\quad + \sum_{\mathbf{k},\lambda}\gamma_{\mathbf{k},\lambda}(t)e^{-i\omega_{\mathbf{k}}t}|g_1,\cdots,g_N\rangle|1_{\mathbf{k},\lambda}\rangle \\ &\quad + \sum_{m<n}\sum_{\mathbf{k},\lambda}\alpha_{mn,\mathbf{k},\lambda}(t)e^{-i(2\omega_0+\omega_{\mathbf{k}})t}|g_1,\cdots,e_m,\cdots,e_n,\cdots,g_N\rangle|1_{\mathbf{k},\lambda}\rangle.\end{aligned} \tag{2.30}$$

These additional states with coefficients α are the only difference with the wave function of Eq. 2.29, where the RWA has been applied. It is because of these states that we will arrive at a different solution then a derivation for which the RWA is applied. These states are therefore important, as we will observe during the derivation of the time evolution of the wave function. During the mathematical derivation of the time evolution of the wave function, we will pinpoint on places where the result differs from a derivation that applies the RWA.

In order to find the unknown coefficients of Eq. 2.30, the Schrödinger equation is written for the wave function given by Eq. 2.30:

$$\hat{H}|\Psi(t)\rangle = i\hbar\frac{d|\Psi(t)\rangle}{dt}. \tag{2.31}$$

The following step is to project the Schrödinger equation three times by different wave functions. The first projection is done with $|g_1,\cdots,e_{j'},\cdots g_N\rangle|0\rangle$, the second with $|g_1,\cdots,g_N\rangle|1_{\mathbf{k}',\lambda'}\rangle$, and the third projection with the wave function $|g_1,\cdots,e_{m'},\cdots,e_{n'},\cdots,g_N\rangle|1_{\mathbf{k}',\lambda'}\rangle$. By comparing the coefficients of the same states on both the left- and right-hand side of Eq. 2.31, the following three differential equations can

be obtained for the coefficients:

$$\begin{aligned}
\dot{\beta}_j(t) &= -i\sum_{\mathbf{k},\lambda} g_{\mathbf{k},\lambda,j}\gamma_{\mathbf{k},\lambda}(t)e^{-i(\omega_{\mathbf{k}}-\omega_0)t}e^{i\mathbf{k}\cdot\mathbf{r}_j} \\
&\quad -i\sum_{\mathbf{k},\lambda}\sum_{j'=1,j'\neq j}^{N} g_{\mathbf{k},j'}\alpha_{jj',\mathbf{k},\lambda}(t)e^{-i(\omega_{\mathbf{k}}+\omega_0)t}e^{i\mathbf{k}\cdot\mathbf{r}'_j}, \qquad (2.32)\\
\dot{\gamma}_{\mathbf{k},\lambda}(t) &= -i\sum_{j=1}^{N} g_{\mathbf{k},\lambda,j}\beta_j(t)e^{i(\omega_{\mathbf{k}}-\omega_0)t}e^{-i\mathbf{k}\cdot\mathbf{r}_j}, \qquad (2.33)\\
\dot{\alpha}_{mn,\mathbf{k},\lambda}(t) &= -ig_{\mathbf{k},\lambda,m}\beta_n(t)e^{i(\omega_{\mathbf{k}}+\omega_0)t}e^{-i\mathbf{k}\cdot\mathbf{r}_m} - ig_{\mathbf{k},\lambda,n}\beta_m(t)e^{i(\omega_{\mathbf{k}}+\omega_0)t}e^{-i\mathbf{k}\cdot\mathbf{r}_n}. \qquad (2.34)
\end{aligned}$$

Both $\gamma_{\mathbf{k}}(t)$ and $\alpha_{mn,\mathbf{k}}(t)$ are found by integrating their differential equations and using the fact that there is initially only a single excitation which is in the atomic part of the wavefunction [so $\gamma_{\mathbf{k},\lambda}(0) = 0$ and $\alpha_{mn,\mathbf{k},\lambda}(0) = 0$]

$$\begin{aligned}
\gamma_{\mathbf{k},\lambda}(t) &= -i\int_0^t \sum_{j=1}^{N} g_{\mathbf{k},\lambda,j}\beta_j(t')e^{i(\omega_{\mathbf{k}}-\omega_0)t'}e^{-i\mathbf{k}\cdot\mathbf{r}_j}dt', \qquad (2.35)\\
\alpha_{mn,\mathbf{k},\lambda}(t) &= -ig_{\mathbf{k},\lambda,n}\int_0^t \beta_n(t')e^{i(\omega_{\mathbf{k}}+\omega_0)t'}e^{-i\mathbf{k}\cdot\mathbf{r}_m}dt' \\
&\quad -ig_{\mathbf{k},\lambda,n}\int_0^t \beta_m(t')e^{i(\omega_{\mathbf{k}}+\omega_0)t'}e^{-i\mathbf{k}\cdot\mathbf{r}_n}dt'. \qquad (2.36)
\end{aligned}$$

Now, γ and α can be substituted in the differential equation for $\beta_j(t)$:

$$\begin{aligned}
\dot{\beta}_j(t) &= -\sum_{\mathbf{k},\lambda}\sum_{j'}\int_0^t g_{\mathbf{k},\lambda,j}g_{\mathbf{k},\lambda,j'}\beta_{j'}(t')e^{i(\omega_k-\omega_0)(t'-t)}e^{i\mathbf{k}\cdot(\mathbf{r}_j-\mathbf{r}_{j'})}dt' \\
&\quad -\sum_{\mathbf{k},\lambda}\sum_{j'=1,j'\neq j}^{N}\int_0^t g_{\mathbf{k},\lambda,j}g_{\mathbf{k},\lambda,j'}\beta_{j'}(t')e^{i(\omega_k+\omega_0)(t'-t)}e^{-i\mathbf{k}\cdot(\mathbf{r}_j-\mathbf{r}_{j'})}dt'. \qquad (2.37)
\end{aligned}$$

We continue the derivation by interchanging the sum over $\mathbf{k}$ with the integral over time. We will assume to have a large volume so that the discrete sum over all modes $\mathbf{k}$ can be replaced by integrals ($\sum_{\mathbf{k}} \mapsto V/(2\pi)^3 \times \int d^3\mathbf{k}$). In our situation of atoms inside vacuum, this is a reasonable assumption. The integrals over $\mathbf{k}$ becomes:

$$\int g_{\mathbf{k},\lambda,j}g_{\mathbf{k},\lambda,j'}e^{ick(t'-t)\pm i\mathbf{k}\cdot(\mathbf{r}_j-\mathbf{r}_{j'})}d^3\mathbf{k}. \qquad (2.38)$$

This integral is not equal, but can be approximated by the form $\delta\{t' - [t - (|\mathbf{r}_j - \mathbf{r}_{j'}|)/c]\}$. The typical distance between atoms is chosen to be the size of the cloud R. The time integral in Eq. 2.37 will lead to terms like $\beta_{j'}(t - R/c)$. When we assume that the decay time of the excitation is larger than the time of flight of a photon through the atomic cloud (R/c), then we can assume $\beta_{j'}(t - R/c) \mapsto \beta_{j'}(t)$. This approximation is called the Markov approximation. A Markovian system is said to be a memoryless system. Since the atomic clouds that we will study have a size which is on the order of a micrometer (so $R/c \sim 10$ fs), and the typical decay time is on the order of 100 ns, we have justified the substitution

$\beta_{j'}(t') \mapsto \beta_{j'}(t)$. We go back to the differential equation for β and make the substitution $\beta_{j'}(t') \mapsto \beta_{j'}(t)$:

$$\begin{aligned}\dot{\beta}_j(t) &= -\sum_{\mathbf{k},\lambda}\sum_{j'}\int_0^t g_{\mathbf{k},\lambda,j}g_{\mathbf{k},\lambda,j'}e^{i(\omega_k-\omega_0)(t'-t)}e^{i\mathbf{k}\cdot(\mathbf{r}_j-\mathbf{r}_{j'})}dt'\beta_{j'}(t) \\ &\quad -\sum_{\mathbf{k},\lambda}\sum_{j'=1,j'\neq j}^{N}\int_0^t g_{\mathbf{k},\lambda,j}g_{\mathbf{k},\lambda,j'}e^{i(\omega_k+\omega_0)(t'-t)}e^{-i\mathbf{k}\cdot(\mathbf{r}_j-\mathbf{r}_{j'})}dt'\beta_{j'}(t). \qquad (2.39)\end{aligned}$$

The time integral is now analytical and results in

$$\begin{aligned}\dot{\beta}_j(t) &= i\sum_{\mathbf{k},\lambda}\sum_{j'}g_{\mathbf{k},\lambda,j}g_{\mathbf{k},\lambda,j'}\frac{1-e^{-i(\omega_k-\omega_0)t}}{\omega_k-\omega_0}\beta_{j'}(t)e^{i\mathbf{k}\cdot(\mathbf{r}_j-\mathbf{r}_{j'})} \\ &\quad +i\sum_{\mathbf{k},\lambda}\sum_{j'=1,j'\neq j}^{N}g_{\mathbf{k},\lambda,j}g_{\mathbf{k},\lambda,j'}\frac{1-e^{-i(\omega_k+\omega_0)t}}{\omega_k+\omega_0}\beta_{j'}(t)e^{-i\mathbf{k}\cdot(\mathbf{r}_j-\mathbf{r}_{j'})}. \qquad (2.40)\end{aligned}$$

As an intermezzo we will discuss about the form of the differential equation. This form of the differential equation can be rewritten in a more general form (apart from some factors)

$$\dot{\beta}_j(t) \propto \sum_m\sum_{j'}\frac{\langle 0|\langle g_1,\cdots,e_j,\cdots,g_N|H_I|m\rangle\langle m|H_I|g_1,\cdots,e_{j'},\cdots,g_N\rangle|0\rangle}{E_i-E_m}, \qquad (2.41)$$

where E_i is the energy of the state $|g_1,\cdots,e_{j'},\cdots,g_N\rangle|0\rangle$, and E_m is the energy of the "intermediate" state $|m\rangle$. The sum over the intermediate states $|m\rangle$ runs over all possible states within the wave function 2.30. The first term of Eq. 2.40 originates from intermediate states having the coefficient γ, whereas the second term comes from states having the coefficient α. Examples of the associated processes for which the intermediate states intervene have been visualized in Fig. 2.1 for a system of two atoms. In that figure we observe that there are two types of intermediate states. One intermediate state ($|m_1\rangle$) is a state where the initially excited atom relaxes under emission of a photon and the second intermediate state ($|m_2\rangle$) is a state where before the excited atom relaxes, the atom in the ground state gets excited and emits a photon. If we did not include the wave functions with coefficient α, we would not have the second term in Eq. 2.40 and the result would be the same as when the RWA would be applied. From the wave function as given in Eq. 2.30, it can be seen that *both* the states with coefficients γ and α do not necessarily have the same *energy* as the system had initially. Including these so-called virtual states, by not applying the RWA so that we are not restricted to $\omega_{\mathbf{k}} \approx \omega_0$, is important when the atoms are spatially close to each other. We will see that this quantum optics treatment results in the same set of coupled-dipole equations as we have found by means of classical optics.

We go back to the derivation of $\beta(t)$. The next step will be splitting up the first sum in the self contribution and the contribution of other atoms:

$$\begin{aligned}\dot{\beta}_j(t) &= i\sum_{\mathbf{k},\lambda}g_{\mathbf{k},\lambda,j}g_{\mathbf{k},\lambda,j'}\frac{1-e^{-i(\omega_k-\omega_0)t}}{\omega_k-\omega_0}\beta_j(t)+i\sum_{\mathbf{k},\lambda}\sum_{j'=1,j'\neq j}^{N}g_{\mathbf{k},\lambda,j}g_{\mathbf{k},\lambda,j'} \\ &\quad \cdot\Big(\frac{1-e^{-i(\omega_k-\omega_0)t}}{\omega_k-\omega_0}\cdot e^{i\mathbf{k}\cdot(\mathbf{r}_j-\mathbf{r}_{j'})}+\frac{1-e^{-i(\omega_k+\omega_0)t}}{\omega_k+\omega_0}e^{-i\mathbf{k}\cdot(\mathbf{r}_j-\mathbf{r}_{j'})}\Big)\beta_{j'}(t). \qquad (2.42)\end{aligned}$$

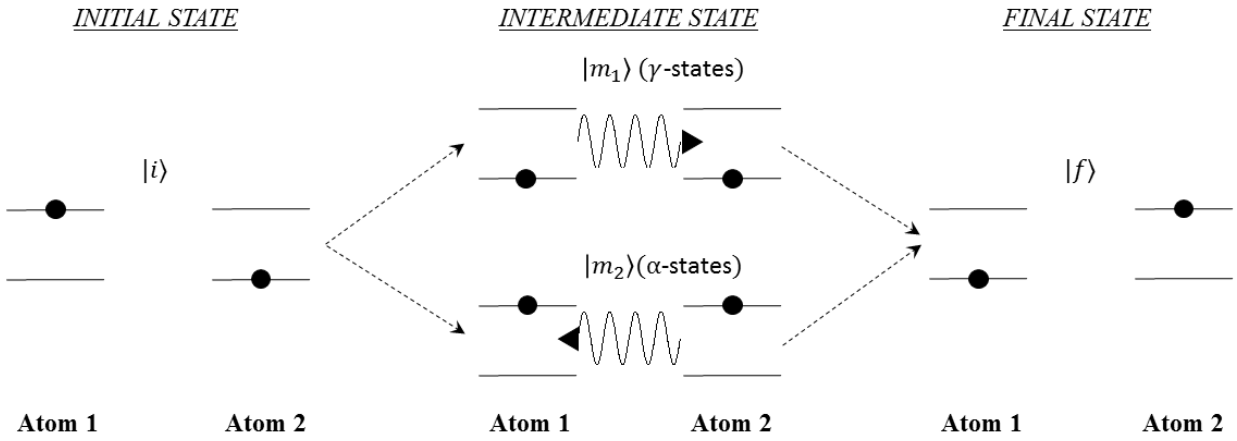

Figure 2.1: *All possible second-order processes are shown between two two-level systems. The intermediate states $|m_1\rangle$ correspond to the wave functions having γ as coefficient, and $|m_2\rangle$ to the wave functions having α as coefficient. Therefore, $|m_1\rangle = |g_1, g_2\rangle|1_{\boldsymbol{k},\lambda}\rangle$, and $|m_2\rangle = |e_1, e_2\rangle|1_{\boldsymbol{k},\lambda}\rangle$.*

After this, we assume to have a large volume so that the discrete sum over all modes $\mathbf{k}$ can be replaced by integrals and we also neglect the time-dependent oscillation terms, as they oscillate fast under integration over k and can be neglected compared to the constant term in the numerator:

$$\begin{aligned}\dot{\beta}_j(t) &= \frac{iV}{(2\pi)^3 c}\iiint d^3\mathbf{k}\sum_\lambda g_{\mathbf{k},\lambda,j}g_{\mathbf{k},\lambda,j'}\frac{1}{k-k_0}\beta_j(t)\\ &+\frac{iV}{(2\pi)^3 c}\iiint d^3\mathbf{k}\sum_\lambda\sum_{j'=1,j'\neq j}^{N} g_{\mathbf{k},\lambda,j}g_{\mathbf{k},\lambda,j'}\Big(\frac{1}{k-k_0}e^{i\mathbf{k}\cdot(\mathbf{r}_j-\mathbf{r}_{j'})}\\ &+\frac{1}{k+k_0}e^{-i\mathbf{k}\cdot(\mathbf{r}_j-\mathbf{r}_{j'})}\Big)\beta_{j'}(t). \qquad (2.43)\end{aligned}$$

We write: $g_{\mathbf{k},\lambda,j}g_{\mathbf{k},\lambda,j'} = g_k^2\hat{\mathbf{p}}_j\cdot\mathbf{e}_{\mathbf{k},\lambda}\mathbf{e}_{\mathbf{k},\lambda}\cdot\hat{\mathbf{p}}_{j'}$. The summation over all polarization components leads to:

$$\sum_\lambda \mathbf{e}_{\mathbf{k},\lambda}\mathbf{e}_{\mathbf{k},\lambda} = \bar{\bar{\mathbb{1}}} - \hat{\mathbf{k}}\hat{\mathbf{k}}. \qquad (2.44)$$

Having this and replacing k_0 by $k_0 + i0$, we can rewrite the differential equation for β_j as:

$$\begin{aligned}\dot{\beta}_j(t) &= \frac{iV}{(2\pi)^3 c}\iiint d^3\mathbf{k}g_k^2\hat{\mathbf{p}}_j\cdot\Big(\bar{\bar{\mathbb{1}}} - \hat{\mathbf{k}}\hat{\mathbf{k}}\Big)\hat{\mathbf{p}}_{j'}\frac{1}{k-k_0-i0}\beta_j(t)\\ &+\frac{iV}{(2\pi)^3 c}\iiint d^3\mathbf{k}\sum_{j'=1,j'\neq j}^{N} g_k^2\hat{\mathbf{p}}_j\cdot\Big(\bar{\bar{\mathbb{1}}} - \hat{\mathbf{k}}\hat{\mathbf{k}}\Big)\hat{\mathbf{p}}_{j'}\Big(\frac{1}{k-k_0-i0}e^{i\mathbf{k}\cdot(\mathbf{r}_j-\mathbf{r}_{j'})}\\ &+\frac{1}{k+k_0+i0}e^{-i\mathbf{k}\cdot(\mathbf{r}_j-\mathbf{r}_{j'})}\Big)\beta_{j'}(t). \qquad (2.45)\end{aligned}$$

We will evaluate each integral separately. In the first integral we note that the only angular dependence is in the projection operator $\bar{\bar{\mathbb{1}}} - \hat{\mathbf{k}}\hat{\mathbf{k}}$. Without loss of generality, we can assume the dipole moment to be pointed along the z axis. Then, one can readily show:

$$\iint \hat{z}\cdot\Big(\bar{\bar{\mathbb{1}}} - \hat{\mathbf{k}}\hat{\mathbf{k}}\Big)\hat{z}d\Omega = 4\pi - \frac{4\pi}{3} = \frac{8\pi}{3}. \qquad (2.46)$$

For the radial part of the integral, we make use of the identity:

$$\frac{1}{x \mp i0} = \mathrm{PV}\frac{1}{x} \pm i\pi\delta(x), \tag{2.47}$$

where PV stands for principal value. The principal value part only corresponds to a frequency shift of the same value for all β_j (Lamb shift) and will be ignored. The first integral then becomes:

$$\dot{\beta}_j(t)\Big|_{\text{First integral}} = -\frac{\Gamma_0}{2}\beta_j(t), \tag{2.48}$$

with $\Gamma_0 = \omega_0^3 p^2/(3\pi\varepsilon_0\hbar c^3)$ being the individual spontaneous decay rate. The second integral reads:

$$\begin{aligned}
\dot{\beta}_j(t)\Big|_{\text{Second integral}} &= \frac{-iV}{(2\pi)^3 c}\sum_{j'=1,j'\neq j}^{N}\hat{\mathbf{p}}_j\cdot\Big(\nabla^2\bar{\bar{\mathbb{1}}}-\nabla\nabla\Big)\hat{\mathbf{p}}_{j'}\iiint d^3\mathbf{k}\frac{1}{k^2}g_k^2 \\
&\quad\Big(\frac{1}{k-k_0-i0}e^{i\mathbf{k}\cdot(\mathbf{r}_j-\mathbf{r}_{j'})}+\frac{1}{k+k_0+i0}e^{-i\mathbf{k}\cdot(\mathbf{r}_j-\mathbf{r}_{j'})}\Big)\beta_{j'}(t) \\
&= \frac{-iV}{2\pi^2 c}\sum_{j'=1,j'\neq j}^{N}\hat{\mathbf{p}}_j\cdot\Big(\nabla^2\bar{\bar{\mathbb{1}}}-\nabla\nabla\Big)\hat{\mathbf{p}}_{j'}\int_0^\infty dk g_k^2\Big(\frac{1}{k-k_0-i0} \\
&\quad+\frac{1}{k+k_0+i0}\Big)\frac{\sin(k|\mathbf{r}_j-\mathbf{r}_{j'}|)}{k|\mathbf{r}_j-\mathbf{r}_{j'}|}\beta_{j'}(t).
\end{aligned} \tag{2.49}$$

The integral over k can be extended from $-\infty$ to $+\infty$. This would not be possible, if the RWA were applied. As the wave functions with the coefficient α would not be there, the term $1/(k+k_0+i0)$ would not be there. Furthermore, if the integral had not been applied at all, since strictly $\omega_{\mathbf{k}} \approx \omega_0$ when the RWA is applied, the consequences would be even more important. These consequences of removing all virtual states have been discussed in the work of Svidzinsky *et al.* [29]. Since we do not apply the RWA, we can extend the integral

$$\begin{aligned}
\dot{\beta}_j(t)\Big|_{\text{Second integral}} &= \frac{-ik_0^2 p^2}{2\pi^2\varepsilon_0\hbar}\sum_{j'=1,j'\neq j}^{N}\hat{\mathbf{p}}_j\cdot\Big(\nabla^2\bar{\bar{\mathbb{1}}}-\nabla\nabla\Big)\hat{\mathbf{p}}_{j'} \\
&\quad\cdot\int_{-\infty}^{\infty}dk\frac{1}{k^2}\frac{\sin(k|\mathbf{r}_j-\mathbf{r}_{j'}|)}{(k-k_0-i0)|\mathbf{r}_j-\mathbf{r}_{j'}|}\beta_{j'}(t).
\end{aligned} \tag{2.50}$$

The sine function can be written in terms of complex exponentials, so that the residue theorem can be applied on

$$\begin{aligned}
\dot{\beta}_j(t)\Big|_{\text{Second integral}} &= \frac{-k_0^2 p^2}{4\pi^2\varepsilon_0\hbar}\sum_{j'=1,j'\neq j}^{N}\hat{\mathbf{p}}_j\cdot\Big(\nabla^2\bar{\bar{\mathbb{1}}}-\nabla\nabla\Big)\hat{\mathbf{p}}_{j'} \\
&\quad\cdot\int_{-\infty}^{\infty}dk\frac{1}{k^2}\Big[\frac{e^{ik|\mathbf{r}_j-\mathbf{r}_{j'}|}}{(k-k_0-i0)|\mathbf{r}_j-\mathbf{r}_{j'}|}-\frac{e^{-ik|\mathbf{r}_j-\mathbf{r}_{j'}|}}{(k-k_0-i0)|\mathbf{r}_j-\mathbf{r}_{j'}|}\Big]\beta_{j'}(t).
\end{aligned} \tag{2.51}$$

Note that there seem to be 2 poles. However, we realize that the pole at $k=0$ is a removable singularity when we look at the original expression in Eq. 2.45. The integral of the second

term vanishes, since the contour in the lower half plane does not have a pole inside. The first integral does not vanish. After the evaluation of the integral, we find:

$$\begin{aligned}\dot{\beta}_j(t)\Big|_{\text{Second integral}} &= \frac{-ip^2}{2\pi\varepsilon_0\hbar}\sum_{j'=1,j'\neq j}^{N}\hat{\mathbf{p}}_j\cdot\Big(\nabla^2\bar{\bar{\mathbb{1}}}-\nabla\nabla\Big)\hat{\mathbf{p}}_{j'}\frac{e^{ik_0|\mathbf{r}_j-\mathbf{r}_{j'}|}}{|\mathbf{r}_j-\mathbf{r}_{j'}|}\beta_{j'}(t)\\ &= -i\frac{3\Gamma_0}{2k_0^3}\sum_{j'=1,j'\neq j}^{N}\hat{\mathbf{p}}_j\cdot\Big(\nabla^2\bar{\bar{\mathbb{1}}}-\nabla\nabla\Big)\hat{\mathbf{p}}_{j'}\frac{e^{ik_0|\mathbf{r}_j-\mathbf{r}_{j'}|}}{|\mathbf{r}_j-\mathbf{r}_{j'}|}\beta_{j'}(t).\end{aligned} \tag{2.52}$$

We write the differential equation slightly differently by using the identity $\nabla^2 G(\mathbf{r},\mathbf{r}') + k_0^2 G(\mathbf{r},\mathbf{r}') = -\delta(\mathbf{r}-\mathbf{r}')$. We make the following substitution:

$$\nabla^2\frac{e^{ik_0|\mathbf{r}-\mathbf{r}'|}}{4\pi|\mathbf{r}-\mathbf{r}'|} = -\delta(\mathbf{r}-\mathbf{r}') - k_0^2\frac{e^{ik_0|\mathbf{r}-\mathbf{r}'|}}{4\pi|\mathbf{r}-\mathbf{r}'|}, \tag{2.53}$$

where we use the fact that we only sum over non-identical dipoles, which means that the delta function vanishes in the identity and we can rewrite the second integral as follows:

$$\begin{aligned}\dot{\beta}_j(t)\Big|_{\text{Second integral}} &= i\frac{3\Gamma_0}{2}\sum_{j'=1,j'\neq j}^{N}\hat{\mathbf{p}}_j\cdot\Big(\bar{\bar{\mathbb{1}}}+\frac{1}{k_0^2}\nabla\nabla\Big)\hat{\mathbf{p}}_{j'}\frac{e^{ik_0|\mathbf{r}_j-\mathbf{r}_{j'}|}}{k_0|\mathbf{r}_j-\mathbf{r}_{j'}|}\beta_{j'}(t)\\ &= i\frac{3\Gamma_0}{2}\sum_{j'=1,j'\neq j}^{N}\hat{\mathbf{p}}_j\cdot\bar{\bar{G}}(\mathbf{r}_j,\mathbf{r}_{j'})\hat{\mathbf{p}}_{j'}\beta_{j'}(t).\end{aligned} \tag{2.54}$$

In the last equation we have introduced the Green's tensor. Note that we would not arrive at the Green's tensor if we had removed the states corresponding to the coefficient α, since the integral of Eq. 2.49 could not be extended. Finally, we have found the differential equation for β_j:

$$\dot{\beta}_j(t) = -\frac{\Gamma_0}{2}\beta_j(t) + i\frac{3\Gamma_0}{2}\sum_{j'=1,j'\neq j}^{N}\hat{\mathbf{p}}_j\cdot\bar{\bar{G}}(\mathbf{r}_j,\mathbf{r}_{j'})\hat{\mathbf{p}}_{j'}\beta_{j'}(t). \tag{2.55}$$

We then assume the coefficients β to be of the form: $\beta_j(t) = \beta_j\exp(-i\omega_j t)$. Substituting this form of $\beta_j(t)$ into Eq. 2.55 gives us the equation

$$\omega_j\beta_j = -i\frac{\Gamma_0}{2}\beta_j - \frac{3\pi\Gamma_0}{k_0}\sum_{j'=1,j'\neq j}^{N}\hat{\mathbf{p}}_j\cdot\bar{\bar{G}}(\mathbf{r}_j,\mathbf{r}_{j'};\omega_0)\hat{\mathbf{p}}_{j'}\beta_{j'}. \tag{2.56}$$

When transforming this equation back to the Schrödinger picture and after putting the terms proportional to β_j together, the equation becomes

$$\Big(\omega_0-\omega_j-i\frac{\Gamma_0}{2}\Big)\beta_j - \frac{3\pi\Gamma_0}{k_0}\sum_{j'=1,j'\neq j}^{N}\hat{\mathbf{p}}_j\cdot\bar{\bar{G}}(\mathbf{r}_j,\mathbf{r}_{j'};\omega_0)\hat{\mathbf{p}}_{j'}\beta_{j'} = 0. \tag{2.57}$$

In the absence of any interaction between the dipoles, we recover the expected result, where

$$\beta_j(t) = \beta_j(0)e^{-i\omega_0 t}e^{-\frac{\Gamma_0}{2}t}. \tag{2.58}$$

Equation 2.57 should be compared with Eq. 2.17 when we remove the incident field (our system has been excited initially), which is exactly the same result. With this we have seen that in the low-excitation limit, classical and quantum optics describe in the same way the interactions between classical dipoles. Although the intermediate states do not have the same energy as the initial state, they turned out to be important in order to arrive at the classical result. These intermediate states are allowed to exist during a finite time interval Δt, because of the Heisenberg's uncertainty relation: $\Delta E \Delta t \geq \hbar/2$. The virtual states borrow or lend some energy from the vacuum.

As a final remark, we observe that dipole-dipole interactions show up at the end, although they have not been included explicitly in the Hamiltonian. The reason for this is that dipole-dipole interactions are actually mediated by the electromagnetic modes of the vacuum [31]. In the next section we will describe these electromagnetic modes in more detail.

2.5 Virtual photons from a classical perspective

In the previous section we have encountered intermediate states which were called virtual states. The photons that are the elementary excitation of the associated electromagnetic waves are called virtual photons. These intermediate states, which should be discarded when applying the RWA, are however the reason of having the $1/(k_0 r)^3$ term in the dipole-dipole interactions. It is precisely these near-field interactions that are important in this thesis, since we study systems where the inter-scatterer distance is small compared to the optical wavelength. From classical electromagnetism it is known that in this dense regime evanescent waves are important for the interaction. Therefore, there should be a connection between evanescent waves and virtual photons. In this section, we study this connection.

The system with which we will study this connection is a system where energy transfer takes place from an excited two-level system to a two-level system in its ground state by using a quantum optics formalism. This quantum treatment is based on the work of Andrews *et al.* [32]. It can be shown from second-order time-dependent perturbation theory that the energy transfer rate from atom A (initially excited) to atom B (initially in ground state) is given by

$$\Gamma = \frac{2\pi}{\hbar}|M|^2 \delta(E_f - E_i), \tag{2.59}$$

with M given by

$$M = \sum_m \frac{\langle f|H_I|m\rangle\langle m|H_I|i\rangle}{E_i - E_m}, \tag{2.60}$$

where $|i\rangle$ is the initial state, $|f\rangle$ the final state, $|m\rangle$ any intermediate state, and E stands for the energy of a particular state. As illustrated in Fig. 2.1, there are two possible kinds of intermediate processes:

- $|m_1\rangle$: The initially excited atom relaxes under emission of a photon with energy $\hbar\omega$ which is not necessarily equal to the transition energy of the atom,
- $|m_2\rangle$: The initially relaxed atom gets excited, under emission of a photon with energy $\hbar\omega$. All processes of this kind are necessarily virtual, since even without taking the

photon in consideration, both atoms are excited and there is therefore more energy present in the intermediate system than in the initial system.

By following the same mathematical steps as in the former section, Andrews *et al.* found that the quantum amplitude M can be written as [32]

$$M = \mathbf{p}_A \cdot \bar{\bar{V}}(k_0, \mathbf{R})\mathbf{p}_B, \tag{2.61}$$

where the coupling tensor is the Green's tensor:

$$\bar{\bar{V}}(k_0, \mathbf{R}) = -k_0^2 \frac{e^{ik_0R}}{4\pi\varepsilon_0 R}\left[\left(1 + \frac{ik_0R - 1}{k_0^2R^2}\right)\bar{\bar{\mathbb{1}}} + \frac{3 - 3ik_0R - (k_0R)^2}{(k_0R)^2}\frac{\mathbf{RR}}{R^2}\right] = -\mu_0\omega^2\bar{\bar{G}}(R). \tag{2.62}$$

What we then observe is that we recover the classical dipole-dipole interaction potential, by including all possible intermediate states in second-order time-dependent perturbation theory. From classical electrodynamics we know that evanescent waves are present in this Green's tensor and that they are crucial for near-field interactions.

We will explain by means of classical electrodynamics how evanescent waves and virtual photons are related. From classical electrodynamics we know that the Green's function in vacuum can be presented in different forms:

$$G(\mathbf{r};\omega) = \frac{e^{i\frac{\omega}{c}r}}{4\pi r} \tag{2.63}$$

$$= \iiint \frac{d^3\mathbf{k}}{(2\pi)^3}\frac{1}{k^2 - \frac{\omega^2}{c^2}}e^{i\mathbf{k}\cdot\mathbf{r}} \tag{2.64}$$

$$= \iint \frac{dk_x \mathrm{d}k_y}{(2\pi)^2}\frac{i\pi}{\gamma}e^{i\gamma z}e^{i(k_x x + k_y y)}, \tag{2.65}$$

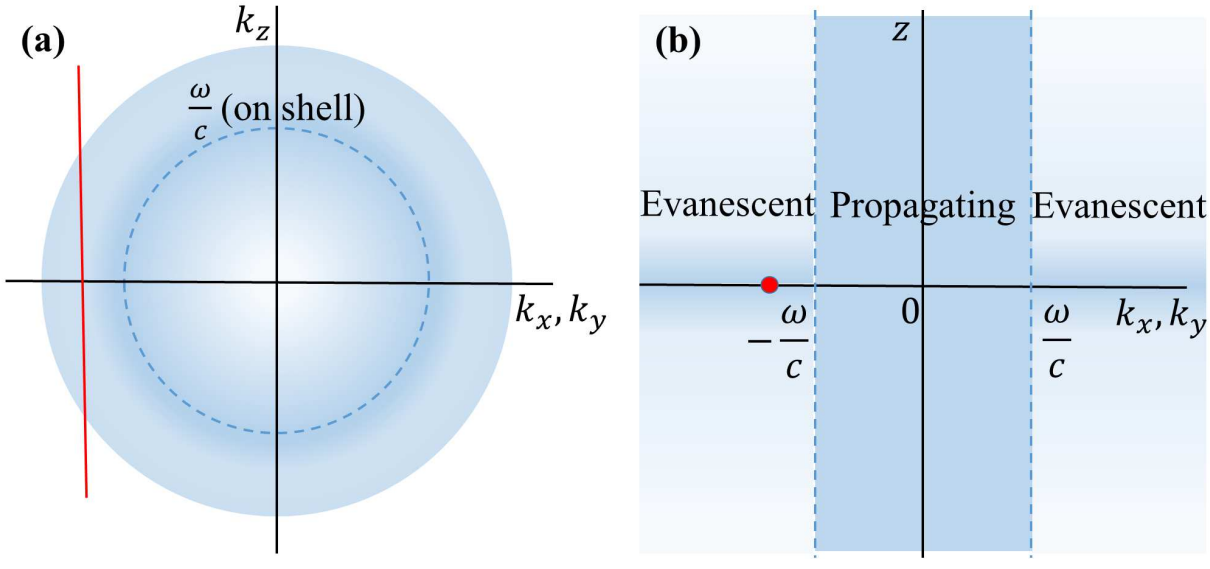

Figure 2.2: *(a) Schematic of reciprocal space (k_x, k_y, k_z). The states on shell, i.e. $\sqrt{k_x^2 + k_y^2 + k_z^2} = \omega^2/c^2$, are indicated by a blue dashed circle. The red line corresponds to the collection of off-shell states that form together the evanescent wave which is indicated by a red dot in (b). (b) Schematic view of $(k_x, k_y; z)$ space. Propagating waves lie in the band within $\sqrt{k_x^2 + k_y^2} < \omega^2/c^2$. Evanescent waves lie outside this band. One evanescent wave is indicated by a red dot.*

with $\gamma = \sqrt{\omega^2/c^2 - k_x^2 - k_y^2}$. The form of the Green's function as given by Eq. 2.64 shows that the field of a dipole is given by a weighted sum over electromagnetic states defined in reciprocal space (k_x, k_y, k_z). A schematic view of reciprocal space is given in Fig. 2.2(a). The on-shell states, which are states for which $k = \omega/c$, are most important, since the weighting factor $1/(k^2 - \omega^2/c^2)$ is the largest for these states. All states for which $k \neq \omega/c$ are called off-shell states. Another representation of the Green's tensor is the Weyl's representation in $(k_x, k_y; z)$ space, as given by Eq. 2.65. This representation is obtained after integration of the integrand of Eq. 2.64 with respect to k_z:

$$\frac{i\pi}{\gamma} e^{i\gamma z} e^{i(k_x x + k_y y)} = \int \frac{dk_z}{2\pi} \frac{1}{k^2 - \frac{\omega^2}{c^2}} e^{i\mathbf{k}\cdot\mathbf{r}}. \tag{2.66}$$

Let us consider an evanescent wave that is characterized by k'_x and k'_z such that: $(k'_x)^2 + (k'_y)^2 > \omega^2/c^2$ [see the red dot in Fig. 2.2(b)]. According to Eq. 2.66, this evanescent wave is constructed out of all possible states (k'_x, k'_y, k_z), each state having a different weighting factor. The integration path is indicated by the red line in Fig. 2.2(a). An evanescent wave is therefore built up of uniquely off-shell states $(k \neq \omega/c)$.

In Appendix A, we have assigned a quantum operator (annihilation operator) to evanescent fields. There we formally show that the elementary excitation of an evanescent wave is a superposition of virtual photons. Virtual photons correspond to elementary excitations of off-shell states. Hereby, we have shown the relationship between evanescent waves and virtual photons.

Finally, let us note that there have already several works been published on the connection between virtual photons and classical electrodynamics [33–35], but the approach presented in this section is different as compared to the others.

2.6 Summary

In this chapter we have summarized the basic elements needed to interpret the results outlined in this thesis. We have recalled some notions of multiple scattering theory. This discussion allowed us to define light scattering that is beyond the mean-field theory of optics. Furthermore, we have discussed light scattering from both a classical and quantum optics perspective. This allowed us to show the equivalence between quantum optics and classical optics in the low-excitation regime, where only a single atomic excitation is present in a system of N atoms. Finally, we gave an original way of comparing virtual photons with evanescent waves. From nanophotonics we know very well that when the inter-atomic distance is small as compared to the optical wavelength, the interactions are dominated by evanescent waves. Similarly, the contribution of virtual photons are important in that situation. Indeed, both evanescent waves and virtual photons are related to each other.

Chapter 3

Light scattering from a dense cloud of cold atoms

3.1 Motivation

We start with a discussion of two specific examples of resonant light scattering. In the first situation, a plane wave is incident upon 5 atoms that are positioned randomly, following a homogeneous distribution, and are distributed inside a box with dimensions $10 \times 10 \times 10$ μm^3, so that the average inter-atomic distance is $3 \times 10^2 \lambda_0$. The total electric field is calculated for a single realization of the atomic cloud with the procedure that has been outlined in Section 2.2.2. The total electric field $\mathbf{E}$ is decomposed as:

$$\mathbf{E}(\mathbf{r}) = \mathbf{E}_{\text{inc}}(\mathbf{r}) + \mathbf{E}_{\text{sc}}(\mathbf{r}), \tag{3.1}$$

where $\mathbf{E}_{\text{inc}}$ is the incident electric field and $\mathbf{E}_{\text{sc}}$ the scattered electric field. The Poynting vector in the far field is given by

$$\mathbf{S}(\mathbf{r}) = \frac{\varepsilon_0 c}{2}\Big\{|\mathbf{E}_{\text{inc}}(\mathbf{r})|^2 + |\mathbf{E}_{\text{sc}}(\mathbf{r})|^2 + 2\text{Re}[\mathbf{E}_{\text{inc}}(\mathbf{r}) \cdot \mathbf{E}^*_{\text{sc}}(\mathbf{r})]\Big\}\hat{\mathbf{r}}, \tag{3.2}$$

where the last interference term leads to extinction. We calculate the scattering cross section, by following the same procedure as outlined in Section 2.2.1. The scattering cross section is normalized by dividing the scattering cross section by the on-resonance single-atom scattering cross section. Figure 3.1(a) shows the normalized scattering cross section as a function of the laser detuning $\delta\omega_L = \omega_L - \omega_0$ in units of Γ_0, where $\omega_0 = 2\pi c/\lambda_0$, with $\lambda_0 = 780$ nm. It is seen that 5 particles scatter 5 times as much as a single particle and that the scattering spectrum is Lorentzian, like it is for resonant light scattering by a single atom. Furthermore, the full width at half maximum (FWHM) of the scattering spectrum is equal to the single-atom spontaneous decay rate Γ_0 and the resonance is centered around the single-atom resonance frequency. Figure 3.1(b) shows the *ensemble-averaged* far-field scattering pattern of only the scattered field, so this pattern is proportional to $\langle|\mathbf{E}_{\text{sc}}|^2\rangle$. This scattering pattern has a doughnut shape, which is the same scattering pattern as for light scattering from a single dipole: light scattering takes place in many directions, except along the polarization direction. Scattering by a very dilute cloud as the one we study here confirms what we know from light scattering in the atmosphere: the sky is blue in all directions. In the forward direction we also observe a peak. This peak is characteristic for the single-scattering regime, since in that regime all scattered fields have the same phase in the *forward direction* and therefore interfere constructively. Next, we

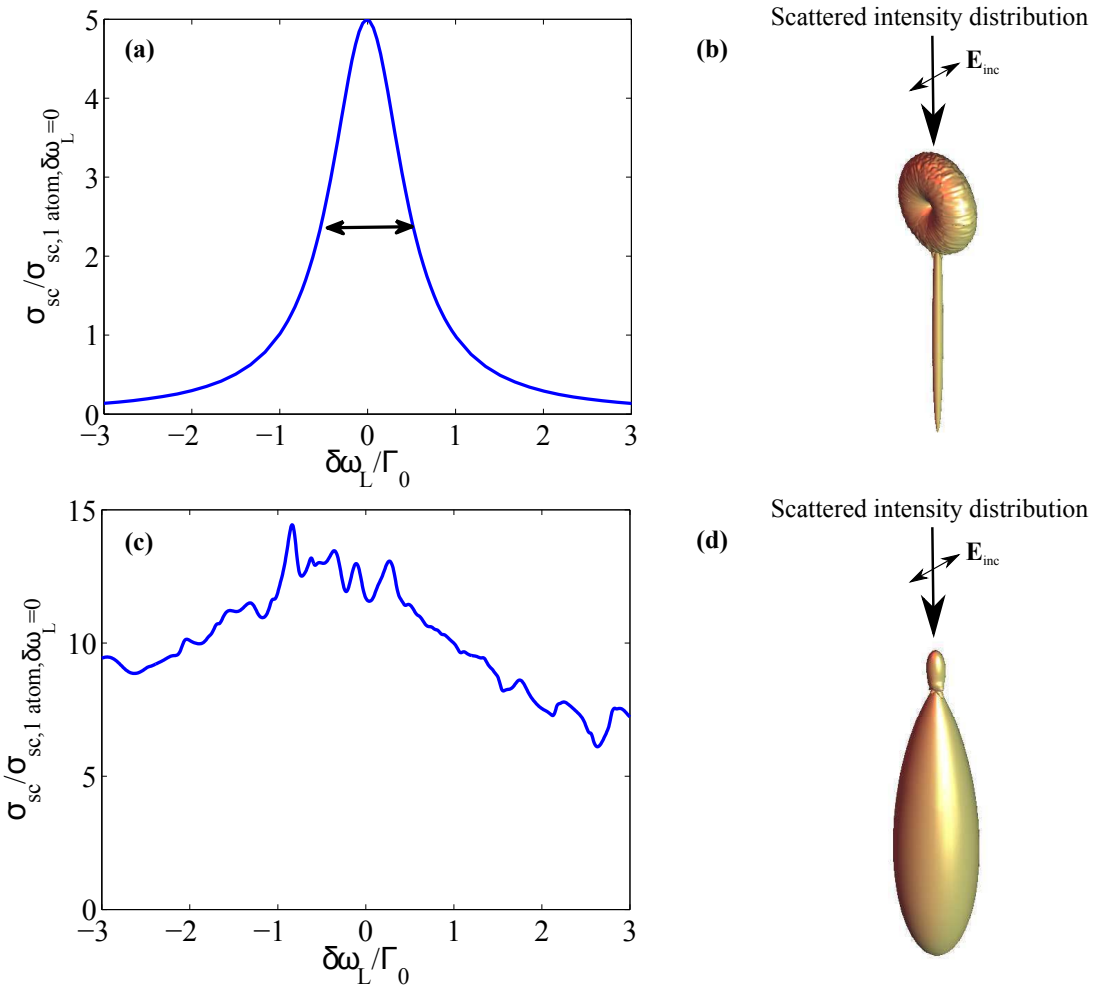

Figure 3.1: *(a) The normalized scattering cross section for a system of 5 homogenously distributed atoms inside a rectangular box with dimensions* $10\times10\times10$ $(\mu m)^3$ *is Lorentzian. The double arrow indicates the FWHM of the spectrum which is equal to the single atom spontaneous emission rate* Γ_0*. (b) The scattering pattern* ($\langle|\boldsymbol{E}_{sc}|^2\rangle$) *after an ensemble average over* 10 000 *realizations for a resonant linearly polarized incident plane wave. Light gets scattered in many directions. (c) The normalized scattering cross section for a system of 100 homogeneously distributed atoms inside a rectangular box with dimensions* $1\times1\times1$ μm^3 *is not Lorentzian. (d) The scattering pattern* ($\langle|\boldsymbol{E}_{sc}|^2\rangle$) *after an ensemble average over* 1 000 *realizations for a linearly polarized incident plane wave with* $\delta\omega_L = 0$*. The scattering pattern has changed into a diffraction pattern.*

do the same calculations, but for $N = 100$ atoms in a box with dimensions $1 \times 1 \times 1$ μm^3, so that the atomic density is 4 orders of magnitude higher and the average inter-atomic distance is $\sim \lambda_0/4$. Because of the much smaller average inter-atomic distance, the resonant dipole-dipole interactions are much stronger in this configuration than in the previous configuration with 5 atoms. The numerical results are presented in Fig. 3.1(c) and Fig. 3.1(d). Figure 3.1(c) shows the normalized scattering cross section for a single realization of the atomic cloud. It is seen that the spectrum for this example is very different from the light scattering spectrum of the previous dilute configuration. Multiple

peaks in the scattering spectrum appear and they are distributed over several single-atom linewidths Γ_0. Figure 3.1(d) shows the *ensemble-averaged* total scattering pattern ($\langle|\mathbf{E}_{\rm sc}|^2\rangle$). Also the scattering pattern has changed drastically. As opposed to being similar to a scattering pattern from a single atom, which is doughnut like, it is this time very similar to a diffraction pattern. From Fig. 3.1 it is clear that we observe the appearance of new physics when resonant dipole-dipole interactions are strong. It is in this regime that we are mainly interested.

3.2 State of the art

In the last section we have seen that the scattering pattern for wavelength-size, dense, and resonant atomic clouds is very different from what is expected for Rayleigh scattering. Being interested by resonant light scattering from dense atomic clouds, let us discuss several experiments that have been conducted on light scattering from atomic clouds. This discussion will allow us to see what has already been done in the field and to what extent the light scattering regime in which we are interested, is still original.

The first example goes back to Faĭn who realized for the first time, in 1959, that apart from line broadening of the spectrum of interacting systems, there is also a change of the eigenfrequencies that should occur, nowadays known as the cooperative Lamb shift (CLS) [36]. The change of eigenfrequencies reflects itself in a change of both the emission and absorption spectra and it was in 1973 that Friedberg, Hartmann, and Manassah theoretically studied in detail the "frequency shifts in emission and absorption by resonant systems of two-level atoms" [37]. The first experiment where the cooperative Lamb shift was observed from the absorption spectrum, has recently been reported by Keaveney *et al.* for a thin slab loaded with a hot atomic vapor [38]. The experimentally observed CLS has been obtained for different layer thicknesses and coincides with a mean-field theory calculation [37].

Another observation done by Keaveney *et al.* for a hot atomic vapor is superluminal pulse propagation [39]. They measured an optical pulse advance of > 100 ps over a propagation distance of only 390 nm. From this, they deduced a group index $n_{\rm g} = -1.0 \times 10^5$, which was at that time the largest negative group index ever measured.

Experimental works on light scattering from cold atomic systems are essentially performed on large (compared to the resonant wavelength), dilute, but optically thick cloud of cold atoms [40–42]. Reference [40] shows an indirect observation of cooperative Mie scattering from a cold atomic cloud by measuring the center-of-mass positions. The idea behind this indirect observation is that the collective radiation pressure force should be larger than a radiation pressure force based on independent atoms, thereby being a signature of collective scattering by the cloud which behaves as a particle with an index of refraction.

Near-resonance light scattering experiments were performed on a big cloud of cold atoms in Ref. [42]. In that work, both the temporal and spectral properties of the scattered light were studied. A very small Lorentz-Lorenz shift was measured ($\delta\omega = -0.07\Gamma_0$), that is of the order of magnitude predicted by Lorentz-Lorenz theory for the atomic density studied in the cloud. For a formal proof, the shift should be larger and for that a denser cloud of atoms would have been needed.

Kwong *et al.* shone a continuous wave laser on an optically thick cloud of strontium-88

atoms and studied the time evolution of the scattered light after the incident laser was switched off abruptly [43]. They have shown that for non-resonant light scattering from a cloud with a large optical thickness, a coherent superflash of light emerges from the cloud. This coherent superflash is special for at least two reasons: (1) its peak intensity is higher than the incident intensity, and (2) the pulse duration is shorter than the single-atom spontaneous emission rate. They understood that with such a system, it would be interesting to create pulse trains. It is one year later that they succeeded in creating a pulse train with both high repetition rates and high intensity [44]. Inspired by this work, Araújo *et al.* have also studied the time evolution of light scattering after the laser got switched off. However, the main difference with the work of Kwong *et al.* is the fact that Araújo *et al.* collected light at a 35° angle from the optical axis. By doing so, they did not detect coherent scattered field, but incoherent scattered light, so that, as they claimed, "light emission at different angles cannot be explained by a phase-matching condition imposed by the initial laser field or a continuous-medium description". By doing so, they have observed both single-photon superradiance [45] and single-photon subradiance [46]. Similarly, Roof *et al.* have reported the observation of both single-photon superradiance, and the CLS [47].

At last, let us mention a recent work on optical atomic clocks. The stability and accuracy of current atomic clocks are ultimately limited by Doppler effect and recoil frequency shifts. One way to suppress both effects is by creating an optical lattice clock, where atoms are loaded in a lattice of strongly confined potentials [48]. However, as was mentioned in Ref. [48], not each electronic state experiences the same confinement and therefore the same perturbation. This leads to a reduction in accuracy of the atomic lattice clock. It is therefore interesting to study motional effects on coherent light scattering from a weakly confined, dense gas of atoms. This has recently be done by Bromley *et al.* They have shown "clear signatures of motional effects on coherent scattering and dipolar coupling" [49]. It was shown that the linewidth is determined by the optical depth of the cloud only, which is in contrast with the frequency shift that seems to depend significantly on motional effects for frequencies with an extremely small linewidth (in Ref. [49]: $\Gamma_0 = 7.5$ kHz).

The systems used to achieve the aforementioned goals have all in common that resonant dipole-dipole interactions are weak, since the dipoles are on average not in each other's near-field region. When resonant dipole-dipole interactions are weak, the experimental results agree with mean-field theory. The first four lines of Table 3.1 summarize some

Reference	(Peak) Density	Inhomog. broad. [Γ_0]	C
[42]	$5 \cdot 10^{13}$	0.04	1.4
[49]	$2 \cdot 10^{12}$	$2 \cdot 10^{-3}$	10^{-2}
[43]	$4.6 \cdot 10^{11}$	3.4	10^{-2}
[38]	$4 \cdot 10^{16}$	$\sim 10^{3}$	10^{-4}
[7]	$\mathbf{2 \cdot 10^{14}}$	**0.06**	**5**

Table 3.1: *The (peak) density in [at/cm^3], inhomogeneous broadening and the parameter C are given for the densest reported systems of different research groups. References [7, 38, 42] study Rb-87 atoms, and Refs. [43, 49] used Sr-88 atoms. The last row is bold, since this is the system of interest in this thesis.*

characteristics that are important for the strength of the resonant dipole-dipole interactions of the densest clouds that have been studied by most of the previously cited research groups. We have listed the (peak) atomic density, inhomogeneous broadening, and the parameter that indicates if resonant dipole-dipole interactions are strong, as we have defined in Eqs 2.24 and 2.25. We assign to this parameter the symbol C, as it is related to the cooperativity, and recall for convenience the expression of this parameter:

$$\text{homogeneously broadened system}: \quad C = \frac{9\pi\rho}{2k^3}, \tag{3.3}$$

$$\text{inhomogeneously broadened system}: \quad C = \frac{9\pi\rho}{8k^3}\left(\frac{\Gamma_0}{\Delta\omega}\right)^2, \tag{3.4}$$

where $\Delta\omega$ is the inhomogeneous broadening. Resonant dipole-dipole interactions are strong when $C > 1$, see Chapter 2. Let us study this parameter for different experimental setups that have been described in literature. From columns three and four, we see that the system reported in Ref. [38] has a huge inhomogeneous broadening, and is not in the strong resonant dipole-dipole interaction regime. The strong inhomogeneous broadening is in the cloud studied in Ref. [38] due to the Doppler effect that cannot be neglected for hot atomic vapors. The Doppler effect effectively reduces the resonant dipole-dipole interactions. Although the density of the atomic cloud is high, it is not sufficient to overcome inhomogeneous broadening. From the last column we can observe that there are no strong resonant dipole-dipole interactions in the clouds that are reported in Refs [43, 49] either. The reason that resonant dipole-dipole interactions are not strong in these clouds is that the density of the clouds is not sufficiently high to have strong resonant dipole-dipole interactions, i.e., the near-field terms of the resonant dipole-dipole interactions are not important. The cloud studied in Ref. [42] satisfies the criterion for strong resonant dipole-dipole interactions, however it is satisfied only slightly at the center of the cloud: the position distribution of the atoms follows a Gaussian distribution, since the atoms are loaded in a dipole trap.

So far we have been discussing atomic systems that were used to successfully observe several physical phenomena like single-photon superradiance and the CLS. As we have seen, these systems have all in common that they are not in the regime of light scattering where strong resonant dipole-dipole interactions exist. An experimentally largely unexplored system is an atomic system where resonant dipole-dipole interactions are strong. It is in this kind of systems that we are interested. Let us stress that the strong resonant dipole-dipole interactions in the atomic cloud that we refer to are near-field interactions in free space, for which the interaction potential varies as $1/r^3$, where r is the inter-atomic distance. We do not consider a modified electromagnetic environment for the atomic cloud. By engineering the electromagnetic environment it is for example possible to induce strong dipole-dipole interactions between atoms that are not in each other's near field. An example is the use of a waveguide along which atoms are placed [50]. Table 3.1 shows in bold the characteristics of the atomic cloud studied by the group of Browaeys. It is seen that the cloud is in the strong resonant dipole-dipole interactions regime, so that recurrent scattering effects are expected from the classical dipole model.

In this chapter we will study theoretically light scattering from cold atomic clouds that have experimentally been studied by the group of Browaeys. The clouds are different from other reported clouds in the sense that resonant dipole-dipole interactions are expected to be stronger. We will compare the experimentally obtained spectral and temporal responses of the atomic clouds with numerical calculations. Some key experimental observations that

are discussed are a negligible CLS [7, 51], suppression of light scattering in the direction orthogonal to the incident light beam [51], and superluminal pulse propagation through the atomic cloud [52].

3.3 Experimental setup

In this section we describe two experimental configurations studied by Joseph Pellegrino [4] and his successor Stephan Jennewein [7]. Figure 3.2 shows a schematic of both setups. Both Pellegrino and Jennewein study near-resonance light scattering from an optically trapped cloud of cold rubidium-87 atoms.

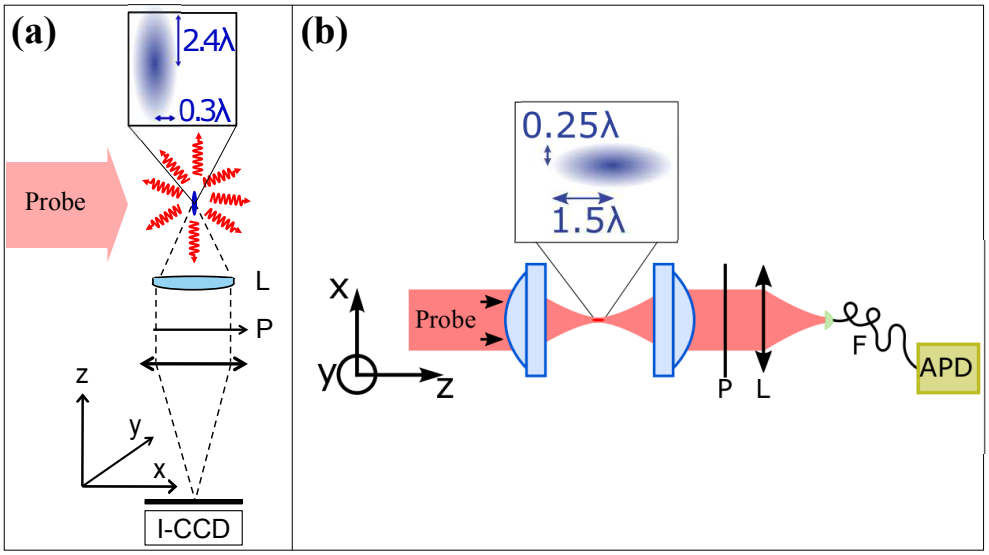

Figure 3.2: *A wavelength-size cloud of cold Rb-87 atoms is loaded in a dipole trap. (a) Experimental setup of Ref. [51]. A wide laser beam gets scattered by the atomic cloud. The light scattered at a 90° angle is collected by means of an NA = 0.5 aspheric lens, after which it passes through a polarizer and a focusing lens. Courtesy of Joseph Pellegrino. (b) Experimental setup of Ref. [7]. A Gaussian probe beam gets focussed by an aspheric lens on the atomic cloud. The light scattered in the forward direction is collected by passing through a NA = 0.5 aspheric lens, polarizer and focusing lens. Courtesy of Stephan Jennewein.*

3.3.1 Atomic density

As a first step, both Pellegrino and Jennewein loaded the atoms in a magneto-optical trap (MOT). However, with such a trap one can typically reach a density of only $\rho = 10^{11}$ at/cm^3, or equivalently $\rho/k^3 = 10^{-4}$, which is not sufficient to have strong resonant dipole-dipole interactions. In order to reach a higher density, the atoms are eventually trapped in a far-off-resonance dipole trap (FORT) [53]. Atomic clouds in these traps can reach higher densities. The atomic density of the clouds studied by Pellegrino and Jennewein follows the same distribution as the Gaussian intensity profile of the trapping beam. From literature it is known that the peak density at the center of a FORT is given by [54, 55]

$$\rho_{\text{peak}} = \frac{2N\lambda_{\text{trap}}}{\pi w_0^4}\left(\frac{U_0}{\pi k_B T}\right)^{\frac{3}{2}}, \tag{3.5}$$

where N is the total number of atoms inside the trap, w_0 the waist of the trap laser, U_0 the trap depth, T the temperature of the ensemble of atoms and k_B the Boltzmann constant. In the experiment presented in Fig. 3.2(b), the waist of the trap beam is 1.2 μm and after filling in the experimental parameters ($\lambda_{\text{trap}} = 940$ nm, $U_0/k_B = 1$ mK, $T = 120$ μK), the peak density can be found to be 2×10^{14} at/cm^3 for $N = 180$ atoms in a cigar shaped wavelength-size atomic cloud. We have seen in Table 3.1 that this atomic density ($\rho/k^3 = 0.38$) is enough for the atomic cloud to be in the strong resonant dipole-dipole interaction regime.

From the atomic density we can estimate the on-resonance scattering mean free path. This parameter tells us if the wavelength-size cloud is in the single scattering or multiple scattering regime. With a peak atomic density of $\rho/k^3 = 0.38$ we obtain for the mean free path:

$$l_{\text{mfp}} = \frac{1}{\rho\sigma_{\text{ext}}(\omega_0)} = \frac{k^2}{6\pi\rho} = 17 \text{ nm}. \tag{3.6}$$

Given the size of the atomic cloud that is on the order of the optical wavelength, this atomic cloud is clearly in the multiple scattering regime.

3.3.2 Doppler effect

To have strong resonant dipole-dipole interactions, the atoms need to have all the same resonance frequency. The presence of a significant Doppler broadening ($\Delta\omega > \Gamma_0$) would spread out the resonance frequencies, thereby reducing resonant dipole-dipole interactions. To avoid strong Doppler broadening, the atomic clouds studied by both Pellegrino and Jennewein are at very low temperatures of about 100 μK. The corresponding Doppler broadening is $\sim$100 kHz, which is small compared to the 6 MHz natural linewidth of the investigated transition. Hence, inhomogeneous broadening due to Doppler effect is negligible. It is both the absence of inhomogeneous broadening and the high atomic density that make the atomic systems as presented in Fig. 3.2 interesting to study the influence of resonant dipole-dipole interactions on light scattering from an ensemble of atoms.

3.3.3 Probe beam and atomic transition

After having discussed the atomic systems, let us give some information on the probe beam. In both setups, the Gaussian laser beam has a wavelength $\lambda_L = 780$ nm, corresponding to the transition wavelength of the D_2 transition between the $(5S_{1/2},\ F = 2)$ and $(5P_{3/2},\ F = 3)$ levels in rubidium-87[1], and spectral width $\sim 0.3\Gamma_0$. From this transition it is understood that the Rb-87 atoms studied here are not classical dipoles, since a classical dipole corresponds to a transition between a $J = 0$ and $J = 1$ state which is a four-level system with equal Clebsch-Gordan coefficients. The atoms we study here are 12-level systems[2], with non-equal Clebsch-Gordan coefficients. Yet, unless stated differently, all calculations

[1] In atomic physics, this notation for the atomic energy levels is very common. The different symbols in the notation $(nL_J,\ F)$ stand for the principal quantum number (n); the orbital angular momentum (L), where L is given as a letter (S corresponds to $L = 0$, P to $L = 1$); the total angular momentum, taking into account the spin angular momentum of the electron (J); and the total atomic angular momentum, where the total angular momentum of the nucleus has been taken into account (F).

[2] For the experiment of Jennewein, there are 5 degenerate states for $(5S_{1/2},\ F = 2)$, and 7 degenerate states for $(5P_{3/2},\ F = 3)$. They are degenerate, since no external magnetic field is applied that lifts the degeneracy.

that have been done in this thesis do assume the atoms to be classical dipoles, since it allows to understand some interesting general notions for resonant light scattering from dense samples.

Concerning the waist of the probe beams, for the setup of Pellegrino we can consider the incident field to be a plane wave as its waist w_0 is 1 mm and therefore very large compared to the size of the cloud. The Gaussian beam in the setup of Jennewein is strongly focused to a waist $w_0 = 1.2$ μm. In both setups, the laser intensity is small compared to the saturation intensity of the D_2 transition of a single Rb-87 atom (setup of Pellegrino: $I/I_s \approx 0.1$, where $I_s = 1.67$ mW/cm^2 for a circularly polarized probe, and for the setup of Jennewein: $I/I_s \approx 0.02$, where $I_s = 3.05$ mW/cm^2 for a linearly polarized probe). The frequency of the laser is tuned by the use of an acousto-optic modulator (AOM) over a frequency range of 72 MHz ($= 12\Gamma_0$: $-6\Gamma_0 < \delta\omega_L < 6\Gamma_0$), in order to observe the spectral response of the atomic cloud.

3.3.4 Measured signal

At last, we discuss the signal that is measured. For Pellegrino's experiment, an I-CCD with a polarizer in front was used, so they measured the power corresponding to the electric field components along the polarizer its direction. In the case of Jennewein's experiment, they used a single-mode fiber to collect the signal. Hence, the signal obtained by Jennewein is not the total energy flow integrated over a given solid angle, but it is the projection of the total field on the fiber mode. The electric field inside the single-mode fiber is given by

$$\mathbf{E}_{\text{fiber}}(\mathbf{r}) = \Big[\int \mathbf{E}_{\text{tot}}(\mathbf{r}') \cdot \mathbf{g}^*(\mathbf{r}') dS\Big]\mathbf{g}(\mathbf{r}), \tag{3.7}$$

where $\mathbf{g}$ is the normalized electric field distribution of the fiber mode, $\mathbf{E}_{\text{tot}} = \mathbf{E}_{\text{inc}} + \mathbf{E}_{\text{sc}}$, and dS is a differential area element perpendicular to the optical axis. The integral in front of the electric field distribution inside the fiber determines how well the fiber mode is excited; it is an overlap integral. In the absence of the atoms, we have $\mathbf{E}_{\text{tot}} = \mathbf{E}_{\text{inc}}$, the electric field inside the fiber is then

$$\mathbf{E}_{\text{fiber},0}(\mathbf{r}) = \Big[\int \mathbf{E}_{\text{inc}}(\mathbf{r}') \cdot \mathbf{g}^*(\mathbf{r}') dS\Big]\mathbf{g}(\mathbf{r}), \tag{3.8}$$

What is actually measured are powers. It can be shown that

$$\frac{P}{P_0} = \frac{|\int \mathbf{E}_{\text{tot}}(\mathbf{r}') \cdot \mathbf{g}^*(\mathbf{r}') dS|^2}{|\int \mathbf{E}_{\text{inc}}(\mathbf{r}') \cdot \mathbf{g}^*(\mathbf{r}') dS|^2}, \tag{3.9}$$

where P is the measured power in the presence of the atoms, and P_0 the measured power in the absence of the atoms. Without atoms, a mode matching of the incident laser beam and the single-mode fiber has been established experimentally, so that $\mathbf{g} \propto \mathbf{E}_{\text{inc}}$ (the direction of both $\mathbf{g}$ and $\mathbf{E}_{\text{inc}}$ are the same due to the polarizer in front of the fiber). Experimentally, there is less than one photon detected per incident pulse. In order to have a good signal-to-noise ratio (SNR), a detection cycle is repeated a thousand times. The precise procedure can be found in Ref. [7]. Because of these many cycles, the measured quantities can be considered to be ensemble averaged. So what can be derived from the experiments is

$$\frac{\langle P \rangle}{P_0} = \frac{\langle |\int \mathbf{E}_{\text{tot}}(\mathbf{r}') \cdot \mathbf{E}^*_{\text{inc}}(\mathbf{r}') dS|^2 \rangle}{|\int |\mathbf{E}_{\text{inc}}(\mathbf{r}')|^2 dS|^2}, \tag{3.10}$$

where the total field $\mathbf{E}_{\text{tot}} = \mathbf{E}_{\text{inc}} + \langle \mathbf{E}_{\text{sc}} \rangle + \delta\mathbf{E}_{\text{sc}}$. The measured signal therefore contains a coherent and incoherent contribution. By means of the Cauchy-Schwarz inequality, it can be shown that the power $\langle P \rangle$ measured in this way is smaller than or equal to the total power just before the single-mode fiber. From a physical perspective this makes sense, since a projection of the electric field is done on the fiber mode, which means that the measured power is bounded from above by the total power just before the optical fiber.

3.4 Spectral change while crossing the focal region: Gouy phase

Before we study the main experimental results, let us discuss focussing of the laser beam on the cloud. In the resonant light scattering experiments of Jennewein, both the atomic cloud and the waist of the laser beam are on the order of the wavelength of the studied electric dipole transition in rubidium-87. It is therefore very challenging to focus the laser beam correctly, i.e., on the center of the atomic cloud. One might think that the consequence of not having the focus exactly in the center of the cloud does not alter the measured spectrum significantly, since the cloud is small compared to the Rayleigh distance ($z_R = 5.8\ \mu$m) and therefore the intensity of the beam experienced by the cloud does not change a lot as the focus spot moves longitudinally. Figure 3.3 shows two (stars and dots) experimentally obtained spectra in the forward direction. Each spectrum corresponds to an experiment that has been done at a different moment in time. Each cloud contains about the same number of atoms (60 and 63 atoms), but the position of the atomic cloud with respect to the focus is not the same. Jennewein measured the difference

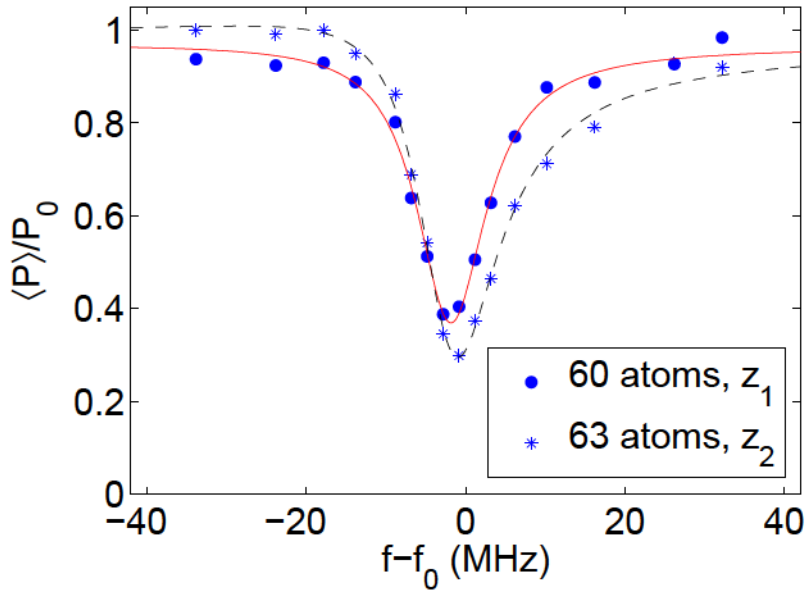

Figure 3.3: *Experimental results obtained with a collecting lens along the optical axis and a numerical aperture NA = 0.5. The position of the laser beam focus with respect to the cloud was different in both experiments (indicated by z_1 and z_2). Both experimental results are fitted by the function: $y = |c_1 - \frac{c_2}{1-2i(x-c_3)/c_4} e^{ic_5}|^2$. For an explanation of this fit function, refer to Section 3.4.1.*

of the position of the atomic clouds to be $z_2 - z_1 = 2.5 \pm 0.3$ μm, which is small compared to the Rayleigh distance. The intensity of the beam on the cloud has therefore changed negligibly. However, it is seen from Fig. 3.3 that although the clouds contain about the same number of atoms, and the intensity of the probe beam did not change significantly, both spectra are not the same. Notably, the asymmetry of the spectra is not the same. Let us mention that similar results were obtained in the group of Havey. In that group, it was observed that the transmission spectrum of a big cloud of atoms is asymmetric in frequency and the asymmetry of the transmission spectrum flips sign when the focus of the beam crosses the atomic cloud [56]. The observed asymmetric transmission spectrum was published in the work of Roof *et al.*, entitled "Microscopic lensing by a dense, cold atomic sample" [56]. The flip of the asymmetry in the frequency response was attributed to focusing and defocusing effects; thereby attributing the asymmetry to a lensing effect of their cloud. Both focusing and defocusing exist in the studied cloud, since the atomic cloud is big ($255 \times 3.5 \times 3.5$ μm^3), and the calculated refractive index of the cloud can attain values smaller and larger than one for different frequencies. A refractive index that is smaller than one gives rise to defocusing and a refractive index larger than one leads to focusing. The atomic system studied by Jennewein *et al.* is different, since that cloud is very small and therefore geometrical optics is not valid. In this section, we propose an alternative explanation of the observed dependence of the spectrum on the longitudinal position of the beam focus with respect to the cloud.

3.4.1 Toy model for light scattering

To explain the different spectra for clouds that were very similar in size and number of atoms, see Fig. 3.3, we study a toy model which only contains essential properties to understand the physics. This toy model is a single atom, which position is varied. A horizontally polarized incident Gaussian beam, propagating along the z axis, has its focus at position $(x_f, y_f, z_f) = (0, 0, 0)$, while the atom is moved along the optical axis and has position $(0, 0, z_{\text{atom}})$. The electric field of the beam, within the paraxial beam approximation, is given by

$$\mathbf{E}_L(\rho, z) = \mathbf{E}_0 \frac{w_0}{w(z)} e^{-\frac{\rho^2}{w(z)^2}} e^{i[kz + k\frac{\rho^2}{2R(z)} - \psi(z)]}, \tag{3.11}$$

where $\rho = \sqrt{x^2 + y^2}$ is the distance to the optical axis, $w(z) = w_0\sqrt{1 + (z/z_R)^2}$ the distance to the optical axis over which the intensity drops by a factor $1/e^2$, $R(z) = z[1 + (z_R/z)^2]$ is the radius of curvature, and $\psi(z) = \arctan(z/z_R)$ is the Gouy phase. On axis ($\rho = 0$) it is seen from Eq. 3.11 that the phase does not evolve the same as the phase of a plane wave. There is an additional phase term, called the Gouy phase. This Gouy phase is precisely the phase difference a Gaussian beam acquires during propagation as compared to a plane wave propagating along the z axis. The origin of the Gouy phase is the fact that around focus, "the average propagation constant" is smaller for a Gaussian beam than for a plane wave. For a plane wave propagating along the z axis, the propagation constant $k_z = k_0$. As a Gaussian beam has a smaller average propagation constant around focus, its phase evolves slower during propagation as compared to the phase of a plane wave propagating along the optical axis. It is this difference in the acquired phase that is called the Gouy phase. The Gouy phase is the key element of this section.

The beam induces an electric dipole moment $\mathbf{p} = \varepsilon_0 \alpha(\omega) \mathbf{E}_L(0, 0, z_{\text{atom}})$, where $\alpha(\omega)$ is the atomic polarizability of a single atom, given by

$$\alpha(\omega) = \frac{3\pi\Gamma_0/k^3}{\omega_0 - \omega - i\frac{\Gamma_0}{2}}. \tag{3.12}$$

The induced dipole creates an electric field which is given by the Green's tensor. As we measure far away from the atom, i.e., $kz_D \gg 1$, and $z_D \gg z_{\text{atom}}$, where the subscript D stands for detector, we only need to consider the far-field term of the Green's tensor. The scattered field along the optical axis is then given by

$$\mathbf{E}_{\text{sc}} = \mu_0 \omega^2 \frac{e^{ik|z_D - z_{\text{atom}}|}}{4\pi|z_D - z_{\text{atom}}|}\mathbf{p} \approx \mu_0 \omega^2 \frac{e^{ik|z_D - z_{\text{atom}}|}}{4\pi|z_D|}\mathbf{p}. \tag{3.13}$$

The position of observation is taken to be positive: $z_D > 0$ and the scattered field is then

$$\mathbf{E}_{\text{sc}}(0, 0, z_D) = \frac{\omega^2}{c^2}\alpha(\omega)\frac{e^{ik(z_D - z_{\text{atom}})}}{4\pi z_D}\mathbf{E}_L(0, 0, z_{\text{atom}}). \tag{3.14}$$

The incident electric field is simply $\mathbf{E}_L(0, 0, z_D)$ at the observation position. When we add the scattered electric field to the incident electric field, we obtain the total electric field at the position of the detector:

$$\mathbf{E}_{\text{tot}} = -i\mathbf{E}_0 \frac{z_R}{z_D} e^{ikz_D} + \frac{\omega^2}{4\pi c^2}\alpha(\omega)\mathbf{E}_0 \frac{1}{\sqrt{1 + \left(\frac{z_{\text{atom}}}{z_R}\right)^2}} e^{-i\psi(z_{\text{atom}})} \frac{e^{ikz_D}}{z_D} \tag{3.15}$$

$$= -i\mathbf{E}_0 \frac{z_R}{z_D} e^{ikz_D} \left[1 + i\frac{\omega^2}{4\pi c^2 z_R}\alpha(\omega) \frac{1}{\sqrt{1 + \left(\frac{z_{\text{atom}}}{z_R}\right)^2}} e^{-i\psi(z_{\text{atom}})}\right]. \tag{3.16}$$

From the total electric field, one can readily obtain the normalized total power on axis

$$\frac{P(\omega)}{P_0} = \left|1 + i\frac{\omega^2}{4\pi c^2 z_R}\alpha(\omega) \frac{1}{\sqrt{1 + \left(\frac{z_{\text{atom}}}{z_R}\right)^2}} e^{-i\psi(z_{\text{atom}})}\right|^2, \tag{3.17}$$

where P_0 is the incident power in the forward direction when no atoms are present. When we assume $\omega \approx \omega_0$, we can find from this formula, and the expression for the polarizability (see Eq. 3.12), the fit function $y = |1 - \frac{c_2}{1 - 2i(x - c_3)/c_4} e^{ic_5}|^2$, which is used in Fig. 3.3 to fit the experimental results[3]. All parameters are free parameters. The coefficient c_3 corresponds to a possible frequency shift of the scatterer, c_4 is the linewidth of the transition, and c_5 is the Gouy phase.

Although this model for the spectrum follows from light scattering from a single atom, it also correctly models light scattering from a sphere with a resonant dielectric constant $\varepsilon(\omega)$, that mathematically has a similar resonance as a single atom, and radius a much smaller than the wavelength if the electric field inside is uniform. The reason this model also works for small resonant spheres is that in that case the optical response can also be described by a polarizability $\alpha(\omega) = 4\pi a^3[\varepsilon(\omega) - 1]/[\varepsilon(\omega) + 2]$ [14]. As we have seen in Fig. 3.3, the same fit function works also well for the elongated cloud of atoms.

[3]Because of the way the measured data points were normalized in Fig. 3.3 (the maximum value of $|S(\omega)|^2$ is set to 1), we need to leave the first term also as a free parameter: $y = |c_1 - \frac{c_2}{1 - 2i(x - c_3)/c_4} e^{ic_5}|^2$, where all parameters are real.

3.4.2 Explanation of asymmetric spectrum

Let us develop the expression given in Eq. 3.17. It can be written in the form

$$\frac{P(\omega)}{P_0} = 1 + A|\alpha(\omega)|^2 + B\Big[(\omega_0 - \omega)\sin\psi(z_{\text{atom}}) - \frac{\Gamma_0}{2}\cos\psi(z_{\text{atom}})\Big], \tag{3.18}$$

where A and B are both real and positive. The third term, which is proportional to the parameter B, originates from interferences between the incident field and the scattered field. This is a very important notion as it follows from this interference term that what is measured with a spectroscopic measurement are interferences between the incident beam and the scattered field. It is precisely the interference term that introduces a dependence of the measured power on the atomic position. When the atom is positioned in the focus, $\psi(z_{\text{atom}}) = 0$. Since $|\alpha(\omega)|^2$ is symmetric around the resonance frequency, $P(\omega)/P_0$ is also symmetric around the resonance frequency for this special case. Contrarily, when the atom is placed out of focus, $\psi(z_{\text{atom}}) \neq 0$ and thus the spectrum becomes asymmetric. It is observed from the term $(\omega_0 - \omega)\sin\psi(z_{\text{atom}})$ that the asymmetry of the spectrum flips sign when the atom crosses the focus. As an illustration, we have numerically calculated the on-axis scattering spectrum for a Gaussian beam with waist $w_0 = 1.2$ μm incident upon a single atom that is put in the focus, and both 1 μm before and after the focus. The spectrum is given in Fig. 3.4. Figure 3.4 shows that the asymmetry of the spectrum indeed flips sign when the atom crosses the focus.

From the previous discussion it follows that what is measured are interferences between the incident and scattered fields. This means that the spectrum does not only contain intrinsic properties of the atom (here its polarizability and in the work of Roof *et al.* [56]

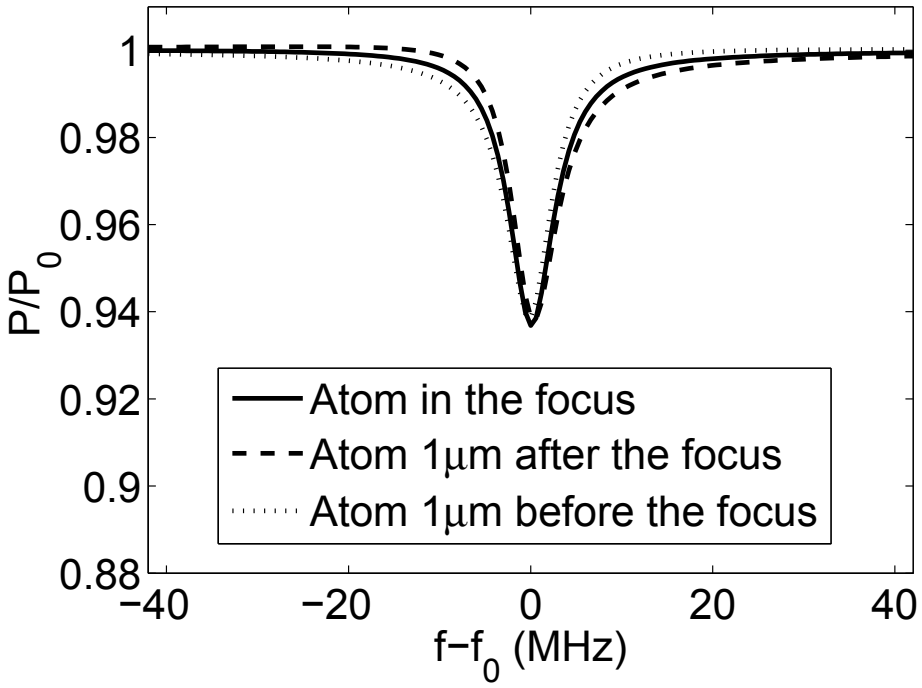

Figure 3.4: *Numerically obtained on-axis spectrum from a single atom being positioned at three different places: before, in and after the beam focus. Input field is a Gaussian beam with waist* $w_0 = 1.2$ μm.

the index of refraction). The spectrum therefore reflects both the intrinsic properties of the atom and the geometrical configuration. It is important to realize that when we would have detected all the scattered light around the atom, the relative power P/P_0 would be one for all frequency detunings, since we consider elastic light scattering for which all incident light is scattered. The interferences between the incident and scattered field are responsible for a redistribution of the energy. Furthermore, for finite apertures, where the numerical aperture is smaller than the beam spreading, it is possible to have a frequency range in which the transmission is superior to one. In the words of Roof *et al.* this originates from a lensing effect [56]. Apart from the asymmetric spectrum which arises due to a displacement of the atom, the dip also shifts in frequency, which finds its origin again in interferences. When the atom is positioned in the focal point, the dip frequency corresponds to the atomic frequency. This is not anymore true when the atom gets displaced. The dip position therefore does not necessarily reflect the resonance frequency.

Now that we have discussed the influence of the Gouy phase on the asymmetric spectrum, we come back to the experimental results that are shown in Fig. 3.3. Although the two clouds were of the same size and contained more or less the same number of atoms, the asymmetry is not the same. When we fitted the experimental data with the function: $y = |c_1 - \frac{c_2}{1-2i(x-c_3)/c_4} e^{ic_5}|^2$, we deduced that the distance between the centers of the two different clouds was 2.0 ± 0.6 μm. Experimentally this distance was measured to be 2.5 ± 0.3 μm, by which we confirm that the Gouy phase is indeed a possible explanation for the observed difference in spectra between two similar clouds. Furthermore, it has experimentally been verified that the fitted Gouy phase (c_5 in the fit function) was independent of the number of atoms in the cloud. This rules out the possibility of a lensing effect in our cloud, since the acquired phase during propagation would depend on the index of refraction, and therefore on the atomic density. Hence, the retrieved phase would depend on the atomic density, if Jennewein *et al.* observed a lensing effect [7].

In this section we have shown that the results of Fig. 3.3 are an experimental demonstration of the influence of the Gouy phase on the measured spectrum. A simple model that takes into account the Gouy phase is able to determine the distance between the focal points of different experimental realizations; therefore showing the ability to facilitate the focusing of the laser beam. Although this notion is already known in for example the field of Coherent anti-Stokes Raman scattering (CARS), the Gouy phase is known for giving rise to asymmetric spectra [57], it is not to the best of our knowledge in the field of cold atoms.

3.5 Scattering suppression

We now study the experimental results obtained by Joseph Pellegrino [51] and Stephan Jennewein [7]. We follow the chronological order in which the experiments were done and therefore start discussing the experimental results of Pellegrino.

3.5.1 Experimental results of Pellegrino *et al.*

In the setup as shown in Fig. 3.2(a), Pellegrino collected the scattered light at 90° with respect to the optical axis. Figure 3.5(a) shows the ensemble-averaged scattered power as a

function of the number of atoms inside the cloud. Experimentally, an ensemble average corresponds to the measurement of a given quantity over several experimental runs. The power measured by an NA = 0.5 optical system is normalized to the measured scattered power for a single atom under illumination with the same frequency detuning. The quantity $\langle P \rangle / P_{0,\Delta}$ can therefore be understood as the average number of atoms effectively scattering light. The experiments were done for the frequency detunings $\Delta\omega_L = \{-2.5, -1, 0, 1, 2.5\} \times \Gamma_0$, which are represented by different markers in Fig. 3.5(a). From Fig. 3.5(a) it can be seen that the closer the laser frequency is to the resonance frequency, the smaller the effective number of atoms scattering light at 90° is. Away from atomic resonance, the scattered power seems to tend towards the dashed line. The dashed line represents Rayleigh scattering, for which the observed scattered power would increase linearly with the number of atoms. Compared to a gas of non-interacting atoms, Pellegrino has therefore observed suppression of light scattering. The largest suppression of light scattering occurs on resonance, where resonant dipole-dipole interactions are the strongest. It is therefore the resonant nature of the interactions that dramatically alters the optical response of the ensemble of atoms. This observation is remarkable, since light scattering is clearly very different in the Rb-87 cloud as compared to Rayleigh scattering from the sky; knowing that the sky is five orders of magnitude denser than the cloud of rubidium atoms. We now proceed to numerical calculations on a similar system where the atoms are modeled as classical dipoles.

3.5.2 Numerical calculations on suppression of light scattering

An advantage of numerical calculations over experiments in this particular case is that we have access to the full scattering pattern and that we can separate coherent and incoherent light scattering easily, as was explained in Section 2.2.3. For an on-resonance circularly polarized incident plane wave, we calculate the scattered power at 90° with respect to the propagation direction of the plane wave and with a numerical aperature NA = 0.5. Figure 3.5(b) shows the same quantity as has been measured experimentally: the total scattered power relative to the scattered power from a single atom. The dashed line represents again Rayleigh scattering. It is seen that as the number of scatterers augments, the scattered power at 90° increases, but the increase declines. So, numerically we also find a suppression of light scattering, but it is stronger than was found experimentally. In order to understand why light scattering gets suppressed, we have calculated the on-resonance ensemble-averaged scattering pattern for a cloud containing $N = 300$ atoms. The result is presented in Fig. 3.5(c). As can be seen, there is a big lobe in the forward direction, reminescent of *diffraction* from the atomic cloud. Apart from the diffraction pattern, there is also light that gets scattered quasi isotropically, as can be seen in the figure at the height of the arrow indicating 90°. It is seen that diffraction is an important part of light scattering. This means that the effective refractive index is very different from 1. The density fluctuations inside the atomic cloud get illuminated by a smaller electric field than the incident field, due to which incoherent light scattering stops growing linearly with the number of atoms; it gets suppressed. From diffraction theory it is known that the diffraction pattern of such a cloud is directional and peaks in the forward direction. However, at 90° there is no diffraction, and it is incoherent light scattering that dominates. When the density of the atomic cloud increases, we observe that diffraction starts playing an important role for light scattering, whereas the importance of incoherent light scattering gets smaller. Going from the regime where incoherent light scattering dominates to a regime where coherent

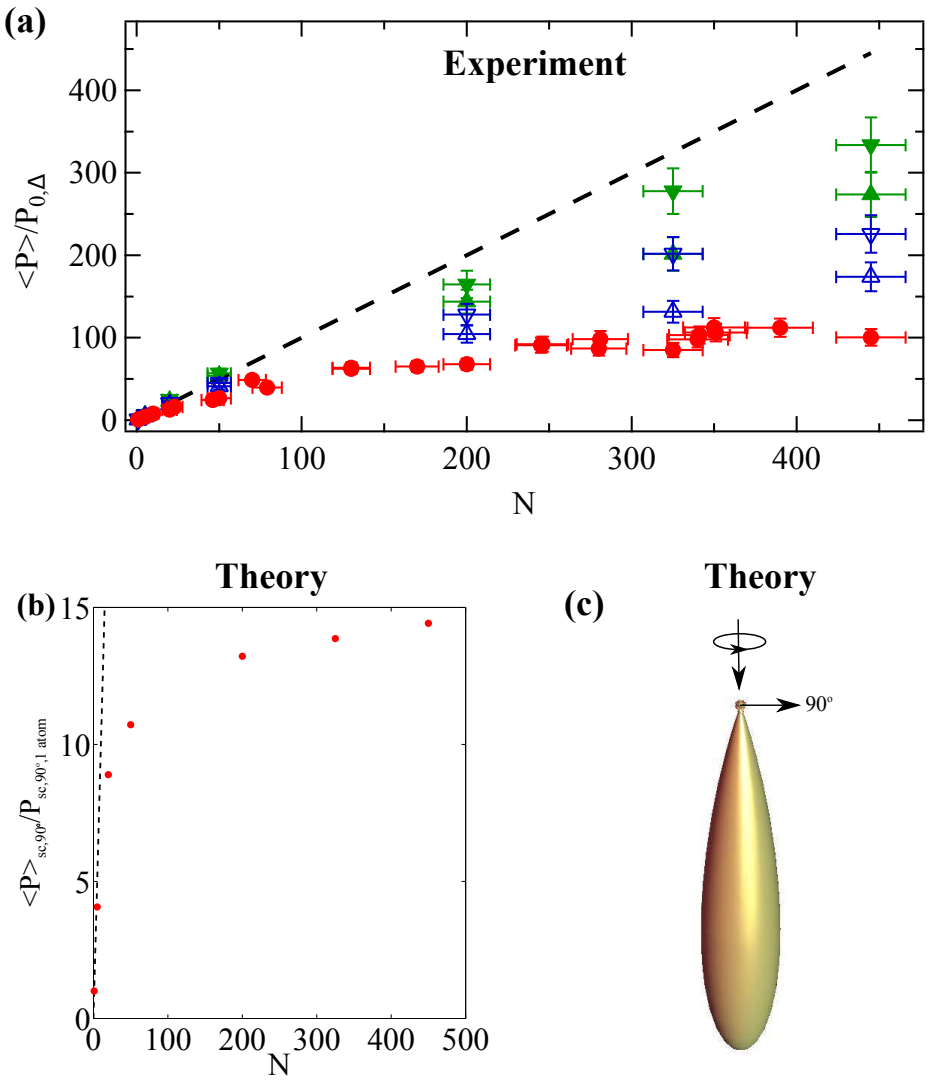

Figure 3.5: *(a) Experimental results of Pellegrino, published in Ref. [51]. The normalized scattered power as a function of the number of atoms inside the cloud (horizontal axis) and for different detunings of the laser beam (markers):* $\Delta\omega_L = 0\Gamma_0$ *(red circles),* $\Delta\omega_L = \pm\Gamma_0$ *(up or down open triangles), and* $\Delta\omega_L = \pm 2.5\Gamma_0$ *(up or down filled triangles). The power has been normalized to the power that would be detected for a single atom in the cloud being illuminated with the same detuning. Dashed line: case of non-interacting atoms. (b) Theoretical results. The red dots represent the total scattered power at* 90° *normalized by the power that a single atom would scatter in the same solid angle as a function of the number of atoms in the cloud. The dashed line corresponds to the line* $y = x$*, which would be the result in the single-scattering regime. Scattering suppression can be observed when the number of atoms increases. (c) On-resonance ensemble-averaged scattering pattern for a cloud containing* $N = 300$ *atoms. The big lobe in the forward direction is reminescent of diffraction from the atomic cloud. Incoherent light scattering occurs quasi isotropically, as can be seen at the height of the arrow indicating* 90°*.*

light scattering dominates forms a homogenization problem. In Chapter 5 we will discuss the homogenization problem for resonant light scattering from a dense cloud of cold atoms.

3.5.3 Towards coherent light scattering

We are particularly interested in the coherent response of the atomic cloud, since we can compare this form of light scattering to the macroscopic Maxwell equations where the cloud is modeled by an effective refractive index. From diffraction theory it is known that in the forward direction constructive interferences exist, due to which enhanced light scattering can be observed. Jennewein *et al.* have studied the coherent optical response by putting the detector along the optical axis. For the remaining part of this chapter, we will thus also discuss the experimental results obtained by Jennewein. In particular, we will discuss the frequency response of both the clouds studied by Pellegrino and Jennewein in Section 3.6.

3.6 Spectral response of the atomic cloud

In the last section we were mainly interested in what happens to light scattering when the number of atoms increases. We have seen that suppression of light scattering occurs. In this section, we focus on the study of the spectral response of both the atomic clouds of Pellegrino (detection at 90° from optical axis) and Jennewein (detection in the forward direction). The former will be refered to as "incoherent spectral response" and the latter to "coherent spectral response" for reasons that have been explained in Section 3.5.

3.6.1 Incoherent spectral response

The experimentally obtained powers by Pellegrino have been plotted in Fig. 3.6(a), where the color of the dots and the corresponding Lorentzian fits corresponds to a given number of atoms in the cloud. We consider clouds with $N = \{1, 5, 20, 50, 200, 325, 450\}$ atoms inside. The measured power has been normalized to the measured scattered power from a single atom in the cloud illuminated on resonance. For all frequency detunings it is observed that as the number of atoms augments (bottom to top), the scattered power increases as well, but saturates; an observation that we have already made in Section 3.5. Some other observations are spectral broadening and a very small red frequency shift. A spectral broadening is in general expected. To first order, this can be understood by the fact that resonant dipole-dipole interactions slightly move the energy levels. This effectively increases the linewidth of the ensemble of atoms. With regard to the small frequency shift: this seems to be in qualitative agreement with a recently published work where the authors claim that "no overt Lorentz-Lorenz local field shift of the resonance, nor a cooperative Lamb shift exist in homogeneously broadened atomic samples" [58].

We have also calculated the normalized optical response at 90°. Figure 3.6(b) shows the theoretical results, where the vertical axis has a log scale. The conditions of the calculations are the same as described in the previous section. It is observed that the theoretically obtained spectra are Lorentzian for clouds with a small number of atoms. As the number of atoms increases, the spectra start to deviate from a Lorentzian; an observation that is in disagreement with the experimental results. The origin of the change of shape of the spectrum for increasing atomic density is the increase of the resonant dipole-dipole interactions that effectively reduce the scattering mean free path and thereby take the wavelength-size cloud out of the single scattering regime. This observation does not question the validity of the argument used to explain suppression of light scattering, but it does provoke the following question: why does Pellegrino not measure a spectrum that is different

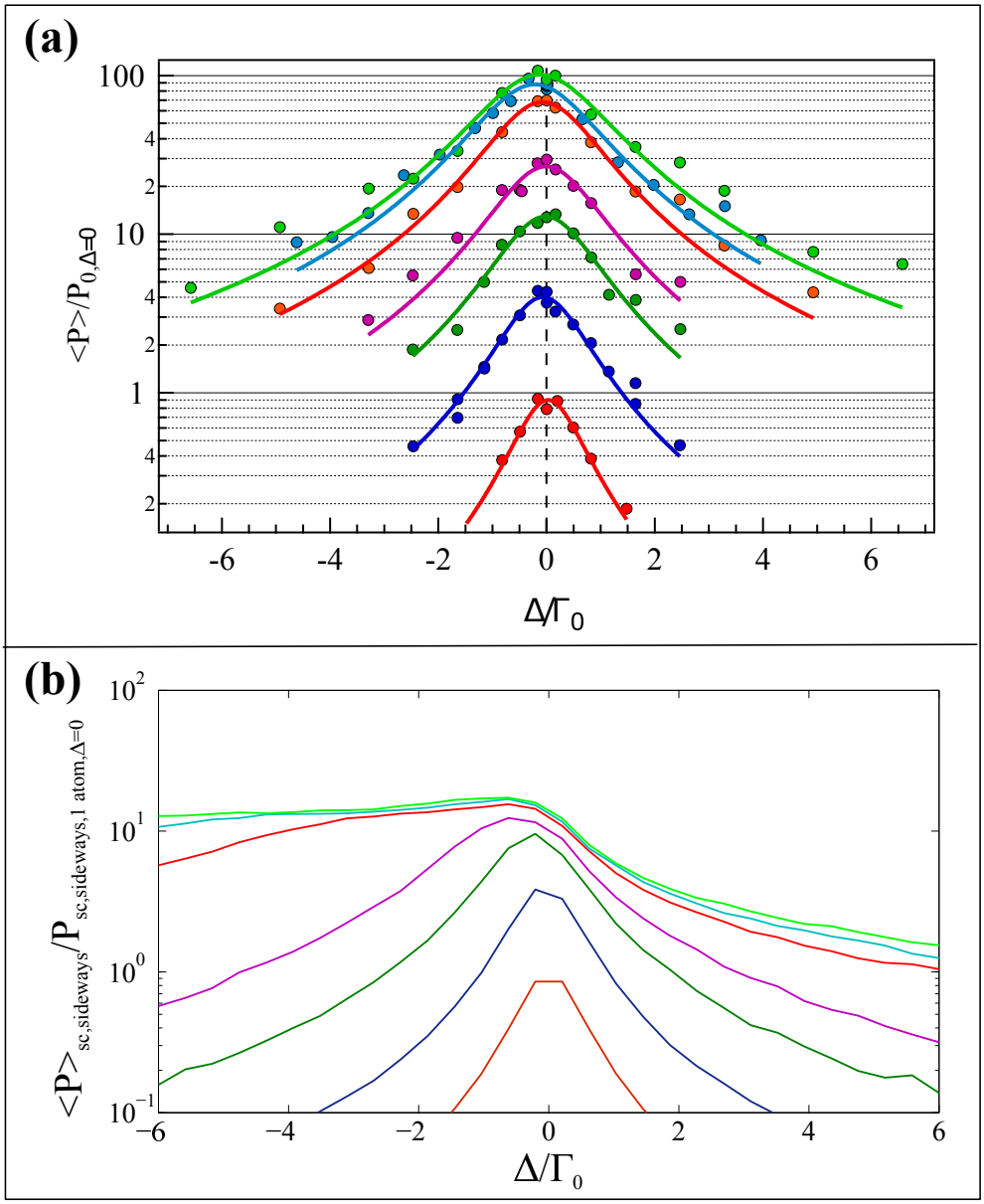

Figure 3.6: *(a) Experimental data, obtained by Pellegrino et al.. Normalized scattered power at a* 90° *angle with respect to the optical axis as a function of the laser detuning* Δ *for different number of atoms inside the cloud, the latter being the color that makes the distinction between different number of atoms. From bottom to top we have* $N = \{1, 5, 20, 50, 200, 325, 450\}$. *(b) For the same values of* N, *we have calculated the normalized scattered light at* 90° *for a circularly polarized incident plane wave.*

from a Lorentzian? It is most likely that the resonant dipole-dipole interactions in the actual experiments are weaker than in our model. Some possible reasons for this are the fact that Rb-87 has in reality a multilevel structure, and that dipole-dipole forces might hinder the atoms to approach each other, thereby effectively reducing the interaction.

3.6.2 Coherent spectral response

In the experiments done by Jennewein *et al.*, light is detected in the forward direction. From Section 3.5, it is understood that in that experiment the coherent optical response of the cloud is measured. Figure 3.7 shows schematically a linearly polarized focussed Gaussian beam (red) that is incident upon the (blue) cloud of Rb-87 atoms. Note that the atomic cloud of Jennewein does not have the same size as the atomic cloud studied by Pellegrino, see Fig. 3.2. On the right of Fig. 3.7, the diffraction pattern ($|\langle \mathbf{E} \rangle|^2$) of a cloud with $N = 180$ atoms on atomic resonance has been shown. The numerical aperture of the optical system corresponds to a full angle of 60° and is indicated by the bold dashed lines. It is observed that essentially all the coherently scattered light in the forward direction reaches the lens. Figure 3.8(a) shows the measured normalized powers that were obtained by Jennewein for different laser detunings. The normalization amounts to dividing the measured power by the measured power in the absence of the atoms. The filled markers are the experimental data points that belong to the cloud of Jennewein with $N = \{10, 83, 180\}$ atoms (top to bottom). We observe similar characteristics for the spectrum as we have previously seen for the setup of Pellegrino in Fig. 3.6: spectral broadening [see Fig. 3.8(d), where the spectral width has been plotted as a function of the number of atoms N in the cloud], very small frequency shift of the dip [see Fig. 3.8(c)], and a minimum value of the dip of the normalized power which saturates [see Fig. 3.8(b)]. When we look at the spectral shift in Fig. 3.8(c), we note that it is a bit larger than the actual position of the dip in Fig. 3.8(a). A likely reason for this is that the laser was not perfectly focused on the center of the cloud, giving rise to a change in the spectrum due to the Gouy phase.

Now, we compare the experimental results from Jennewein to numerical calculations. The negligible frequency shift that has been observed agrees qualitatively with the prediction of Javanainen *et al.*: the Lorentz-Lorenz shift and cooperative Lamb shift are absent in homogeneously broadened, dense atomic samples [58]. In the same work, it was explained that inhomogeneous broadening recovers the predictions of mean-field

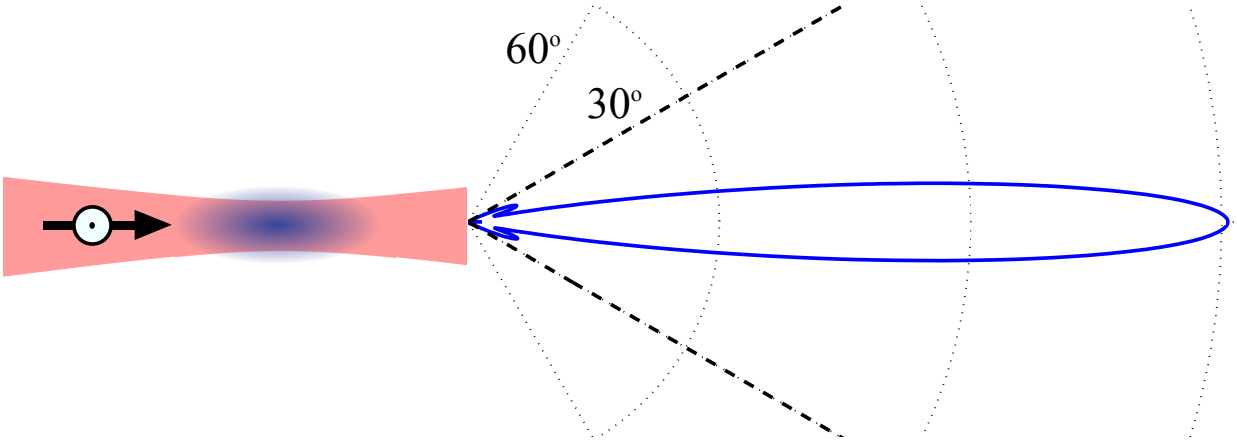

Figure 3.7: *Numerical results of coherent light scattering with a Gaussian beam (red) incident on a cloud of $N = 180$ atoms (blue) with zero detuning. The right part of the figure shows the numerically obtained diffraction pattern, where the detection system can measure the light over a full angle of 60° ($NA = 0.5$). The schematic view of the incident light does not have the same scale as the numerical results at the right.*

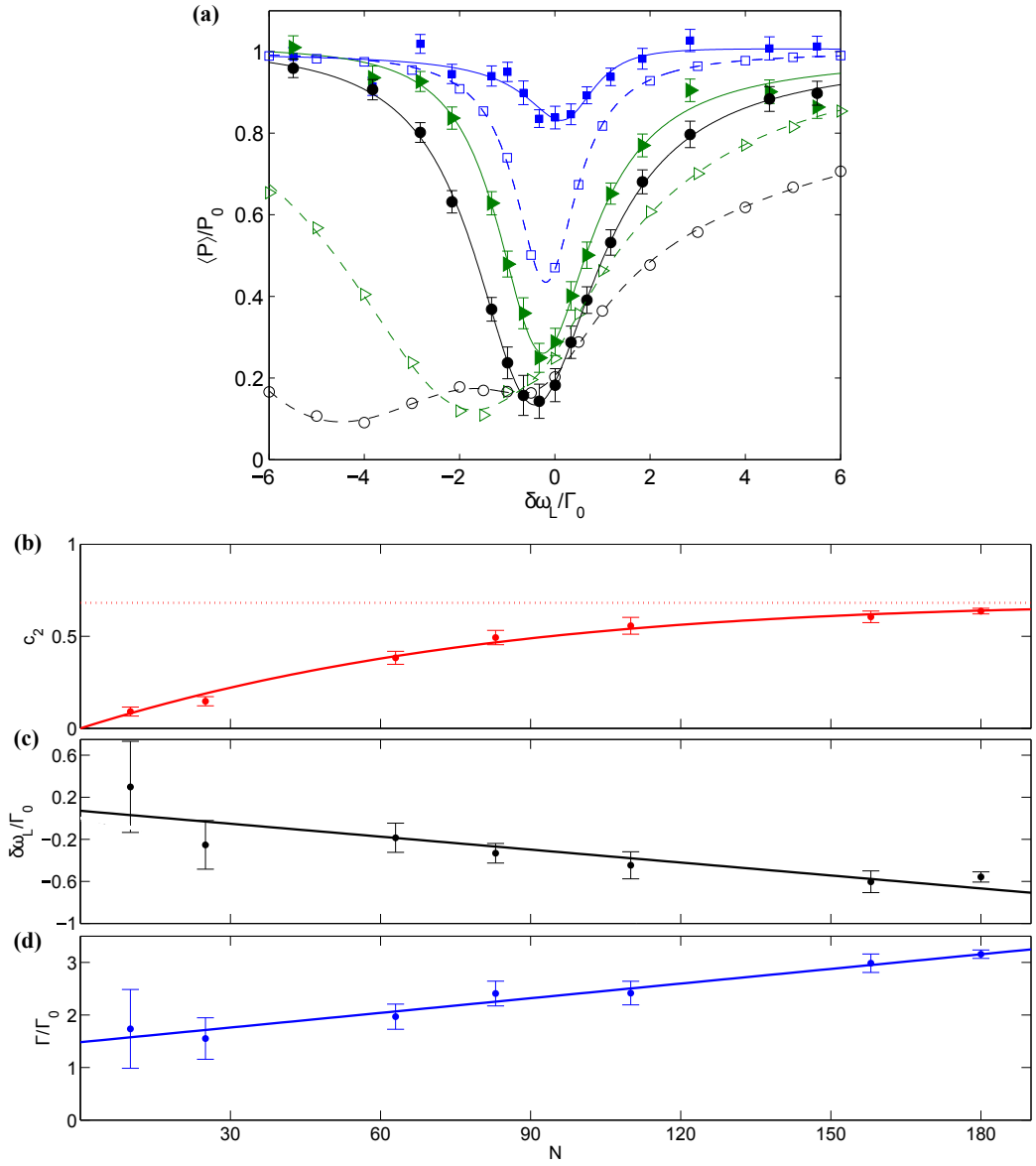

Figure 3.8: *(a) Both experimental (filled markers) and theoretical spectra (open markers). The theoretical spectra are obtained by using the coupled-dipole equations and assuming the atoms to be classical dipoles. The experimental data have been fitted with the function* $y = |1 - \frac{c_2}{1-2i(x-c_3)/c_4} e^{ic_5}|^2$ *and the theoretical data have been interpolated with the function* $y = |1 - \frac{c_2}{1-2i(x-c_3)/c_4} e^{ic_5} - \frac{c_6}{1-2i(x-c_7)/c_8} e^{ic_9}|^2$*. The number of atoms inside the cloud are* $N = \{10, 83, 180\}$ *(from top to bottom). (b) The experimentally obtained minimal value of the spectrum as a function of the number of atoms in the cloud. This value seems to saturate to the value indicated by the dashed line. The interpolation is done with the function:* $c_2(N) = 1 - \sqrt{a + (a-a)e^{-bN}}$*. (c) The shift of the resonance as a function of the number of atoms deduced from the experimental data. It has been linearly fitted (solid line). (d) The linewidth derived from the experiment plotted as a function of the number of atoms. It has been fitted with a linear function.*

theory, because resonant dipole-dipole interactions become weaker [58]. Indeed, for the hot atomic vapor of Keaveney *et al.*, a cooperative Lamb shift was observed and agreed

with the prediction of mean-field theory [38]. Similarly, Ref. [47] discusses light scattering from a cloud of cold Rb-87 atoms with a peak density varying up to $\rho_{\text{peak}} = 6 \times 10^{12}$ at/cm^3, which corresponds to $\rho/k^3 = 0.01$, and they have also observed a frequency shift that agrees with mean-field theory [37, 59]. The measured frequency shift is substantial: $2\Gamma_0$ [47], although the system is more dilute than the system studied by Jennewein *et al.* Because of weak resonant dipole-dipole interactions, the atomic cloud is not in the regime as described in Ref. [58] and mean-field theory predictions are therefore expected to be correct.

From the qualitative agreement of Jennewein's results with the predictions of Javanainen *et al.*, it seems that light scattering from the cloud of Jennewein indeed needs to be described by a beyond mean-field theory. We will therefore check if we can reproduce similar results with an exact calculation of the scattered power by means of the set of coupled-dipole equations. The incident field is taken to be a Gaussian beam, which has an angular spread of $\sin(\theta) = \lambda_L/(\pi w_0) = 0.21$. Since it is a strongly focused beam (waist of 1.2 μm), we do not use the paraxial beam approximation. The electric field is written as a plane wave decomposition [60]:

$$\mathbf{E}_L(\mathbf{r}_\parallel, z) = \frac{w_0^2 k^2}{4\pi} \iint e^{-\frac{w_0^2 k^2 \mathbf{s}^2}{4}} \mathbf{u}_{s/p}(\boldsymbol{\nu}) e^{ik\mathbf{s}\cdot\mathbf{r}_\parallel + ikcz} d^2\mathbf{s}, \tag{3.19}$$

where $k = \frac{\omega_L}{c}$, $\boldsymbol{\nu} = \langle \mathbf{s}, \sqrt{1-s^2} \rangle$, $\mathbf{s} = \frac{\mathbf{k}_\parallel}{k}$, and the polarization $\mathbf{u}_s = \frac{\mathbf{z}\times\boldsymbol{\nu}}{|\mathbf{z}\times\boldsymbol{\nu}|}$ or $\mathbf{u}_p = \boldsymbol{\nu} \times \mathbf{u}_s$ (s standing for a TE-polarized beam and p for a TM-polarized beam). In our configuration there is not a big difference between TE and TM polarization, because of the rotational symmetry of the problem after the ensemble averaging. The integral is rewritten in polar coordinates ($|\mathbf{s}|$ and θ), where the angular integral is done analytically. By doing so, there is only a single integral to be evaluated numerically. We have calculated the power for several detunings and like for the experiment we calculated light scattering for $N = \{10, 83, 180\}$ atoms, while taking into account the presence of the single-mode fiber. The results of the calculations are shown in Fig. 3.8(a) by the open markers, where the dashed lines are used to guide the eye. It is observed that these numerical results do not agree with the experimental results. Notably, a second resonance dip appears for both the $N = 83$ and $N = 180$ clouds. This second resonance is not a single-atom resonance, but a resonance of the shape of the cloud. Experimentally, the presence of a second resonance has never been observed by Jennewein. A question which remains open is why this second resonance has not been observed. For a more thorough discussion, refer to Jennewein *et al.* in Ref. [7].

3.7 Superluminal pulse propagation through an atomic cloud

In this section we discuss the temporal properties of a pulse propagating through the atomic cloud. It is known that pulse propagation in a resonant medium can lead to "fast" or "slow" light, due to the dispersive response of such a resonant medium [61–64]. Fast (slow) light corresponds to a situation where the peak of the outcoming pulse could be detected earlier (later) than the peak of a pulse which would travel through vacuum. Fast light corresponds therefore to a situation where *the peak* of the pulse travels faster than the speed of light in vacuum. An interesting application for slow light would be an optical

delay line. Fast light also finds interest in the field of quantum information processing, since it is accompanied with an imprinted phase shift on the laser field, which is strongly frequency dependent. Although there have been several examples of superluminal pulse propagation in an atomic cloud [65, 66], we highlight the pulse advancement that has been reported in a hot vapor of Rb-87 by the group of Adams. Keaveney *et al.* measured an advance of an optical pulse of more than 100 ps over a propagation distance of 390 nm [39].

Jennewein has done an experiment where the temporal properties of pulse propagation through the cold atomic cloud were studied. He measured the group delay for $N = 170$ atoms in the cloud and for different laser detunings. The group delay is defined by the delay of the *peak* of the pulse. Figure 3.9 shows the measured group delay as a function of the frequency detuning. The solid curve follows from a fit, as explained in Jennewein *et al.* [52]. In the same work, one can find a discussion about the asymmetry visible in this curve. For our discussion, this aspect is irrelevant. Jennewein has measured negative group delays, which means a group advance. He measured a group advance as large as 10 ns, which is two orders of magnitude larger than observed by Keaveney *et al.*, although the cloud is only one order of magnitude longer.

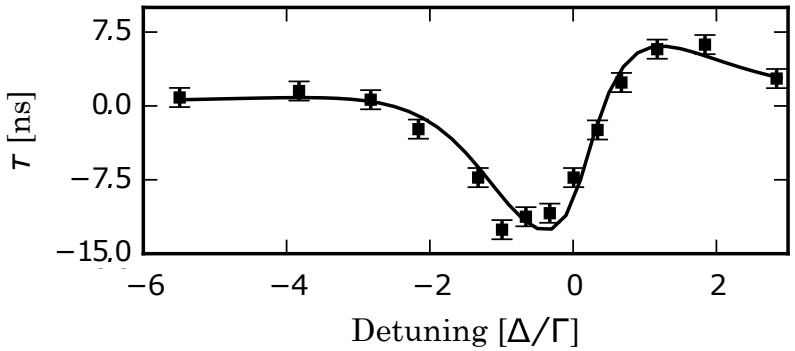

Figure 3.9: *The group delay for $N = 170$ atoms inside the cloud, measured by Jennewein. The data points have been fitted. For an explanation of this fit, refer to Ref. [52]. Group delays as large as -10 ns have been measured.*

Next, we calculate the group delay inside the atomic cloud of Jennewein by means of a classical electrodynamics calculation. The calculation is a steady-state calculation, where a monochromatic Gaussian beam is incident on the cloud. It is essentially the same calculation which led to Fig. 3.7. The phase ϕ of the electric field in the forward direction (far field, $z \gg z_R, L$, where L is the typical size of the cloud) is calculated as a function of the normalized laser detuning $\Delta/\Gamma = (\omega_L - \omega_0)/\Gamma$. From this, the group delay τ can be calculated with the formula [61]

$$\tau = \frac{d\phi}{d\omega}. \tag{3.20}$$

Since the phase ϕ varies strongly over a frequency range on the order of Γ_0, this equality is understood to be valid only when the bandwidth of the optical pulse is very small compared to the single-atom spontaneous decay rate. Remember that the bandwidth of the optical pulse is $0.3 \times \Gamma$ in the experiments. This might reduce the observed time delay during experiments.

An example of the phase ϕ for $N = 12$ atoms inside the cloud of Jennewein as a function of the detuning is given in Fig. 3.10(a) (black circles), where the blue solid line is a phenomenological fit. It is observed that the phase of the total field varies close to atomic resonance. For a denser cloud of atoms, e.g. a cloud with $N = 170$, the phase has also been plotted in Fig. 3.8(a) (red dots). The small step visible for $N = 170$ is reminescent of the presence of a second resonance in the system. From $\phi(\omega)$, we can derive the group delay. In order to calculate the derivative, we made use of the phenomenological fit for $N = 170$ [see Fig. 3.10(b)]. We observe in Fig. 3.10(b) that numerically the same order of magnitude for the group delay is found as was found experimentally, yet a big difference is seen: there are two dips, as opposed to only one for the experimental results given in Fig. 3.9. This is consistent with the spectral data of Fig. 3.8(a), where a second resonance was also absent in the experiment. This shows that we systematically do not observe experimentally the presence of a second resonance, a resonance that is predicted by classical theory. Next, we define the maximum advance by the value of τ at the dip. In the case of two dips, we take the left dip, as indicated by the dashed line in Fig. 3.10(b). The calculation has been done for several numbers of atoms inside the cloud. Figure 3.10(c) shows that the largest advance ranges from a few nanoseconds to the order of ten nanoseconds, depending on the

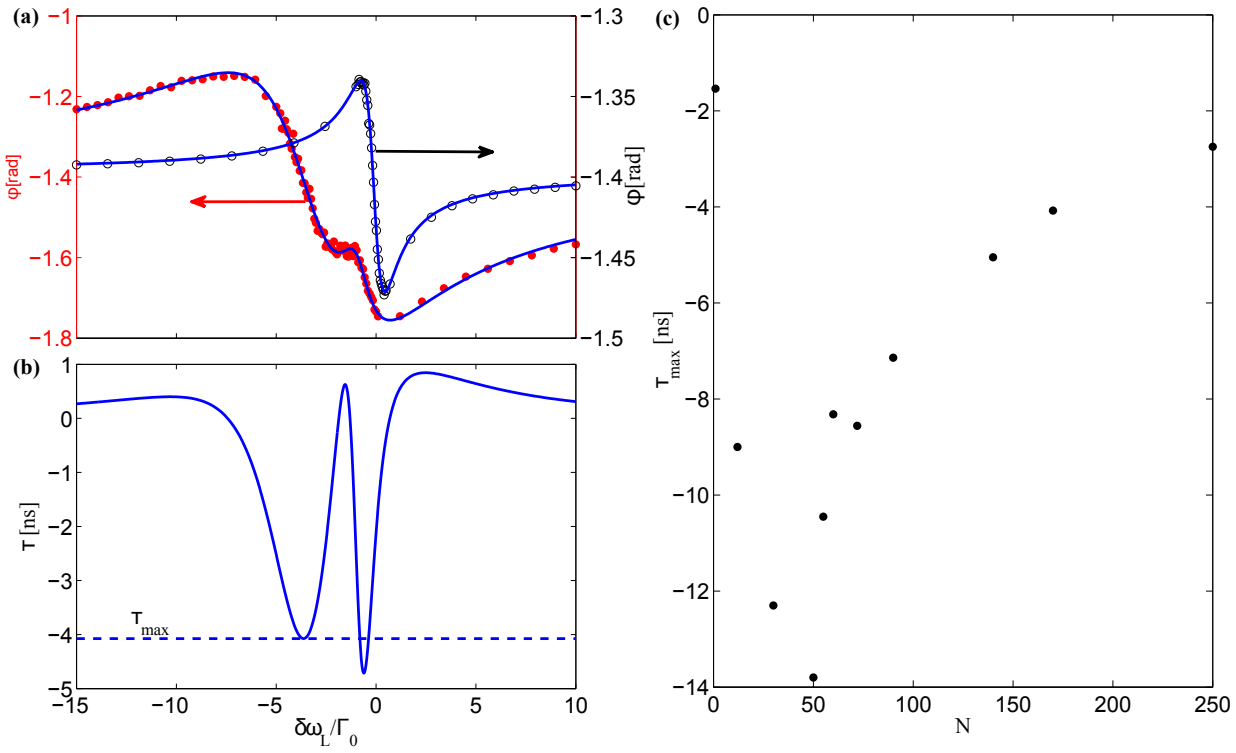

Figure 3.10: *(a) The phase of the total electric field in the far field as a function of the laser detuning for $N = 12$ atoms (black circles) and $N = 170$ atoms (red dots). To interpolate, for $N = 12$ the fit function: $y = -|c_1 - \frac{c_2}{1-2i\frac{x-c_3}{c_4}}e^{ic_5}|^2$ has been used. For $N = 170$, the fit function is: $y = -|c_1 - \frac{c_2}{1-2i\frac{x-c_3}{c_4}}e^{ic_5} - \frac{c_6}{1-2i\frac{x-c_7}{c_8}}e^{ic_9}|^2$ (both are blue solid curves). (b) The derivative $\tau = \frac{d\phi}{d\omega}$ has been calculated from the fit in Fig. 3.10(a) for $N = 170$ atoms only. The dashed line indicates what we define to be τ_{max} in Fig. 3.10(c). (c) The maximum delay has been plotted as a function of the number of atoms inside the cloud.*

number of atoms inside the cloud. It is observed that the maximum time advance reduces For $N > 50$. The reason for this is the spectral broadening of the system, which makes the slope of the $\phi(\omega)$-curve smoother. In the experiment, a reduction of the time advance when the number of atoms increases has never been observed, since one cannot load an arbitrarily large number of atoms in the cloud.

3.8 Summary

In this chapter we have described and analyzed the experiments that have been conducted by Pellegrino and Jennewein. The atomic clouds are both dense and cold, making it therefore interesting to study the influence of resonant dipole-dipole interaction on light scattering. The way the laser beam was focused on the cloud, was based on the experimental fact that the asymmetry of the spectrum flips sign when the focus crosses the center of the cloud. In this chapter we have proposed a physical explanation of this phenomenon that is based on the Gouy phase.

From theoretical considerations it was understood that Pellegrino studied incoherent light scattering. Jennewein has changed the experiment in order to also measure coherent light scattering in the forward direction. The experimentally obtained spectra from Pellegrino and Jennewein show a very small shift of the transmission dip. By solving the set of coupled-dipole equations, we also found a a very small frequency shift. However for both the spectrum and the group delay we observe in the numerical simulations the presence of a second resonance, as opposed to what has been observed experimentally. So far it remains an open question why the experimental results do not show a second resonance. From a literature study, it follows that weakly interacting atomic systems are properly described with mean-field theory. As opposed to these systems, the systems studied by Pellegrino and Jennewein, where interactions are stronger, cannot be understood from mean-field theory. No theoretical model, that we are familiar with, exists so far that is able to reproduce the experimental results.

Chapter 4

Polaritonic modes in a dense cloud of cold atoms

4.1 Motivation

In the previous chapter we studied light scattering from a cloud of cold atoms. Although the atomic cloud we study is much more dilute than the sky, we have seen that resonant light scattering from a cold wavelength-size atomic cloud is very different from Rayleigh scattering. We have discussed in the last two chapters that the reason for this lies in the presence of strong resonant dipole-dipole interactions in the system under study. We have seen that as the atomic density increases, light scattering changes from a purely diffusive to a partially diffusive and partially diffractive regime. In the latter regime, light scattering from the cloud occurs as if the cloud were an object that is described by an effective refractive index. When a finite-size object is described by an index of refraction that is different from its optical environment, the object is known to diffract light. Apart from this "macroscopic point of view" of light scattering, we can also interpret diffraction in another way: what happens at a microscopic level that makes the atomic cloud diffracting light? A similar question would be: what is the physical origin at the microscopic level of the index of refraction, which is a macroscopic notion, and makes an object diffracting light? It is in this chapter that we study the connection between a microscopic and macroscopic description of an ensemble of homogeneously broadened scatterers. However, the conclusions drawn in this chapter are expected to be correct as well for inhomogeneously broadened systems like a dense ensemble of quantum dots. Apart from Section 4.8, this chapter has been adapted from our recently published paper, called "Polaritonic modes in a dense cloud of cold atoms" [67].

4.2 Introduction

In Chapter 2 we have seen that resonant light scattering from an atomic cloud can be modeled in two ways. On one hand it can be described with a microscopic theory for which a set of coupled-dipole equations is solved, and on the other hand by means of a macroscopic theory where the atomic cloud is replaced by a homogeneous medium described by a dielectric constant, or equivalently by a refractive index. Sokolov *et al.* [68] used both ways of modeling light scattering and analyzed the response of an ensemble of cold resonant scatterers in a spherical volume and they compared a modal microscopic description with a macroscopic description based on the effective dielectric constant under the mean-field

approximation; both approaches are in good agreement for low densities. When the density increases, deviations between both approaches occur. In contexts such as random lasing, light localization, and subradiance, microscopic modes of a system of interacting atoms in the scalar approximation have been studied [8, 9, 29, 69–72]. As opposed to the previously mentioned works, we study dense ($\rho/k^3 \gtrsim 1$), disordered and homogeneously broadened systems consisting of N resonant dipoles in a small volume with dimensions comparable to the resonant wavelength. We study light scattering by this system using, on one hand, a microscopic model accounting for all interactions between atoms [see Fig. 4.1(a)] and, on the other hand, a macroscopic model based on a homogeneous system with an effective dielectric constant ε_{eff} [see Fig. 4.1(b)]. The effective dielectric constant is then derived numerically by fitting the scattered intensity averaged over an ensemble of 300 different realizations of the system. This allows us to compare both the eigenfrequencies and spatial structure of the eigenmodes of both microscopic and macroscopic systems.

As we will see, mainly superradiant modes are responsible for coherent light scattering. In this chapter, we observe that some of them have the following properties: (i) all atoms contribute to the mode, (ii) the frequency and the spatial structure of the mode are independent of the realization but depend on the geometry and density of the system so that they are very robust against disorder. Hence, despite the fact that the system is disordered, these modes are analogous to the polaritons introduced by Hopfield to analyze collective excitations in condensed matter for ordered systems [73]. We thus refer to these superradiant modes as polaritonic modes. We further observe that the spatial structure of

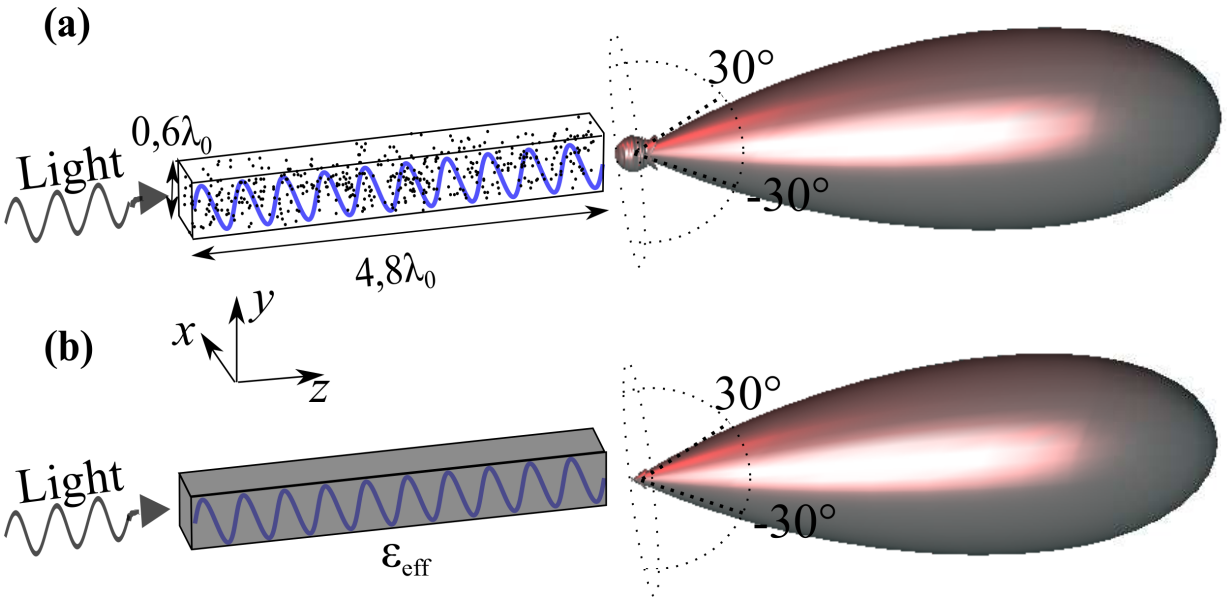

Figure 4.1: *(a) System under study: $N = 450$ atoms uniformly distributed in a rectangular box. The atomic density is $\rho/k^3 = 1$. The incoming light excites the collective eigenmodes of the system (visualized by the blue sinusoid), which gives rise to a scattering pattern in, essentially, the forward direction. Here, we have plotted the modulus square of the electric field radiated in the far field at resonance, averaged over 1 500 realizations, $\langle |\boldsymbol{E}|^2 \rangle$. (b) Homogeneous medium described by an effective dielectric constant ε_{eff} exhibiting optical resonances. The scattering pattern, $|\boldsymbol{E}|^2$, is found to be similar to (a) except for the diffuse light, which is by definition null in (b).*

these modes coincides with the spatial structure of the modes of the effective homogeneous particle with effective dielectric constant. We thus conclude that there is a one-to-one correspondence between modes of a particle with effective dielectric constant and polaritonic modes in an atomic system.

The analysis developed in this chapter is not limited to cold-atom systems but is also applicable to condensed-matter systems acting like coupled oscillators such as an ensemble of quantum dots and layers of organic molecules with electronic transitions or vibrations in a crystal. Let us give two examples where the polaritonic behavior survives the introduction of disorder and can be described in the framework of an effective dielectric constant. As a first example, we consider surface phonon polaritons (SPhPs). A phonon is a collective excitation which results from the interaction potential between neighbors. It is a normal mode of a lattice, i.e., a periodically arranged set of atoms or ions. For optical phonons, these collective mechanical excitations are coupled to the electromagnetic field, resulting in a polariton [74]. The presence of a polaritonic mode results in a dielectric constant that takes negative values within a frequency window. The concept of polaritons can be applied to many different crystals such as SiC or quartz. It is now interesting to consider amorphous glass. There, the concept of phonon disappears as there is no periodicity of the system. However, it turns out that the dielectric constant still has a negative real part so that SPhPs are still predicted by classical electrodynamics and indeed observed experimentally. Since phonons formally do not exist, this raises the question how it is possible that SPhPs still exist, despite of the randomness of the underlying microscopic structure. The concepts that are introduced in this chapter in the context of atoms that are coupled via resonant dipole-dipole interactions, allow to understand the phenomenon of SPhPs in amorphous glass as well, since the underlying mechanisms are comparable.

The second example is the optical behavior of a disordered ensemble of densely packed quantum dots or organic molecules such as J aggregates. It has been observed that layers of these resonant materials deposited on metallic films display strong coupling with surface plasmons [75–82]. The experimental results can be explained using a resonant effective dielectric constant for the ensemble of scatterers. It has further been observed that the modes are spatially coherent. The previous examples share the basic physical ingredients with our model consisting of N cold atoms in a cloud. They are dense and disordered systems of N resonant scatterers.

The chapter is organized as follows. First, using a microscopic model, we study the collective eigenmodes of the system consisting of N cold atoms in a small volume as depicted in Fig. 4.1(a). We find that some of them, called hereafter polaritonic modes, are robust against disorder, involve all atoms, and are superradiant. We then analyze light scattering by the system using this model and compare it with an effective dielectric constant as sketched in Fig. 4.1(b). We show that polaritonic modes can be identified with the macroscopic optical modes of that system. We also discuss the origin of losses in the effective dielectric constant. Finally, we will discuss the influence of polaritonic modes on light scattering.

4.3 Model

In this chapter, we consider a cloud of atoms uniformly distributed in a rectangular box [see Fig. 4.1(a)]. The main differences between this system and the atomic clouds studied in the previous chapter are the fact that the atoms are uniformly distributed instead of normally

distributed and the density is slightly higher: $\rho/k^3 = 1$. The uniform distribution has been chosen to facilitate the comparison with a macroscopic theory based on a dielectric constant. The dipoles, being cold atoms in vacuum, do not experience nonradiative losses and have a negligible Doppler shift with respect to the radiative linewidth Γ_0 of the atoms. In the numerical simulations presented below, we have taken rubidium-87 atoms, $\lambda_0 = 780\,\text{nm}$, and $\Gamma_0 = 2\pi \times (6\,\text{MHz})$. The number of atoms, $N = 450$, and the dimensions of the box, $4.8\lambda_0 \times 0.6\lambda_0 \times 0.6\lambda_0$, correspond to typical experimental conditions obtained by laser cooling and trapping techniques in wavelength-size optical dipole traps [51]. With such parameters, $\rho/k^3 \sim 1$, so recurrent scattering has to play a significant role. We also show some results for a rectangular cloud with dimensions $2.1\lambda_0 \times 0.4\lambda_0 \times 0.4\lambda_0$ and density $\rho/k^3 \sim 5$. Like in the experiment, the cloud is investigated in the weak-excitation limit, where its optical properties can be described by classical optics [29, 72].

The microscopic eigenmodes of the atomic cloud are obtained by searching for a self-consistent solution of the coupled-dipole equations (see Eq. 2.16) in the absence of a driving electric field

$$\mathbf{p}_i = \frac{\omega^2}{c^2} \sum_{j=1, j\neq i}^{N} \Big[\alpha(\omega)\bar{\bar{G}}(\mathbf{r}_i, \mathbf{r}_j; \omega)\mathbf{p}_j\Big]. \tag{4.1}$$

This set of equations can be put in the form $\bar{\bar{A}}(\omega)\mathbf{P} = \omega\mathbf{P}$, which is a nonlinear eigenvalue problem, since the ω dependence of the equations is not linear. In order to arrive at the standard form of an eigenvalue problem, we assume $\omega^2\bar{\bar{G}}(\mathbf{r}_j, \mathbf{r}_i, \omega) \approx \omega_0^2\bar{\bar{G}}(\mathbf{r}_j, \mathbf{r}_i, \omega_0)$. Because of the narrow atomic linewidth and the nonresonant character of the free-space Green tensor, this is an accurate assumption. The eigenvalue problem can then be put in the standard form of an eigenvalue problem: $\bar{\bar{A}}(\omega_0)\mathbf{P}_\beta = \omega_\beta\mathbf{P}_\beta$, where the matrix

$$\bar{\bar{A}}(\omega_0) = \begin{pmatrix} (\omega_0 - i\frac{\Gamma_0}{2})\bar{\bar{\mathbb{1}}} & \frac{-3\pi c\Gamma_0}{\omega_0}\bar{\bar{G}}_{2\to1} & \dots \\ \frac{-3\pi c\Gamma_0}{\omega_0}\bar{\bar{G}}_{1\to2} & (\omega_0 - i\frac{\Gamma_0}{2})\bar{\bar{\mathbb{1}}} & \\ \vdots & & \ddots \end{pmatrix},$$

of which all submatrices are of size 3×3. Since the matrix $\bar{\bar{A}}$ contains complex diagonal elements and $\bar{\bar{G}}^\dagger_{i\to j} \neq \bar{\bar{G}}_{j\to i}$, it is a non-Hermitian matrix. Because the system loses energy by the radiation in the far field of the dipoles, and there are resonant dipole-dipole interactions, the problem is mathematically non Hermitian. Therefore, the eigenfrequencies ω_β are complex, and we write the eigenfrequencies as

$$\omega_\beta = (\omega_0 + \Omega_\beta) - i\frac{\Gamma_\beta}{2}, \tag{4.2}$$

where Ω is the collective frequency shift and Γ_β the collective linewidth. When we substitute this expression for ω_β into the eigenvalue problem, the eigenvalue problem becomes

$$\bar{\bar{A}}(\omega_0)\mathbf{P}_\beta = (\omega_\beta - i\frac{\Gamma_\beta}{2})\mathbf{P}_\beta. \tag{4.3}$$

This eigenvalue problem has $3N$ eigenvalues as each dipole has three dipole moment components. The corresponding eigenvectors $\mathbf{P}_\beta$ are composed of the vector components of all N dipole moments, $\mathbf{P}_\beta = [p^\beta_{1x}, p^\beta_{1y}, p^\beta_{1z}, \cdots p^\beta_{Nx}, p^\beta_{Ny}, p^\beta_{Nz}]^\intercal$. They are normalized such that $|\mathbf{P}_\beta|^2 = \sum_j |\mathbf{p}^\beta_j|^2 = 1$. It is observed that the (complex) eigenfrequencies are the same

as the atomic eigenfrequencies in the absence of resonant dipole-dipole interactions, which corresponds to $\bar{\bar{A}}$ being a diagonal matrix. These resonant dipole-dipole interactions give rise to collective eigenmodes. Each eigenvalue has both a collective frequency shift and a collective linewidth that can be different than the single-atom frequency shift and linewidth. In the next section, we will analyze the spectrum of the matrix $\bar{\bar{A}}$.

4.4 Eigenspectrum analysis

Figure 4.2 shows all 405 000 eigenfrequencies in the complex plane obtained from 300 realizations of the clouds ($300 \times 3N = 300 \times 3 \times 450 = 405\,000$ eigenfrequencies). We observe three families of modes, each defined in terms of their collective linewidth and their collective frequency shift: (1) $\Gamma_\beta \in \{0, 2\Gamma_0\}$ and $|\Omega_\beta| \gg \Gamma_0$, (2) $\Gamma_\beta \gg \Gamma_0$, and (3) others. Type 1 eigenmodes have a collective linewidth of either $\Gamma \approx 2\Gamma_0$ or $\Gamma \ll \Gamma_0$ and a large frequency shift. Figure 4.3(a) shows a typical eigenmode of type 1. It contains only two excited atoms, so we call it a dimer mode. When two dipoles oscillate in phase and are very close together, the electric fields of both dipoles interfere constructively. Therefore,

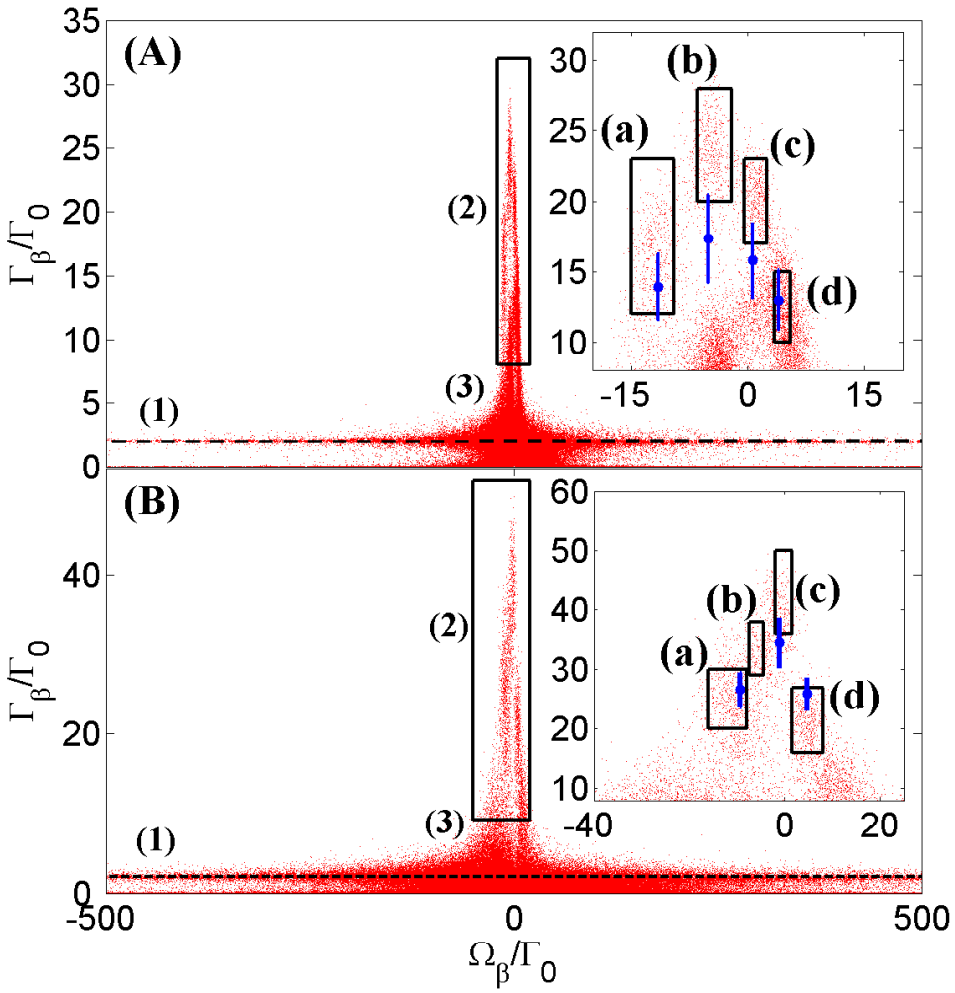

Figure 4.2: *The three types of eigenmodes are indicated by the numbers (1) through (3). The inset shows a closeup of the boxed part of the main figure, where the polaritonic modes (a), (b), (c) and (d) for both (A) $\rho/k^3 = 1$ and (B) $\rho/k^3 = 5$ are visualized in Fig. 4.7.*

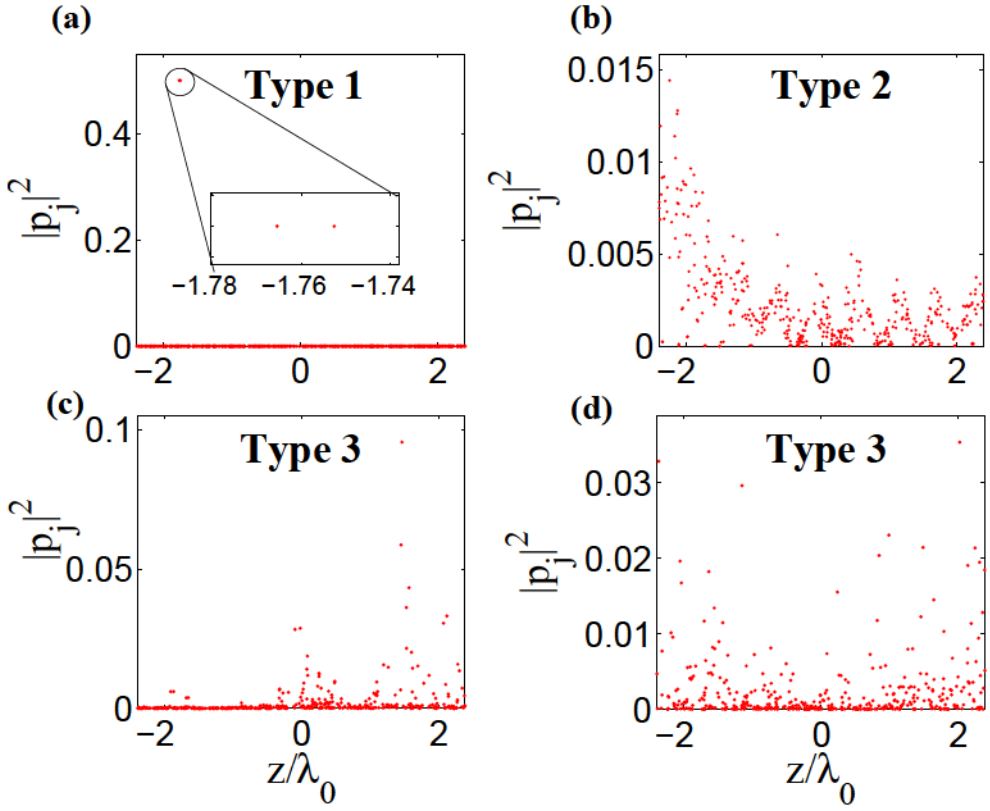

Figure 4.3: *Typical eigenmodes for the cloud with $\rho/k = 1$ are shown. (a) Type 1 eigenmodes are called dimer modes. The dipoles are very close to each other. (b) A polaritonic mode shows an oscillatory behavior. (c) Bunches of dipoles oscillate. (d) Many dipoles oscillate, but without the oscillatory behavior, so there is no periodic arrangement of the dipoles.*

the pair of dipoles radiates twice as fast ($\Gamma = 2\Gamma_0$) as they would independently. However, when the dipoles oscillate out of phase, their electric fields interfere destructively, and the pair of dipoles is strongly subradiant ($\Gamma \ll \Gamma_0$). The large level splitting is due to the large resonant dipole-dipole interaction. Within the type 2 family of modes, one can distinguish a few patches (four in these cases) of modes (see rectangles in inset in Fig. 4.2), which we denote as *polaritonic* modes for reasons explained below. More precisely, for a given realization, the spectrum of eigenfrequencies always contains the same number of polaritonic modes, with each mode falling into one of these patches[1]. For a dense atomic system, in the scalar approximation, these patches have also been obtained numerically by Goetschy *et al.* [8, 71]. Figure 4.3(b) shows a plot of the dipole moments squared $|\mathbf{p}_j|^2$ for a typical mode of type 2. For this collective mode, most of the atoms are excited and Fig. 4.3(b) suggests $|\mathbf{p}_j|^2$ oscillates spatially along the z axis. We have checked that this oscillation is an intrinsic property of the homogeneous system, i.e., that it is a property of the shape and density of the sample but not of the exact positions of the atoms. To do this, we calculate the average dipole moment squared $\langle|\mathbf{p}|^2\rangle$, where $\langle\cdots\rangle$ denotes this time averaging both inside thin slices perpendicular to the long axis of the box, and over 300 realizations of the

[1]Due to the symmetry of the average atomic sample in the (x,y)-plane, polaritonic modes are actually found in pairs with very close eigenfrequencies for each realization.

uniform atomic distribution. Only the modes inside rectangle (a) in the inset of Fig. 4.2(A) are taken into account in the average. Here, the rectangles are taken such that they contain most of the polaritonic modes of a specific kind. Figure 4.4(b) shows that the spatial oscillation observed in Fig. 4.4(a) survives the ensemble averaging. Note that for a single realization, the polaritonic mode is in general not symmetric around $z = 0$, since the atoms are not positioned symmetrically around the axis. This can be seen in Fig. 4.4(a). The symmetry of the macroscopic mode structure with respect to the plane $z = 0$ is restored by the averaging procedure. Their spatial structure is the same for all realizations: it depends on the density and shape of the cloud. These facts confirm that these few type 2 eigenmodes are polaritonic by nature. This is in contrast with the other types of modes, which do not show this spatial periodicity along the z axis nor involve all the dipoles simultaneously.

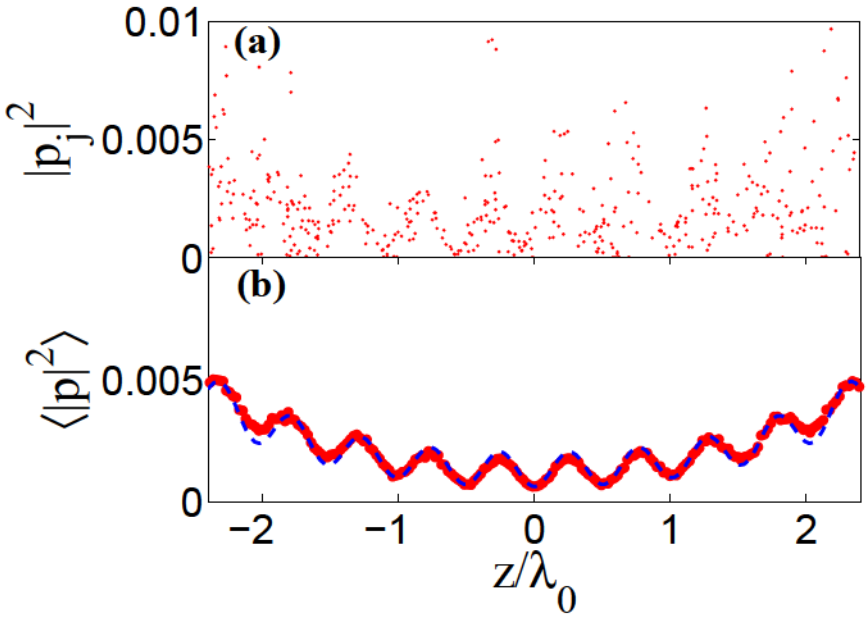

Figure 4.4: *(a) Spatial structure of a typical microscopic eigenmode of type 2 for* $\rho/k^3 = 1$. *The dipole moment squared* $|\boldsymbol{p}_j|^2$ *of each atom* j *has been plotted, with the atoms being sorted by their* z *coordinate. (b) Average dipole moments squared* $\langle|\boldsymbol{p}|^2\rangle$ *(red dots). The ensemble average is performed over the polaritonic modes inside the black solid rectangle (a) in the inset of Fig. 4.2(A). The macroscopic mode of the homogeneous cloud (blue solid line) coincides very well with the average polaritonic mode, taking into account a small offset due to the fluctuations of the dipoles amplitudes from one realization to another. Refer to the main text for a discussion about this offset.*

All modes we have not discussed so far belong to type 3. These modes involve either many dipoles distributed throughout the whole volume but without a regular spatial structure [Fig. 4.3(d)] as the one observed in Fig. 4.3(b), or a localized mode involving only a subset of dipoles [Fig. 4.3(c)]. In order to demonstrate that neither type 1 nor type 3 modes have a spatial structure, as opposed to polaritonic modes, we have calculated the average dipole moment square along the long axis of the box for these modes. It is seen in Fig. 4.5 that these modes do not possess the oscillatory structure observed for type 2 modes.

The periodic arrangement of the dipole moments, which only exists for the type 2 eigenmodes, allows phase matching of the radiation by the dipoles and therefore single-photon superradiance along the axis of the object. Note that this phase matching only

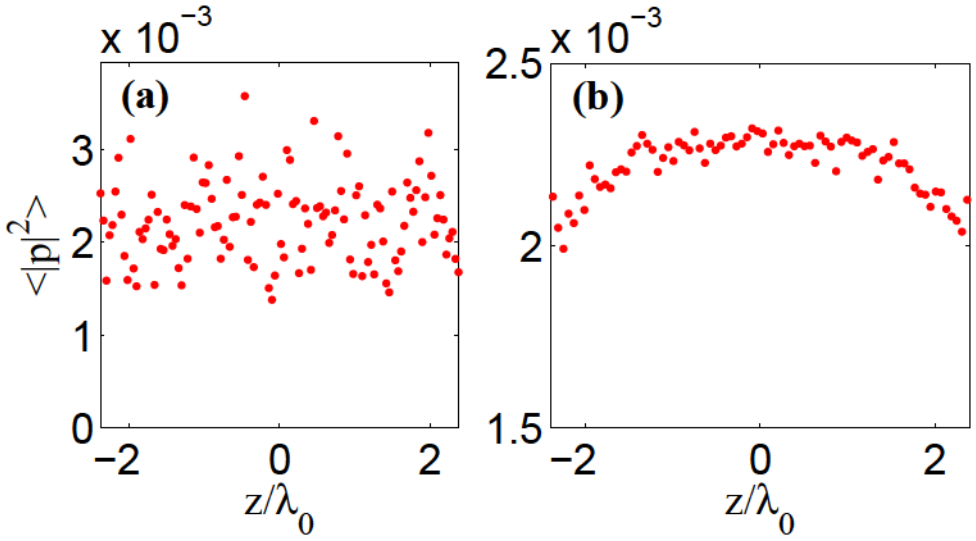

Figure 4.5: *The average dipole moment square of type 1 (a) and type 3 (b) eigenmodes along the long axis of the box do not show any spatial structure, like type 2 does. (a) All eigenmodes with $|\Omega_\beta| > 150\Gamma_0$ have been taken into account for the averaging. (b) All modes within the region defined by $|\Omega_\beta| < 19$ and $\Gamma_\beta < 3\Gamma_0$ have been taken into account for the averaging.*

occurs within a rather limited solid angle ($\Delta\Omega \sim 2\pi/15$). This is why the linewidth is not enhanced by a factor N as is the case for single-photon superradiance by N emitters in a subwavelength volume, but lowered by a factor of roughly $\Delta\Omega/(4\pi)$.

4.5 Light scattering

We now study light scattering by the cloud of atoms. Solving the coupled-dipoles equations using the laser field as an external driving source allows us to calculate the scattered field $\mathbf{E}$ in the far field for a given realization of the cloud when it is illuminated by an x-polarized plane wave, as is done in the work of Chapter 3. After averaging over 1 500 realizations, the scattering pattern obtained near resonance ($\omega = \omega_0$) exhibits one lobe in the forward direction [see Fig. 4.1(a)] and some diffuse light which is on average quasi-isotropic and has a smaller amplitude. However, we find that these two features have comparable contributions when integrated over the full solid angle with 54% and 46% of the total scattered light, respectively. The lobe in the forward direction is very similar to the diffraction pattern originating from a homogeneous particle, suggesting that one could replace the cloud, with its random graininess, by a homogeneous cloud with the same shape and extract an effective dielectric constant.

These observations can be understood with the formalism outlined in Section 2.2.3. We decompose the electric field $\mathbf{E}$ scattered by the random medium into an ensemble-averaged field $\langle\mathbf{E}\rangle$ and a fluctuating field $\delta\mathbf{E}$. It is known that $\langle\mathbf{E}\rangle$ is the field diffracted by an effective medium with effective dielectric constant ε_{eff} and with the same shape as the cloud. The scattered intensity can also be decomposed in a coherent and incoherent contribution $\langle|\mathbf{E}|^2\rangle = |\langle\mathbf{E}\rangle|^2 + \langle|\delta\mathbf{E}|^2\rangle \propto I_{\text{coh}} + I_{\text{incoh}}$. The first term corresponds to the lobe in the forward direction in Fig. 4.1(a), while the second term is the quasi-isotropic diffuse light.

4.6 Effective dielectric constant

We now proceed to the extraction of the effective dielectric constant of the cloud as a function of frequency. In textbooks such as Jackson [83], the index of refraction of dense media is well reproduced by the Lorentz-Lorenz relation between the macroscopic dielectric constant of the media and the polarizability of the scatterers:

$$\frac{\varepsilon_{\mathrm{LL}}(\omega)-1}{\varepsilon_{\mathrm{LL}}(\omega)+2}=\frac{\rho\alpha(\omega)}{3}. \tag{4.4}$$

This formula takes only partially resonant dipole-dipole interactions into account by the local-field correction [23, 24]. Recurrent scattering is not included, while its impact on the effective refractive index is expected to be of importance for the dense systems of cold atoms studied here [16, 27, 84].

In order to derive the effective dielectric constant by accounting for all multiple scattering events, we solve an inverse problem. We compare the coherent contribution $|\langle\mathbf{E}\rangle|^2$ of the far-field scattering pattern of the atomic cloud with that of an effective homogeneous particle with a dielectric constant $\varepsilon_{\mathrm{eff}}$ and the same geometry as the cloud. The latter is numerically calculated with an aperiodic Fourier modal method (a-FMM) [85] mainly developed by Philippe Lalanne and Jean-Paul Hugonin, using $\varepsilon_{\mathrm{eff}}$ as a fitting parameter. The use of a Fourier modal method for light scattering of a rectangular box seems contradictory. The main idea of using an aperiodic Fourier modal method is that the structure, in this case a rectangular box, is periodized in the two transverse directions x and y. By doing so, one can use the rigorous coupled wave analysis (RCWA). Each cell needs to be optically isolated. This can be done by for example putting perfectly matched layers (PML) at the borders of the cell, or by using complex coordinate transformations at the borders of each cell [86]. It is the latter that is used in this work. We find that the far-field scattering pattern computed using either the effective homogeneous particle or the ensemble average microscopic cloud agree within $\sim 1\%$ for each angle [compare Figs. 4.1(a) and (b)], showing that the effective dielectric constant approach is valid. We conclude that this macroscopic approach captures both the recurrent scattering and the collective effects of the microscopic picture. By repeating this procedure for different frequency detunings $\delta\omega=\omega-\omega_0$, we obtain the spectrum of the effective dielectric constant (see Fig. 4.6). The numerically retrieved values of the dielectric constant have been fitted with the function

$$\varepsilon(\omega)=1+\frac{c_1}{c_2-\omega-ic_3}, \tag{4.5}$$

where all coefficients are taken real. Hence, both the real and imaginary part of the dielectric constant were fitted simultaneously. It is noteworthy that at resonance the gas is described by a dielectric constant with a negative real part and thus optically behaves as a metal. The numerically retrieved dielectric constant is found to be significantly different from the prediction by Eq. (4.4). Our results evidence that the Lorentz-Lorenz formula is not valid for a dense cloud of resonant scatterers; the discrepancy between the simulation and the Lorentz-Lorenz theory increases with the density, reflecting that the resonant dipole-dipole interactions become stronger [27, 87]. As we described in Chapter 3, this result has recently been studied experimentally by Jennewein *et al.* by using a cloud of cold atoms with similar shape and density [7]. They have shown that for light scattering from a dense cloud of cold atoms mean-field theory becomes invalid, as expected. Although it was expected, since

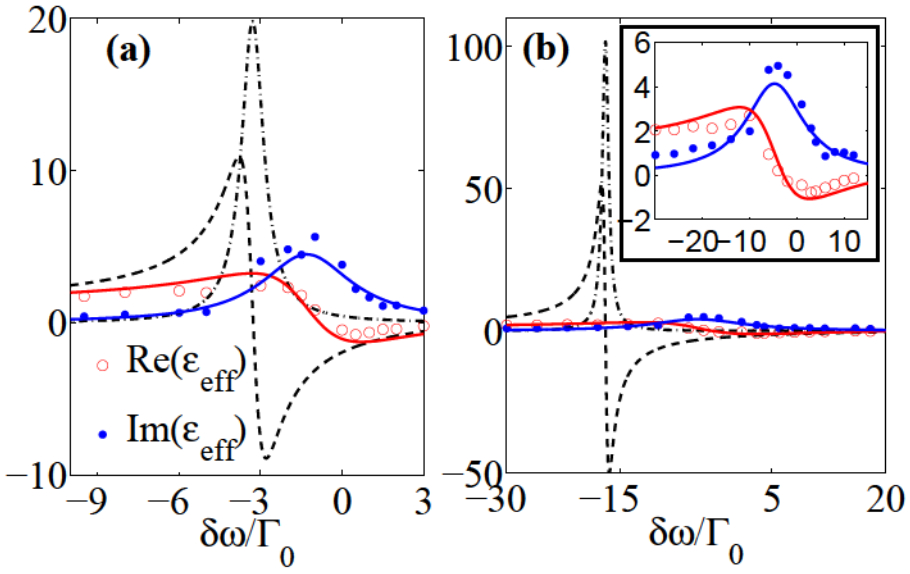

Figure 4.6: *Effective dielectric constant $\varepsilon_{eff}(\omega)$ for (a) $\rho/k^3 = 1$, and (b) $\rho/k^3 = 5$. The real and imaginary parts of the effective dielectric constant (circles and dots) largely differ from the predictions of Lorentz-Lorenz theory (dashed curves). Solid lines: Lorentzian fit of the numerical data.*

resonant dipole-dipole interactions are strong near resonance, we want to highlight that our atomic system is five orders of magnitude more dilute than a gas at ambiant conditions, for which the Lorentz-Lorenz theory is an accurate description.

4.6.1 Anderson localization

In this section we will briefly discuss about Anderson localization of light in 3D. So far, no one has ever observed Anderson localization of light in 3D. It is claimed that, under the application of an external magnetic field, cold atoms are a possible candidate for the observation [88].

A criterion of the observation of Anderson localization is that the mean free path should be smaller than the wavelength: $l_{\mathbf{mfp}} < 1/k$, which is also called the Ioffe-Regel criterion for wave localization [18]. From the dielectric constant that we have just derived, we can obtain the imaginary part of the refractive index $n_{\text{eff}} = \varepsilon_{\text{eff}}^{1/2}$ and thus find the mean free path: $l_{\text{mfp}} = 1/[2k\text{Im}(n_{\text{eff}})]$. At atomic resonance, we find $l_{\text{mfp}} = 1/(3k)$. This indicates that the Ioffe-Regel criterion for wave localization ($kl_{\text{mfp}} < 1$) is satisfied [18]. Yet, we have found many modes extended throughout the whole system, indicating that the localization length, if any, is larger than the size of the system. We believe therefore that the small atomic clouds we study here, in the absence of an external magnetic field, are no candidates for the observation of Anderson localization, despite of the fact that the Ioffe-Regel criterion is satisfied.

The belief that the small atomic clouds we study here are no condidates for the observation of Anderson localization is supported by another criterion of Anderson localization, which is called the Thouless criterion. According to this criterion, all modes need to be spectrally separated and therefore not overlap [89, 90]. Let us consider the polaritonic modes in particular. From the insets of Fig. 4.2(A) we can observe that the collective linewidth Γ_β of

a polaritonic mode is on the order of $20\Gamma_0$, whereas the typical spacing between polaritonic modes is on the order of $5\Gamma_0$. The Thouless criterion is thus not satisfied and Anderson localization is not expected to be observed. This observation is consistent with a recent theoretical work in which the absence of Anderson localization for a random ensemble of classical dipoles is predicted [91].

4.7 Connection between polaritonic modes and macroscopic modes

We have seen that the far-field scattering pattern of the atomic cloud is very similar to that of an effective homogeneous particle with an effective dielectric constant. We now make explicit the relation between the (macroscopic) modes of the homogeneous particle and the (microscopic) polaritonic modes. To do that, we use the fitted effective dielectric constant $\varepsilon_{\text{eff}}(\omega)$ (see solid lines in Fig. 4.6) and calculate the macroscopic modes of the homogeneous particle, which are poles of the scattering matrix, by iteratively solving Maxwell's equations in the complex frequency plane [92]. Remarkably, we find that the complex eigenfrequencies of the macroscopic modes coincide, within error bars, with the complex eigenfrequences of the above-mentioned polaritonic modes (see Fig. 4.2). The reason that error bars are given in this theoretical calculation is the fact that the the coefficients of the Lorentzian fit of the dielectric constant have uncertainties. The coefficient c_1 of the fit function given by Eq. 4.5 has been varied within the 95% confidence bounds. As the imaginary part of some resonance frequencies of macroscopic modes falls outside the domain defined by the black boxes, we have indicated by the errorbars in Fig. 4.2 how much the imaginary part of the resonance frequencies changes while varying c_1.

Despite the fact that the geometrical length of the cloud is fixed and the frequency of the laser is almost fixed (close to ω_0), it is possible to find several longitudinal modes because of the strong dispersion of the medium close to resonance. This provides a physical explanation of the results reported by Li *et al.* [72], in which they studied the spontaneous emission spectrum of both Dicke ($|D\rangle$) and timed-Dicke ($|T_{\mathbf{k},I}\rangle$) states from a spherical cloud of uniformly distributed two-level systems. These two states are defined as

$$|D\rangle = \frac{1}{\sqrt{N}} \sum_j |e_j, 0\rangle, \tag{4.6}$$

and

$$|T_{\mathbf{k},I}\rangle = \frac{1}{\sqrt{N}} \sum_j e^{i\mathbf{k}_I \cdot \mathbf{r}_j} |e_j, 0\rangle, \tag{4.7}$$

where $\mathbf{k}_I$ is the wave vector of the single-photon field which prepared the state, $|e_j, 0\rangle$ is a combined state of N atoms, where only atom j is excited and all the others are in their ground state, and zero photons are present. They observed numerically that the spontaneous emission spectrum of these states were strongly dependent on both geometry and density. Notably, they observed that the sign of the cooperative Lamb shift can be reversed by suitably modifying the ensemble properties. Both the Dicke and timed-Dicke states are not eigenmodes of the set of coupled-dipole equations and therefore they can be written as a linear superposition of eigenmodes of the system. Hence, they partially overlap with polaritonic modes of the system. The frequency position of these polaritonic modes depends indeed strongly on both the density and the geometry.

Figure 4.4(b) shows that the frequency coincidence between the macroscopic and microscopic modes is not accidental: the microscopic and macroscopic modes have not only the same frequency and linewidth, but also the same spatial structure along the z axis. Before we continue with the analysis of the other macroscopic modes, we make a remark about how $|\mathbf{E}|^2$ for the macroscopic mode is superposed on $\langle|\mathbf{p}|^2\rangle$. Let us note that the dipole moment square for a single realization [see Fig. 4.4(a)] corresponds to a single eigenmode. The procedure of obtaining these eigenmodes has been explained in Section 4.3. From the derivation, it follows that these modes are calculated in the *absence* of an external driving field, so the dipole moments are known apart from a multiplication factor. This multiplication factor is obtained by normalizing the modes, which has been done as explained in the main text by imposing $\sum_j |\mathbf{p}_j^\beta|^2 = 1$. Obviously, the normalization issue also arises for the electric field of the macroscopic modes. The latter has been normalized such that the intensity profile coincides well with the average dipole moment square. This way of comparing macroscopic and microscopic modes is consistent with the fact that $\mathbf{p} \propto \mathbf{E}$, which is the underlying assumption of the model as we study the low-excitation limit. Lastly, we note that $\langle|\mathbf{p}|^2\rangle = |\langle\mathbf{p}\rangle|^2 + \langle|\delta\mathbf{p}|^2\rangle$. As a consequence, $\langle|\mathbf{p}|^2\rangle$ exhibits an offset, which is due to dipole moment fluctuations. This explains the fact that a significant offset as for $\langle|\mathbf{p}|^2\rangle$ is not present for $|\mathbf{E}|^2$ of the macroscopic mode. In order to superimpose them, we have added a constant offset to the macroscopic $|\mathbf{E}|^2$.

Now, we come back to the analysis of the other macroscopic modes. We note that the spatial agreement as seen in Fig. 4.4(b) is not unique. Figure 4.7 shows the spatial agreement for all polaritonic modes for both $\rho/k^3 = 1$ and $\rho/k^3 = 5$, except for the mode (b) of $\rho/k^3 = 5$, since we could not find this macroscopic mode numerically. That does not mean this mode does not exist. A possible reason that we could not find the mode is that the fit of $\varepsilon_{\text{eff}}(\omega)$ in that frequency region is actually not very good, and mode (b) lies very close to (a) and (c). The coincidence of most polaritonic modes illustrates that the coincidence is not restricted to a particular value of the interaction strength parameter ρ/k^3. The same agreement holds for the transverse dimensions of the box. Figure 4.8 shows an example of this agreement. Since we have found both a frequence and mode profile coincidence between the macroscopic and microscopic modes, our analysis esthablished the connection between the microscopic and macroscopic approaches of light scattering.

Let us remark that the modes inside the homogeneous rectangular box are Fabry-Perot resonances. For atoms distributed inside a spherical volume, the modes would be Mie resonances [9], and in the case of a trapped atomic cloud with normally distributed atoms, polaritonic modes also exist, but they are localized in the high density region, like for guided modes in a graded-index fiber.

4.8 Light scattering from polaritonic modes

In this section, we discuss light scattering from the cloud of particles. As observed experimentally, and extensively discussed in Chapter 3, when the density increases, the contribution of coherent light scattering increases. Given the identification of the coherent macroscopic modes with the polaritonic modes, this suggests that polaritonic modes are mostly responsible for the scattering of the cloud. This is expected as they are superradiant. In this section, we study directly their contribution to scattering. More generally, we need to calculate the scattered electric field from a subset of eigenmodes. According to Eq. 2.16,

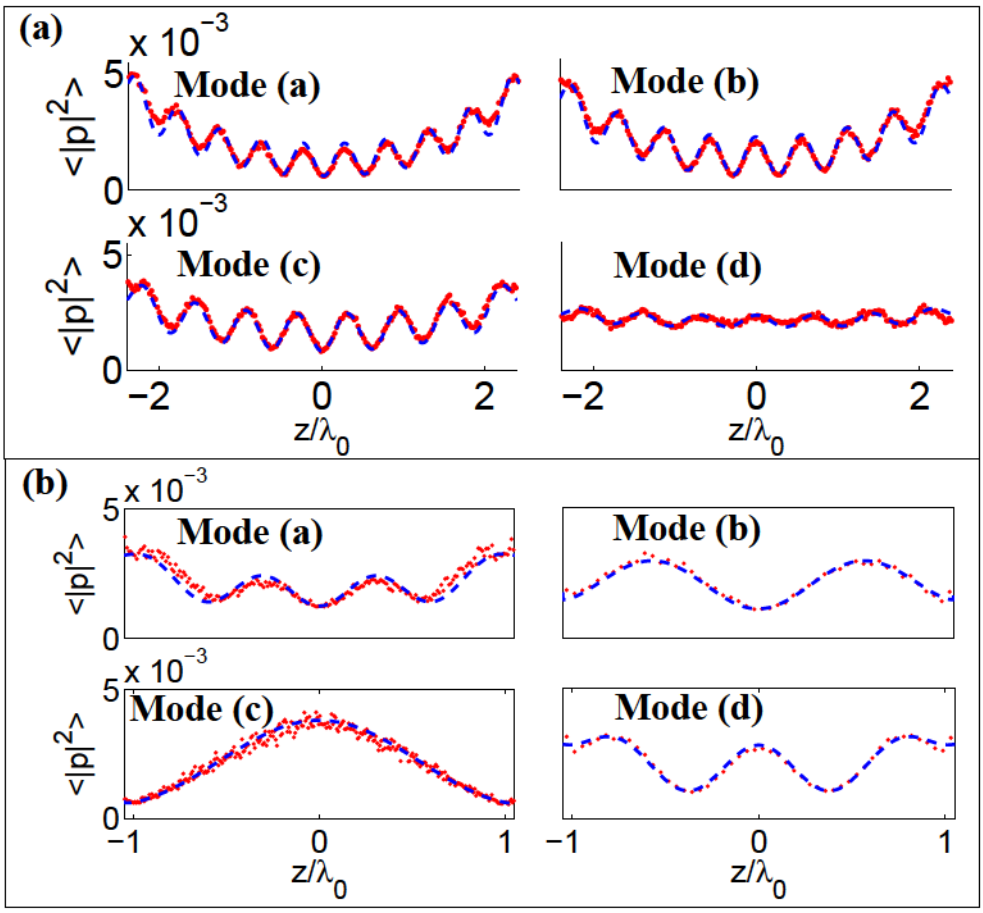

Figure 4.7: *The average dipole moment squared of polaritonic modes (red dots) is plotted along the long axis of the rectangular box. Superimposed (blue dashed curve) is* $|\boldsymbol{E}|^2$ *of the macroscopic mode of the homogeneous object. Each panel belongs to a different polaritonic mode. Refer to Fig. 4.2 for the eigenfrequencies of the modes. For the averaging procedure, we divided the system along its long axis in thin slices. The dipole moment squared is averaged per slice and then averaged over 300 realizations. (a)* $\rho/k^3 = 1$ *and (b)* $\rho/k^3 = 5$.

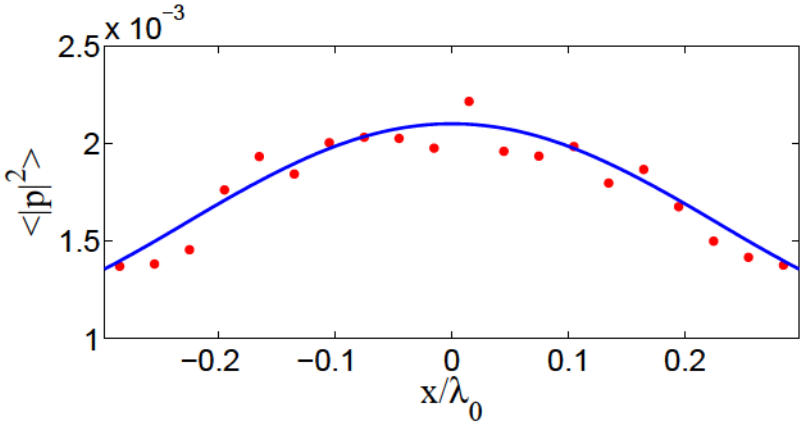

Figure 4.8: *Transverse profile of the polaritonic mode (a) of Fig. 4.2(A) (red dots) and of the macroscopic mode (blue solid curves). The profile has been obtained by averaging the dipole moments squared inside a thin slice at* $z \simeq -1.3\lambda_0$ *and along the* y *axis.*

the set of coupled-dipole equations are given by

$$\mathbf{p}_j(\mathbf{r}_j) \;=\; \varepsilon_0\alpha(\omega)\Big[\sum_{j'\neq j}\mu_0\omega^2\bar{\bar{G}}(\mathbf{r}_j,\mathbf{r}_{j'};\omega)\mathbf{p}_{j'}+\mathbf{E}_{\rm inc}(\mathbf{r}_j)\Big]. \tag{4.8}$$

The dipole moments can be calculated by solving this set of equations. The obtained dipole moments are then written in terms of the eigenvectors $\mathbf{P}_\beta$, which are defined in Eq. 4.3:

$$\begin{pmatrix} p_{1,x}\\ p_{1,y}\\ p_{1,z}\\ \vdots\\ p_{N,x}\\ p_{N,y}\\ p_{N,z}\end{pmatrix} = \sum_\beta c_\beta \mathbf{P}_\beta. \tag{4.9}$$

By inverting this linear system of equations, one can deduce the coefficients c_β. In order to calculate the scattering pattern which originates from a subset of eigenmodes, it is sufficient to calculate all the dipole moments $\tilde{\mathbf{p}}_i$ due to the excitation of the wanted polaritonic modes S, $S\in\beta$:

$$\begin{pmatrix} \tilde{p}_{1,x}\\ \tilde{p}_{1,y}\\ \tilde{p}_{1,z}\\ \vdots\\ \tilde{p}_{N,x}\\ \tilde{p}_{N,y}\\ \tilde{p}_{N,z}\end{pmatrix} = \sum_S c_S \mathbf{P}_S. \tag{4.10}$$

The scattered electric field due to these dipoles can be calculated

$$\mathbf{E}_{{\rm sc},S}(\mathbf{r}) = \mu_0\omega^2\sum_j \bar{\bar{G}}(\mathbf{r},\mathbf{r}_j;\omega)\tilde{\mathbf{p}}_j. \tag{4.11}$$

Although the different eigenmodes $\mathbf{P}_\beta$ are not orthogonal, since the matrix $\bar{\bar{A}}$ which defines them is non-Hermitian, the scattered electric field due to a single eigenmode or a subset of eigenmodes can always be calculated. It is understood that the total scattered electric field is a sum of both the fields calculated from the subset $S\in\beta$ and the remainder of states: $\mathbf{E}_{\rm sc}=\mathbf{E}_{{\rm sc},S}+\mathbf{E}_{{\rm sc,\ not\ }S}$. When we calculate the scattering pattern that is due to the modes S only, it is understood that the interferences between $\mathbf{E}_{{\rm sc},S}$ and $\mathbf{E}_{{\rm sc,\ not\ }S}$ are not included. We now apply this formalism to light scattering from the atomic cloud defined in Fig. 4.1(a). We have calculated light scattering from the eigenmodes inside the rectangles defined in Fig. 4.2(A); the polaritonic modes. The result is presented in Fig. 4.9 by the blue curve, together with the coherent scattering pattern of all the modes together. It is seen that light scattering from the modes within the rectangles, the number of modes within the rectangles is only 0.54% of all the modes, reproduces an important part of the total scattering pattern. However, it is also seen that in the backwards direction, the polaritonic modes give rise to a too large intensity. The fact that the backward scattering is so dominant can be explained by symmetry arguments. Polaritonic modes are modes of the average system and radiate

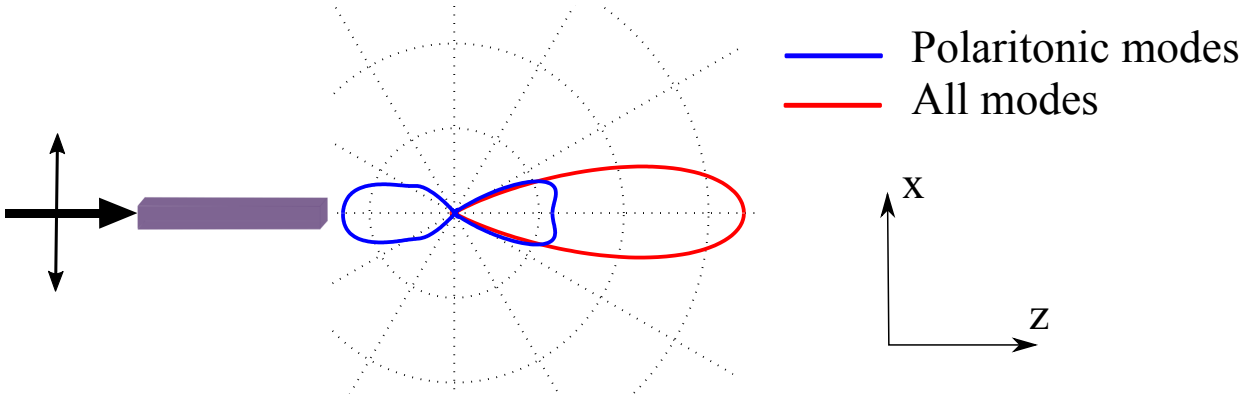

Figure 4.9: *Scattering pattern of an x-polarized plane wave incident on the atomic cloud (schematically indicated by the purple box) with density $\rho/k^3 = 1$ and with $\omega = \omega_0$. The arrow indicates the incident wavevector, and the double-arrow its polarization. The red curve corresponds to the coherent scattered intensity from all modes. The blue curve comes from coherent light scattering from the polaritonic modes as defined by the rectangles in Fig. 4.2(A). Only 0.54% of all collective eigenmodes are within the black rectangles. A significant part of the scattering pattern can be attributed to only a very few modes, which are called polaritonic modes.*

thereby symmetrically. All modes are needed to recover the precise scattering pattern. Notably, nonpolaritonic modes are needed to interfere destructively with the backwards scattered fields of the polaritonic modes. The fact that such a small amount of modes is able to reproduce a significant part of the scattering pattern is remarkable. However, we know from classical electrodynamics that light scattering at a frequency close to a resonance is dominated by the resonances of the system. This notion seems to be confirmed by the fact that light scattering is dominated by only a few modes: the polaritonic modes.

4.9 Absorption

In the macroscopic model, the appearance of an imaginary part of the effective dielectric constant (see Fig. 4.6) accounts for losses. In our situation of elastic light scattering, absorption corresponds to energy transfer from the coherent field to the incoherent field. Here, we demonstrate that the total absorption in the system is equal to the total amount of incoherent light scattering. First, we discuss the microscopic system. From an energy balance, we know that for a system without absorption $P^{\text{micro}}_{\text{s,coh}} + P^{\text{micro}}_{\text{s,incoh}} - P^{\text{micro}}_{\text{ext}} = 0$, where $P^{\text{micro}}_{\text{s,coh}}$ is the coherent scattered power and $P^{\text{micro}}_{\text{s,incoh}}$ the incoherent scattered power [15]. In the macroscopic system, there is both absorption and light scattering: $P^{\text{macro}}_{\text{ext}} = P^{\text{macro}}_{\text{s}} + P^{\text{macro}}_{\text{abs}}$. As the ensemble-averaged electric field follows the Helmholtz equation with an effective dielectric constant, $P^{\text{micro}}_{\text{s,coh}} = P^{\text{macro}}_{\text{s}}$. Because of the equivalence between the microscopic and macroscopic systems, their extinction is the same. From this simple reasoning, it follows that

$$P^{\text{micro}}_{\text{s,incoh}} = P^{\text{macro}}_{\text{abs}}. \tag{4.12}$$

While losses are generally considered as being irreversible as a result of dephasing processes, e.g., coupling to phonons, we note that this cannot be the case here, as there is no loss mechanism in the microscopic model. Before averaging, the field scattered by a single

realization of the cloud can be time reversed, provided that the scatterers' positions have not changed. After averaging, only the coherent field has a well-defined phase and can be time reversed. In summary, in the presence of dephasing processes, or when the positions of the atoms are changed randomly from one realization to another (as is the case when we ensemble average), the coupling of the incident light to dipole fluctuations leads to an irreversible radiation of incoherent light.

We are now able to explicitly address the question at the beginning of this chapter: what is the physical origin at the microsopic level of the index of refraction? Since the index of refraction includes both the diffractive properties of an object and the absorption of light, it is understood that the polaritonic modes give an important contribution to it, but not the unique contribution. The subradiant modes that give rise to incoherent light scattering, which corresponds to absorption in the homogeneous medium, due to the random orientation of the dipole moments have also an important contribution to the index of refraction. This means that all modes are important, but the polaritonic modes dominate the diffractive properties of the homogeneous object.

4.10 Conclusion

In conclusion, in this chapter we have shown the existence of polaritonic modes in a dense atomic system. These polaritonic modes do not depend on the atomic positions but only on the shape, and size of the cloud, and on the atomic density; they are spatially delocalized and strongly superradiant. We have shown that they can be identified to the macroscopic modes of a homogeneous object with an effective dielectric constant. These results apply not only to cold atomic clouds but also to any dense system of resonant scatterers such as molecules or quantum dots. This chapter thus provides a unified vision of scattering by dense systems of resonant scatterers.

Chapter 5

Revisiting homogenization for interacting resonant scatterers

5.1 Motivation

When light impinges on a liquid or a solid, it gets refracted: the optical response is uniquely given by the index of refraction. This is as opposed to light scattering from a gas, for which incoherent light scattering due to density fluctuations dominates. One way to homogenize the system is to increase the density: moving from a water vapor, for which incoherent light scattering dominates, towards liquid water, where coherent light scattering dominates.

In Chapter 3 we studied the experimental results obtained by Pellegrino and Jennewein. They studied near-resonance light scattering from a dense cloud of resonant, cold atoms. Pellegrino measured incoherent light scattering. As the number of atoms augmented, the amount of incoherent light scattering increased untill it saturated. For a similar atomic density, Jennewein has also observed saturation of coherent light scattering. It seems that even though the cloud becomes denser, incoherent light scattering keeps being a significant part of light scattering. This is as opposed to what we know from light scattering by liquids and solids, where despite the fact they are denser than a cloud of cold atoms, there is no incoherent light scattering. This raises the question if resonant atomic systems, such as those studied in the group of Browaeys, can actually reach the "homogenization regime", a regime in which the optical response is uniquely determined by an effective refractive index and thus not by fluctuations. We will see that resonant light scattering from a cloud of cold atoms is more subtle than light scattering from liquids and solids. We will show that incoherent light scattering cannot be eliminated close to atomic resonance.

5.2 Introduction

In this section, we describe what homogenization amounts to. After giving some examples of homogenization problems for non-resonant light scattering, we will pose the problem of homogenization for near-resonance light scattering.

5.2.1 What is homogenization?

Let us consider a system that is composed of small constituents, for example a cloud of atoms, a cloud containing microdroplets, or a solid that has a crystalline structure with an atomic lattice. One way of calculating the response of a compound system to an external

excitation is by rigorously calculating the response by means of a microscopic theory that takes each constituent into account. Another way of calculating the response of a compound system is by approximating the system as a homogeneous medium, and by studying the response of the system for an external excitation. The former approach is often used for light scattering from the sky, whereas the latter approach is very common for light scattering by a liquid.

Let us consider some examples of the latter approach where the compound system is described as a homogeneous medium. The relation between excitation and response is in many situations given by a linear response function. Some examples of linear response functions are the electric susceptibility χ_{e}, the electrical conductivity σ, the thermal conductivity k, and Young's modulus E. Within the framework of linear response theory, the following linear relations are some examples of the relation between an excitation (right-hand side) and the response (left-hand side):

$$\mathbf{J}_p = \varepsilon_0 \chi_e \mathbf{E}, \tag{5.1}$$

$$\mathbf{J}_q = \sigma \mathbf{E}, \tag{5.2}$$

$$\mathbf{J}_\phi = -k \nabla T, \tag{5.3}$$

$$\frac{\Delta L}{L_0} = E \sigma_{\mathrm{strain}}, \tag{5.4}$$

where $\mathbf{J}_p$ is the polarization current density, $\chi_e = \varepsilon - 1$, with ε being the dielectric constant, $\mathbf{J}_q$ being the free-charge current density, $\mathbf{J}_\phi$ being the heat flux, T being the temperature, and L_0 being the original length of an object that varies by an amount ΔL under the application of an extensional strain σ_{strain}. Typically, these *macroscopic* linear response functions can be obtained by an effective medium theory. In the case of electromagnetism, there are several models which relate microscopic properties like the atomic polarizability [17] or the dielectric constants of spherical particles in a composite dielectric random medium [93–95] to the macroscopic dielectric constant.

When we stick to the example of light scattering from a system containing dielectric particles dispersed in a host medium, we realize that there are two different points of view to assess if a medium can be homogenized:

1. One may be interested in the propagation of the ensemble-averaged field in the homogeneous effective medium. Here, the question is whether the effective refractive index describes *accurately* the behavior of the medium,

2. The second possible point of view is to require that there is *no incoherent light scattering*. This is a more strict formulation of homogenization than the first formulation, since the first formulation allows to have incoherent light, although its field needs to be small compared to the coherent field.

The first point of view is generally used in many research fields. For example, when an electrical current flows through an electrical conductor and one measures the total current, the experimental results can be fitted by Ohm's law (Eq. 5.2). One does not have separately access to a fluctuating current due to possible inhomogeneities of the medium. However in optics, incoherent scattered light is an obvious manifestation of the fluctuations of the medium. The ability of separately measuring the average response of a system and its

fluctuating response is a particular property of optics [7, 51]. Since we have separately access to both coherent and incoherent light, we will adopt the more stringent formulation of homogenization: there should be no incoherent light. In other words, we adopt a definition which requires that not only the effective dielectric constant exists, but its imaginary part associated to scattering losses has to be negligible.

5.2.2 Homogenization in optics

For the case of diffraction from periodic media, the second formulation of homogenization ($P_{\text{incoh}} = 0$) can be used. The zeroth-order diffracted mode continues propagating in the same direction as the incident field, whereas higher order diffracted modes get diffracted under an angle. When the period Λ of the periodic medium is smaller than λ, where λ is the wavelength, only the zeroth-order diffracted mode is propagative; all higher-order modes are evanescent and therefore do not reach the far field. It is only under the condition $\Lambda < \lambda$ that the optical response of the periodic medium can be described by an effective refractive index, since no propagating modes exist with angles different than the angle of incidence. In this simple case, the homogenization validity condition is thus given by the requirement that the wavelength should be larger than a length scale given by the period [96]. It is often assumed that this condition can be extended to random media [18]. If we consider for example incident light on a random dilute medium like a gas, there are density fluctuations on the wavelength scale which give rise to incoherent light scattering. When the system typical length scale l is chosen as the mean inter-particle distance $\langle r \rangle = \rho^{-\frac{1}{3}}$, where ρ is the number density, and $\langle r \rangle \ll \lambda$, the medium is expected to be self averaged and incoherent scattering is expected to be negligible [18]. This is certainly the case for dense media. As an example, consider light incident on pure water or amorphous silica. These media only refract, reflect and/or diffract light; they do not diffuse light. However, many observations for *near-resonance* light scattering from optically thick clouds of cold atoms [40, 42, 46, 51] do show that incoherent light scattering continues being significant, even though the atomic density of the clouds increases. This result is surprising because the effective dielectric constant can be as large as 5, as we have seen in Fig. 4.6, so that the medium optically behaves as a dense medium, but nevertheless exhibits a lot of incoherent light scattering [51]. It is because of this experimental result that we want to revisit the concept of homogenization in light scattering from dense, resonant and cold atomic systems, since the condition $\langle r \rangle \ll \lambda$ seems to be insufficient for this kind of systems. Although homogenization in light scattering is textbook material, there are few reports regarding the particular case of resonant light scattering from dense and cold atomic gases.

5.2.3 Contents

This chapter is organized as follows. First, we describe the system that has been modeled and we formally introduce the quantities of interest. We then summarize the known mechanisms of scattering suppression for non-resonant light scattering. This summary will enable us to pinpoint the differences with resonant light scattering by dense atomic systems which is treated thereafter. After the summary on non-resonant light scattering, we will consider resonant light scattering for which we study the relative importance of coherent and incoherent light scattering. Finally, we study a particular class of small systems composed of

many atoms, which, surprisingly, scatter less light than a single atom and which can never be homogenized, although it satisfies the condition $\langle r \rangle \ll \lambda$.

5.3 System description

We study light scattering from a disordered wavelength-size cloud of cold atoms, as illustrated in Fig. 5.1. As in Chapter 4, we take a cuboid-shape cloud with dimensions $4.8\lambda_0 \times 0.6\lambda_0 \times 0.6\lambda_0$, where $\lambda_0 = 780$ nm is the resonance wavelength of the studied transition of rubidium-87 atoms. The atoms are uniformly distributed and are modeled as classical dipoles. Classical dipoles are modeled by an isotropic electric polarizability matrix $\bar{\bar{\alpha}}(\omega) = \alpha(\omega)\bar{\bar{\mathbb{1}}}$, where

$$\alpha(\omega) = \frac{3\pi\Gamma_r/k^3}{\omega_0 - \omega - i\frac{\Gamma_r+\Gamma_{nr}+\Gamma^*}{2}}, \tag{5.5}$$

with $\omega_0 = 2\pi c/\lambda_0$ the transition frequency, c the speed of light in vacuum, Γ_r, Γ_{nr} and Γ^* respectively the radiative, nonradiative and dephasing rate. When $\Gamma_{nr} = \Gamma^* = 0$, this polarizability model corresponds to a classical $J = 0 \to J = 1$ atom, as used in the previous chapter. This model can also include nonradiative decay channels (Γ_{nr}) and dephasing processes (Γ^*). Unless stated differently, we assume elastic scattering and no dephasing processes to occur, i.e., $\Gamma_{nr} = \Gamma^* = 0$, which is a good model for a cold gas of identical classical dipoles, where no collisions take place. We take $\Gamma_r = \Gamma_0 = 2\pi \times 6$ MHz. As we discuss dense atomic systems, i.e. $k\langle r \rangle \lesssim 1$, the full Green's tensor is used to describe resonant dipole-dipole interactions, including the terms proportional to $1/(kr)^2$ and $1/(kr)^3$ which cannot be neglected in this dense regime [12, 29, 97]. The scattered electric field $\mathbf{E}_{sc}$ can be calculated from the set of coupled-dipole equations (see Eq. 2.15 and Eq. 2.16). The far-field scattering pattern is proportional to $|\mathbf{E}_{sc}|^2$. After several realizations, the ensemble-averaged scattering pattern is obtained and decomposed in a coherent and incoherent part respectively: $\langle |\mathbf{E}_{sc}|^2 \rangle = |\langle \mathbf{E}_{sc} \rangle|^2 + \langle |\delta\mathbf{E}_{sc}|^2 \rangle$. The coherent scattering pattern corresponds to the diffraction pattern of a homogeneous object described by a dielectric constant and the incoherent scattering pattern is quasi isotropic. Figure 5.1 shows the scattering pattern for a *single realization*. It is seen that there is one big lobe in the forward direction and in

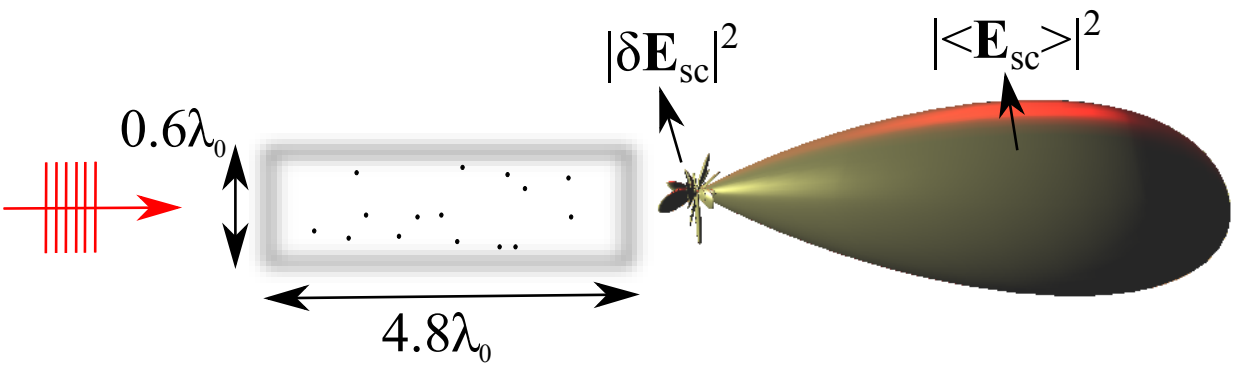

Figure 5.1: *Angular scattering pattern for a single realization of a cloud illuminated by a plane wave. The volume has dimensions* $4.8\lambda_0 \times 0.6\lambda_0 \times 0.6\lambda_0$. *Several peaks are visible. A big lobe in the forward direction indicates that the optical response is dominated by a coherent contribution of all scatterers.* $|\delta\boldsymbol{E}_{sc}|^2$ *and* $|\langle\boldsymbol{E}_{sc}\rangle|^2$ *indicate what are the main contributions to the scattering pattern.*

the other directions there are many spikes visible. The big lobe in the forward direction indicates that light scattering is indeed dominated by the ensemble-averaged electric field, even for a single realization. The presence of several peaks in the other directions indicates incoherent light scattering. In order to quantitatively characterize homogenization, we will compare the *scattered* powers of both coherent and incoherent light scattering that are calculated after averaged over many realizations. The powers that will enable us to discuss homogenization are defined as

$$P_{\text{coh}} = \frac{\varepsilon_0 c}{2} \oiint |\langle \mathbf{E}_{\text{sc,far field}} \rangle|^2 dS, \tag{5.6}$$

and

$$P_{\text{incoh}} = \frac{\varepsilon_0 c}{2} \oiint \langle |\delta \mathbf{E}_{\text{sc,far field}}|^2 \rangle dS, \tag{5.7}$$

where the integral is evaluated over a closed spherical surface in the far-field region, as is indicated by the subscripts "far field". We define the total scattered power as $P_{\text{tot}} = P_{\text{coh}} + P_{\text{incoh}}$, which is defined in this chapter after the ensemble averaging.

5.4 Non-resonant light scattering

In this section we summarize well-known physics about non-resonant light scattering by dilute ensembles of particles [17, 98]. In particular, we illustrate the factors leading to suppression of light scattering. In other words, we review the usual conditions to obtain homogenization in the non-resonant light scattering regime. We illustrate these conditions by keeping the same system of cold atoms and the same geometry as described in Section 5.3.

The illuminating frequency is far detuned from atomic resonance ($-10^4\Gamma_0$), so that we consider non-resonant light scattering. We calculate the coherent and incoherent scattered powers, as we defined them in the previous section. The powers are calculated as a function of the number of atoms inside the cloud, and normalized by the scattered power of a single atom. Figure 5.2 shows the numerical results in a log–log scale. We see that incoherent light scattering scales linearly with the number of atoms inside the fixed volume: $P_{\text{incoh}} \propto N$, and that coherent light scattering scales quadratically with the number of atoms: $P_{\text{coh}} \propto N^2$, where N is the number of atoms in the cloud. This result is in agreement with theory on single light scattering (Born approximation), as we will demonstrate next. The wavelength-size atomic cloud is within the single scattering regime, since the scattering mean free path, which is given by $l_{\text{sc}} = 1/[\rho\sigma_{\text{sc}}(\omega)] = 3$ m for $N = 450$ atoms inside the cloud, is much larger than the size of the atomic cloud. It is the small scattering cross section far from resonance that leads to a large scattering mean free path. Light scatters therefore at most once inside the cloud. In the single scattering regime, each scatterer is uniquely illuminated by the incident electric field [99]. When a linearly polarized plane wave, $\mathbf{E}(\mathbf{r}) = \mathbf{E}_{0,\text{inc}} e^{i\mathbf{k}_L \cdot \mathbf{r}}$, is incident upon such a system, the total scattered field in the far field is given by

$$\mathbf{E}_{\text{sc}}(\mathbf{r}) = \frac{\omega^2}{c^2}\alpha(\omega)\frac{e^{ikr}}{4\pi r}[\mathbf{E}_{0,\text{inc}} - (\mathbf{E}_{0,\text{inc}} \cdot \mathbf{u})\mathbf{u}] \sum_j^N e^{i\mathbf{q}\cdot\mathbf{r}_j}, \tag{5.8}$$

where we define $\mathbf{q} = \mathbf{k}_{\text{L}} - \frac{\omega}{c}\mathbf{u}$, with $\mathbf{u}$ being the direction of observation, and $\mathbf{k}_{\text{L}}$ the wave vector of the incident plane wave. From Eq. 5.6 and Eq. 5.7, we know that the scattering

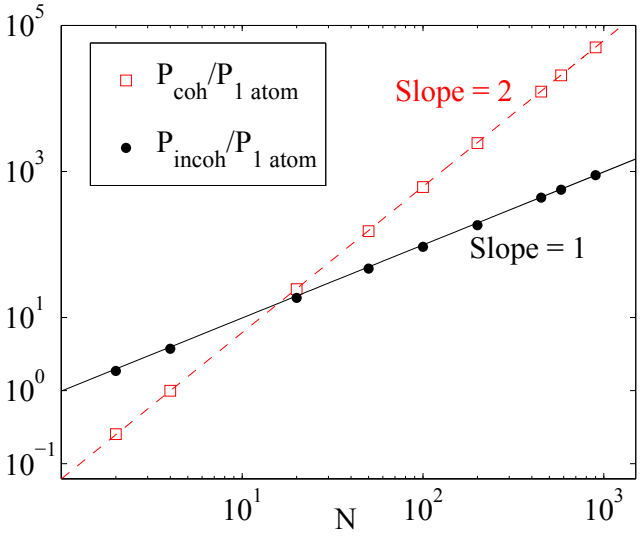

Figure 5.2: *Scattered power calculated for a linearly polarized incident plane wave propagating along the long axis of the cloud with a frequency detuning* $\delta\omega_L = \omega_L - \omega_0 = -10^4\Gamma_0$. *All powers are normalized by the scattered power for a single atom at the same detuning and plotted on a log–log scale. The fraction of coherently scattered light increases as a function of the number of atoms. The red dashed line is a quadratic fit and the black solid line a linear fit.*

pattern, i.e., the integrand of the surface integrals, is proportional to $|\mathbf{E}_{\text{sc}}|^2$ in the far field. From Eq. 5.8, it follows that the scattering pattern is therefore given by

$$|\mathbf{E}_{\text{sc}}|^2 = \frac{\omega^4}{c^4}|\alpha(\omega)|^2\frac{|\mathbf{E}_{0,\text{inc}}|^2}{(4\pi r)^2}\sin^2(\theta)S(\mathbf{q}), \tag{5.9}$$

where θ is the angle between the observation direction and the polarization direction, and $S(\mathbf{q})$ is given by the so-called structure factor

$$S(\mathbf{q}) = |\sum_{j=1}^{N} e^{i\mathbf{q}\cdot\mathbf{r}_j}|^2. \tag{5.10}$$

We see that in the single scattering regime, the scattering pattern is determined by the structure factor. The structure factor can be decomposed as follows

$$S(\mathbf{q}) = \sum_{j=1}^{N} e^{i\mathbf{q}\cdot(\mathbf{r}_j-\mathbf{r}_j)} + \sum_{j,l,j\neq l}^{N} e^{i\mathbf{q}\cdot(\mathbf{r}_j-\mathbf{r}_l)} = N + \sum_{j,l,j\neq l}^{N} e^{i\mathbf{q}\cdot(\mathbf{r}_j-\mathbf{r}_l)}. \tag{5.11}$$

The ensemble-averaged structure factor gives the ensemble-averaged scattering pattern:

$$\langle S(\mathbf{q})\rangle = N + N(N-1)\langle e^{i\mathbf{q}\cdot(\mathbf{r}-\mathbf{r}')}\rangle, \tag{5.12}$$

which can be rewritten as

$$\langle S(\mathbf{q})\rangle = N[1 - \langle e^{i\mathbf{q}\cdot(\mathbf{r}-\mathbf{r}')}\rangle] + N^2\langle e^{i\mathbf{q}\cdot(\mathbf{r}-\mathbf{r}')}\rangle, \tag{5.13}$$

where the average of the exponential function is this time given by

$$\langle e^{i\mathbf{q}\cdot(\mathbf{r}-\mathbf{r}')}\rangle = \iint \mathrm{P}(\mathbf{r},\mathbf{r}')e^{i\mathbf{q}\cdot(\mathbf{r}-\mathbf{r}')}d^3\mathbf{r}d^3\mathbf{r}', \tag{5.14}$$

with $\mathrm{P}(\mathbf{r},\mathbf{r}')$ being the joint probability distribution of finding one atom at position $\mathbf{r}$ and one atom at position $\mathbf{r}'$, so that $\iint \mathrm{P}(\mathbf{r},\mathbf{r}')d^3\mathbf{r}d^3\mathbf{r}' = 1$. From Eq. 5.9, and Eq. 5.13 it follows that for systems that are much smaller than the scattering mean free path and therefore in the single scattering regime, the incoherent scattering spectrum scales linearly with N. The coherent scattering spectrum is the second term in the structure factor and scales quadratically with N. We observe that the fraction $P_{\mathrm{incoh}}/P_{\mathrm{coh}} \propto 1/N \to 0$ for increasing number of atoms in a fixed volume. Yet, incoherent light scattering keeps increasing linearly when N increases. In view of our strict formulation of homogenization (number 2: $P_{\mathrm{incoh}} = 0$), the result that $P_{\mathrm{incoh}} \propto N$ has as a consequence that far from resonance, dense clouds of atoms are not in the homogenization regime. The finding that a system which is illuminated far from resonance cannot be homogenized is indeed what is observed in the sky, where Rayleigh scattering occurs. The molecular number density of the sky is 10^7 molecules/μm^3. Although the air is very dense for visible wavelengths ($k\langle r\rangle \sim 0.003$), the sky appears blue in all observation directions. It is incoherent light scattering that we observe in the sky[1]. The strong condition that P_{incoh} should be negligible is thus not satisfied. The condition to reach homogenization: $\langle r\rangle \ll \lambda$, is clearly not sufficient for this system.

5.4.1 Effect of position correlations on non-resonant light scattering

Next, we introduce position correlations in the cloud of scatterers. When position correlations are present, the joint probability density function $\mathrm{P}(\mathbf{r}_1,\mathbf{r}_2)$ of having scatterer 1 at position $\mathbf{r}_1$ and scatterer 2 at position $\mathbf{r}_2$ cannot be factorized as $\mathrm{P}(\mathbf{r}_1)\mathrm{P}(\mathbf{r}_2)$ anymore. Instead, the joint probability density can be written as

$$\mathrm{P}(\mathbf{r}_1,\mathbf{r}_2) = \frac{1}{V^2}[1 + g(\mathbf{r}_1 - \mathbf{r}_2)], \tag{5.15}$$

where V is the volume of the system and g is the pair correlation function, for which an example (hard sphere approximation) is given in Fig. 5.3. This is numerically implemented by introducing a spherical exclusion volume with diameter d around each scatterer. This diameter sets the minimum distance between nearest-neighbor scatterers: $d = r_{\mathrm{nn,min}}$, so they cannot approach one another within a distance d. The exclusion volume is illustrated in Fig. 5.4(a), where the dashed circles correspond to the virtual boundaries. Figure 5.4(b) shows again the normalized coherent and incoherent scattered power, but this time as a function of the nearest-neighbor distance. Figure 5.4(b) shows that incoherent light scattering gets reduced by introducing order in the system. An evaluation of the integral given in Eq. 5.14 for an infinite volume leads to

$$\langle S(\mathbf{q})\rangle \approx N\Big[1 - f_V\Big] + N(N-1)\delta(\mathbf{q}), \tag{5.16}$$

where f_V is the volume fraction that is occupied by the exclusion volumes. We observe that as the exclusion volume of each scatterer increases, incoherent light scattering diminishes. More generally, i.e., beyond the single scattering regime, it can can be understood that creating order in a system reduces density fluctuations. The reduction of density fluctuations

[1] This is not true when one looks towards the sun, since in that direction we observe "coherent" light scattering, where "coherent" should be interpreted in our way as an ensemble average.

reduces fluctuations in the polarization density when the system is illuminated, and thereby incoherent light scattering gets reduced. Hence, it is possible to reach homogenization when introducing spatial correlations. This illustrates what we know about light scattering from a pure liquid: it scatters less light than a gas, although there are more scatterers. This effect where incoherent light scattering gets reduced by correlations is also responsible for the transparency of the cornea despite its heterogeneous structure [100].

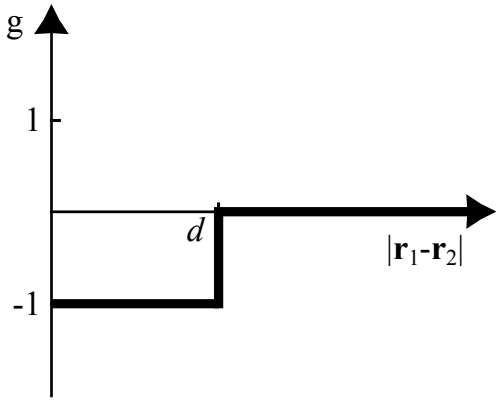

Figure 5.3: *An example of the pair correlation function for the case of the hard sphere approximation. The atoms cannot approach each other within a distance d.*

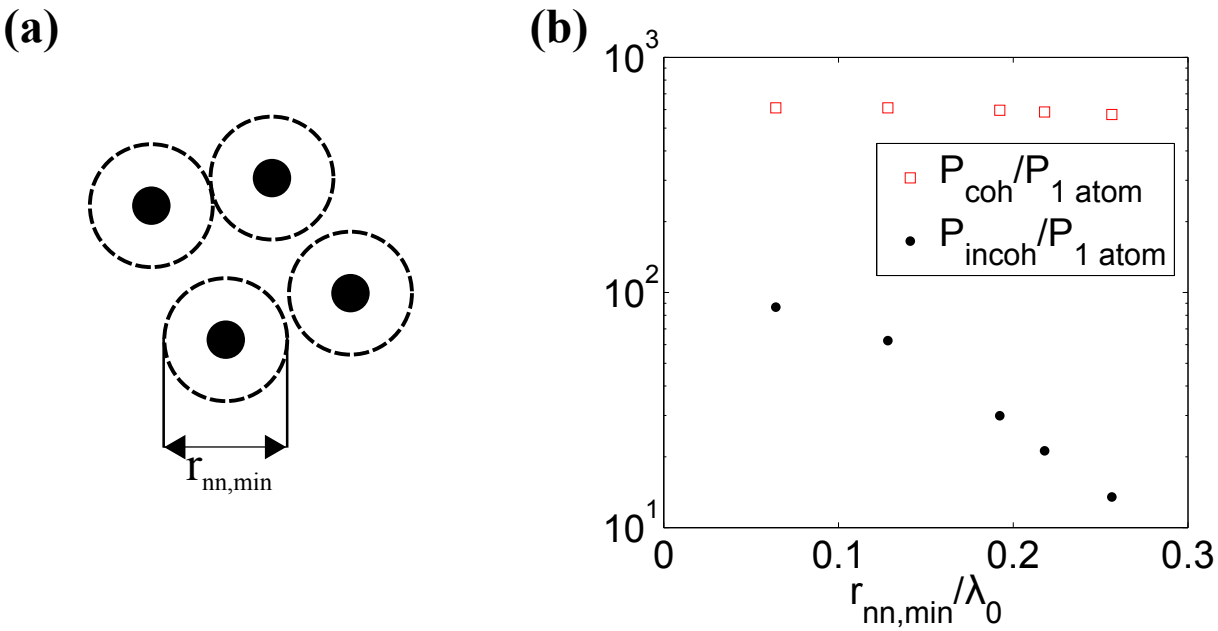

Figure 5.4: *Correlations reduce incoherent scattering. The scattered power has been calculated for a linearly polarized incident plane wave propagating along the long axis of the cloud with a frequency detuning $\delta\omega_L = -10^4\Gamma_0$ and 100 atoms in the cloud. All powers are normalized by the scattered power for a single atom at the same detuning. Atomic positions are uniformly distributed, while taking into account a spherical exclusion volume around each atom with a diameter $d = r_{nn,min}$ which corresponds to the minimum nearest-neighbor distance. Suppression of incoherent light scattering is observed.*

Elastic mean free path The regime of suppression of light scattering can be characterized by an elastic mean free path l_{mfp} which can be connected to the imaginary part of the effective refractive index $1/l_{\mathrm{sc}} = 4\pi \mathrm{Im}(n_{\mathrm{eff}})/\lambda$, as we have seen in Section 2.2.3. The condition for suppressing scattering is given by $L \ll l_{\mathrm{sc}}$ where L stands for a typical size of the system, so that photons do not scatter multiple times. Position correlations can increase the elastic mean free path and thereby bring a system of a given size and a given number of atoms into the homogenization regime.

5.4.2 Effect of nonradiative decay on non-resonant light scattering

Finally, we note that another mechanism which leads to homogenization is losses in a system. If *each scatterer* has an absorption cross section σ_{abs} that is much larger than its scattering cross section σ_{sc}, the scatterers do not scatter a lot of light. Incoherent light scattering is said to be suppressed, since light absorption is preferable. However, an *ensemble of absorbing scatterers* can still scatter light coherently. An example is a droplet of Indian ink (also known as China ink in British English), which consists of a suspension of colloidal carbon nanoparticles. While each nanoparticle absorbs light, the droplet containing the nanoparticles scatters light coherently: light that is incident upon a droplet of Indian ink gets for example reflected. The ink droplet can be described as a homogeneous droplet with a complex refractive index to account for the role of the nanoparticles. Such a system is in the homogenization regime as the incoherent component vanishes. The condition for this regime can be written in terms of decay length $l_{\mathrm{sc/abs}} = 1/(\rho\sigma_{\mathrm{sc/abs}})$. The homogenization condition is thus $l_{\mathrm{sc}} \gg l_{\mathrm{abs}}$ to ensure that absorption is the leading contribution to extinction.

5.5 Resonant light scattering

We now turn to the resonant scattering case. For the atomic systems we study here, it is possible to find a dielectric constant with values similar to the ones encountered in condensed matter physics. In Chapter 4, we have found that a cloud with a density of $\rho k^3 = 1$ has an effective permittivity with a real part varying in the range $[-2, 2]$ close to atomic resonance. Although the system is more dilute than air, it is the resonant nature of excitation that leads to this large value.

Figure 5.5(a) shows the coherent and incoherent scattered power as a function of the number of atoms in a cloud with fixed volume, for an incident plane wave on atomic resonance. In stark contrast with the off-resonance case (dashed lines), both coherent and incoherent powers do not keep increasing with the number of atoms. The saturation of the incoherent power when N increases has been observed experimentally by Pellegrino *et al.* in Ref. [51] and the saturation of the coherent power has been observed by Jennewein *et al.* in Ref. [7]; both experiments have been discussed in Chapter 3 of this thesis. Whereas coherent light scattering (diffraction) gives rise to a large peak in the forward direction, incoherent light scattering occurs in all directions. After an angular integration over the full solid angle, the coherent and incoherent contributions turn out to be of *similar importance*, as can be seen in Fig. 5.5(a)[2]. This is as opposed to what is expected for light scattering from

[2]If a detector is placed in the forward direction, with a polarizer and a small collecting aperture in front of the detector, one can reduce significantly the amount of *detected* incoherent light. This situation corresponds to the experiments of Jennewein.

a system for which the inter-atomic distance is small: coherent light scattering might be expected to dominate. According to the second formulation of homogenization, $P_{\text{incoh}} = 0$, this atomic system can therefore not reach the homogenization regime. Importantly, this system cannot reach the homogenization regime according to the first formulation either, as incoherent light scattering is as important as coherent light scattering.

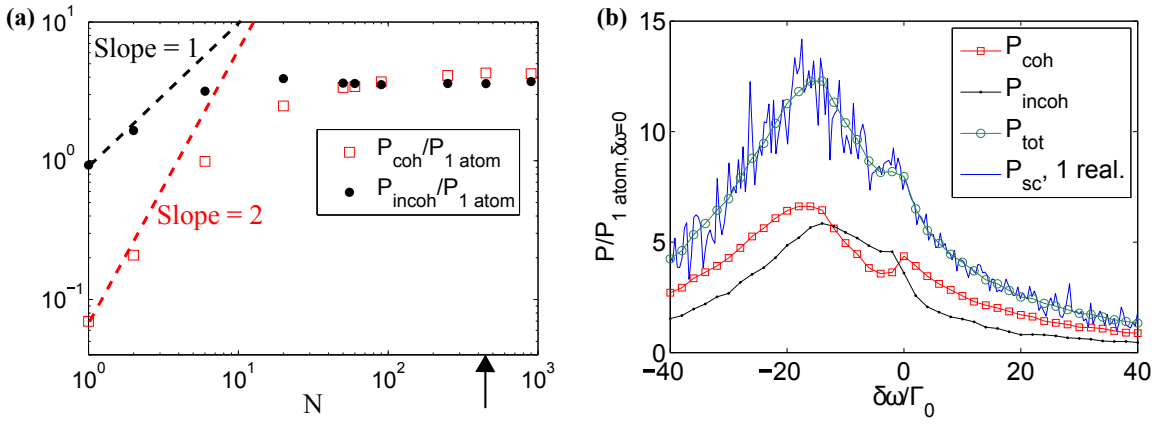

Figure 5.5: *(a) Scattered power has been calculated for a resonant ($\delta\omega_L = 0$) linearly polarized incident plane wave propagating along the long axis of the cloud. All powers are normalized by the scattered power for a single atom on resonance. The black arrow indicates for which number of atoms the spectrum has been plotted in Fig. 5.5(b). (b) For $N = 450$ atoms, the scattered power for a single realization has been plotted, together with the ensemble averaged coherent, incoherent and total scattered powers. All quantities are normalized by the single atom scattered power on resonance.*

5.5.1 Scattering spectra for coherent and incoherent light

In order to further analyze the resonant scattering regime, we study the spectrum of the scattered light, i.e., the amount of light scattered coherently or incoherently as a function of the detuning of the laser. We plot in Fig. 5.5(b) four spectra of: (1) ensemble-averaged coherent scattered light, (2) ensemble-averaged incoherent scattered light, (3) the sum of the ensemble-averaged coherent and incoherent scattered light, and (4) the scattered light for a single realization. One feature is that the spectrum is significantly different from a Lorentzian spectrum. The peaks that are visible for a single realization correspond to excited collective modes, which were introduced in Chapter 4. Furthermore, it is observed that the coherent and incoherent spectra show some similarities, notable both seem to have a second peak for a negative detuning.

Next, we will interpret the observed coherent and incoherent spectra from both a microscopic and macroscopic perspective. We start with the microscopic point of view.

Microscopic view on spectrum Following the idea developed in Chapter 4, we adopt the collective modes point of view to analyze the spectra. It was shown that there exist a few polaritonic modes, which have two key features: (i) they are robust against disorder (i.e., they depend on density and geometry but not on the detailed position of the scatterers), and (ii) they are superradiant and therefore responsible for most of the coupling between

the incident field and the system. Here, the term superradiant is used to define states with a decay rate larger than $8\Gamma_0$, and these modes can be found in the closeup of Fig. 4.2(A). We limit the study to the low-excitation regime where a classical model is valid. These collective modes were shown to be identical to the Fabry-Perot-like modes of the effective homogeneous particle (see Chapter 4). It was expected that the light scattered by these modes accounts for a large part of coherent light scattering. This is indeed what has been observed in Fig. 4.9 where a comparison of the the overall coherent scattering pattern with the scattering pattern of a subset of modes (polaritonic modes) is given. The spectrum of coherent light scattering is therefore expected to be affected by polaritonic modes. Notably, the second peak at red detuning can be attributed to polaritonic modes. We have shown that the position of this peak changes according to the size of the cloud; indeed polaritonic modes depend on the size of the cloud as well.

Next we explain why the incoherent light scattering spectrum shows similarities with the coherent light scattering spectrum. Incoherent light scattering is due to the modes which are not superradiant. They are the majority of the modes. These modes are excited via the coupling with polaritonic modes, because the modes are not orthogonal. Indeed, when the set of coupled-dipole equations is put in the form of an eigenvalue problem, we can see in Section 2.2 that the corresponding matrix is not Hermitian. Therefore, the eigenvectors are not orthogonal. Together with the fact that subradiant modes exist over a large frequency range, as we have seen in Chapter 4, the coupling between polaritonic modes and subradiant modes lies at the origin of the similarities between the coherent ($\sim$polaritonic modes) and incoherent ($\sim$subradiant modes) light scattering spectra.

Macroscopic view on spectrum The similarities between both spectra can be understood from a macroscopic view from the fact that the effective homogeneous medium has an imaginary dielectric constant accounting for losses (see Chapter 4). In the absence of "real" losses (conversion into heat), these losses account for the energy transfer from the coherent (average) field to the incoherent (fluctuating) field. As the excitation of the system is mediated by the resonances of the homogeneous system, both coherent and incoherent power are expected to have a similar spectrum.

5.5.2 Effect of nonradiative decay and dephasing on resonant light scattering

The fact that close to resonance a lossless system consisting of cold atoms cannot reach the homogenization regime makes us wonder if there exists any system of resonant scatterers that can reach the homogenization regime. In Section 5.4.2 we have mentioned the role of losses for nonresonant scatterers. We report in Fig. 5.6 the results obtained for resonant light scattering from atoms, when adding nonradiative losses and/or dephasing following Eq. 5.5. Nonradiative losses exist in quantum dots and dephasing might exist in the case of an atomic system due to motional effects. From Fig. 5.6 it is seen that the incoherent power gets significantly reduced whereas the coherent power is only weakly affected. This can easily be understood by using the mode picture to analyze scattering. It can be seen from Eq. 4.3 that the only change of the (complex) eigenfrequency of a collective eigenmode β by introducing nonradiative and dephasing rates is: $\tilde{\omega}_\beta = \omega_0 - i\frac{\Gamma_r}{2} \mapsto \tilde{\omega}_\beta - i\frac{\Gamma_{nr}+\Gamma^*}{2}$. This formula gives a clear picture of the competition between radiative and nonradiative decay for each mode: it follows that light which gets scattered by subradiant modes is filtered

out by the presence of nonradiative losses and dephasing. This can be understood as follows: subradiant modes emit light over a very long time period. When nonradiative decay channels exist, they let the mode decay faster via this nonradiative channel, i.e., its radiative efficieny gets reduced significantly. As opposed to the strong influence of nonradiative decay on subradiant modes, light scattered by a polaritonic mode is only weakly affected by nonradiative decay as long as the radiative decay rate dominates and therefore the radiative efficiency is high. Figure 5.6 shows that also coherent light scattering starts to decay when $\Gamma_{nr}+\Gamma^*$ becomes comparable to the radiative decay rate of superradiant modes. This happens for the same reason as for subradiant modes. Finally, from Fig. 5.6 the introduction of losses appears as an efficient way to achieve homogenization in the sense of suppressing incoherent scattered light.

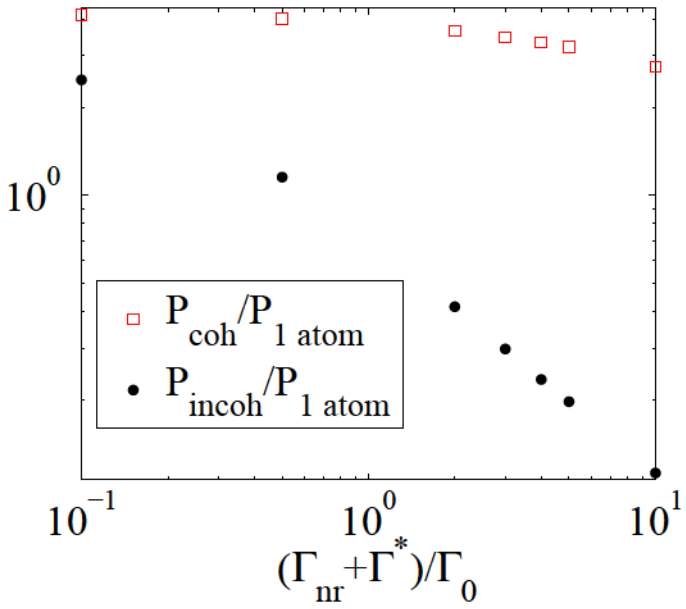

Figure 5.6: *Coherent and incoherent scattered powers are given for $N = 450$ atoms under variation of the nonradiative and dephasing rate. All powers are normalized by the scattered power for a single atom at resonance.*

5.6 Giant fluctuations of the scattered power by resonant atoms in a subwavelength volume

In this last section we discuss light scattering in the extreme case of a dense *subwavelength-size* cloud of atoms. This subwavelength system corresponds to the system initially envisioned by Dicke to discuss superradiance effects [101]. There the focus was on the building of coherence between an ensemble of identical atoms all initially excited. As opposed to the regime that was envisioned by Dicke, we consider the low-excitation regime, i.e., a single excitation is present in the atomic system. As we have done in Chapters 2 through 5, we include the interaction between atoms in order to derive the collective eigenmodes of the system, something that was not done in Dicke's formalism, who assumed non-interacting atoms. By discussing the system in terms of collective modes, we will observe that very

dense, subwavelength, disordered atomic systems scatter less light than a single atom and in a very fluctuative manner. Other works have discussed a similar system, but they discussed the atomic system as an ensemble of atoms instead of an ensemble of collective modes [5, 6]. Although their conclusions are the same as the conclusions presented in this section, we believe that due to the strong interactions, dense and cold atomic systems should be treated in terms of collective eigenmodes instead of an ensemble of individual atoms.

5.6.1 Scattering spectrum for subwavelength-size atomic cloud

We consider the situation where a resonant plane wave is incident upon a subwavelength-size cloud of atoms. The cloud has a shape of a box with sides $\lambda_0/(2\pi)$, so that each atom is in each other's near-field region. While changing the number of atoms inside this small cloud, we calculate the ensemble-averaged total scattered power. The total scattered power is normalized by the total scattered power for a single atom. The results are plotted in Fig. 5.7. It is seen that a system with several atoms inside the cubic box scatters less than a single atom. It is also seen that the scattered power is almost independent of the number of atoms. To analyze this behavior, we plot the spectrum of the scattered light in the inset for a single realization and 10 atoms. We observe that by varying the incident frequency, several modes are excited. These modes are spectrally separated. The amount of light scattered for each mode does not vary much and is close to that of a single atom. This is remarkable, since we never find a mode that scatters more than a single atom would; which is characteristic for a superradiant mode. Instead, we observe a *spectral repulsion* of the modes due to resonant dipole-dipole interaction. For an atomic system without any

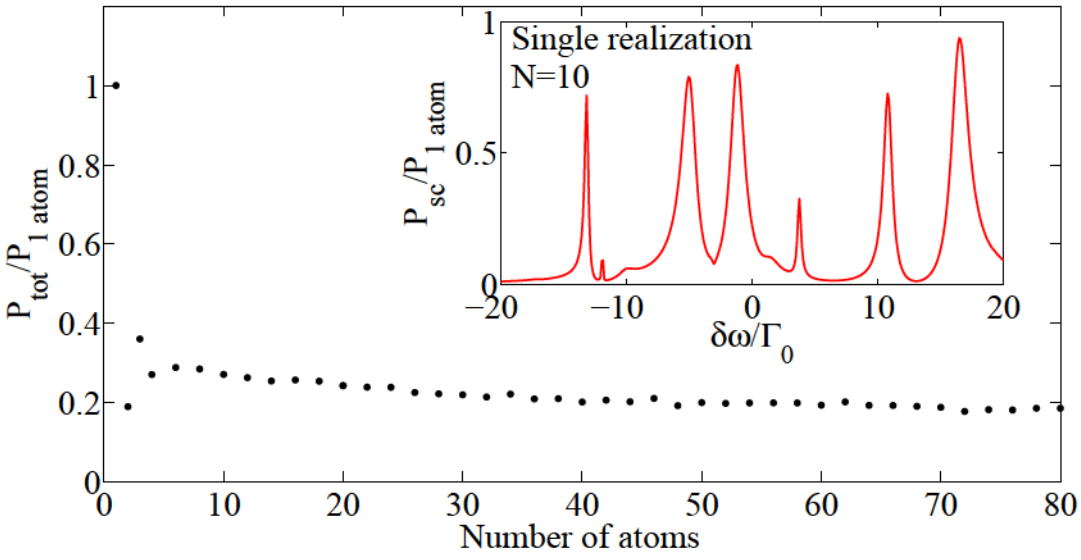

Figure 5.7: *A resonant plane wave gets scattered by atoms inside a cubic box with sides $\lambda_0/(2\pi)$. The total scattered power is normalized by the scattered power for a single atom at resonance. It is seen that the system of N atoms scatters less than a single atom. It is also seen that the total scattered power is almost independent on the number of atoms. In the inset, the spectrum for a single realization of the box with $N = 10$ atoms inside is shown by the red, solid curves. The collective eigenmodes are spectrally separated.*

interaction, all modes are degenerate. It is the resonant dipole-dipole interaction that lifts the degeneracy of these modes.

To explain why on average the system scatters much less than a single atom, as we can see from the main panel of Fig. 5.7, we use the spectrum as presented in the inset of Fig. 5.7, in which the modes are spectrally separated. Let us denote $\delta\omega$ the typical spacing between two peaks and take Γ_0 as the average width of each peak. The probability that a given laser line excites a mode is thus $\Gamma_0/\delta\omega$. As $\delta\omega > \Gamma_0$, most of the realizations the system does not get excited. Therefore, the average scattered power is smaller than that of a single atom. This is confirmed in the main panel of Fig. 5.7.

5.6.2 Average mode spacing

In an actual experiment, atoms are moving so that the spectral positions of the modes will fluctuate over time. For a monochromatic incident laser, it follows that the scattering signal is expected to display giant fluctuations in time. This will be a clear signature of this interaction regime. Let us discuss the conditions for observation of this particular scattering regime with a low average scattering cross section and giant fluctuations. We use as a definition of this scattering regime a system where the scattering peaks are well separated as displayed in the inset of Fig. 5.7. The condition to be in this regime is given by $\delta\omega > \Gamma_0$. Next, we study this condition for the observation of giant fluctuations and see under which experimental conditions this regime can be attained. Instead of calculating the scattering spectra, let us calculate the eigenfrequencies of the system. The total spread of the eigenfrequencies $\Delta\Omega$ is divided by the total number of modes, so that we obtain the average distance between modes $\delta\omega$. In order to determine $\Delta\Omega$, we arbitrarily select 90% of the modes. We repeat this procedure for cubes with varying volume and varying number of atoms inside. Figure 5.8(a) shows the typical spacing $\delta\omega/\Gamma_0$ of the modes as a function of the volume for $N = \{20, 40, 80\}$ atoms. The results are fitted with the function: $\delta\omega/\Gamma_0 = c_1\{V/[\lambda_0/(2\pi)]\}^{c_2}$, where c_1 and c_2 are the free fit parameters. It is observed that the mode spacing is independent of the number of atoms and that it is inversely proportional to the volume. These results are consistent with a back-of-the-envelope calculation. In order to estimate the average spacing between two modes $\delta\omega$, we first estimate the total spread $\Delta\Omega$. For this estimate, we assume the frequency spread is bounded by the shift which is due to the interaction between two atoms that are in each other's near-field region: $\Gamma_0/(kr)^3$, where we take r to be the typical inter-atomic distance. For r we have the relationship $Nr^3 = V$, where V is the volume of the atomic cloud. The typical spacing between modes is estimated by dividing the total frequency spread by the total number of modes ($3N$). It follows that the typical spacing

$$\delta\omega/\Gamma_0 \propto \frac{1}{Vk^3} \qquad \text{Full Green's tensor.} \tag{5.17}$$

(5.18)

The average mode spacing is therefore indeed independent of the number of atoms and inversely proportional to the volume. This explains what we have seen in Fig. 5.7, where the total scattered power is independent of the number of atoms inside the cloud.

Importance of near-field interaction We now assess the importance of the near-field interaction which varies as $1/r^3$. For this, we assume that only the far-field interaction

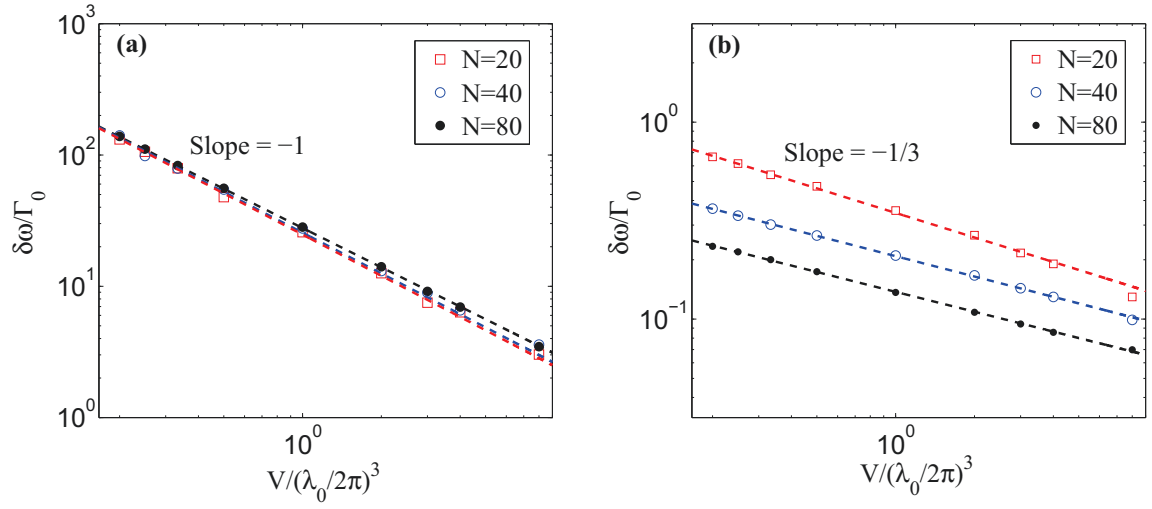

Figure 5.8: *Typical spacing $\delta\omega$ between two modes is given as a function of the volume of the box for three different numbers of atoms inside. The numerical results are fitted with a power function. (a) The entire Green's tensor has been taken, i.e., also the $1/r^3$ term. It is observed that the typical spacing is independent of the number of atoms and $\delta\omega \propto V^{-1}$. (b) Only the $1/r$ term of the Green's tensor has been used in the calculation. It can be seen here that the typical spacing depends on the number of atoms and that $\delta\omega \propto V^{-1/3}$.*

term proportional to $1/r$ is present. The average mode separation as a function of the volume for different numbers of atoms is shown in Fig. 5.8(b), where the same fit function $\delta\omega/\Gamma_0 = c_1\{V/[\lambda_0/(2\pi)]\}^{c_2}$ is used. We observe that the typical spacing depends on the number of atoms and is roughly proportional to $V^{-1/3}$. By using the same formalism as described above, but by replacing the typical interaction energy by $\Gamma_0/(kr)$, the typical spacing can be shown to be

$$\delta\omega/\Gamma_0 \propto \frac{1}{N^{2/3}(Vk^3)^{1/3}} \qquad \text{Only the } 1/r \text{ contribution of Green's tensor.} \tag{5.19}$$

Figure 5.9 shows the fit parameter c_1 as a function of the number of atoms. The fit function for the $c_1(N)$ plot is also a power function and the fit results in $\delta\omega/\Gamma_0 \propto N^{-\alpha}$, with the power $\alpha = 0.68 \pm 0.07$ with 95% confidence bounds. This result coincides with the predicted dependence of the mode spacing $\delta\omega/\Gamma_0 \propto N^{-2/3}$. With this we proved the theoretical estimate of the mode spacing: $\delta\omega/\Gamma_0 \propto 1/[N^{2/3}(Vk^3)^{1/3}]$ for the situation where we only take the far-field term of the Green's tensor into account.

5.6.3 Condition for nonobservation of single-photon superradiance

Now we study a consequence of this result. It follows that the condition $\delta\omega/\Gamma_0 > 1$, for which no single-photon superradiance can occur, within a constant factor, can be put in the form

$$Vk^3 < 1 \qquad \text{Full Green's tensor,} \tag{5.20}$$

$$Vk^3 < \frac{1}{N^2} \qquad \text{Only the } 1/r \text{ contribution of Green's tensor.} \tag{5.21}$$

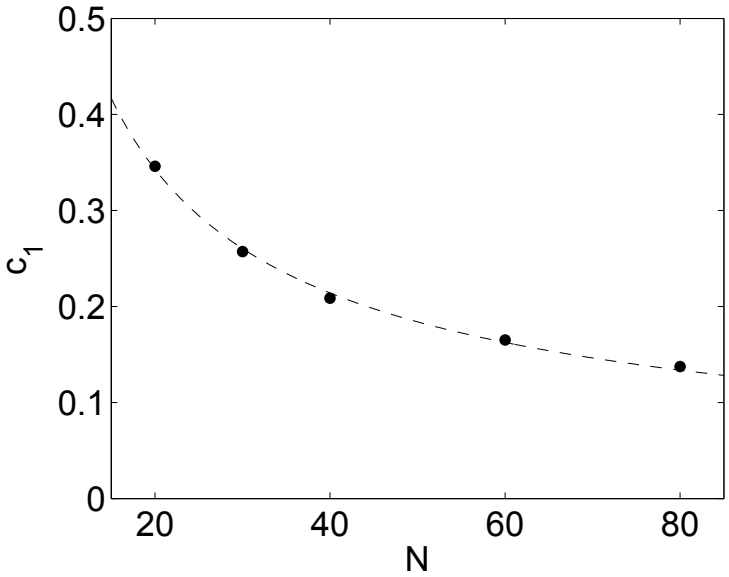

Figure 5.9: *The fit parameter used in Fig. 5.8(b) is plotted as a function of the number of atoms inside the cloud. The fit function of $c_1(N)$ scales as $N^{-\alpha}$, where $\alpha = 0.68 \pm 0.07$ with 95% confidence bounds.*

This shows that for systems that do not strongly interact, i.e., only the far-field term is present in the Green's tensor, one cannot reasonably reach the regime where single-photon superradiance is absent, as it would require $V < \lambda^3/[(2\pi)^3 N^2]$, which is hard to achieve experimentally in the visible regime. Yet, for systems where near-field dipole-dipole interactions are included (Eq. 5.20), this regime can be reached for *any number of atoms*. In other words, in the regime of N atoms in a subwavelength-size volume and the full Green's tensor is considered, the system is driven by collective modes spectrally separated and displays giant fluctuations. As soon as the volume increases beyond $\lambda/(2\pi)^3$, the modes start overlapping spectrally thereby allowing single-photon superradiance to show up; an example is given in Fig. 5.5(b), where we observe that the scattering pattern reaches values that are superior to 1. In summary, the condition $Vk^3 < 1$, which is a condition for single-photon superradiance for noninteracting scatterers, becomes a condition of *nonobservation* of single-photon superradiance for interacting resonant scatterers. We explain the nonobservation of single-photon superradiance in terms of modes repulsion.

5.6.4 Thouless criterion for Anderson localization

Finally, we make a small remark on Anderson localization. A criterion to observe Anderson localization is that all modes are spectrally separated, so that $\delta\omega > \Gamma_0$ [89, 90]. This condition is known as the Thouless criterion for Anderson localization. We have seen that a subwavelength-size atomic cloud satisfies the Thouless criterion. An interpretation of the Thouless criterion is that an excited localized mode cannot hop to another localized mode and eventually to the other side of the system, since the modes do not overlap spectrally, thus assuring the localization of light. However, the subwavelength-size cloud is very small. Note however that to observe Anderson localization, the system should be smaller than the localization length, a condition that may not be verified for the very small systems we have studied here. Since we do not know the localization length of this system, we cannot conclude on the possibility of observing Anderson localization in these small clouds.

We note that Skipetrov and Sokolov have theoretically studied Anderson localization in random ensembles of resonant point scatterers [91]. In that work, the Thouless criterion is never met under the vectorial description of the resonant dipole-dipole interactions. The observation that the Thouless criterion is met for a subwavelength-size cloud is not in contradiction with Ref. [91], since Ref. [91] only considers atomic clouds that are larger than $[\lambda/(2\pi)]^3$.

5.7 Superradiance from ordered, dense atomic clouds

The conclusions we have drawn so far are based on *disordered* systems. For completeness, we briefly discuss how the image of collective modes can be used to show that it might be possible to observe superradiance in *ordered*, not moving, subwavelength-size clouds. An ordered system of N particles has, like a disordered system, also $3N$ collective eigenmodes. However, due to the order of the system, it is expected that there is a certain level of degeneracy of the collective modes. When several modes spectrally overlap, an incident continuous-wave laser will excite several modes at the same time, as opposed to the case of disordered, subwavelength clouds, thereby making the observation of superradiance possible.

A particular ordered, finite-size system is one for which a primitive unit cell can be defined. An example of a situation for which this is possible is one where atoms are regularly placed on a subwavelength circle (see Ref. [6]). Such a system has a high level of degeneracy, since there are only $3N_{\text{unit cell}}$ different collective eigenmodes, where $N_{\text{unit cell}}$ is the number of atoms inside the primitive unit cell. It would be interesting to experimentally study superradiance from these kind of systems, although it is a complicated task due to geometrical constraints.

5.8 Conclusion

The initial motivation of this study was the numerical observation that incoherent light scattering by an ensemble of atoms does not decrease as the number density increases for a system with a fixed volume. Motivated by this numerical observation, we have revisited the conditions of homogenization. We adopt a strict formulation of homogenization: the power associated to the fluctuating field should be negligible. According to this definition, it is understood that for non-resonant light scattering the condition $\langle r \rangle \ll \lambda$, where r is a typical length scale of the problem, is not a sufficient condition. Yet, by introducing local order or losses in a system, the incoherent power can become negligible. The former increases the typical scattering length, and when $L < l_{\text{sc}}$, the criterium of homogenization is satisfied; for the latter $l_{\text{sc}} \gg l_{\text{abs}}$ needs to be reached.

When studying a system of interacting resonant atoms, we cannot analyze the results with the same concepts as we are used to for noninteracting particles. The spectral analysis of the scattered light demonstrates the onset of collective modes with spectral signatures that are markedly different from the atomic Lorentzian profiles. For large systems, we found in Chapter 4 that incoherent light scattering is mostly due to the nonpolaritonic modes whereas the coherent scattered power associated to the ensemble-averaged field is due to polaritonic modes. It is found in this chapter that when the number of atoms increases, incoherent light scattering does not vanish and is actually equally important as coherent light scattering, so that this is a class of system that cannot reach the homogenization

regime. We find that here again, the introduction of losses or dephasing mechanisms such as motion of the scatterers, may be used to suppress incoherent light scattering.

Finally, we have observed a particular class of systems: ensembles of atoms in a volume V smaller than $1/k^3$. When this condition is fulfilled, the collective modes are spectrally separated. It is found that when increasing the number of atoms, the collective modes stay spectrally separated and scatter less than a single atom. However, after an ensemble average, the system scatters less than a single atom does. These systems cannot reach the homogenization regime by increasing the number of atoms. Finally, we find that for interacting resonant atoms, the condition $V < 1/k^3$ is a condition that ensures that no single-photon superradiance is observed.

Chapter 6

Theory of electroluminescence by quantum-dots based metasurface light-emitting devices

6.1 Introduction

In the previous chapters, we discussed collective effects in *light scattering* from dense atomic systems. We have seen that the coherent optical response is determined by the effective index of refraction which is found to be beyond the Lorentz-Lorenz model for the effective index of refraction, and that fluctuations in either density or spectrum are responsible for incoherent light scattering. The coherent optical response is dominated by polaritonic modes (Chapter 4). The incoherent optical response stays important as compared to the coherent optical response as the density increases (Chapter 5). In this chapter we study the *emission* properties of a dense ensemble of emitters close to resonant nanostructures. More specifically, we study the emission properties of a dense ensemble of PbS colloidal quantum dots (cQDs) close to plasmonic nanoantennas. The interest in the emission properties of a dense ensemble of cQDs within this thesis comes from the fact that quantum dots have very similar properties as atoms. Some examples of similarities are

- the presence of quantized energy levels, thereby making them resonant entities,
- resonant dipole-dipole interactions exist between the individual particles of which the ensemble is composed,
- a dense ensemble can be created, which is especially true for colloidal quantum dots.

Quantum dots are considered to be very important for many industrial applications, an example being quantum-dot based light-emitting sources [102]. A key property for lighting applications is their tunable bandgap. By slightly varying the size of the quantum dot, the bandgap and thereby the wavelength of the emitted light can be chosen. However, as quantum dots cannot be perfectly identical due to the fabrication, they all have slightly different emission and absorption spectra. This inhomogeneous broadening is a big difference between cold atoms and quantum dots.

In this chapter we study the electroluminescence (EL) properties of a dense ensemble of PbS cQDs. In the next section, we will explain the physical mechanism of electroluminescence and see what is the state of the art in the field of quantum-dot based electro-

luminescence. In Section 6.3 we describe the experimental results obtained in the group of dr. Aloyse Degiron at Institut d'Électronique Fondamentale (IEF) in Université Paris Sud. This will allow us to consider if the quantum dots in their experiments should be modeled as independent entities or as an ensemble. Based on this section, we will discuss in Section 6.4 the standard electroluminescence model for a LED. The electroluminescence model for a LED will be generalized to the situation of quantum dots in the near vicinity of nanostructures in Section 6.5. In Section 6.6 we will apply the proposed generalized electroluminescence model to experiments that have been conducted in the group of Degiron on two different nanoantennas.

6.2 Electroluminescence from quantum dots

After we introduced the idea of electroluminescence from quantum dots, we will summarize what has already been done on electroluminescence from quantum dots.

6.2.1 Quantum-dot based electroluminescence

To explain electroluminescence from quantum dots, we use the schematic presented in Fig. 6.1. In order to observe an electroluminescence signal, a voltage is applied across a multilayer system that contains cQDs. The applied voltage will make that holes and electrons move towards the light-emitting layer, which is in this drawing a single layer of cQDs. Holes are transported via a so-called hole transport layer (HTL) and electrons via an electron transport layer (ETL) towards the cQD layer. There are three possible combinations of the charge transport layers: (1) all inorganic, (2) all organic, or (3) hybrid, where typically the ETL is chosen to be inorganic and the HTL to be organic. The device that is treated in particular in this chapter has an all-inorganic architecture, with the ETL being TiO_2 and the HTL being MoO_x. The electron and hole form an exciton that can recombine at the level of the quantum dots under emission of a photon. The energy of the photon is defined by the bandgap energy of the cQD. The photon that is created needs to

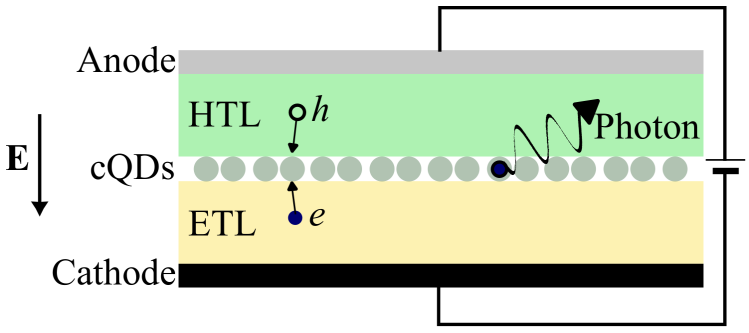

Figure 6.1: *Simplified vision of a quantum-dot based light-emitting device. Electrons leaving the cathode are transported via an electron transport layer (ETL) towards the light-emitting layer that is composed of colloidal quantum dots. From the anode there are holes which are transported via a hole transport layer (HTL) towards the colloidal quantum dots. Inside the quantum dots, the hole and electron form an exciton that can recombine under emission of a photon. The anode is chosen to be optically transparent, so that light can escape.*

escape the device. This is why in practice one of the electrodes is chosen to be optically transparent.

6.2.2 History of quantum-dot based light-emitting devices

We give here a short, non-exhaustive, historical outline of the development of quantum-dot based light-emitting devices (QD-LED). It was in 1994 that a similar idea as presented in Fig. 6.1 was used to create the first quantum-dot based light-emitting device [103]. For this, Colvin *et al.* used a CdSe colloidal quantum dot film of a few tens of nanometers. This layer of cQDs served both as ETL and emissive layer. For the transport of holes, they used an organic layer. A very important parameter for light-emitting diodes (LEDs) is the external quantum efficiency (EQE), which is defined as the number of photons that escape from the device per electron that passes through the device. The very first device of Colvin *et al.* had EQE = 0.01% and a turn-on voltage of 4 V [103]. This EQE was at that time three orders of magnitude smaller than the EQE that was reached for conventional p–n junction based LEDs: there, by texturing the surface in order to extract more light, EQE = 30% was reached in 1993 [104]. The next important improvement for QD-LEDs was by creating organically capped CdSe/CdS core-shell cQDs. This allowed to improve the EQE by a factor 22 to EQE = 0.22%, while keeping the same turn-on voltage of 4 V [105]. It was in 2002 that Coe *et al.* realized that by using a single monolayer of cQDs instead of a multilayer, the poor conduction through the multilayer cQDs could be avoided. They used an organic layer as an ETL, thereby increasing the performance of the device [106]. They reported an EQE of 0.52% and a 25-fold improvement in luminescent power efficiency which corresponds to the luminous intensity per unit of surface [106]. Three years later, it was realized that by placing the cQDs inside a GaN p–n junction, thereby creating an all in-organic device, the electrical injection of carriers could be improved [107]. However, the EQE of this system was only 0.01%. Another type of QD-LED was introduced soon after for which the ETL was an inorganic layer and the HTL an organic layer. QD Vision has worked on such kind of QD-LED and reported in 2012 an 18%-EQE QD-LED [108]; an EQE that was much higher than all previously published external quantum efficiencies [102]. Although there is a lot of progress for QD-LEDs, their EQE is still far behind the EQE of conventional LEDs for which there exist devices with EQE > 60%. In order to improve the EQE, attention was not uniquely drawn on optimizing the electrical injection of carriers anymore. It was understood that it is very important to optimize the optics of the device as well. Two challenges are for example to extract most of the emitted light from the device and to enhance the radiative recombination rate of excitons. It is only very recently that one introduced metals in the vicinity of the cQDs so that plasmonic modes are used to enhance the radiative decay rate [109–112].

6.3 Quantum-dot based metasurface light-emitting device

Recently, a new class of QD-LEDs has been introduced by the group of Degiron: quantum-dot based *metasurface* light-emitting devices (QD-MLED) [10, 11]. An example of such a device is shown in Fig. 6.2. We will introduce the idea behind the introduction of a metasurface and discuss qualitatively the experimental results obtained by Le-Van *et al.* The main objective of this chapter is to propose a model to describe electroluminescence

from QD-MLED devices where the quantum dots are densely packed. We believe that the model will be important for future design of QD-MLEDs.

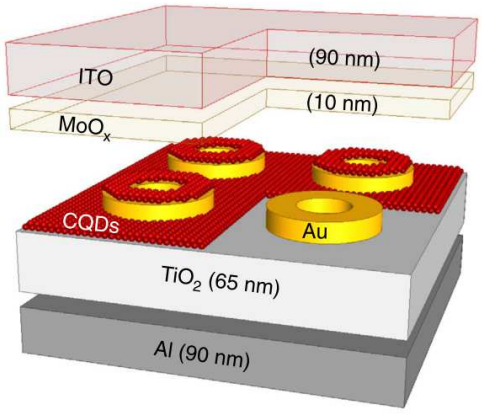

Figure 6.2: *Schematic view of the device used by Le-Van et al. in Ref. [11]. cQDs are densely packed and put close to metallic nanorings which form a periodic lattice. Courtesy of Quynh Le-Van.*

6.3.1 Introduction

The group of Degiron implemented a plasmonic metasurface inside a QD-LED, together forming a QD-MLED. The plasmonic metasurface consists of a subwavelength array of gold nanorings, see Fig. 6.2. Quantum dots have been placed in the near vicinity of the plasmonic metasurface. Each nanoring can be seen as a nanoantenna. Nanoantennas are typically used to make the bridge between the nanometer scale of the quantum dots and the much larger wavelength of the emitted light [113], thereby typically increasing the spontaneous emission rate of an emitter. Another property of an antenna is the ability of directing the emission pattern [113]. For the kind of nanorings that are studied by Le-Van *et al.*, it was theoretically shown that spontaneous emission enhancement as high as 60 can be expected, and also a higher directivity of the emission pattern [114]. The presence of nanoantennas in QD-LEDs can therefore improve the system from an optics point of view.

6.3.2 Experimental results

Le-Van *et al.* performed electroluminescence experiments on several devices. Here, we will show some experimental results that will motivate the study of electroluminescence from this kind of devices.

Figure 6.3(a) shows the EL intensity as a function of the applied voltage for three different devices. The presence of the gold nanorings reduces the turn-on voltage from 6 V to only 1.3 V. One mechanism behind the reduction of the turn-on voltage is the presence of a path of least resistance that facilitates the electrical injection [11]. This result of a reduction of the turn-on voltage is in itself very promising for QD-MLEDs as candidate in the market of light-emitting devices.

Figure 6.3(b) shows the electroluminescence signal that comes from the system where the cQDs touch the gold nanorings. It is seen that light only appears from the region where nanorings are present. The system presented in Fig. 6.3(c) contains a 5-nm-thick

dielectric spacer between the cQDs and the gold nanorings. For this configuration, it seems that the electroluminescence signal is not enhanced by the gold nanorings. The presence of a dielectric spacer of only 5 nm prevents electroluminescence to occur. This result is surprising, as one typically introduces a thin dielectric spacer in order to prevent for fluorescence quenching, i.e., nonradiative energy transfer from the emitter to the metal, thereby reducing the radiation efficiency of the quantum dots.

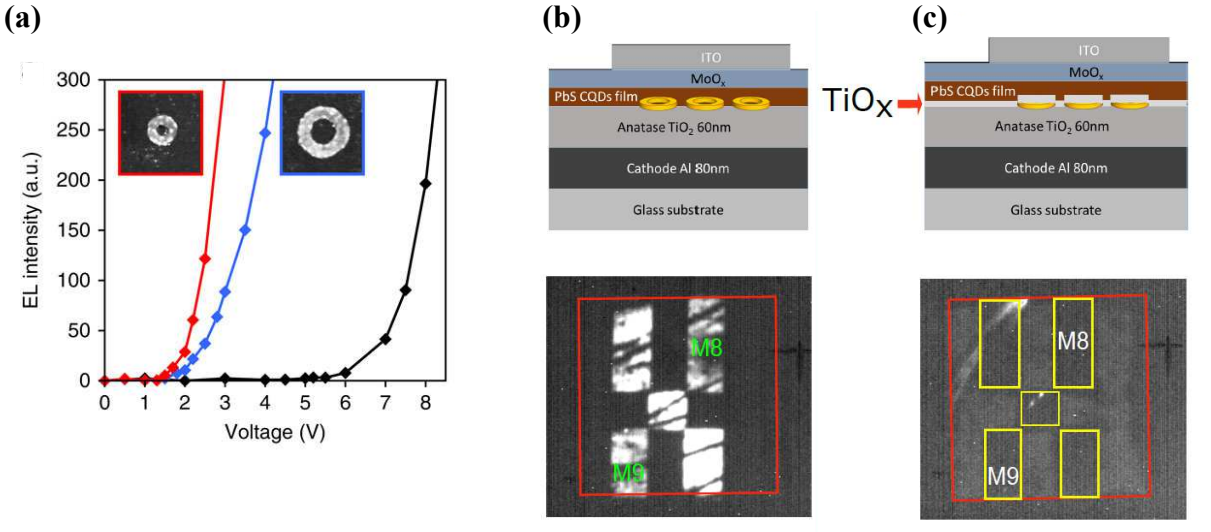

Figure 6.3: *(a) The EL intensity in arbitrary units is given as a function of the applied voltage for different devices. From left to right: "small" rings, "large rings", and no gold nanoantennas. The "small" and "large" rings have been visualized in the graph. The turn-on voltage goes down from 6 V to 1.3 V when gold nanorings are introduced. (b,c) A schematic view of experiments without (b) and with (c) a 5-nm-thick TiO_x spacer between the PbS cQDs and the nanorings are presented in the upper parts of Fig. 6.3(b) and Fig. 6.3(c). Below the electroluminescence signals are shown. The applied voltage was (b) 5 V and (c) 10.5 V. The yellow rectangles indicate the regions in which gold nanorings are present. In (c), no electroluminescence is observed from these regions. The differences between the patches and the symbols M8 and M9 are irrelevant for this thesis. Courtesy of Quynh Le-Van.*

6.3.3 Description of a dense ensemble of colloidal quantum dots

From the experimental results presented in Fig. 6.3(b,c), it follows that cQDs touching plasmonic nanoantennas is favorable for the electroluminescence signal. However, it is known that *individual* quantum emitters close to a metallic object containing a plasmonic resonance have a reduced radiation efficiency due to fluorescence quenching [115–121]. In order to prevent fluorescence quenching to take place, a spacer was introduced between the emitters and the metal in electroluminescence experiments [109–112]. Similar to them, Le-Van *et al.* did the same thing, but the experimental results show that enhanced electroluminescence is only visible in the absence of a dielectric spacer [10]. This result challenges a description of the ensemble of cQDs as a collection of individual entities. In this section, we theoretically study if the ensemble of cQDs should be considered as an ensemble of independent emitters or as an ensemble of collective modes. The latter

case has been thoroughly discussed for a dense cloud of cold atoms in Chapter 4. The answer to this problem will have an important consequence on the way electrolumince from QD-MLEDs should be modeled.

Quantum dots: are they independent or not? The question of whether quantum dots can be considered to be dependent or independent entities comes down to the question of the resonant dipole-dipole interactions between the cQDs being strong or not, i.e., is energy transfer between cQDs a faster process than the *radiative* decay?

To address this question, we show an SEM image of the PbS QD film used by Le-Van *et al.* is displayed in Fig. 6.4(a). It shows that the cQDs are almost touching each other. When emitters are so close to each other, nonradiative energy transfer can take place between an excited cQD and a cQD in its ground state. This process is called Förster resonance energy transfer (FRET). A schematic of a FRET process is given in Fig. 6.4(b). FRET takes place due to resonant dipole-dipole interactions. FRET being a pure near-field effect, the rate of the energy transfer scales as $\Gamma_{D\to A} \propto 1/r^6$, where D and A stand for donor and acceptor, respectively, and r is the inter-particle distance [12]. This transfer rate can be compared to the single particle spontaneous emission rate and it can be shown (Ref. [12]) that within the electric dipole approximation

$$\frac{\Gamma_{D\to A}}{\Gamma_r} = \left(\frac{r_0}{r}\right)^6 = \frac{1}{r^6} \times \frac{3c^4}{4\pi} \int_0^\infty \frac{f_D(\omega)\sigma_A(\omega)}{n^4(\omega)\omega^4} d\omega, \tag{6.1}$$

where c is the speed of light in vacuum, n is the refractive index of the host medium, r_0 is

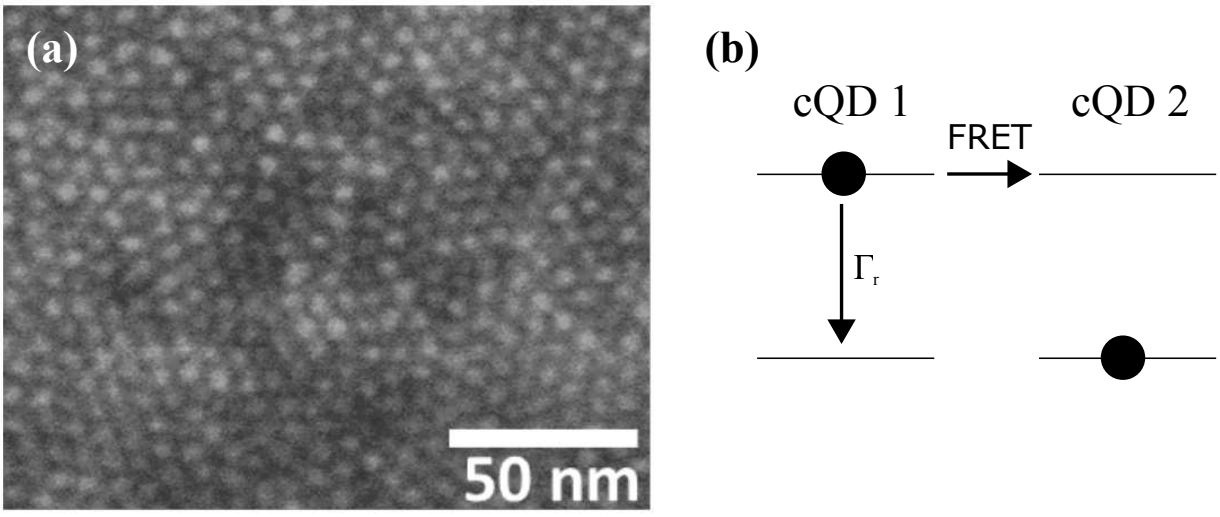

Figure 6.4: *(a) An SEM image of the PbS QD film that is used for the electroluminescence experiments of Le-Van. Courtesy of Quynh Le-Van. It is seen that the quantum dots are touching each other. (b) An exciton in cQD 1 can either decay radiatively within a time* $1/\Gamma_r$*, or nonradiatively be exchanged with cQD 2 by means of Förster resonance energy transfer (FRET) within a typical timescale* $1/\Gamma_{D\to A}$*, where D stands for donor and A for acceptor. The diameter of each quantum dot is 9 nm.*

the Förster radius, that can be calculated as follows:

$$r_0^6 = \frac{3c^4}{4\pi}\int_0^\infty \frac{f_D(\omega)\sigma_A(\omega)}{n^4(\omega)\omega^4}d\omega. \tag{6.2}$$

The variables σ_A and f_D stand respectively for: the absorption cross section of the acceptor and f_D for the normalized emission spectrum of the donor. The normalization of f_D is defined by

$$\int_0^\infty f_D(\omega)d\omega = 1. \tag{6.3}$$

The absorption cross section is related to the polarizabillity of the exciton by the equation

$$\sigma_A(\omega) = k\mathrm{Im}[\alpha_{\mathrm{exciton}}(\omega)], \tag{6.4}$$

where the exciton is modeled as a classical dipole:

$$\alpha_{\mathrm{exciton}}(\omega) = \frac{6\pi c^3\Gamma_{\mathrm{r}}}{\omega_0^2(\omega_0^2 - \omega^2 - i\omega(\Gamma_{\mathrm{r}} + \Gamma_{\mathrm{nr}} + \Gamma^*)}, \tag{6.5}$$

with ω_0 being the resonance frequency and Γ^* being the pure dephasing rate. From Eq. 6.4 and Eq. 6.5 it follows that the absorption cross section of the exciton is Lorentzian. In order to obtain $f_D(\omega)$, we have taken the same function as the absorption cross section, but with a different resonance frequency ω_0 and we normalized this function according to Eq. 6.3. Therefore, in our calculations we assume $f_D(\omega)$ to be Lorentzian as well.

We proceed to the calculation of the Förster radius of the PbS colloidal quantum dots in a homogeneous medium within the electric dipole approximation. For this, we assume the host medium to have an index $n = 1$. The full width at half maximum (FWHM) of the frequency spread due to inhomogeneous broadening is 160 meV ($\sim$ 180 nm) for the PbS cQDs studied by Le-Van *et al.* at room temperature [122]. Figure 6.5(a) shows the two absorption spectra together of two quantum dots for a situation where the quantum dots have resonance wavelengths $\lambda_1 = 1.11$ μm and $\lambda_2 = 1.29$ μm. The result of the calculation of the Förster radius r_0 is presented in Fig. 6.5(b), where $\Delta\lambda = \lambda_2 - \lambda_1$ and indicates the distance between the two resonant wavelengths which are symmetrically positioned around $\lambda = 1.2$ μm. The black (red) curve corresponds to the situation that QD 1 (2) is the acceptor and QD 2 (1) the donor. The black dashed lines correspond to the Förster radius for two cQDs that are spectrally separated by the FWHM of the inhomogeneous broadening, which is 180 nm. It is seen that the typical Förster radius is about 8–10 nm. Since the inter-particle distance dependence of FRET is inversely proportional to r^6, nonradiative energy transfer dominates radiative decay as soon as the inter-particle distance is smaller than the Förster radius.

Mork *et al.* have recently shown that the actual Förster radius of densely packed CdSe/CdZnS core-shell colloidal quantum dots is larger than the Förster radius that is predicted under the electric dipole approximation [123]. From experiments they derived that the CdSe/CdZnS quantum dots under study, having a resonance wavelength around 570 nm, show a Förster radius of 8–9 nm instead of the predicted 5–6 nm. In Ref. [123] it is reported that one of the possible reasons for the larger Förster radius is the presence of dipole–quadrupole interactions that are nonnegligible when the surface-to-surface distance is small compared to the center-to-center distance between cQDs. Similarly, Bose *et al.* have infered a Förster radius of 12–13 nm at room temperature for PbS colloidal quantum

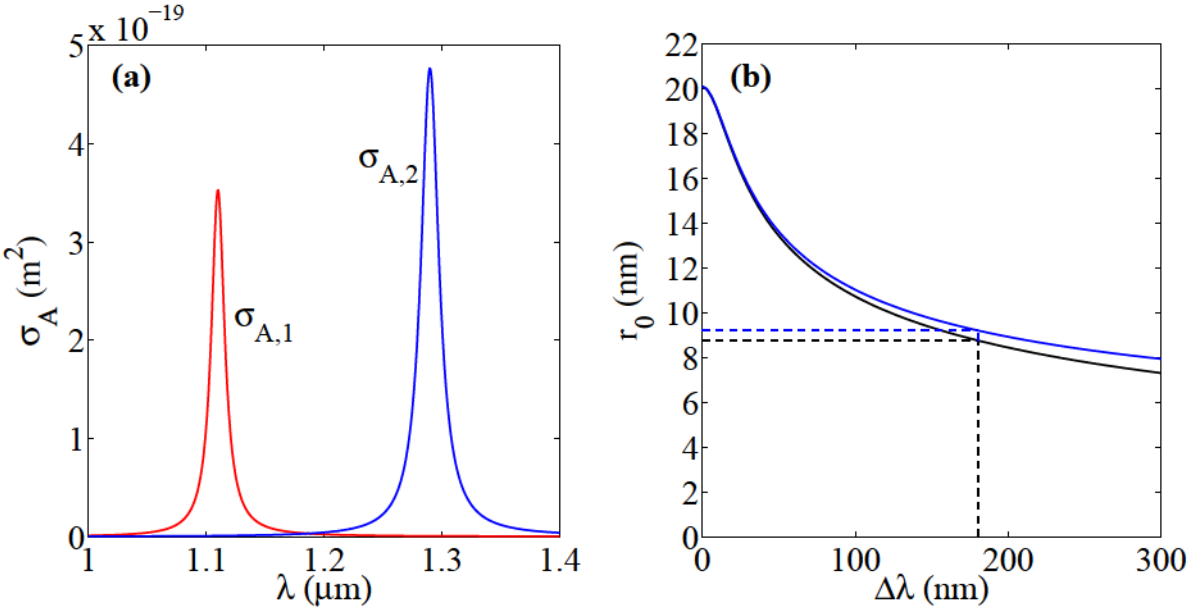

Figure 6.5: *(a) An example of two absorption spectra is given for two cQDs with* $\lambda_1 = 1.11$ *μm and* $\lambda_2 = 1.29$ *μm. (b) The calculated Förster radius within the electric dipole approximation is given as a function of the difference in resonance wavelength of two cQDs. The resonance wavelength of both cQDs is symmetrically positioned around* $\lambda = 1.2$ *μm. The black dashed lines indicate the situation* $\Delta\lambda = 180$ *nm.*

dots for an interdot separation distance of 10 nm [124]. We expect that the actual Förster radius of the dense film of PbS cQDs studied in the group of Degiron is also larger than the prediction by Förster's theory. This experimental fact, together with the observation that the cQDs touch each other[1], where the average interdot distance is ~ 10 nm, make the assumption reasonable that FRET is a faster process than spontaneous emission in densely packed ensembles of PbS cQDs. As the FRET rate is superior to the radiative decay rate, any energy excitation present in a given quantum dot is no longer localized in that quantum dot and must be considered delocalized over the ensemble of cQDs. In fact, we believe that due to FRET, in reality one excites collective modes of the system and not individual quantum dots. The PbS cQDs can therefore not be considered to be independent.

Quantum dots film: a homogeneous medium The fast interaction between quantum dots brings the system at *local thermodynamic equilibrium*, i.e., one can locally define intensive parameters like temperature and the electrochemical potential of the electrons and holes separately. The ensemble of excited states inside this system that is at local thermodynamic equilibrium can therefore be described by a single conduction band, which width is determined by the inhomogeneous linewidth of the ensemble of quantum dots. Instead of modeling the quantum dots as individual quantities, we model the thin film as a homogeneous medium. This homogeneous medium has an effective refractive index. The film of quantum dots is therefore treated similar as a bulk semiconductor. As we have seen from Chapter 4, we know that a model of the ensemble of quantum dots as an effective medium takes automatically into account the potential presence of polaritonic modes.

[1]Each quantum dot has a 2-nm-thick ligand layer surrounding it, which makes that the least interdot distance is 4 nm.

6.4 Electroluminescence model for a LED

We have suggested that the ensemble of cQDs can be modeled as a bulk semiconductor. The standard model of electroluminescence by a semiconductor at *thermodynamic equilibrium* predicts that the emitted power of a LED scales exponentially with the applied voltage. This model is based on a modified theory of *thermal radiation*. We will describe the model used to calculate the emitted power of a LED and emphasize the hypotheses that are done and are not valid for QD-MLEDs. It is in the next section that this discussion will allow us to generalize the LED model to QD-MLEDs.

The emitted power of a LED is calculated by a model that is derived from Kirchhoff's law. This law, which was published in 1860 by Kirchhoff, states that any material at *thermodynamic equilibrium*, absorbs as much of energy as it emits:

$$I_e(\omega, T) = \varepsilon(\omega, T) I_{\mathrm{BB}}(\omega, T), \tag{6.6}$$
$$I_a(\omega, T) = \alpha(\omega, T) I_{\mathrm{BB}}(\omega, T), \tag{6.7}$$

where I_e=I_a, and where both I_e and I_a have units $\mathrm{W{\cdot}m^{-2}{\cdot}Hz^{-1}{\cdot}sr^{-1}}$. From this it follows that the emissivity ε and absorptivity α are the same: $\varepsilon = \alpha$. They are both unitless and cannot exceed 1. The spectral irradiance of a black body follows from Planck's law[2]:

$$I_{\mathrm{BB}}(\omega, T) = \frac{\omega^2}{4\pi^2 c^2} \frac{\hbar\omega}{\exp[\hbar\omega/(k_B T) - 1]}. \tag{6.8}$$

Kirchhoff's law applies to thermal radiation. This law was generalized to electroluminescence from semiconductor materials, electroluminescence being an example of nonthermal radiation, by Shockley *et al.* in 1961 [126]. In order to do so, Planck's law needs to be modified under the introduction of an electrochemical potential in Planck's function [127]. For a LED, this generalization of Planck's law reads

$$I_{\mathrm{BB}}(\omega, T) = \frac{\omega^2}{4\pi^2 c^2} \frac{\hbar\omega}{\exp[\hbar\omega/(k_B T)] - 1} \mapsto \frac{\omega^2}{4\pi^2 c^2} \frac{\hbar\omega}{\exp[(\hbar\omega - e\phi)/(k_B T)] - 1}, \tag{6.9}$$

where $e = |q|$, where q is the charge of an electron, and ϕ is the voltage. When we assume the voltage drop in the center of the LED to be smaller than the gap energy of the LED, and $\exp[(\hbar\omega - e\phi)/(k_B T)] \gg 1$, we can simplify the generalized Kirchhoff's law:

$$I_e(\omega, T, \phi) = \alpha(\omega) I_{\mathrm{BB}}(\omega, T) \exp[e\phi/(k_B T)]. \tag{6.10}$$

[2]For historical reasons, we note that Kirchhoff's law can be written in a similar notation as was introduced by Kirchhoff [125]: $I_e(\omega, T)/\alpha(\omega) = I_{\mathrm{BB}}(\omega, T)$. As an interesting side note to put Kirchhoff's discovery in historical context, let us mention that when Kirchhoff published his seminal work on the relationship between emission and absorption in 1860, Planck's function was not known yet, but Kirchhoff knew it should be independent of the properties of the object and only depend on the wavelength and temperature [125]. He wrote: "Es ist eine Aufgabe von hoher Wichtigkeit, diese Function zu finden", which means "It is of very high importance to find this function". He continued: "Trotzdem scheint die Hoffnung gegründet, sie durch Versuche ermitteln zu können, da sie unzweifelhaft von einfacher Form ist, wie alle Functionen es sind, die nicht von den Eigenschaften einzelner Körper abhängen, und die man bisher kennen gelernt hat", which can be translated by "Nevertheless, it appears that there is foundation for the hope, that it can be determined by research, as it is undoubtedly of a simple form, like all functions, that are not dependent of the characteristics of a single body, and which are known sofar". Kirchhoff was right and it was Max Planck who correctly described black-body radiation in 1901 by quantizing radiation. Planck's law was the birth of quantum mechanics.

We recover the exponential dependence of the emitted power from a LED on the applied voltage. It is observed that the electroluminescence spectrum is the same as that of a thermal source composed of the same materials. However, the intensity increases exponentially with the applied voltage. The physical origin lies in the fact that by applying a voltage the number of electrons in the conduction band increases, thereby also increasing the number of holes in the valence band. The consequence of this is that the electrochemical potential of electrons in the conduction band and holes in the valence band are not the same anymore. The system is out of equilibrium and the increased number of electron-hole pairs makes the system radiating more. Since at room temperature $k_B T = 26$ meV, a change of voltage across the p–n junction will drastically change the emitted power. We anticipate that this effect explains the observation of electroluminescence from the sample without a dielectric spacer between the cQDs and gold, see Fig. 6.3(b,c). From an electrical perspective, the cQDs, spacer and gold form a series circuit. An additional spacer will reduce the voltage drop across the cQDs film, because of the "voltage divider" property of a series circuit.

6.5 Electroluminescence model in the presence of nanoantennas

For a p–n junction LED, both the absorptivity and electrochemical potentials are uniform in the light-emitting region. Therefore, the generalized Kirchhoff's law as given in Eq. 6.10 models electroluminescence correctly. However in QD-MLEDs, the colloidal quantum dots are put in both a non-uniform electromagnetic environment and a non-uniform electrical environment, due to the presence of plasmonic nanoantennas. The non-uniform electromagnetic environment of the cQDs is expected to make light absorption not uniform inside the cQD film and the non-uniform electrical environment is expected to give rise to a non-uniform electrochemical potential.

Non-uniform light absorption To illustrate the nonuniform light absorption, we have calculated the electric field distribution close to the metallic nanoring for an x-polarized (horizontally polarized) incident plane wave. The in-house numerical code has been developed by Jean-Paul Hugonin at the Institut d'Optique. The method was first introduced by Bonod *et al.* [128]. The electric field is calculated by means of a modal method for which the electric field is written in the Fourier-Bessel basis, respecting in this way the cylindrical symmetry of the problem. The angular dependence of the electric field is written in the Fourier basis and the radial dependence is expanded in Bessel functions. Figure 6.6(b) shows the real part of the z component of the electric field, which originates from diffraction of light by the nanostructure. The contours of the different materials that are displayed in Fig. 6.6(a) are drawn by dashed lines. Note that the scales of Fig. 6.6(a) and Fig. 6.6(b) are the same. It is observed in Fig. 6.6(b) that the z component of the electric field is the strongest above and below the metallic nanoring. Therefore, the quantum dots that are positioned above the gold nanorings have the highest absorption cross section for a plane wave that is incident from above. Quantum dots that are positioned in the inside of the nanoring or outside the nanoring have a smaller absorption cross section for the same incident plane wave. From this calculation, we conclude that the absorptivity of a QD-MLED system is not uniform and the standard theory of electroluminescence from conventional LEDs is therefore not valid for this kind of systems.

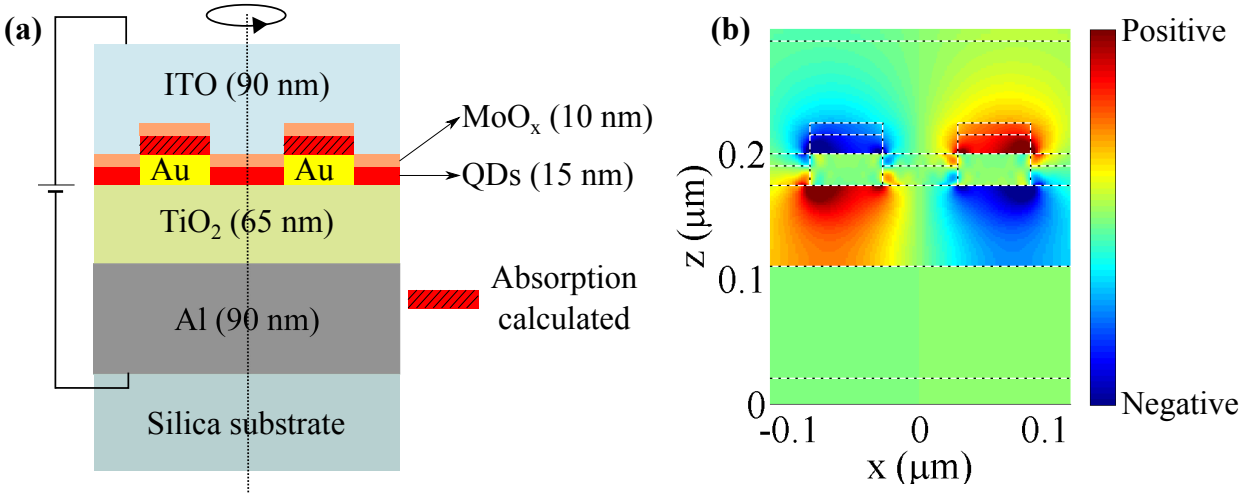

Figure 6.6: *(a) Schematic of a single gold nanoring embedded in a QD-MLED system. The stripes indicate where the absorption has been calculated. The dashed line corresponds to the symmetry axis of the cylindrically symmetric system. (b) Map of the real part of E_z for a linearly polarized plane wave incident along the z axis from above ($\lambda = 1.2$ μm). Color scale from blue to red: negative to positive values. The contours are indicated by the dashed lines. Compare the structure with the structure given in (a). It is observed that the QDs above gold absorb most of the incident light.*

Non-uniform electrochemical potential Because of the non-uniform electrical environment, the electrochemical potential is expected to change locally. This difference lies in the fact that the voltage drop ϕ is not uniform in the cQDs layer. A voltage is applied across ITO and aluminium, as indicated in Fig. 6.6(a). We consider the multilayer as a series circuit. As gold is a good electrical conductor, the local current density is higher in the region vertical to the gold nanoring. Because the current density close to gold is higher than outside the gold region, the voltage drop at the level of the quantum dots above the gold nanorings is higher than for the once that are placed outside the nanoring region.

Since both the absorptivity (optics) and the voltage drop (electronics) is the highest for the cQDs right above the gold nanorings, and according to Eq. 6.10 both are relevant for the electroluminescence signal, it is expected that most of the electroluminescence signal comes from the region above gold. This is confirmed by Fig. 6.3(b) which shows that electroluminescence signal comes only from the regions with gold nanorings.

6.5.1 Generalized model for QD-MLED-based electroluminescence experiments

After having discussed electroluminescence from conventional LEDs, we propose a model for electroluminescence from QD-MLEDs. Very recently, it has been shown by Greffet *et al.* that Kirchhoff's law can be generalized to a system that is at local thermodynamic equilibrium [129–131]. We have seen in Section 6.3.3 that due to the near-field interactions between the cQDs, our system is at thermodynamic equilibrium: we can define locally the absorptivity and the electrochemical potential. Hence, we can use the extension of Kirchhoff's law. In Ref. [129], the authors have shown that in order to calculate the total

emitted power P_e under the application of a voltage, the absorbed power needs to be calculated locally at the position $\mathbf{r}'$ for a plane wave incident along the direction $\mathbf{u}$ and with angular frequency ω:

$$P_e^{(l)} = \int_0^\infty d\omega \int_{V_{obj}} \int_{4\pi} \alpha^{(l)}(\mathbf{u}, \mathbf{r}', \omega) \exp\left[\frac{e\phi(\mathbf{r}')}{k_B T(\mathbf{r}')}\right] \frac{I_{BB}[\omega, T(\mathbf{r}')]}{2} d^3\mathbf{r}' d\Omega, \tag{6.11}$$

where

$$\sigma_{abs}^{(l)}(\mathbf{u}, \omega) = \int_{V_{obj}} \alpha^{(l)}(\mathbf{u}, \mathbf{r}', \omega) d^3\mathbf{r}', \tag{6.12}$$

so that $\alpha(\mathbf{u}, \mathbf{r}', \omega)$ can be considered an absorption cross section density; not to be confused with the absorptivity as introduced in Section 6.3, V_{obj} is the volume of the object that radiates, and l indicates the polarization. Since there are two polarizations possible, the black-body spectral irradiance has been divided by two. It is important to highlight that the local absorption is represented by the absorption cross section density α. Electroluminescence originates predominantly from the excitons inside the layer of cQDs, which limits the spatial extent of the volume integral V_{obj} to the cQD film only. In QD-MLEDs at room temperature, we can assume that all parts of the sample are at the same temperature. Since the cQD film is very thin, we can assume the voltage to be constant inside the film, so that after the volume integral we end up with

$$P_e^{(l)} = \exp\left[\frac{e\phi}{k_B T}\right] \int_0^\infty d\omega \int_{4\pi} \sigma_{abs}^{(l)}(\mathbf{u}, \omega) \frac{I_{BB}[\omega, T]}{2} d\Omega, \tag{6.13}$$

for which it is important to remind that ϕ is the voltage drop at the level of the cQDs, which is not equal to the applied voltage. In order to calculate the absorption cross section of the quantum dots that are inside the region indicated by the stripes in Fig. 6.6(a) (as explained before, electroluminescence originates from this region), we calculate the electric field inside the structure for an incident plane wave along the $\mathbf{u}$ direction. The reason the electric field is needed is because the absorbed power can be calculated from it according to

$$P_{abs}(\omega) = \frac{1}{2} \int \mathrm{Im}[\varepsilon(\omega)] |\mathbf{E}(\mathbf{r})|^2 d^3\mathbf{r}. \tag{6.14}$$

From the absorbed power, we can derive the absorption cross section by means of the following definition of the absorption cross section:

$$P_{abs}(\omega) = \sigma_{abs}(\mathbf{u}, \omega) \frac{c\varepsilon_0 |\mathbf{E}_{inc}|^2}{2}. \tag{6.15}$$

With this generalization of Kirchhoff's law, we have a model that allows to calculate the electroluminescence signal of systems as the one presented by Le-Van *et al.* in Ref. [11].

6.5.2 Effective refractive index calculation

From now on, we will present numerical results of calculations that are based on the system that is schematically presented in Fig. 6.6. To do so, we need to explain how we calculated the absorption cross section. The layer of cQDs is optically modeled by an effective refractive index, according to the results presented in Section 6.3.3. In this section we discuss how to calculate the effective refractive index.

Lorentz-Lorenz formula One model to calculate the effective refractive index is the Lorentz-Lorenz formula. As we have seen in Chapter 2, we need to verify the validity of this formula for our system, since we will calculate resonant light absorption by a dense ensemble of resonant scatterers. We know from Eq. 2.25 that in order to have a break down of the Lorentz-Lorenz formula for inhomogeneously broadened system, the system needs to satisfy the condition

$$C = \frac{9\pi}{8}\frac{\rho}{k^3}\left(\frac{\Gamma_r}{\Delta\omega}\right)^2 > 1. \tag{6.16}$$

In the particular case of the system of Le-Van, one can show that $C = \frac{9\pi}{8}\frac{\rho}{k^3}\left(\frac{\Gamma_r}{\Delta\omega}\right)^2 \sim 10^{-10}$, by using the parameters: $\hbar\Delta\omega = 160$ meV, $\tau_r = 2\pi/\Gamma_r = 0.5$ μs, $\rho = 10^{18}$ QDs/cm^3, and $\lambda = 2\pi/k = 1.2$ μm. As $C \ll 1$, the Lorentz-Lorenz formula is expected to be valid; recurrent scattering is not an important process due to the very strong inhomogeneous broadening present in this system.

Lorentz-Lorenz formula for a core-shell quantum dot Each quantum dot of Le-Van is modeled as a core-shell particle with inner radius b and outer radius a. The core is made of PbS with dielectric constant $\varepsilon_{\rm c}$ and the shell is a ligand with dielectric constant $\varepsilon_{\rm s}$. The quantum dots are embedded in a host medium with dielectric constant $\varepsilon_{\rm h}$. We decompose the total polarizability $\alpha(\omega)$ of a quantum dot in a core-shell part and an exciton part, according to $\alpha(\omega) = \alpha_{\text{core-shell}}(\omega) + \alpha_{\text{exciton}}(\omega)$, which is based on the fact that the dipole moment and the incident electric field are linearly related: $\mathbf{p} = \varepsilon\alpha(\omega)\mathbf{E}$. By taking into account the inhomogeneous broadening for the excitonic part, the Lorentz-Lorenz formula becomes:

$$\frac{\varepsilon_{\rm LL}(\omega) - \varepsilon_{\rm h}}{\varepsilon_{\rm LL}(\omega) + 2\varepsilon_{\rm h}} = \frac{1}{3}\int \rho(\omega')\alpha_{\text{exciton}}(\omega;\omega')d\omega' + \frac{\rho_0\alpha_{\text{core-shell}}(\omega)}{3}, \tag{6.17}$$

where ρ_0 is the homogeneous cQD density. The inhomogeneous broadening $\rho(\omega')$ is assumed to follow a Gaussian distribution, and $\int_0^\infty \rho(\omega')d\omega' = \rho_0$. The polarizability of the exciton is given by

$$\alpha_{\text{exciton}}(\omega;\omega') = \frac{6\pi c^3\Gamma_{\rm r}}{\omega'^2(\omega'^2 - \omega^2 - i\omega(\Gamma_{\rm r} + \Gamma_{\rm nr} + \Gamma^*)}, \tag{6.18}$$

and the polarizability of the core-shell is given by [132]

$$\alpha_{\text{core-shell}}(\omega) = 4\pi a^3\frac{a^3(\varepsilon_c + 2\varepsilon_s)(\varepsilon_s - \varepsilon_h) + b^3(\varepsilon_c - \varepsilon_s)(2\varepsilon_s + \varepsilon_h)}{2b^3(\varepsilon_c - \varepsilon_s)(\varepsilon_s - \varepsilon_h) + a^3(\varepsilon_c + 2\varepsilon_s)(\varepsilon_s + 2\varepsilon_h)}. \tag{6.19}$$

For the parameters of the Gaussian distribution of resonance frequencies, we have taken the central wavelength $\lambda_{\text{central}} = 1.2$ μm, and a FWHM inhomogeneous broadening of 160 meV ($\sim$ 180 nm). The other parameters are taken as follows: $\Gamma_{\rm r} = \frac{2\pi}{0.5\ \mu\text{s}}$, $\Gamma^* = \frac{2\pi}{300\ \text{fs}}$ (which corresponds to 16 nm), $a = 4.3$ nm, and $b = 2.3$ nm. For a cQD density $\rho = 1 \times 10^{20}$ cQDs/cm^3, we have found the dielectric constant that is shown in Fig. 6.7 which shows in a semilog scale both the real (red dashed curve) and imaginary (blue solid curve) part of the dielectric constant of the cQD film. We assume PbS to be lossless itself, so that the absorption that is calculated uniquely originates from the absorption by the excitons. We only want to know the absorption by the exciton, since we are only interested in emission from the excitons. It is due to reciprocity that both quantities are related. The Lorentz-Lorenz formula is hereafter used in order to calculate the absorption cross section of the excitons above the gold nanoring.

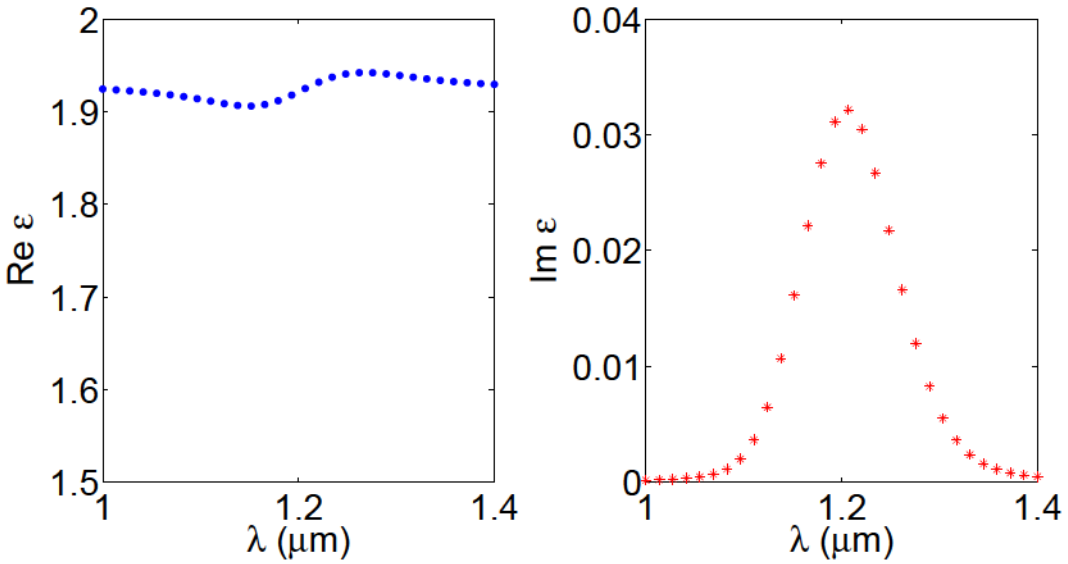

Figure 6.7: *The dielectric constant of a layer with* $\rho = 1 \times 10^{20}$ *cQDs/cm*^{3}. *(a) The real part of the dielectric constant. (b) The imaginary part of the dielectric constant. The imaginary part contains the excitonic contribution only.*

6.6 Application of electroluminescence model to experiments

In this section we present results from numerical calculations on two different systems that were studied in the group of Degiron.

6.6.1 Electroluminescence enhancement by nanorings

We present the numerical calculations on the enhancement of the absorption cross section from an ensemble of PbS CQDs in the near vicinity of a gold nanoring as presented in Fig. 6.3(b) and Fig. 6.3(c). We consider both systems *with* and *without* a 5-nm-thick layer of TiO_x. Figure 6.8 shows the absorption enhancement as a function of the wavelength, where the red dots correspond to the situation where the cQDs touched the gold nanorings and the blue stars to the situation with a 5-nm-thick spacer. It is observed from the red dots that absorption gets enhanced up to a factor 50 when the cQDs touch gold. Enhanced absorption is attributed to the local electric field enhancement that was shown in Fig. 6.6(b). The presence of a 5-nm-thick spacer reduces the calculated absorption enhancement by about 25%. Figure 6.3(b) and Fig. 6.3(c) show images of the electroluminescence signal for the system with and without a 5-nm-thick spacer. From Fig. 6.3(b) and Fig. 6.3(c) it seems reasonable to say that the reduction of electroluminescence signal is more than 25%.

From Fig. 6.8 we have observed that the presence of TiO_x spacer has an effect on the electroluminescence signal, but only weakly. As opposed to this numerical observation, electroluminescence seems to be strongly amplified in Fig. 6.3(b) as compared to Fig. 6.3(c), although no quantitative comparison can be done. We believe therefore that the observation of a big enhancement of the electroluminescence signal in the experiment without the spacer is mainly due to a higher electrical voltage drop across the cQD film in the absence of the spacer.

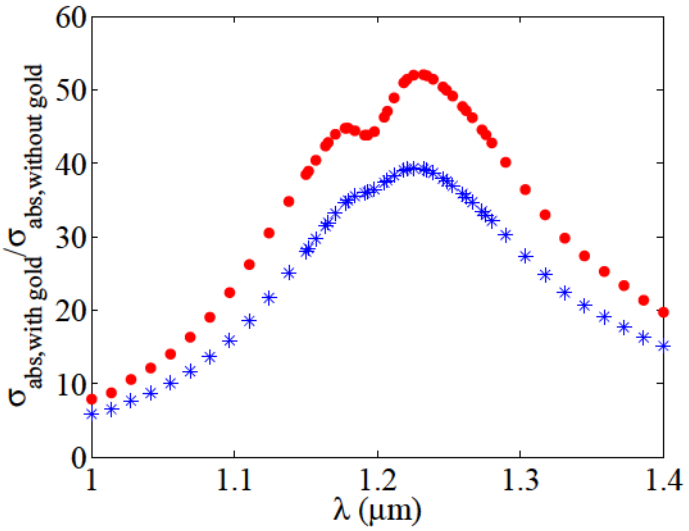

Figure 6.8: *For a normal incidence plane wave, the electroluminescence enhancement due to the presence of gold nanorings has been calculated for different wavelengths. The red dots correspond to the situation where the cQDs touch the gold nanorings. The electroluminescence enhancement can reach values up to 50. The blue stars correspond to the situation presented in Fig. 6.3(c), where a layer of 5 nm TiO_x is put between the cQDs and the nanorings. The electroluminescence enhancement drops slightly.*

6.6.2 Polarized electroluminescence

In this section we will study some experiments that have been conducted by Le-Van *et al.* for which the gold nanorings were replaced by gold nanorods that have dimensions $150 \times 70 \times 70$ nm^3. Nanorods break the cylindrical symmetry and therefore create a polarization dependence of electroluminescence, as was presented in Ref. [11]. The inset of Fig. 6.9(a) shows the periodic array of nanorods and the main panel shows the experimental results. The electroluminescence intensity has been shown for two different polarizations of light. The highest electroluminescence intensity comes from light which is polarized along the long axis of the nanorods. The plasmonic resonance being strongly anisotropic, the electroluminescence signal for light polarized along the short axis is much smaller. The experimental data has some rapid fluctuations around the maximum electroluminescence intensity. Since water vapor has an absorption band around $\lambda = 1.38$ μm, it is likely that the noise in the spectrum is due to the presence of water molecules in the environment where the atoms are placed.

Similar as before, we calculate the absorption by the excitons, but this time for two different polarizations of the incident plane wave. We only consider a single unit cell of the plasmonic metasurface. In order to calculate the electric field inside the structure, an aperiodic-Fourier modal method is used. There are at least two different ways to isolate each cell optically. The isolation can either be done by for example putting perfectly matched layers (PML) at the borders of the cells, or by using complex coordinate transformations at the borders of each cell [86]. It is the latter that is used in this work.

Figure 6.9(b) shows the calculated absorption cross section for two incident polarizations (orange solid curve: parallel to long axis of nanorod, and black dashed curve: perpendicular to long axis of nanorod). From the numerical calculation we can observe that the absorption

cross section is polarization dependent. Based on this result we can infer that light emission is polarization dependent, as was observed experimentally by Le-Van *et al.* [11].

At the end we should mention that a formal validation of the used model is not possible for time reasons. It would be very interesting in the future to do a systematic study where the proposed model for electroluminescence in the presence of nanoantennas can be verified.

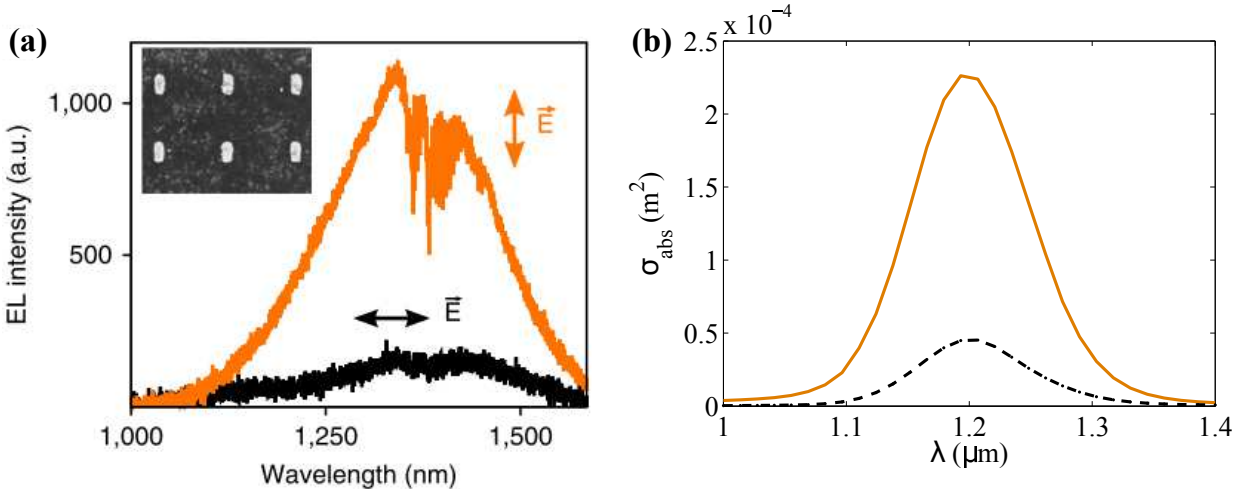

Figure 6.9: *(a) The experimental electroluminescence results are presented for both light polarizations as a function of the wavelength for a setup with nanorods. Light polarized along the long axis of the nanorods gives more electroluminescence signal than light polarized along the short axis. Courtesy of Quynh Le-Van. (b) Numerical results of the calculation of the absorption cross section for quantum dots on top of a single nanorod with dimensions* $170 \times 50 \times 50$ nm^3.

6.7 Conclusion

Based on what we have discussed in this chapter, we believe that densely-packed PbS cQDs in the near vicinity of metallic nanostructures cannot be modeled as independent entities. Due to strong near-field interactions, any excitation of the system would be delocalized throughout the cQD film. Instead of studying electroluminescence by considering the cQDs as being independent, we believe that the ensemble forms a homogeneous system that consists of electronic bands, like a bulk semiconductor does. Therefore, the cQD film is optically described by an effective refractive index. Electroluminescence from a cQD film close to a plasmonic nanostructure does however not occur in the same way as it does for a conventional p–n junction LED. The origin of this lies in the fact that the electron-hole pair density is not uniform throughout the cQD film and also light emission does not occur homogeneously due to the presence of the gold nanostructure. We have therefore proposed to model electroluminescence from this kind of systems by means of the generalized Kirchhoff that has recently been reported in Ref. [129]. We have seen that the model qualitatively succeeds in modeling electroluminescence from the QD-MLEDs, but a more quantitative study needs to be done in order to check the validity of the proposed generalized Kirchhoff law.

We have also studied collective effects in electroluminescence. By modeling the cQD layer as an effective medium, we did not observe enhanced absorption by the film, since the absorption increases linearly with the cQD density. From the generalized Kirchhoff law we can conclude that the electroluminescence signal is therefore linearly dependent on the cQD density.

Chapter 7

Conclusion and outlook

In this Ph.D. thesis we have studied theoretically light scattering and light emission by dense ensembles of resonant dipoles. The majority of this manuscript concerns light scattering from dense clouds of cold atoms. In the last chapter, Chapter 6, we studied electroluminescence from a dense film of colloidal quantum dots placed in the near vicinity of a plasmonic metamaterial.

Chapter 2

We have shown that in the weak-excitation regime, i.e., the incident intensity is so low that at most one atom is excited, classical and quantum models of light scattering lead to the same set of coupled-dipole equations. This set of coupled-dipole equations describes the resonant dipole-dipole interactions between the dipoles. Since both models are equivalent in the regime we are interested in, which is the regime that is relevant for the experiments conducted in the group of Browaeys, we studied light scattering from a dense cloud of cold atoms classically.

In this chapter we have tried to make a link between the terminology used by various communities. Finally, we studied the relationship between evanescent waves and virtual photons. It follows that an evanescent wave is built up of many virtual photons.

Chapter 3

When the number of scatterers in a dilute gas increases, the amount of scattered light increases accordingly. However, recently it has experimentally been observed that the incoherent power scattered orthogonally to the incident beam from a dense, wavelength-size cloud of cold atoms does not increase linearly with the number of atoms [51]. We attribute the observation of this suppression to strong resonant dipole-dipole interactions between the atoms. Because of the strong resonant dipole-dipole interactions, the cloud also partially diffracts light in the forward direction. We understood that Pellegrino *et al.* were studying incoherent light scattering [51]. In order to study coherent scattering, we also stuied light scattering in the forward direction. Theoretically and experimentally obtained spectra do not agree. The precise nature of this disagreement is not fully understood yet. The combined experimental and theoretical work of coherent scattering, where the experimental results were compared to results from the coupled-dipole equations, has recently been published by Jennewein *et al.* in the journal Physical Review Letters [7].

Chapter 4

We have shown that strong resonant dipole-dipole interactions in a wavelength-size cloud

of cold atoms give rise to the onset of collective modes that are extended throughout the cloud. These modes, which are superradiant and therefore couple very efficiently to light, are sensitive to the shape of the object and to the atomic density distribution; not to the precise position of the atoms. As these modes are similar to polaritons that were introduced by Hopfield to analyze collective excitations in ordered condensed matter systems, we call the superradiant modes that are extended throughout the sample polaritonic modes.

We have numerically retrieved the effective refractive index, which does not follow Lorentz-Lorenz theory due to the strong resonant dipole-dipole interactions. The spectrum of the effective refractive index allowed us to calculate the modes of the macroscopic Maxwell equations for an object with the same shape as the atomic cloud and an effective refractive index. It turns out that the modes of the macroscopic Maxwell equations are identical to the polaritonic modes found in the atomic cloud. Similar to the importance of the modes of a homogeneous object on light diffraction, the few polaritonic modes that exist have a significant impact on coherent light scattering by the atomic cloud. The fact that polaritonic modes are important for light scattering illustrates that we cannot consider the atoms in a dense, wavelength-size cloud of cold atoms as being independent entities: we need to consider the atomic cloud as being an ensemble of collective eigenmodes.

This work on polaritonic modes in a dense cloud of cold atoms has been published in the journal Physical Review A [67].

Chapter 5

The coherent response of the atomic cloud is determined by its refractive index, which naturally takes the polaritonic modes from microscopic theory into account. However, there are many other modes present in the atomic cloud that are not necessarily taken into account by the refractive index. The question whether the optical response is *uniquely* determined by the index of refraction, belongs to a homogenization problem. We have shown that the amount of incoherent light scattering is comparable to the amount of coherent light scattering for a dense, wavelength-size cloud. This observation has shown that the criterion for homogenization which is based on an inter-atomic distance that should be small as compared to the wavelength is invalid. This brings us to revision homogenization in resonant atomic systems. Strikingly, we have numerically shown that a resonant random medium cannot reach the homogenization regime. We show that as is the case of light scattering from non-resonant systems, the presence of nonradiative losses and pure dephasing are effective means to arrive at a homogeneous medium.

Furthermore, we have demonstrated by means of a collective mode point of view that a subwavelength-size cloud of resonant atoms always scatters less light than a single atom due to collective modes that are spectrally separated. The Dicke regime for the observation of superradiance: a subwavelength-size cloud, is shown to be the condition for nonobservation of single-photon superradiance effects.

Chapter 6

In this chapter we studied the emission of light by a dense ensemble of quantum dots. The dense film of colloidal quantum dots (cQDs) was placed in near vicinity of a plasmonic metasurface and emitted light under the application of a voltage (electroluminescence). The theoretical study is based upon experimental research conducted in the team of Aloyse Degiron at Institut d'Électronique Fondamentale [11]. In Chapter 6 we propose a model to understand the physics of electroluminescence from a dense film of colloidal quantum dots in the near vicinity of metallic metasurfaces. We propose a model for electroluminescence

from this kind of system that is based upon a generalized model for light emission from a p–n junction LED. The model of a conventional LED has been adapted to systems where the emission of light is strongly position dependent. This is done by invoking the generalized Kirchhoff law of thermal radiation that was introduced in Ref. [129].

Outlook

Superradiant pulse in strongly interacting atomic system

In 1968, Ernst and Stehle have theoretically shown that light emission from an ensemble of excited atoms is characterized by the emission of a superradiant pulse [133]. The pulse duration $\Delta t \propto 1/(N\Gamma)$, where N is the number of atoms and Γ is the single-atom spontaneous emission rate [6, 133, 134]. This conclusion follows from a model where the atoms do not interact with each other. However, we have understood that a dense cloud of cold atoms, in which resonant dipole-dipole are very strong, needs to be studied from a collective modes point of view. It would be interesting to study both theoretically and experimentally how the emergence of collective modes modifies the superradiant pulse formation for an initally fully inverted dense cloud of cold atoms.

Observing superradiance from ordered ensemble of Rydberg atoms

No superradiance is expected from *disordered and subwavelength-size* atomic clouds, as we have seen in Chapter 5 and as it was proposed with a different point of view by Gross and Haroche [6]. From a modal perspective, we drew the conclusion that superradiance could be expected for ordered systems, like regularly placed atoms on a subwavelength circle. The geometrical constraint being strong for optical transitions, this constraint would be strongly relaxed by using Rydberg atoms that have transitions in the microwave regime. With the ability of positioning individual Rydberg atoms by means of optical microtraps, it is now experimentally possible to study superradiance from regularly placed atoms on a subwavelength-size circle [135].

Validation of proposed generalized electroluminescence model

We propose a model for electroluminescence experiments that are based on a dense ensemble of quantum dots in the near vicinity of a plasmonic metasurface. The study presented in this work stays very qualitative. It would be interesting to quantitatively compare the electroluminescence signal as a function of the wavelength, in order to validate the proposed model.

Appendices

Appendix A

Quantization of evanescent waves in absorbing media

We present the quantization of evanescent waves in absorbing media. The goal of this chapter is to formally show the correspondance between evanescent waves and virtual photons.

Evanescent waves exist in several situations. A few of them are: (1) a point source with evanescent waves surrounding it, (2) an incident wave incident beyond the critical angle at an interface between two dielectrics, and (3) fluctuations in current densities in lossy media. We have tried to quantize the evanescent field for situation (1), but we did not succeed as the electric field has a singularity at the position of the source, by which the electric field contains an infinite amount of energy. The second situation is the situation that has been considered by Carniglia and Mandel [33]. The inconvenience of this situation is that one cannot describe the evanescent wave independently of the incident and reflected fields. Here, we consider the quantization of evanescent waves in a lossy dielectric.

Quantization of electromagnetic modes in free space can be found in many textbooks, like Refs [13, 136]. In free space, one typically quantizes plane waves. Something that is less known is the quantization of evanescent waves. Let us discuss what has been done on this topic in the past.

In 1971, Carniglia and Mandel published the work "Quantization of evanescent electromagnetic waves" [33]. In their work, they considered a single interface between two dielectric materials. When an incident field is incident with an angle beyond the critical angle, there is reflection of light and an evanescent tail in the other dielectric. The triplets of incident, reflected and transmitted waves form orthogonal modes and it is these modes that have successfully been quantized.

In 1973, Twareque Ali has published the paper called "Evanescent waves in quantum electrodynamics with unquantized sources" [34]. By using classical sources, he has shown that evanescent waves are related to virtual photons. However, the evanescent waves were pure c-numbers and therefore not written in a quantum optics formalism.

To the best of our knowledge, no theory exists so far that quantizes evanescent fields only. Here, we propose a scheme to quantize evanescent waves. This quantization will allow us to show the relationship between evanescent waves and virtual photons in a more formal setting than was done in Chapter 1 of this thesis.

A.1 Quantization of the electromagnetic field in dispersive and absorbing media

Huttner and Barnett were the first to quantize radiation in dispersive and absorptive linear bulk dielectrics [137]. Gruner and Welsch generalized the quantization scheme [138]. One element of this generalization was that the system did not need to be a bulk medium. Gruner and Welsch realized that the introduction of a noise current operator in the Maxwell equations was necessary to account for the dissipation-assisted quantum noise in a lossy system. When a source term is added in the Maxwell equations, the Green's tensor naturally arises when the electric field is calculated. It is the introduction of the Green's tensor that led to the generalization of the quantization scheme to non-uniform media. The electric field was shown to be:

$$\mathbf{E}^{+}(\mathbf{r}) = i\int_0^\infty d\omega \frac{\hbar}{\pi\varepsilon_0}\frac{\omega^2}{c^2}\int d^3\mathbf{r}\sqrt{\varepsilon''(\mathbf{r}',\omega)}\bar{\bar{G}}(\mathbf{r},\mathbf{r}';\omega)\hat{\mathbf{f}}(\mathbf{r}',\omega), \tag{A.1}$$

where ε'' is the imaginary part of the dielectric constant, and $\hat{\mathbf{f}}(\mathbf{r},\omega)$ is called in the words of Gruner and Welsch the "operator basic field" and is a linear superposition of operators for the electric field and matter field. This operator is such that the Hamiltonian of the problem is

$$\hat{H} = \int d^3\mathbf{r}\int_0^\infty d\omega\hbar\omega\hat{\mathbf{f}}^\dagger(\mathbf{r},\omega)\cdot\hat{\mathbf{f}}(\mathbf{r},\omega). \tag{A.2}$$

With the expression of the electric field as given in Eq. A.1, we have a means for quantizing evanescent waves that exist due to the presence of quantum noise currents.

A.2 Evanescent wave operator

In this section we define the evanescent wave operator. We consider a homogeneous, absorbing medium, so that $\varepsilon''(\mathbf{r},\omega) = \varepsilon''(\omega)$ and $\bar{\bar{G}}(\mathbf{r},\mathbf{r}';\omega) = \bar{\bar{G}}(\mathbf{r}-\mathbf{r}';\omega)$. We recognize that the spatial integral in Eq. A.1 is a convolution integral. Thanks to the convolution theorem we can rewrite the electric field in terms of an inverse Fourier transform over the wavevector $\mathbf{k}$:

$$\mathbf{E}^{+}(\mathbf{r}) = i\int_0^\infty d\omega \frac{\hbar}{\pi\varepsilon_0}\frac{\omega^2}{c^2}\sqrt{\varepsilon''(\omega)}\int d^3\mathbf{k}\bar{\bar{G}}(\mathbf{k};\omega)\hat{\mathbf{f}}(\mathbf{k},\omega)e^{i\mathbf{k}\cdot\mathbf{r}} \tag{A.3}$$

with

$$\bar{\bar{G}}(\mathbf{k};\omega) = \frac{\bar{\bar{\mathbb{1}}} - \frac{\mathbf{k}\mathbf{k}}{k^2}}{k^2 - \varepsilon\frac{\omega^2}{c^2}}. \tag{A.4}$$

As a next step we write the noise operator $\hat{\mathbf{f}}$ in its two polarization states

$$\hat{\mathbf{f}}(\mathbf{k},\omega) = \sum_{\lambda=1}^{2}\mathbf{e}_\lambda(\mathbf{k})\hat{C}_\lambda(\mathbf{k},\omega), \tag{A.5}$$

where $\hat{C}_\lambda(\mathbf{k},\omega)$ is a linear combination of the bosonic destruction and creation operators of the matter fields and the photon destruction and creation operators and for which the following commutation relations hold [139]:

$$[\hat{C}_\lambda(\mathbf{k},\omega),\hat{C}^\dagger_{\lambda'}(\mathbf{k}',\omega') = \delta_{\lambda,\lambda'}\delta(\mathbf{k}-\mathbf{k}')\delta(\omega-\omega'), \tag{A.6}$$

and

$$[\hat{C}_\lambda(\mathbf{k},\omega),\hat{C}_{\lambda'}(\mathbf{k}',\omega')=0. \tag{A.7}$$

By substituting both the expression of the Green's tensor and the noise operator, the electric field turns into the following form

$$\mathbf{E}^+(\mathbf{r})=i\int_0^\infty d\omega\frac{\hbar}{\pi\varepsilon_0}\frac{\omega^2}{c^2}\sqrt{\varepsilon''(\omega)}\sum_{\lambda=1}^{2}\int d^3\mathbf{k}\frac{\bar{\bar{\mathbb{1}}}-\frac{\mathbf{kk}}{k^2}}{k^2-\varepsilon\frac{\omega^2}{c^2}}e^{i\mathbf{k}\cdot\mathbf{r}}\mathbf{e}_\lambda(\mathbf{k})\hat{C}_\lambda(\mathbf{k},\omega). \tag{A.8}$$

The key step of this section follows now. We define the quantum operator for evanescent waves:

$$\hat{\mathbf{a}}(\mathbf{k}_\parallel,z;\omega)=\sum_{\lambda=1}^{2}\hat{\bar{a}}_\lambda(\mathbf{k}_\parallel,z;\omega)\mathbf{e}_\lambda(\mathbf{k}), \tag{A.9}$$

where $\hat{\bar{a}}_\lambda(\mathbf{k}_\parallel,z;\omega)$ is a matrix:

$$\boxed{\hat{\bar{a}}_\lambda(\mathbf{k}_\parallel,z;\omega)=\frac{\sqrt{\varepsilon''}\omega}{c}\int_{-\infty}^{\infty}\frac{dk_z}{2\pi}\frac{\bar{\bar{\mathbb{1}}}-\frac{\mathbf{kk}}{k^2}}{k_z^2-\left(\varepsilon\frac{\omega^2}{c^2}-k_\parallel^2\right)}e^{ik_zz}\hat{C}_\lambda(\mathbf{k},\omega).} \tag{A.10}$$

It is at this moment that we see the formal relation between evanescent waves and virtual photons. Let us consider for the moment a system for which ε is real. Modes with $k_\parallel<(\sqrt{\varepsilon})\omega/c$ are propagative modes. We observe that modes for which $k_z^2=\varepsilon\frac{\omega^2}{c^2}-k_\parallel^2$ are dominating. This is as opposed for modes with $k_\parallel>\sqrt{\varepsilon}\omega/c$, which are evanescent waves. For these modes, there is no resonance in k_z and therefore all modes are important: both modes for which $k_x^2+k_y^2+k_z^2=\varepsilon\omega/c$ and $k_x^2+k_y^2+k_z^2\neq\varepsilon\omega/c$. The latter modes are modes that can be excited by virtual photons. From this observation, and from Eq. A.10, it follows that an evanescent wave is built up of many modes that are described quantum optically by the operator $\hat{C}_\lambda(\mathbf{k},\omega)$, which is an operator that annihilates a virtual photon.

Under the introduction of this operator, the electric field operator reduces to

$$\mathbf{E}^+(\mathbf{r})=i\int_0^\infty d\omega\sqrt{\frac{\hbar}{\pi\varepsilon_0}}\frac{\omega}{c}\int\frac{d^2k_\parallel}{(2\pi)^2}\hat{\mathbf{a}}(\mathbf{k}_\parallel,z;\omega')e^{i\mathbf{k}_\parallel\cdot\mathbf{r}'_\parallel}. \tag{A.11}$$

We proceed with the calculation of the commutation relation $[\hat{\bar{a}}_\lambda(\mathbf{k}_\parallel,z;\omega),\hat{\bar{a}}^\dagger_{\lambda'}(\mathbf{k}'_\parallel,z';\omega')]$, since this quantity is closely related to the correlation function of the electric field operators, and thereby closely related to the power spectral density function [139].

A.3 Commutation relation for evanescent wave operators

The commutation relation for the evanescent wave operators is derived mathematically. As a first step, we fill in the expression of the quantum operators and use the commutation relation for the $\hat{C}$ operator:

$$\begin{aligned}[\hat{\bar{a}}_\lambda(\mathbf{k}_\parallel,z;\omega),\hat{\bar{a}}^\dagger_{\lambda'}(\mathbf{k}'_\parallel,z';\omega')] &= \frac{\varepsilon''\omega^2}{c^2}\int_{-\infty}^{\infty}\frac{dk_z}{2\pi}\int_{-\infty}^{\infty}\frac{dk'_z}{2\pi}\frac{\bar{\bar{\mathbb{1}}}-\frac{\mathbf{kk}}{k^2}}{k^2-\varepsilon\frac{\omega^2}{c^2}}\times\frac{\bar{\bar{\mathbb{1}}}-\frac{\mathbf{k}'\mathbf{k}'}{k'^2}}{k'^2-\varepsilon^*\frac{\omega^2}{c^2}}e^{i(k_zz-k'_zz')}\\ &\quad\times\delta_{\lambda,\lambda'}\delta(\mathbf{k}-\mathbf{k}')\delta(\omega-\omega').\end{aligned} \tag{A.12}$$

The integral over k_z' is straightforward to evaluate, because of the delta function $\delta(\mathbf{k}-\mathbf{k}')$. After the integration we obtain:

$$\begin{aligned}[\hat{\bar{\bar{a}}}_\lambda(\mathbf{k}_\parallel,z;\omega),\hat{\bar{\bar{a}}}^\dagger_{\lambda'}(\mathbf{k}'_\parallel,z';\omega')] &= \frac{\varepsilon''\omega^2}{c^2}\int_{-\infty}^{\infty}\frac{dk_z}{2\pi}\frac{\bar{\bar{\mathbb{1}}}-\frac{\mathbf{kk}}{k^2}}{|k^2-\varepsilon\frac{\omega^2}{c^2}|^2}e^{ik_z(z-z')}\\ &\quad\times\delta_{\lambda,\lambda'}\delta(\mathbf{k}_\parallel-\mathbf{k}'_\parallel)\delta(\omega-\omega'). \qquad (A.13)\end{aligned}$$

The integral can be evaluated by means of a complex contour integral and the residue theory. This results in

$$\begin{aligned}[\hat{a}_\lambda(\mathbf{k}_\parallel,z;\omega),\hat{a}^\dagger_{\lambda'}(\mathbf{k}'_\parallel,z';\omega')] &= \frac{\pi}{2}\Big[\frac{1}{\gamma}\Big(\bar{\bar{\mathbb{1}}}-\frac{\mathbf{k}_1\mathbf{k}_1}{k_1^2}\Big)e^{i\gamma|z-z'|}+\frac{1}{\gamma^*}\Big(\bar{\bar{\mathbb{1}}}-\frac{\mathbf{k}_2\mathbf{k}_2}{k_2^2}\Big)e^{-i\gamma^*|z-z'|}\Big]\\ &\quad\times\delta_{\lambda,\lambda'}\delta(\omega-\omega')\delta(\mathbf{k}_\parallel-\mathbf{k}'_\parallel), \qquad (A.14)\end{aligned}$$

where we have defined the parameters

$$\gamma^2 = \varepsilon\frac{\omega^2}{c^2}-k_\parallel^2, \qquad (A.15)$$

$$\mathbf{k}_1 = \langle k_x,k_y,\mathrm{sign}(z-z')\gamma\rangle, \qquad (A.16)$$

$$\mathbf{k}_2 = \langle k_x,k_y,\mathrm{sign}(z-z')\times-\gamma^*\rangle. \qquad (A.17)$$

From this commutation relation we observe that the commutator decays exponentially with the distance between z and z'.

Next, we take the limit of a nonabsorbing medium, i.e., $\varepsilon''=0$, and assume that $k_\parallel \gg \sqrt{\varepsilon}\omega/c$. We define $\gamma=i\kappa$, so that $\kappa>0$. The commutation relation simplifies to

$$[\hat{a}_\lambda(\mathbf{k}_\parallel,z;\omega),\hat{a}^\dagger_{\lambda'}(\mathbf{k}'_\parallel,z';\omega')]=0. \qquad (A.18)$$

Evanescent waves are bosonic of nature, and therefore this commutation relationship should not be strictly zero. The observation that this commutator is zero, leads therefore to the conclusion that the operator belongs to a field that physically does not exist. Indeed, from classical optics we know that evanescent waves do not exist in a uniform, nonabsorbing medium without an electric source.

When we take a propagating wave, i.e., $k_\parallel \ll \sqrt{\varepsilon}\omega/c$ the commutator becomes

$$\begin{aligned}[\hat{a}_\lambda(\mathbf{k}_\parallel,z;\omega),\hat{a}^\dagger_{\lambda'}(\mathbf{k}'_\parallel,z';\omega')] &= \frac{\pi}{2\gamma}\Big[\Big(\mathbb{1}-\frac{\mathbf{k}_1\mathbf{k}_1}{k_1^2}\Big)e^{i\gamma(z-z')}+\Big(\mathbb{1}-\frac{\mathbf{k}_2\mathbf{k}_2}{k_2^2}\Big)e^{-i\gamma(z-z')}\Big]\\ &\quad\times\delta_{\lambda,\lambda'}\delta(\omega-\omega')\delta(\mathbf{k}_\parallel-\mathbf{k}'_\parallel), \qquad (A.19)\end{aligned}$$

where

$$\mathbf{k}_1 = \langle k_x,k_y,\gamma\rangle, \qquad (A.20)$$

$$\mathbf{k}_2 = \langle k_x,k_y,-\gamma\rangle, \qquad (A.21)$$

with $\gamma\in\mathbb{R}$. This commutator is not strictly zero. Indeed, propagating modes are physically allowed in a uniform, nonabsorbing medium without an electric source.

A.4 Conclusion

We presented the quantization of evanescent waves in an absorbing medium. We have formally established the relationship between evanescent fields and virtual photons. The creation and annihilation operators for evanescent waves can be expressed as a linear superposition of creation and annihilation operators of photonic modes that do virtual.

Appendix B

Numerical calculations on off-axis source in a cylindrically symmetric nanostructure

We present an improvement of an aperiodic-Fourier modal method (aperiodic FMM) that has been developed by Bigourdan *et al.* [140]. This code enables to calculate the electric field produced by a point source inside any cylindrically symmetric system. When the point source is positioned away from the symmetry axis, the calculation becomes numerically more demanding, since the symmetry of the problem is broken. Here, we present a numerical trick to improve both convergence and convergence time of this numerical method for a source that is positioned off axis.

B.1 System description

The system that was studied with the aperiodic FMM, and was used to improve the convergence of the numerical calculation, has two InAs/GaAs quantum dots that are spatialy separated by roughly 300 nm. They are embedded in a multilayer system. This multilayer system contains a distributed Bragg reflector (DBR) and on top there is a gold disk, see Fig. B.1. This gold disk has a diameter of 2.6 μm and is positioned such that the quantum dots are symmetrically positioned around the center of the gold disk. The quantum dots are 44 nm underneath the gold. For the other system parameters, refer to the caption of Fig. B.1. In order to obtain the Green's tensor of the problem, we need to calculate the electric field for a pointlike electrical dipole. In the next section we briefly discuss the idea behind the numerical method that is used.

B.2 Numerical method

B.2.1 Electric field decomposition

There are several numerical methods possible to model a cylindrically symmetric system. In this Appendix, we study an aperiodic-Fourier modal method (aperiodic FMM) that is developed by Bigourdan *et al.* [140]. In the current section, we briefly discuss their method. For a more thorough discussion, refer to Ref. [140]. For this aperiodic FMM, the aperiodic structure [an example is given in Fig. B.2(a)] is periodically repeated in the z direction as

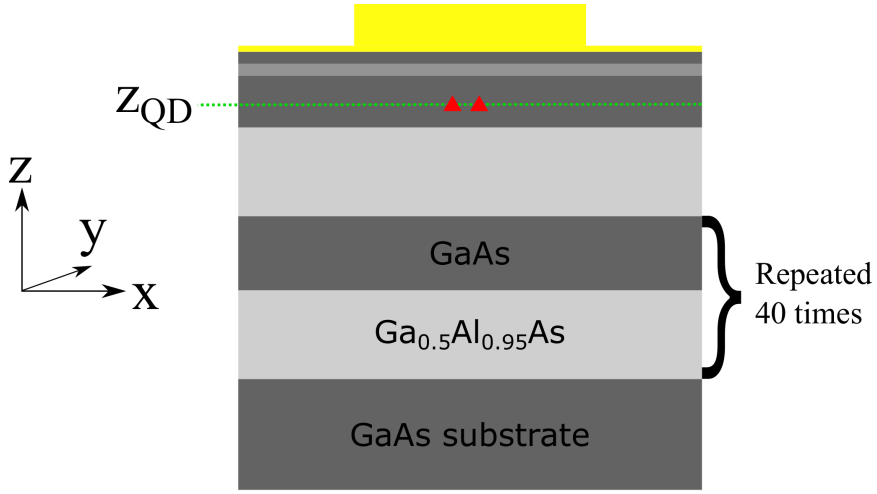

Figure B.1: *Schematic of the structure. All dimensions, apart the dimensions of the quantum dots and the substrate, are on scale. The diameter of the gold disk is 2.6 μm. The materials, in order and per layer are: Au, Au, GaAs, $Al_{0.1}Ga_{0.9}As$, GaAs,QDs,GaAs, $Ga_{0.05}Al_{0.95}As$, {GaAs, $Ga_{0.05}Al_{0.95}As$} nm (between curly brackets: repeated 40 times), GaAs. The heights are from top to bottom: 45, 5, 10, 10, 24, QDs, 19, 74, {60, 72} (between curly brackets: repeated 40 times). The z position where the QDs are found is indicated by z_{QD} and is 44 nm underneath gold.*

illustrated in Fig. B.2(b), so that a Fourier modal method can be used. Next, each cell should be optically isolated. This can be done by for example putting perfectly matched layers (PML) at the borders of the cell along the z direction, or by using complex coordinate transformations at the borders of each cell [86]. It is the latter that is used in this work.

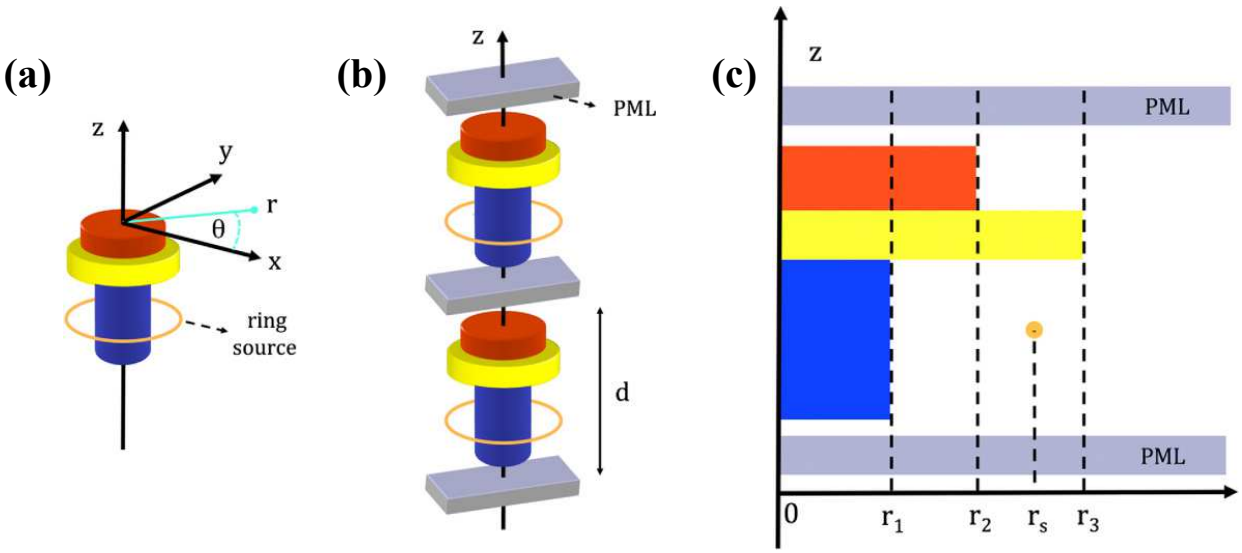

Figure B.2: *(a) Example of a rotationally invariant nanostructure with the presence of a ring source. (b) The aperiodic nanostructure is periodized with period d along the symmetry axis. The cells are separated by either a PML or, in our calculations, by complex coordinate transforms. (c) In the radial direction, the structure is divided in slabs for which the optical properties are invariant along the radial direction. Figure has been extracted from Ref. [140].*

In our case, we study a rotationally invariant nanostructure. Because of the symmetry, the electric and magnetic field are written in cylindrical coordinates and decomposed in an appropriate basis:

$$\mathbf{F}(r,z,\theta) = \sum_{L=-\infty}^{+\infty} \sum_{m=-\infty}^{+\infty} e^{iL\theta} e^{i\beta_m z} \tilde{\mathbf{F}}_m^L(r), \tag{B.1}$$

where $\mathbf{F}$ can stand for both the electric and magnetic field and $\beta_m = \beta_0 + m\frac{2\pi}{d}$, d being the artificial period that has been introduced while periodically repeating the aperiodic structure. Each basis element is characterized by the the azimuthal number L and the order m of a Floquet mode. The azimuthal number L is natural to the physical problem, which is in contrast with the order m, that is purely mathematical and does not have any physical meaning, as we have artificially created a periodicity along the z axis. For a numerical analysis, not all terms of the sums can be included. Therefore the sums over L and m are truncated:

$$\mathbf{F}_t(r,z,\theta) = \sum_{L=-L_{\max}}^{L_{\max}} \sum_{m=-m_{\max}}^{m_{\max}} e^{iL\theta} e^{i\beta_m z} \tilde{\mathbf{F}}_m^L(r), \tag{B.2}$$

so that we keep $2L_{\max}+1$ and $2m_{\max}+1$ terms of each sum. The subscript t indicates that the solution follows from a truncation of the sums. Bigourdan *et al.* have shown that for each mode defined by the pair (m, L), the tangential field components $[\tilde{F}_\theta(r)$ and $\tilde{F}_z(r)]$ at the borders of each slice [see Fig. B.2(c) for the definition of a slice] are related by a so called scattering matrix (S matrix) [140]

$$\begin{bmatrix} \tilde{E}_z(r_j) \\ \tilde{E}_\theta(r_j) \\ \tilde{H}_z(r_i) \\ \tilde{H}_\theta(r_i) \end{bmatrix} = \bar{\bar{S}}(r_j - r_i, r_i) \begin{bmatrix} \tilde{E}_z(r_i) \\ \tilde{E}_\theta(r_i) \\ \tilde{H}_z(r_j) \\ \tilde{H}_\theta(r_j) \end{bmatrix}. \tag{B.3}$$

The S-matrix formalism is typically used for multilayer systems in cartesian coordinates; here this formalism is used for a multilayer system along the radial direction. Apart from calculating the electric and magnetic fields at the border of each slices, the same formalism allows to calculate the electric and magnetic fields at any position inside and outside the nanostructure.

B.2.2 Source decomposition

So far we have only discussed the electric and magnetic fields. They need to be excited, which is numerically done by a point source. This point source at position $\mathbf{r}_0$: $\mathbf{J}\delta(\mathbf{r}-\mathbf{r}_0)$, needs to be written in the same basis as the electromagnetic fields. After periodically repeating the point source, the source term is

$$\sum_{m=-\infty}^{+\infty} \mathbf{J}\delta[\mathbf{r} - (\mathbf{r}_0 + m\cdot d\hat{z})] = \frac{\mathbf{J}}{2\pi r_0 d} \sum_{L=-\infty}^{+\infty} \sum_{m=-\infty}^{+\infty} e^{iL(\theta-\theta_0)} e^{i\beta_m(z-z_s)} \delta(r-r_0)\delta(z-z_0). \tag{B.4}$$

A point source is therefore expanded as a sum of ring sources [see Fig. B.2(a)], so that each term respects the symmetry of the problem. A linear superposition of ring sources,

with appropriate (complex) coefficients in front of each term, approaches a point source by summing over all values of L. Let us briefly discuss two distinct situations: (1) A point source is located at the center ($r_0 = 0$), and (2) a point source is located off center ($r_0 \neq 0$). It can be shown that for a point source at the center, the sum over L is limited to only a few terms. If the source is polarized along the z axis, only $L = 0$ should be considered, and for any rectilinear polarization only $L = \{-1, 1\}$ are needed. As soon as the source is off centered, one theoretically needs to take all terms into account. Similarly as for the electric field, this is not possible and we therefore truncate this sum to the same order as the fields. The consequence of this truncature of the source is that we do not have a true point source: the source is spread out on a ring. An example of this is given in Fig. B.3(a), where we calculated the electric field in the plane z_{QD} (see Fig. B.1). The truncature parameters are: $m_{\max} = 100$ and $L_{\max} = 3$. One can readily see that determining the electric field somewhere close to the ring is problematic and therefore also the calculation of the total emitted power, since we calculate the total emitted power by

$$P = \frac{1}{2}\mathrm{Re}\left[\mathbf{J} \cdot \mathbf{E}^*(\mathbf{r}_{\mathrm{QD}})\right]. \tag{B.5}$$

This effect has potentially a big influence on our calculations in particular. Since each quantum dot is positioned about 150 nm from the center, they lie on "each other's ring". Therefore, the convergence for the electric field at the position of QD 2 is therefore very bad.

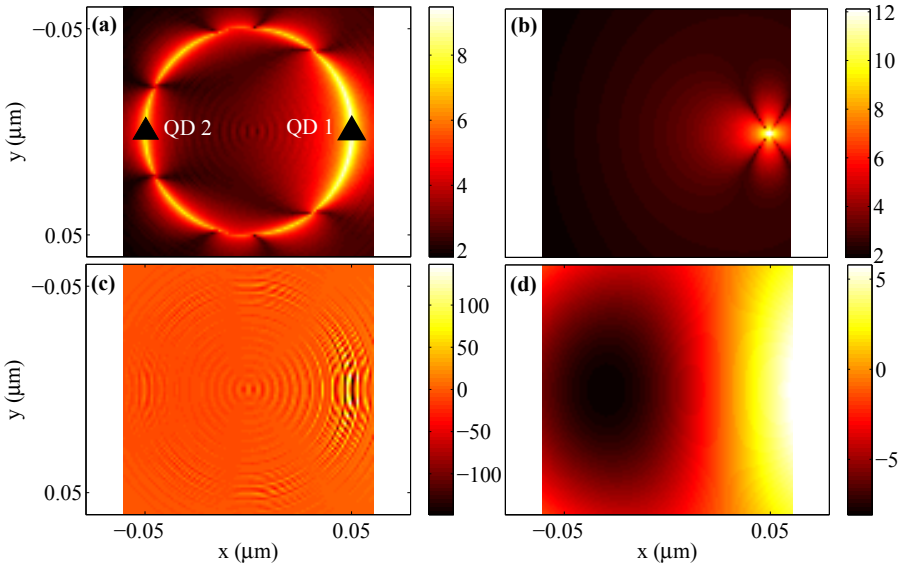

Figure B.3: *A map of the electric field in the plane of an x-polarized quantum dot positioned at* $(x, y) = (50\ nm, 0)$. $m = \{-100 \cdots 100\}$ *and* $L = \{-3 \cdots 3\}$. *(a)* $\log_{10}|E_x|^2$ *obtained without a plane wave expansion (PWE). The source is indicated by QD 1. QD 2 indicates the place where the other quantum dot could be positioned. (b)* $\log_{10}|E_x|^2$ *obtained with a PWE. (c)* $Im(E_z)$ *obtained without a PWE. (d)* $Im(E_z)$ *obtained with a PWE.*

B.2.3 Improving electric field calculation

We came up with a technique to improve the field calculation. This technique is illustrated in Fig. B.4. From the electric field calculated with the aperiodic FMM, we substract the

electric field calculated with the same method but with the gold disk that has been made spatially extended. The strong electric field on the circle which is due to the source, as shown in Fig. B.3(a), is effectively removed in this way. Next, the electric field corresponding to an emitter in a multilayer system needs to be added. For this, another numerical method is used that is more appropriate to such a multilayer system and converges much faster. This method consists of expanding the electric field in plane waves, a natural basis of the system. The solution, based on a plane wave expansion (PWE), is added to the field calculated by means of the aperiodic FMM and we end up with an electric field that does not have the problem of a source that is spread out over a circle. The improvement of Fig. B.3(a) is depicted in Fig. B.3(b). As can be visually observed, the solution of Fig. B.3(b) is indeed much better converged than the solution of Fig. B.3(a). Similarly, we see an improvement of the imaginary part of E_z when comparing Fig. B.3(d) with Fig. B.3(c).

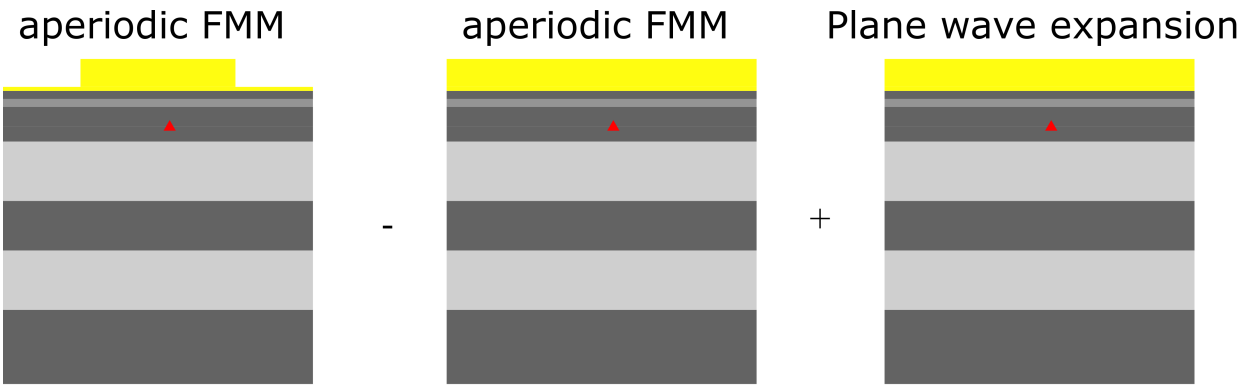

Figure B.4: *A schematic view of the method used to improve the convergence of the electric field calculation in the vicinity of the quantum dot. From the electric field calculated by means of the aperiodic FMM as explained in the main text, we subtract the electric field calculated by the same aperiodic FMM, but with the gold disk extended in two dimensions, effectively making it a multilayer system. The electric field created by a point source in this multilayer system is calculated by a plane wave expansion and added.*

B.2.4 Convergence

Next, we study the convergence quantitatively. Both methods (with and without PWE) have been used to calculate the total emitted power P for an x-polarized point source located at $(x, y, z) = (150\text{ nm}, 0, z_{\text{QD}})$. For the moment we truncate the sum over L to $L_{\text{max}} = 3$. Figure B.5(a) shows the total emitted power as a function of the truncature of the sum over the order of the Floquet modes. It is seen that the method which makes use of the PWE converges with 2.5 times less modes. Figure B.5(b) shows the computational time for a single value of L as a function of the truncature m_{max} for both methods. It is seen that convergence is reached 8.3 times faster with PWE than without, eventhough we perform two aperiodic FMM calculations, as can be seen in Fig. B.4[1]. Apart from the faster convergence in terms of m, there is also a faster convergence for L when the PWE is applied. Table B.1 shows the emitted power per azimuthal number L relative to the total emitted power, where we define total emitted power in this table as the total emitted power

[1] In principle it should be possible to combine both calculations in only a single calculation, because of the linearity of the electric fields. This improvement of the calculation has not been implemented yet.

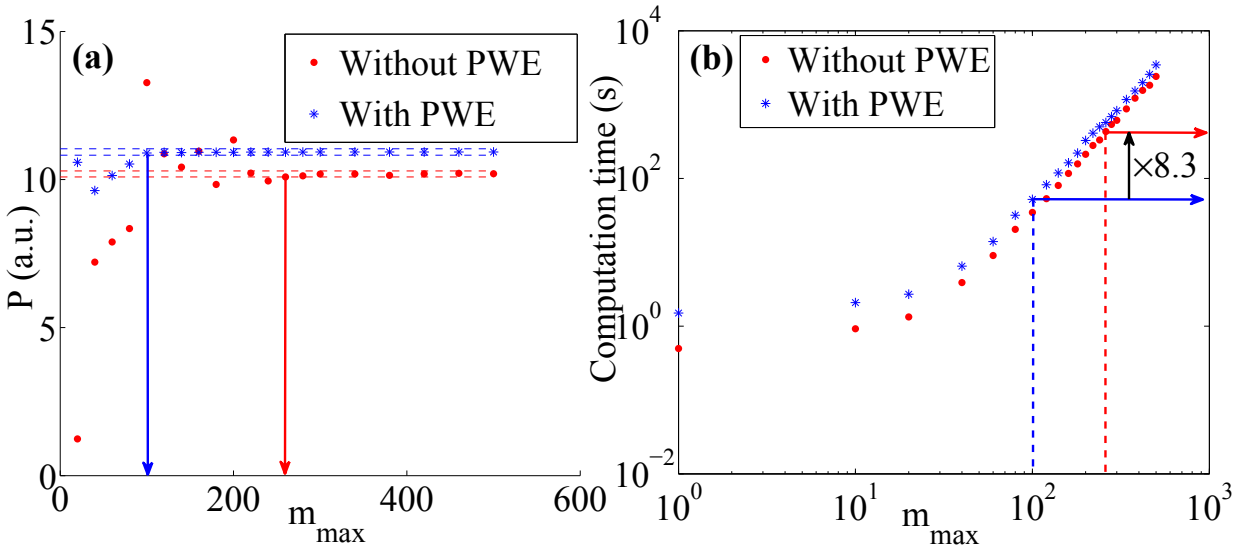

Figure B.5: *(a) The total emitted power has been calculated for an x polarized point source at* $(x, y, z) = (150\ nm, 0, z_{QD})$ *and* $L_{max} = 3$*. The dashed lines indicate the regions for which the calculated power deviates by* 1% *of the value obtained when* $m_{max} = 500$*. PWE stands for plane wave expansion and is used to improve the convergence. (b) The computation time as a function of the truncature on m. This calculation is done for* $L = 0$*.*

for $L = \{-9 \cdots 9\}$. This calculation has been done for the same situation as described for the results of Fig. B.5. We note that with only $L = \{-2 \cdots 2\}$, the solution that uses the PWE is sufficiently well converged, as opposed to the solution where the PWE has not been used. The reason for this difference is simple. When a PWE is used, the emission which is due to a source in the multilayer is calculated very accurately without the use of an expansion based on L. The aperiodic FMM is only used for the part which is due to the fact that the gold disk has a finite radius. We have therefore included this contribution to $L = 0$ in the table and it shows that 94.7% of the total emitted power is already accounted for. For the method where the PWE is not applied, the source needs to be approximated by adding up ring sources. Depending on the position of the source, many azimuthal numbers L are needed to approximate the ring source correctly. From the table we find that at least $L = \{-5 \cdots 5\}$ are needed for this method. Note that the computational time grows linearly with $L_{\max}$.

We see that the trick as illustrated by Fig. B.4 dramatically improves the calculation. Due to this improvement, we have now access to the electric field at the height of the quantum dots; a parameter that is important to evaluate the dipole-dipole interactions between two quantum dots.

L	0	1	2	3	4
$\frac{P^L_{\text{no PWE}}}{P_{\text{total}}}$	0.129	0.473	0.258	0.095	0.028
$\frac{P^L_{\text{PWE}}}{P_{\text{total}}}$	0.947	0.089	−0.037	0.003	−0.003

L	5	6	7	8	9
$\frac{P^L_{\text{no PWE}}}{P_{\text{total}}}$	0.024	0.005	−0.001	−0.003	−0.007
$\frac{P^L_{\text{PWE}}}{P_{\text{total}}}$	0.003	−0.001	$-3 \cdot 10^{-4}$	$1 \cdot 10^{-4}$	$-1 \cdot 10^{-5}$

Table B.1: *The fraction of power emitted by the mode with azimuthal number L is given for both methods where either the PWE is applied or not. It is seen that the method that uses a PWE converges faster than the method without.*

Bibliography

[1] D. Pines, *Elementary Excitations in Solids*, (Benjamin, New York, 1964).

[2] A. Fuhrmanek, Ph.D. thesis, Institut d'Optique, 2011.

[3] R. Bourgain, Ph.D. thesis, Institut d'Optique, 2014.

[4] J. Pellegrino, Ph.D. thesis, Institut d'Optique, 2014.

[5] R. Friedberg, S.R. Hartmann, and J.T. Manassah, *Limited superradiant damping of small samples*, Phys. Lett. **40A**, 365-366 (1972).

[6] M. Gross and S. Haroche, *Superradiance: An essay on the theory of collective spontaneous emission*, Phys. Rep. **93**, 301-396 (1982).

[7] S. Jennewein, M. Besbes, N.J. Schilder, S.D. Jenkins, C. Sauvan, J. Ruostekoski, J.-J. Greffet, Y.R.P. Sortais, and A. Browaeys, *Coherent scattering of near-resonant light by a dense microscopic cold atomic cloud*, Phys. Rev. Lett. **116**, 233601 (2016).

[8] A. Goetschy and S.E. Skipetrov, *Non-Hermitian Euclidean random matrix theory*, Phys. Rev. E **84**, 011150 (2011).

[9] R. Bachelard, Ph.W. Courteille, R. Kaiser, and N. Piovella, *Resonances in Mie scattering by an inhomogeneous atomic cloud*, Eur. Phys. Lett. **97**, 14004 (2012).

[10] Q. Le-Van, Ph.D. thesis, Institut d'Électronique Fondamentale, 2016.

[11] Q. Le-Van, X. Le Roux, A. Aasime, and A. Degiron, *Electrically driven optical metamaterials*, Nat. Comm. **7**, 12017 (2016).

[12] L. Novotny and B. Hecht, *Principles of Nano-optics*, (Cambridge University Press, Cambridge, UK, 2006).

[13] G. Grynberg, A. Aspect, and C. Fabre, *Introduction to quantum optics: from the semi-classical approach to quantized light*, (Cambridge University Press, New York, 2010).

[14] C.F. Bohren and D.R. Huffman, *Absorption and scattering of light by small particles* (John Wiley & Sons, New York, 2008).

[15] M. Born and E. Wolf, *Principles of Optics*, 7th ed. (Cambridge University Press, Cambridge, UK, 1999).

[16] A. Lagendijk and B. van Tiggelen, *Resonant multiple scattering of light*, Physics Reports **270**, 143 (1996).

[17] U. Frisch, in *Probabilistic methods in applied mathematics*, edited by A.A. Bharuch-Reid (Academic, New York, 1968), Vols. I and II.

[18] P. Sheng, *Introduction to Wave Scattering, Localization, and Mesoscopic Phenomena*, (Academic Press, New York, 1995).

[19] L. Apresyan and Y. Kravtsov, *Radiation transfer: statistical and wave aspects*, (Gordon and Breach, 1996)

[20] S. Durant, O. Calvo-Perez, N. Vukadinovic, and J.-J. Greffet, *Light scattering by a random distribution of particles embedded in absorbing media: diagrammatic expansion of the extinction coefficient*, J. Opt. Soc. Am. A, **24**, 2943-2952 (2007).

[21] C. Cohen-Tannoudji, J. Dupont-Roc, and G. Grynberg, *Atom-Photon Interactions: Basic Processes and Applications* (John Wiley & Sons, New York, 1992).

[22] R.P. Feynman, R.B. Leighton, and M.L. Sands, *The Feynman lectures on physics II*, (Addison-Wesley, 1963).

[23] N.W. Ashcroft and N.D. Mermin, *Solid state physics*, (Saunders College, Philadelphia, 1976).

[24] A. Lagendijk, B. Nienhuis, B.A. van Tiggelen, and P. de Vries, *Microscopic approach to the Lorentz cavity in dielectrics*, Phys. Rev. Lett. **79**, 657 (1997).

[25] L. Tsang and J.A. Kong, *Scattering of Electromagnetic Waves, Volume III: Advanced Topics* (Wiley, 2001).

[26] O. Morice, Y. Castin, and J. Dalibard, *Refractive index of a dilute Bose gas*, Phys. Rev. A **51**, 3896 (1995).

[27] J. Javanainen and J. Ruostekoski, *Light propagation beyond the mean-field theory of standard optics*, Opt. Express **24**, 993-1001 (2016).

[28] V. Weisskopf and E. Wigner, *Berechnung der natürlichen Linienbreite auf Grund der Diracschen Lichttheorie*, Z. Physik **63**, 54-73 (1930).

[29] A.A. Svidzinsky, J.-T. Chang, and M.O. Scully, *Cooperative spontaneous emission of N atoms: many-body eigenstates, the effect of virtual Lamb shift processes, and analogy with radiation of N classical oscillators*, Phys. Rev. A **81**, 053821 (2010).

[30] I.M. Sokolov, D.V. Kupriyanov, and M.D. Havey, *Microscopic theory of scattering of weak electromagnetic radiation by a dense ensemble of ultracold atoms*, J. Exp. Theor. Phys. **112**, 246-260 (2011).

[31] M. Kiffner, M. Macovei, J. Evers, and C.H. Keitel, *Vacuum-induced processes in multilevel atoms*, Prog. Opt. **55**, 85-197 (2010).

[32] D.L. Andrews and D.S. Bradshaw, *Virtual photons, dipole fields and energy transfer: a quantum electrodynamical approach*, Eur. J. Phys. **25**, 845 (2004).

[33] C.K. Carniglia and L. Mandel, *Quantization of evanescent electromagnetic waves*, Phys. Rev. D **3**, 280 (1971).

[34] S. Twareque Ali, *Evanescent waves in quantum electrodynamics with unquantized sources*, Phys. Rev. D **7**, 1668 (1973).

[35] A.A. Stahlhofen and G. Nimtz, *Evanescent modes are virtual photons*, Europhys. Lett. **76**, 189 (2006).

[36] V.M. Faĭn, *On the theory of the coherent spontaneous emission*, Soviet Phys. JETP (U.S.S.R.) **36**, 798 (1959).

[37] R. Friedberg, S.R. Hartmann, and J.T. Manassah, *Frequency shifts in emission and absorption by resonant systems of two-level atoms*, Phys. Rep. **7**, 101–179 (1973).

[38] J. Keaveney, A. Sargsyan, U. Krohn, I.G. Hughes, D. Sarkisyan, and C.S. Adams, *Cooperative Lamb shift in an atomic vapor layer of nanometer thickness*, Phys. Rev. Lett. **108**, 173601 (2012).

[39] J. Keaveney, I.G. Hughes, A. Sargsyan, D. Sarkisyan, and C.S. Adams, *Maximal refraction and superluminal propagation in a gaseous nanolayer*, Phys. Rev. Lett. **109**, 233001 (2012).

[40] H. Bender, C. Stehle, S. Slama, R. Kaiser, N. Piovella, C. Zimmermann, and Ph.W. Courteille, *Observation of cooperative Mie scattering from an ultracold atomic cloud*, Phys. Rev. A **82**, 011404(R) (2010).

[41] M. Chalony, R. Pierrat, D. Delande, and D. Wilkowski, *Coherent flash of light emitted by a cold atomic cloud*, Phys. Rev. A **84**, 011301(R) (2011).

[42] S. Balik, A.L. Win, M.D. Havey, I.M. Sokolov, and D.V. Kupriyanov, *Near-resonance light scattering from a high-density ultracold atomic ^{87}Rb gas*, Phys. Rev. A **87**, 053817 (2013).

[43] C.C. Kwong, T. Yang, M.S. Pramod, K. Pandey, D. Delande, R. Pierrat, and D. Wilkowski, *Cooperative emission of a coherent superflash of light*, Phys. Rev. Lett. **113**, 223601 (2014).

[44] C.C. Kwong, T. Yang, D. Delande, R. Pierrat, and D. Wilkowski, *Cooperative emission of a pulse train in an optically thick scattering medium*, Phys. Rev. Lett. **115**, 223601 (2015).

[45] M.O. Araújo, I. Krešić, R. Kaiser, and W. Guerin, *Superradiance in a large cloud of cold atoms in the linear-optics regime*, Phys. Rev. Lett. **117**, 073002 (2016).

[46] W. Guerin, M.O. Araújo, and R. Kaiser, *Subradiance in a large cloud of cold atoms*, Phys. Rev. Lett. **116**, 083601 (2016).

[47] S.J. Roof, K. Kemp, M.D. Havey, and I.M. Sokolov, *Observation of single-photon superradiance and the cooperative Lamb shift in an extended sample of cold atoms*, Phys. Rev. Lett. **117**, 073003 (2016).

[48] A.D. Ludlow, M.M. Boyd, J. Ye, E. Peik, and P.O. Schmidt, *Optical atomic clocks*, Rev. Mod. Phys. **87**, 637–701 (2015).

[49] S.L. Bromley, B. Zhu, M. Bishof, X. Zhang, T. Bothwell, J. Schachenmayer, T.L. Nicholson, R. Kaiser, S.F. Yelin, M.D. Lukin, A.M. Rey, and J. Ye, *Collective atomic scattering and motional effects in a dense coherent medium*, Nature Comm. **7**, 11039 (2016).

[50] A. Goban, C.-L. Hung, J.D. Hood, S.-P. Yu, J.A. Muniz, O. Painter, and H.J. Kimble, *Superradiance for atoms trapped along a photonic crystal waveguide*, Phys. Rev. Lett. **115**, 063601 (2015).

[51] J. Pellegrino, R. Bourgain, S. Jennewein, Y.R.P. Sortais, A. Browaeys, S.D. Jenkins, and J. Ruostekoski, *Observation of suppression of light scattering induced by dipole-dipole interactions in a cold-atom ensemble*, Phys. Rev. Lett. **113**, 133602 (2014).

[52] S. Jennewein, Y.R.P. Sortais, J.-J. Greffet, and A. Browaeys, *Propagation of light through small clouds of cold interacting atoms*, arXiv:1511.08527 (unpublished).

[53] R. Bourgain, J. Pellegrino, A. Fuhrmanek, Y.R.P. Sortais, and A. Browaeys, *Evaporative cooling of a small number of atoms in a single-beam microscopic dipole trap*, Phys. Rev. A **88**, 023428 (2013).

[54] J.D. Miller, R.A. Cline, and D.J. Heinzen, *Far-off-resonance optical trapping of atoms*, Phys. Rev. A **47**, R4567 (1993).

[55] R. Newell, J. Sebby, and T.G. Walker, *Dense atom clouds in a holographic atom trap*, Opt. Lett. **28**, 1266–1268 (2003).

[56] S. Roof, K. Kemp, M. Havey, I.M. Sokolov, and D.V. Kupriyanov, *Microscopic lensing by a dense, cold atomic sample*, Opt. Lett. **40**, 1137–1140 (2015).

[57] K.I. Popov, A.F. Pegoraro, A. Stolow, and L. Ramunno, *Image formation in CARS microscopy: effect of the Gouy phase shift*, Opt. Express **19**, 5902–5911 (2011).

[58] J. Javanainen, J. Ruostekoski, Y. Li, and S.-M. Yoo, *Shifts of a resonance line in a dense atomic sample*, Phys. Rev. Lett. **112**, 113603 (2014).

[59] J.T. Manassah, *Cooperative radiation from atoms in different geometries: decay rate and frequency shift*, Adv. Opt. Photon. **4**, 108–156 (2012).

[60] J.-J. Greffet and C. Baylard, *Nonspecular astigmatic reflection of a 3D Gaussian beam on an interface*, Opt. Comm. **93**, 271–276 (1992).

[61] L. Brillouin, *Wave propagation and group velocity*, (Academy Press, New York, 1960).

[62] L.V. Hau, S.E. Harris, Z. Dutton, and C.H. Behroozi, *Light speed reduction to 17 metres per second in an ultracold atomic gas*, Nature **397**, 597–598 (1999).

[63] R.W. Boyd and D.J. Gauthier, *"Slow" and "fast" light*, Progress in Optics **43**, 497–530 (2002).

[64] W. Withayachumnankul, B.M. Fischer, B. Ferguson, B.R. Davis, and D. Abbott, *A systemized view of superluminal wave propagation*, Proceedings of the IEEE **98**, 1775–1786 (2010).

[65] L.J. Wang, A. Kuzmich, and A. Dogariu, *Gain-assisted superluminal light propagation*, Nature **406**, 277–279 (2000).

[66] G.M. Gehring, A. Schweinsberg, C. Barsi, N. Kostinski, and R.W. Boyd, *Observation of backward pulse propagation through a medium with a negative group velocity*, Science **312**, 895–897 (2006).

[67] N.J. Schilder, C. Sauvan, J.-P. Hugonin, S. Jennewein, Y.R.P. Sortais, A. Browaeys, and J.-J. Greffet, *Polaritonic modes in a dense cloud of cold atoms*, Phys. Rev. A **93**, 063835 (2016).

[68] I.M. Sokolov, M.D. Kupriyanova, D.V. Kupriyanov, and M.D. Havey, *Light scattering from a dense and ultracold atomic gas*, Phys. Rev. A **79**, 053405 (2009).

[69] T. Bienaimé, R. Bachelard, N. Piovella, and R. Kaiser, *Cooperativity in light scattering by cold atoms*, Fortschr. Phys. **61**, 2 (2013).

[70] S.E. Skipetrov, and A. Goetschy, *Eigenvalue distributions of large Euclidean random matrices for waves in random media*, J. Phys. A: Math. Theor. **44**, 065102 (2011).

[71] A. Goetschy, and S.E. Skipetrov, *Euclidean matrix theory of random lasing in a cloud of cold atoms*, Europhys. Lett. **96**, 34005 (2011).

[72] Y. Li, J. Evers, W. Feng, and S.-Y. Zhu, *Spectrum of collective spontaneous emission beyond the rotating-wave approximation*, Phys. Rev. A **87**, 053837 (2013).

[73] J.J. Hopfield, *Theory of the contribution of excitons to the complex dielectric constant of crystals*, Phys. Rev. **112**, 1555 (1958).

[74] A.S. Davydov, in *Theory of Solids*, (Nauka, Moscow, 1980).

[75] J. Bellessa, C. Bonnand, J.C. Plenet, and J. Mugnier, *Strong coupling between surface plasmons and excitons in an organic semiconductor*, Phys. Rev. Lett. **93**, 036404 (2004).

[76] J. Dintinger, S. Klein, F. Bustos, W.L. Barnes, and T.W. Ebbesen, *Strong coupling between surface plasmon-polaritons and organic molecules in subwavelength hole arrays*, Phys. Rev. B**71**, 035424 (2005).

[77] T.K. Hakala, J.J. Toppari, A. Kuzyk, M. Pettersson, H. Tikkanen, H. Kunttu, and P. Törmä, *Vacuum Rabi splitting and strong-coupling dynamics for surface-plasmon polaritons and rhodamine 6G molecules*, Phys. Rev. Lett. **103**, 053602 (2009).

[78] S. Aberra Guebrou, C. Symonds, E. Homeyer, J.C. Plenet, Yu. N. Gartstein, V.M. Agranovich, and J. Bellessa, *Coherent emission from a disordered organic semiconductor induced by strong coupling with surface plasmons*, Phys. Rev. Lett. **108**, 066401 (2012).

[79] D.E. Gómez, K.C. Vernon, P. Mulvaney, and T.J. Davis, *Surface plasmon mediated strong exciton-photon coupling in semiconductor nanocrystals*, Nano Lett. **10**, 274-278 (2010).

[80] L. Shi, T.K. Hakala, H.T. Rekola, J.-P. Martikainen, R.J. Moerland, and P. Törmä, *Spatial coherence properties of organic molecules coupled to plasmonic surface lattice resonances in the weak and strong coupling regimes*, Phys. Rev. Lett. **112**, 153002 (2014).

[81] H. Fidder, J. Knoester, and D.A. Wiersma, *Superradiant emission and optical dephasing in J-aggregates*, Chem. Phys. Lett. **171**, 529 (1990).

[82] D.E. Gómez, S.S. Lo, T.J. Davis, and G.V. Hartland, *Picosecond kinetics of strongly coupled excitons and surface plasmon polaritons*, J. Phys. Chem. B **117**, 4340-4346 (2012).

[83] D.J. Jackson, *Classical Electrodynamics*, (John Wiley and Sons, New York, 1998).

[84] L. Chomaz, L. Corman, T. Yefsah, R. Desbuquois, and J. Dalibard, *Absorption imaging of a quasi-two-dimensional gas: A multiple scattering analysis*, New Journal of Physics **14**, 055001 (2012).

[85] E. Silberstein, P. Lalanne, J.-P. Hugonin, and Q. Cao, *Use of grating theories in integrated optics*, J. Opt. Soc. Am. A, **18**, 2865 (2001).

[86] J.-P. Hugonin and P. Lalanne, *Perfectly matched layers as non-linear coordinate transforms: A generalized formalization*, J. Opt. Soc. Am. A **22**, 1844-1849 (2005).

[87] R. Pierrat and R. Carminati, *Spontaneous decay rate of a dipole emitter in a strongly scattering disordered environment*, Phys. Rev. A **81**, 063802 (2010).

[88] S.E. Skipetrov, I.M. Sokolov, and M.D. Havey, *Control of light trapping in a large atomic system by a static magnetic field*, arXiv:1603.02968 (unpublished).

[89] D.J. Thouless, *Electrons in disordered systems and the theory of localization*, Phys. Rep. **13**, 93-142 (1974).

[90] A. Lagendijk, B. van Tiggelen, and D.S. Wiersma, *Fifty years of Anderson localization*, Physics Today **62**, 24-29 (2009).

[91] S.E. Skipetrov and I.M. Sokolov, *Absence of Anderson localization of light in a random ensemble of point scatterers*, Phys. Rev. Lett. **112**, 023905 (2014).

[92] Q. Bai, M. Perrin, C. Sauvan, J.-P. Hugonin, and P. Lalanne, *Efficient and intuitive method for the analysis of light scattering by a resonant nanostructure*, Opt. Express, **21**, 27371 (2013).

[93] J.C. Maxwell-Garnett, *Colors in metal glasses and in metallic films*, Phil. Trans. R. Soc. London A **203**, 385 (1904).

[94] D.A.G. Bruggeman, *Berechnung verschiedener physikalischer Konstanten von heterogenen Substanzen. I. Dielektrizitätskonstanten und Leitfähigkeiten der Mischkörper aus isotropen Substanzen*, Ann. Phys. **24**, 7 (1935).

[95] P. Mallet, C.A. Guérin, and A. Sentenac, *Maxwell-Garnett mixing rule in the presence of multiple scattering: derivation and accuracy*, Phys. Rev. B **72**, 014205 (2005).

[96] R.G. Driggers, *Encyclopedia of Optical Engineering*, (CRC Press, New York, 2003), Vol. 1, p. 65.

[97] L. Bellando, A. Gero, E. Akkermans, and R. Kaiser, *Cooperative effects and disorder: a scaling analysis of the spectrum of the effective atomic Hamiltonian*, Phys. Rev. A **90**, 063822 (2014).

[98] F.S. Crawford, *Waves: Berkeley physics course*, (McGraw-Hill, 1968), Vol. 3, p. 559.

[99] L.D. Landau and E.M. Lifshits, *Electrodynamics of continuous media*, (Pergamon Press, Oxford, 1981).

[100] R.W. Hart and R.A. Farrell, *Light scattering in the cornea*, J. Opt. Soc. Am. **59**, 6 (1969).

[101] R.H. Dicke, *Coherence in spontaneous radiation processes*, Phys. Rev. **93**, 99 (1954).

[102] Y. Shirasaki, G.J. Supran, M.G. Bawendi, and V. Bulović, *Emergence of colloidal quantum-dot light-emitting technologies*, Nat. Photon. **7**, 13-23 (2013).

[103] V.L. Colvin, M.C. Schlamp, and A.P. Alivisatos, *Light-emitting diodes made from cadmium selenide nanocrystals and a semiconducting polymer*, Nature **370**, 354-357 (1994).

[104] I. Schnitzer, E. Yablonovitch, C. Caneau, T.J. Gmitter, and A. Scherer, 30% *external quantum efficiency from surface textured, thin-film light-emitting diodes*, Appl. Phys. Lett. **63**, 2174 (1993).

[105] M.C. Schlamp, X. Peng, and A.P. Alivisatos, *Improved efficiencies in light emitting diodes made with CdSe(CdS) core/shell type nanocrystals and a semiconducting polymer*, J. Appl. Phys. **82**, 5837 (1997).

[106] S. Coe, W.-K. Woo, M. Bawendi, and V. Bulović, *Electroluminescence from single monolayers of nanocrystals in molecular organic devices*, Nature **480**, 800-803 (2002).

[107] A.H. Mueller, M.A. Petruska, M. Achermann, D.J. Werder, E.A. Akhadov, D.D. Koleske, M.A. Hoffbauer, and V.I. Klimov, *Multicolor light-emitting diodes based on semiconductor nanocrystals encapsulated in GaN charge injection layers*, Nano Lett. **5**, 1039-1044 (2005).

[108] S. Coe-Sullivan, *Nanotechnology for displays: a potential breakthrough for OLED displays and LCDs*, SID Display Week 2012 (2012).

[109] X. Wu, L. Liu, W.C.H. Choy, T. Yu, P. Cai, Y. Gu, Z. Xie, Y. Zhang, L Du, Y. Mo, S. Xu, and Y. Ma, *Substantial performance improvement in inverted polymer light-emitting diodes via surface plasmon resonance induced electrode quenching control*, ACS Appl. Mater. Interfaces **6**, 11001-11006 (2014).

[110] N.-Y. Kim, S.-H. Hong, J.-W. Kang, N. Myoung, S.-Y. Yim, S. Jung, K. Lee, C.W. Tu, and S.-J. Park, *Localized surface plasmon-enhanced green quantum dot light-emitting diodes using gold nanoparticles*, RSC Adv. **5**, 19624-19629 (2015).

[111] X. Yang, P.L. Hernandez-Martinez, C. Dang, E. Mutlugun, K. Zhang, H.V. Demir, and X.W. Sun, *Electroluminescence efficiency enhancement in quantum dot light-emitting diodes by embedding a silver nanoisland layer*, Adv. Opt. Mater. **3**, 1439-1445 (2015).

[112] J. Pan, J. Chen, D. Zhao, Q. Huang, Q. Khan, X. Liu, Z. Tao, Z. Zhang, and W. Lei, *Surface plasmon-enhanced quantum dot light-emitting diodes by incorporating gold nanoparticles*, Opt. Express **24**, A33-A43 (2016).

[113] P. Biagioni, J.-S. Huang, and B. Hecht, *Nanoantennas for visible and infrared radiation*, Rep. Prog. Phys. **75**, 024402 (2012).

[114] T.V. Teperik and A. Degiron, *Numerical analysis of an optical toroidal antenna coupled to a dipolar emitter*, Phys. Rev. B **83**, 245408 (2011).

[115] J. Azoulay, A. Débarre, A. Richard, and P. Tchénio, *Quenching and enhancement of single-molecule fluorescence under metallic and dielectric tips*, Europhys. Lett. **51**, 374 (2000).

[116] M. Thomas, J.-J. Greffet, R. Carminati, and J.R. Arias-Gonzalez, *Single-molecule spontaneous emission close to absorbing nanostructures*, Appl. Phys. Lett. **85**, 3863 (2004).

[117] Y.-P. Hsieh, C.-T. Liang, Y.-F. Chen, C.-W. Lai, and P.-T. Chou, *Mechanism of giant enhancement of light emission from Au/CdSe nanocomposites*, Nanotechnology **18**, 415707 (2007).

[118] K. Hosoki, T. Tayagaki, S. Yamamoto, K. Matsuda, and Y. Kanemitsu, *Direct and stepwise energy transfer from excitons to plasmons in close-packed metal and semiconductor nanoparticle monolayer films*, Phys. Rev. Lett. **100**, 207404 (2008).

[119] M. Haridas, L.N. Tripathi, and J.K. Basu, *Photoluminescence enhancement and quenching in metal-semiconductor quantum dot hybrid arrays*, App. Phys. Lett. **98**, 063305 (2011).

[120] A.E. Ragab, A.-S. Gadallah, T. Da Ros, M.B. Mohamed, and I.M. Azzouz, *Ag surface plasmon enhances luminescence of CdTe QDs*, Opt. Comm. **314**, 86-89 (2014).

[121] L.N. Tripathi, T. Kang, Y.-M. Bahk, S. Han, G. Choi, J. Rhie, J. Jeong, and D.-S. Kim, *Quantum dots-nanogap metamaterials fabrication by self-assembly lithography and photoluminescence studies*, Opt. Express **23**, 14937-14945 (2015).

[122] Q. Le-Van, X. Le Roux, T.V. Teperik, B. Habert, F. Marquier, J.-J. Greffet, and A. Degiron, *Temperature dependence of quantum dot fluorescence assisted by plasmonic nanoantennas*, Phys. Rev. B **91**, 085412 (2015).

[123] A.J. Mork, M.C. Weidman, F. Prins, and W.A. Tisdale, *Magnitude of the Förster radius in colloidal quantum dot solids*, J. Phys. Chem. C **118**, 13920-13928 (2014).

[124] R. Bose, J.F. McMillan, J. Gao, K.M. Rickey, C.J. Chen, D.V. Talapin, C.B. Murray, and C.W. Wong, *Temperature-tuning of near-infrared monodisperse quantum dot solids at 1.5 μm for controllable Förster energy transfer*, Nano Lett. **8**, 2006-2011 (2008).

[125] G. Kirchhoff, *Ueber das Verhältniß zwischen dem Emissionsvermögen und dem Absorptionsvermögen der Körper für Wärme und Licht*, Ann. Phys. **185**, 275-301 (1860).

[126] W. Shockley and H.J. Queisser, *Detailed balance limit of efficiency of $p-n$ junction solar cells*, J. Appl. Phys. **32**, 510 (1961).

[127] P. Würfel, *The chemical potential of radiation*, J. Phys. C: Solid State Phys., **15**, 3967-3985 (1982).

[128] N. Bonod, E. Popov, and M. Nevière, *Differential theory of diffraction by finite cylindrical objects*, J. Opt. Soc. Am. A **22**, 481-490 (2005).

[129] J.-J. Greffet, P. Bouchon, G. Brucoli, E. Sakat, and F. Marquier, *Generalized Kirchhoff law*, arXiv:1601.00312v1 (unpublished).

[130] C.H. Henry and R.F. Kazarinov, *Quantum noise in photonics*, Rev. Mod. Phys. **68**, 801-853 (1996).

[131] C. Otey and S. Fan, *Numerically exact calculation of electromagnetic heat transfer between a dielectric sphere and plate*, Phys. Rev. B **84**, 245431 (2011).

[132] U.K. Chettiar and N. Engheta, *Internal homogenization: Effective permittivity of a coated sphere*, Opt. Express **20**, 22976-22986 (2012).

[133] V. Ernst and P. Stehle, *Emission of radiation from a system of many excited atoms*, Phys. Rev. **176**, 1456 (1968).

[134] N.E. Rehler and J.H. Eberly, *Superradiance*, Phys. Rev. A **3**, 1735 (1971).

[135] H. Labuhn, D. Barredo, S. Ravets, S. de Léséleuc, T. Macrì, T. Lahaye, and A. Browaeys, *Tunable two-dimensional arrays of single Rydberg atoms for realizing quantum Ising models*, Nature **534**, 667-670 (2016).

[136] R. Loudon, *The Quantum Theory of Light*, (Clarendon Press, Oxford, UK, 1986).

[137] B. Huttner and S.M. Barnett, *Quantization of the electromagnetic field in dielectrics*, Phys. Rev. A **46**, 7 (1992).

[138] T. Gruner and D.-G. Welsch, *Green-function approach to the radiation-field quantization for homogeneous and inhomogeneous Kramers-Kronig dielectrics*, Phys. Rev. A **53**, 3 (1996).

[139] T. Gruner and D.-G. Welsch, *Correlation of radiation-field ground-state fluctuations in a dispersive and lossy dielectric* , Phys. Rev. A **51**, 4 (1995).

[140] F. Bigourdan, J.-P. Hugonin, and P. Lalanne, *Aperiodic-Fourier modal method for analysis of body-of-revolution photonic structures*, J. Opt. Soc. Am. A **31**, 1303-1311 (2014).

université PARIS-SACLAY

ÉCOLE DOCTORALE
Ondes et Matière (EDOM)

Titre : Etude théorique de la diffusion et de l'émission de lumière par un ensemble dense de dipôles résonants

Mots clés : diffusion de la lumière, atomes froids, effets collectifs, nanophotonique, optique quantique, électroluminescence, boîtes quantiques

Résumé : Nous présentons une étude théorique des propriétés optiques d'un ensemble dense de dipôles résonants. Nous traitons deux cas particuliers: la diffusion de la lumière par des nuages d'atomes froids et l'électroluminescence par un film de boîtes quantiques colloïdales (BQCs) placées au voisinage d'une métasurface plasmonique. En faisant varier progressivement la densité atomique, nous avons montré que la diffusion de la lumière passe d'un comportement purement diffusif à un comportement mixte comportant à la fois de la diffraction par une particule effective homogène et de la diffusion. Nous avons montré que la lumière n'est plus due à la diffusion par des atomes individuels mais à l'effet de modes collectifs étendus dans tout l'objet. Ces modes microscopiques peuvent être identifiés à des modes des équations de Maxwell pour des objets ayant la même forme et un indice effectif. Nous avons étudié l'apparition du régime d'homogénéisation, c'est-à-dire de la suppression de la partie diffuse. Un nuage atomique, dense au point d'avoir à résonance un indice comparable à celui d'un métal, continue à diffuser fortement la lumière. Finalement, nous avons étudié l'émission de lumière d'un film dense de BQCs. Nous introduisons un modèle de l'électroluminescence de BQCs placées près d'une métasurface plasmonique.

Title: Theoretical study of light scattering and emission from dense ensembles of resonant dipoles

Keywords: light scattering, cold atoms, collective effects, nanophotonics, quantum optics, electroluminescence, quantum dots

Abstract: We present a theoretical study of the optical properties of a dense ensemble of resonant dipoles. We consider two particular cases: scattering of light by cold atomic clouds and electroluminescence by a thin film of colloidal quantum dots (cQDs) placed in the vicinity of a plasmonic metasurface. By numerically varying the atomic density, we have shown that light scattering by an atomic cloud gradually moves from a purely diffusive regime towards a partially diffractive and diffusive one. It has been found that light scattering is no longer due to single atom scattering but due to collective modes extended throughout the sample. These microscopic modes can be identified with the modes of Maxwell's equations for an object with the same shape and an effective refractive index. We have studied the onset of the homogenization regime, namely the suppression of diffuse light. An atomic cloud, with a refractive index at resonance that is comparable to that of a metal, never reaches the homogenization regime and thus continues to scatter light. Finally, we have also studied the electroluminescence of a dense film of cQDs. We propose a model for electroluminescence from cQDs located close to a plasmonic metasurface.